



Kent Academic Repository

Oikonomidou, Sofia Nikoleta (2021) *3D printed Microneedles for Transdermal Drug Delivery*. Doctor of Philosophy (PhD) thesis, University of Kent,.

Downloaded from

<https://kar.kent.ac.uk/93435/> The University of Kent's Academic Repository KAR

The version of record is available from

<https://doi.org/10.22024/UniKent/01.02.93435>

This document version

UNSPECIFIED

DOI for this version

Licence for this version

CC BY (Attribution)

Additional information

Versions of research works

Versions of Record

If this version is the version of record, it is the same as the published version available on the publisher's web site. Cite as the published version.

Author Accepted Manuscripts

If this document is identified as the Author Accepted Manuscript it is the version after peer review but before type setting, copy editing or publisher branding. Cite as Surname, Initial. (Year) 'Title of article'. To be published in *Title of Journal*, Volume and issue numbers [peer-reviewed accepted version]. Available at: DOI or URL (Accessed: date).

Enquiries

If you have questions about this document contact ResearchSupport@kent.ac.uk. Please include the URL of the record in KAR. If you believe that your, or a third party's rights have been compromised through this document please see our [Take Down policy](https://www.kent.ac.uk/guides/kar-the-kent-academic-repository#policies) (available from <https://www.kent.ac.uk/guides/kar-the-kent-academic-repository#policies>).

3D PRINTED MICRONEEDLES FOR TRANSDERMAL DRUG DELIVERY

SOFIA NIKOLETA OIKONOMIDOU

A thesis submitted in partial fulfilment of the requirements of the University of Kent
for the Degree of Doctor of Philosophy in the Medway School of Pharmacy

APRIL 2021

*'The secret of joy in work
is contained in one word-excellence.
To know how to do something is to enjoy it.'*

-Pearl Buck

To love and friendship

DECLARATION

I certify that this work has not been accepted in substance for any degree and is not concurrently being submitted for any degree other than that of Doctor of Philosophy being studied at University of Kent. I also declare that this work is the result of my own investigations except where otherwise identified by references and that I have not plagiarised the work of others.

Parts of this work have been published in:

Economidou, S.N. and Douroumis, D. (2021). 3D printing as a transformative tool for microneedle systems : Recent advances , manufacturing considerations and market potential. *Advanced Drug Delivery Reviews* **173**:60–69.

Economidou, S. *et al.* (2021). Optimisation of Design and Manufacturing Parameters of 3D Printed Solid Microneedles for Improved Strength, Sharpness, and Drug Delivery. *Micromachines* **12**:117.

Economidou, S.N. *et al.* (2021). A novel 3D printed hollow microneedle microelectromechanical system for controlled, personalized transdermal drug delivery. *Additive Manufacturing* **38**:101815.

Economidou, S.N., Lamprou, D.A. and Douroumis, D. (2018). 3D printing applications for transdermal drug delivery. *International Journal of Pharmaceutics* **544**:415–424.

I certify that I am the main contributing author of the aforementioned articles and the text and data from these articles included in the present thesis are products of my own work.



Signed _____ (Student) Ms Sofia Nikoleta Oikonomidou
(S.N. Economidou)

Signed _____ (Supervisor) Professor Dennis Douroumis

Signed _____ (Second supervisor) Dr. Gurprit Lall

Date: _____

ACKNOWLEDGEMENTS

I would like to express my deepest gratitude to all my friends, family and colleagues whose support, guidance, patience and love gave me the strength and motivation to accomplish this lifetime goal.

First, many thanks to my PhD supervisor, Prof. Dennis Douroumis, who believed in me like no other and always supplied his scientific advice and support promptly and efficiently. I would also like to thank all the academics, technicians and collaborators for their valuable contributions to the experimental aspect of the present thesis: Dr Md Jasim Uddin, Dr Manuel J. Marques, Prof. Adrian Podoleanu, Prof. James Windmill, Dr Andrew Reid, Darren Hamilton, Kristian Woodhams and Dr Michael Okereke.

I would also like to thank all of my colleagues in the Douroumis Lab, for their immense support, both professionally and personally. Special thanks go to Dr Cristiane P. Pissinato Pere, who is an example of strength and will power, a truly loving friend and a good teacher. Many thanks to Dr Steven Ross, who always made the time within his busy schedule to help and teach me things in the lab, listen to me and be a valuable and loyal friend.

Moreover, my gratitude goes to the academics and fellow PhD students in Medway School of Pharmacy, especially to my second supervisor, Gurpit Lall as well as Dr Stratos Sitsanidis, Dr Sarah Corlett, Katrin Jones and Dr Elisa Vasilopoulou for helping me go through several hardships.

Of course, I could not leave out the people who inspired me to pursue a career in research. One of the most influential people was Prof. George C. Papanicolaou whose passion for science was a true inspiration for me. I would also like to acknowledge the influence of Prof. Dimitris Karalekas who introduced me to the world of 3D printing and helped me build my career.

I would not have been able to achieve this goal without the support of my beloved friends and family. I would like to thank my parents, Michael and Chryssoula, for inspiring my love for learning, for motivating and supporting me to fulfill my dreams and for teaching me to fight, stay strong, stay grounded and believe in myself. I would also like to thank my stepparents, Vaggelis and Stamatia for their kind support and my

brothers, Lampros and Aggelos for bearing with me and being such good brothers. I deeply thank my dearest late grandmother, Sophia, whose unconditional love made me the person I am today and is so greatly missed. Last but not least, I want to thank my best friend and now family, Despoina, and my life partner, Tassos, who have been true pillars throughout my life.

ABSTRACT

3D printing is a revolutionary manufacturing and prototyping technology that has altered the outlooks of numerous industrial and scientific fields since its introduction. Recently, it has attracted attention for its potential as a manufacturing tool for transdermal microneedles for drug delivery. In the present thesis, the 3D printability of solid and hollow microneedles via photopolymerisation-based 3D printing was investigated, aiming at establishing robust manufacturing strategies for reproducible, mechanically strong and versatile microneedles. The developed microneedles were employed as drug delivery systems for the treatment of diabetes via insulin administration.

Solid microneedles featuring different geometries were designed and 3D printed. It was demonstrated that the printing and post-printing parameters affected the printed quality, a finding that was employed to optimise the manufacturing strategy. Microneedle geometry was also found to have an impact on the piercing and fracture behaviour; however all microneedle designs were found to be mechanically safe upon application. The solid microneedles were subsequently coated with insulin-polymer films, using a 2D inkjet printing technology. The coating process achieved spatial control of the drug deposition, with quantitative accuracy. The microneedle geometry was shown to influence the morphology of the coating film, an effect that was pronounced during in the *in vitro* delivery studies of insulin to porcine skin.

Furthermore, hollow microneedles were designed and 3D printed, featuring different heights. Two photopolymerisation-based technologies were studied, and their performance was compared. The key influential parameters of the printing outcome and microneedle quality were identified to be the printing angle and the size of the microneedle opening. The hollow microneedles were found to be effective in piercing porcine skin without structural damaging. The hollow microneedles were incorporated into complex patches with internal microfluidic structures for the provision and distribution of drug-containing solutions. The developed complex hollow microneedle patches were coupled with a microelectromechanical system to create a novel platform device for controlled, personalised transdermal drug delivery. Advanced imaging techniques revealed that the device achieved distribution of the liquid within porcine skin tissue without the creation of depots that would delay absorption. The device was

evaluated for its efficacy to transdermally deliver a model dye and insulin *in vitro*. *In vivo* trials were also conducted using diabetic rodents, with the device achieving faster onset of insulin action and sustained glycemic control, in comparison to subcutaneous injections.

Overall, the findings of the present research are anticipated to elucidate key problematic areas associated with the application of 3D printing for microneedle manufacturing and propose feasible solutions. The outermost goal of this work is to contribute to the advancement of knowledge in the field of 3D printed transdermal drug delivery systems, in order to bring them one step closer to their adoption in the clinical setting.

TABLE OF CONTENTS

CHAPTER 1 INTRODUCTION AND LITERATURE REVIEW	1
1.1 The structure and barrier function of the human skin	2
1.2 Transdermal Drug Delivery	4
1.3 Passive Transdermal Drug Delivery Systems	5
1.4 Drug Penetration Enhancers.....	7
1.5 Microneedles	7
1.5.1 Microneedle types and delivery mechanisms	8
1.5.2 Conventional microneedle manufacturing methods.....	12
1.5.3 Microneedle-mediated diabetes therapy	12
1.6 3D printing	14
1.6.1 Inkjet 3D printing.....	15
1.6.2 Photopolymerisation-based 3D printing	17
1.6.2.1 Laser Stereolithography: Two-Photon Polymerisation and conventional technologies.....	18
1.6.2.2 Projection Stereolithography: Digital Light Processing and Continuous Liquid Interphase Printing	23
1.6.3 Extrusion-based printing	29
1.7 Applicability of 3D printing for microneedle fabrication: Technical challenges	31
1.7.1 Resolution	31
1.7.2 Materials.....	33

1.8 Regulatory framework	39
1.9 3D printed microneedles: Potential market and societal impact.....	41
1.10 Key objectives	43
CHAPTER 2 3D PRINTED SOLID MICRONEEDLES.....	44
2.1 INTRODUCTION	44
2.1.1 Aims and objectives	45
2.2 MATERIALS AND METHODS	46
2.2.1 Computer Aided Design (CAD)	46
2.2.2 Additive Manufacturing and printing material	46
2.2.3 Dental SG compression testing	47
2.2.4 Scanning Electron Microscopy (SEM)	47
2.2.5 Preparation of porcine skin samples	47
2.2.6 Piercing tests in porcine skin.....	47
2.2.7 Axial force mechanical testing.....	48
2.2.8 Margin of safety	48
2.3 RESULTS AND DISCUSSION	48
2.3.1 Microneedle design	48
2.3.2 3D printing	52
2.3.3 Optimisation of post-printing curing conditions for enhanced mechanical properties.....	53
2.3.4 Optimisation of printing angle	55
2.3.5 Piercing tests	60

2.3.6 Microneedle axial force mechanical testing.....	63
2.3.7 Safety Index	66
2.4 CONCLUSIONS.....	66
CHAPTER 3 INKJET 2D PRINTING OF DRUG FILMS ON 3D PRINTED SOLID MICRONEEDLES	68
3.1 INTRODUCTION	68
3.1.1 Aims and objectives	69
3.2 MATERIALS AND METHODS.....	70
3.2.1 Materials.....	70
3.2.2 Coating formulations.....	70
3.2.3 Inkjet 2D printing of insulin films on 3D printed microneedles.....	70
3.2.4 Scanning Electron Microscopy	71
3.2.5 Circular Dichroism (CD)	71
3.2.6 Stability of insulin films.....	71
3.2.7 Geometrical modelling of droplet on a curved surface.....	72
3.2.8 High Performance Liquid Chromatography (HPLC) method and validation.....	73
3.2.9 Coating efficiency	75
3.2.10 Preparation of porcine skin samples	75
3.2.11 <i>In vitro</i> release of insulin.....	75
3.3 RESULTS AND DISCUSSION	76
3.3.1 Inkjet Coating.....	76
3.3.2 Correlation of microneedle geometry with coating morphology	78

3.3.4 Circular Dichroism (CD)	80
3.3.5 Insulin stability.....	85
3.3.6 High Performance Liquid Chromatography (HPLC) method and validation.....	87
3.3.7 Coating efficiency	92
3.3.8 <i>In vitro</i> release studies.....	92
3.4 CONCLUSIONS.....	94
CHAPTER 4 3D PRINTED HOLLOW MICRONEEDLES.....	95
4.1 INTRODUCTION	95
4.1.1 Aims and objectives	96
4.2 MATERIALS AND METHODS.....	97
4.2.1 Materials.....	97
4.2.2 Computer Aided Design (CAD) of hollow microneedles and complex patches	98
4.2.2 Additive Manufacturing: Stereolithography and Digital Light Processing	99
4.2.3 Scanning Electron Microscopy	99
4.2.4 Preparation of porcine skin for insertion tests.....	100
4.2.5 Insertion tests in porcine skin.....	100
4.2.6 Axial force compression testing.....	100
4.2.7 Margin of safety	100
4.3 RESULTS AND DISCUSSION	101
4.3.1 Design and Additive Manufacturing of tall hollow microneedles	101
4.3.2 Design and Additive Manufacturing of short hollow microneedles	107

4.3.3 Skin insertion testing.....	113
4.3.4 Axial force compression testing.....	115
4.3.6 Margin of safety	118
4.3.7 Development of complex microneedle patch with microfluidic internal structures .	119
4.4 CONCLUSIONS.....	125
CHAPTER 5 3DMNMEMS	127
5.1 INTRODUCTION	127
5.1.1 Aims and objectives	128
5.2 MATERIALS AND METHODS.....	129
5.2.1 Materials.....	129
5.2.2 Fabrication of the hollow microneedle patch.....	129
5.2.3 Microelectromechanical System (MEMS).....	129
5.2.4 X-ray Micro Computer Tomography	130
5.2.5 Preparation of porcine skin samples	130
5.2.6 Optical Coherence Tomography	131
5.2.7 <i>In vitro</i> release studies in porcine skin.....	131
5.2.8 UV/Vis Spectrophotometry.....	132
5.2.9 High-performance liquid chromatography (HPLC).....	132
5.2.10 <i>In vivo</i> clinical studies	132
5.3 RESULTS AND DISCUSSION	133
5.3.1 The 3D printed microneedle patch.....	133

5.3.2 X-ray Micro Computer Tomography (μ CT).....	135
5.3.3 Development of the 3DMNMEMS and accuracy evaluation	136
5.3.4 Optical Coherence Tomography	138
5.3.5 <i>In vitro</i> release through porcine skin.....	142
5.3.6 <i>In vivo</i> clinical studies	144
5.4 CONCLUSIONS.....	149
CHAPTER 6 GENERAL CONCLUSIONS.....	151
CHAPTER 7 FUTURE WORK.....	153
REFERENCES.....	155
APPENDIX I	176

LIST OF FIGURES

Figure 1.1 Skin structure	3
Figure 1.2 Microneedle types and delivery mechanisms (a) Solid microneedles that are applied and removed to create transient micropores, followed by application of the API on the skin; (b) Solid microneedles coated with drug for instant delivery, which are removed after the coating material dissolves; (c) Soluble polymeric microneedles containing drug that dissolves in skin interstitial fluid over time, thereby delivering the drug; (d) Hollow microneedles for delivery of fluids containing drug; (e) Novel hydrogel-forming polymeric microneedles for controlled transdermal drug delivery (Rzhevskiy <i>et al.</i> 2018).	11
Figure 1.3 Schematic illustration of 3D printing technologies that have been used for the fabrication of TDD systems. a) Inkjet; b) Fused Deposition Modelling (FDM); c) Laser Stereolithography (Laser SLA); d) Digital Light Processing (DLP)	14
Figure 1.4 SEM images of 2PP printed microneedles. (a) cylindrical polymer microneedle, blank and (b) coated with a 120 nm thick Fe layer; (c) patch of cylindrical needles after coating with 6 μm length and 12 μm pitch on a silicon substrate; (d) 3D printed pyramid microneedle with triangular base and (e) square base; (f) cylindrical microneedle with sharp tip and (g) conical needles with their respective arrays on a Si polished substrate (Kavalzhiev <i>et al.</i> 2017).	21
Figure 1.5 Photopolymerisation-based 3D printing of microneedle masters for micromoulding. a) hollow prototypes with interconnecting channels fabricated by 2PP (Faraji Rad <i>et al.</i> 2017), b) pyramidal microneedle masters with bio-inspired surface microstructures made by 2PP (Plamadeala <i>et al.</i> 2020), c) microneedle basins made by laser SLA, d) microneedle masters fabricated via laser SLA (Lopez-Ramirez <i>et al.</i> 2020) and e) microneedle prototypes made by DLP (Johnson and Procopio 2019).....	25
Figure 1.6 SLA and DLP microneedle printing using the direct, single step approach. (a) Hollow laser SLA printed microneedles (Yeung <i>et al.</i> 2019), (b) solid laser SLA printed microneedles coated by inkjet 2D printing with anti-cancer agents, (c) CLIP fabricated polycaprolactone microneedles, (d) multifunctional hydrogel microneedle fabricated via DLP (Yao <i>et al.</i> 2020) and (e) 3D scan of human volunteer employed to print customized microneedle patches (f), (g) SEM image of the microneedle on the curved patch (Lim <i>et al.</i> 2020).....	28

Figure 1.7 Extrusion based microneedle printing using the direct approach, combined with post-printing processing for microneedle refinement. (a) FDM printed microneedles before and (b) after chemical etching (Luzuriaga <i>et al.</i> 2018), (c) bioprinted microneedles before and (d) after stretching (Wu <i>et al.</i> 2020).....	30
Figure 2.1 Engineering drawings of a) pyramid, b) cone and c) spear microneedle patch.	52
Figure 2.2 Optimisation of post-printing curing regime in respect to compressive mechanical properties: (a) Digital image of compression specimens for different curing settings, (b) compression testing in progress, with the specimen displaying the ‘barrelling’ effect, (c) compressive moduli, and (d) yield strengths obtained by specimens subjected to different curing regimes.	55
Figure 2.3 Optimisation of the printing angle. (a,b,c) CAD captions; (d,h,l) virtual models of supported microneedle arrays for 0°, 90° and 45°, where the bottom of the base is adhered to the printing platform; (e,f,g) SEM captions of microneedles built at 0°; (i,j,k) SEM captions of microneedles built at 90°; and (m,n,o) SEM captions of microneedles built at 45°	57
Figure 2.4 Dimensional discrepancies of printed microneedles in respect to printing angle; (a) tip diameter; (b) height at the longitudinal axis; and (c) width at the base.....	58
Figure 2.5 Piercing tests (a) schematic configuration, (b) digital photograph captured when the moving probe has inserted the microneedles into the skin sample.....	60
Figure 2.6 Post-piercing digital images of the porcine skin samples with (a) cone, (c) pyramid, and (e) spear microneedles; and (b,d,f) post-testing SEM images of the microneedle tips.	61
Figure 2.7 Data derived from piercing tests: (a) force/needle vs displacement data for all designs; (b) insertion force/needle.	63
Figure 2.8 Microneedle fracture testing for different microneedle geometries (a) Schematic representation of the experimental configuration, (b) Force vs. displacement curve, featuring magnified captions at the fracture points and (c) fracture forces.	65
Figure 3.1 Microneedle coating. (a) Nanoplotter coating configuration, (b) Nanoplotter camera caption post-coating, showing the coalesced droplets prior to solvent evaporation and film formation, (c) SEM caption showing the spatially controlled	

coating on the 3D printed microneedles and (d) SEM caption of spear microneedles coated on both lateral surfaces.	77
Figure 3.2 Inkjet coating; (a,b) static contact angle of inkjet droplet upon impingement on the microneedle surface for convex (cone) and flat (spear and pyramid) surfaces; (c,d,e) scheme of the coating configuration for cone, pyramid, and spear microneedles; and (f,g,h) SEM images of the coated microneedles.	80
Figure 3.3 Far UV CD spectrum of insulin solution (1 mg mL ⁻¹).	81
Figure 3.4 Far UV spectra of pure insulin solution (1 mg mL ⁻¹) and insulin-polymer formulations in solution (5:1).....	82
Figure 3.5 Far UV spectra of insulin-polymer films rehydrated in PBS 7.4 and insulin solution (1 mg mL ⁻¹).	83
Figure 3.6 Far UV spectra of insulin solution (1 mg mL ⁻¹) and insulin-polymer films after storage for 14 days at 4±1°C and rehydration in PBS 7.4.	86
Figure 3.7 Far UV CD spectra of the rehydrated insulin-polymer films in PBS 7.4, analysed at (a) T ₀ and (b) T ₁₄	87
Figure 3.8 Chromatograms of (a) pure insulin solution, (b) insulin-PVP formulation and (c) insulin-P407 formulation.	88
Figure 3.9 Calibration curve and regression line	89
Figure 3.11 Insulin chromatogram at 7 µg/mL	91
Figure 3.12 Cumulative release profiles for insulin delivered by 3D printed coated microneedles with polymers as carriers; (a) P407; (b) PVP.	93
Figure 4.1 Tall Bevel microneedles. (a) Engineering designs and (b) SEM of the printed structures.	103
Figure 4.2 Tall Ellipsis400150 microneedles. (a) Engineering designs and (b) SEM of the printed structures.	104
Figure 4.3 Gaussian distribution of laser radiance when the laser cures two spots in close proximity. Recurring exposure due to overlapping of the Gaussian tails can cause dimensional discrepancies.....	104
Figure 4.4 Tall Ellipsis600200 microneedles. (a) Engineering designs and (b) SEM of the printed structures.	105

Figure 4.5 Short Ellipsis400300 microneedles. (a) Engineering designs and SEM images of the structures printed with (b) laser SLA and (c) DLP.....	108
Figure 4.6 Short Ellipsis300150 microneedles. (a) Engineering designs and (b) SEM images of the structures printed with DLP.....	110
Figure 4.7 SEM images of short 3D printed microneedles (height=500 μm). (a) SLA printed Ellipsis400300, (b) DLP printed Ellipsis400300 (printing angle=45°) and (c) DLP printed Ellipsis300150 (printing angle=0°).	112
Figure 4.8 Piercing test of tall hollow microneedles. a) Force vs displacement curve obtained from microneedle insertion in porcine skin using a Texture Analyzer and b) pores in porcine skin after test.	114
Figure 4.9 Insertion testing of short hollow microneedles printed with SLA and DLP in porcine skin. (a) Force vs displacement curve and (b) post printing image of the porcine skin sample.....	115
Figure 4.10 Force per needle vs displacement curve from fracture testing of tall hollow microneedles.	117
Figure 4.11 Force per needle vs displacement curve from fracture testing of short hollow microneedles printed by laser SLA and DLP. Dash lines are linear regressions of the initial segment with intercept at (0,0).....	118
Figure 4.12 Complex microneedle patch for fluid entry and circulation with internal reservoir. (a) Engineering designs. Virtual 3D model sectioned at (b) a plane parallel to the microneedle height and (c) the plane perpendicular to the patch thickness, at the height of the reservoir.	121
Figure 4.13 Digital images of the complex microneedle patch with internal reservoir printed with SLA. (a) Post-curing image and (b) ejection of fluid from the microneedles.	122
Figure 4.14 Complex microneedle patch for fluid entry and circulation with internal microchannels. (a) Engineering designs. Virtual 3D model sectioned at (b) a plane parallel to the microneedle height and (c) the plane perpendicular to the patch thickness, at the height of the microchannels.	123
Figure 15 Complex microneedle patches with internal microchannel circulation systems. (a) SLA printed patch, featuring tall hollow microneedles. The formation of	

the microchannels was unsuccessful. (b) DLP printed patch, featuring short hollow microneedles, filled with red dye (spots are residuals of the support contact points, which are superficial on the bottom of the patch and not influence functionality)..... 124

Figure 5.1 Hollow microneedle complex patch for integration with MEMS 134

Figure 5.2 μ CT images of the hollow microneedle patch. (a) Caption of the whole patch, (b) tomographic caption of the horizontal cross section bellow the microneedle bores and (c) tomographic caption of the perpendicular cross section, sectioning along the longitudinal axes of the microneedle shafts. The images reveal that internal structures have been printed accurately and no internal blockages will obstruct fluid circulation. 136

Figure 5.3 Assembled 3DMNMEMS device 138

Figure 5.4 OCT image of a MN inserted in a sample of full thickness porcine skin.... 139

Figure 5.5 OCT captions of the progressive distribution of liquid solution (marked with green arrows) delivered from a single microneedle (red dashed arrows indicate the microneedle tip) within porcine skin tissue. The captions a-d were sequentially captured. The recorded video can be found as Supplementary Material of the respective published article (Economidou *et al.* 2021) 141

Figure 5.6 Cumulative *in vitro* release of sodium fluorescein salt injected to porcine skin by the 3DMNMEMS. 143

Figure 5.7 Cumulative *in vitro* release of insulin injected to porcine skin by the 3DMNMEMS..... 144

Figure 5.8 *In vivo* animal studies using a diabetic mice model for the treatment of diabetes using the 3DMNMEMS. a) No restriction of in-house movement 2 hours prior to the experiment, b) blank application site after shaving, c) application of the 3D printed hollow MN patch, d) after insulin delivery using the 3DMNMEMS, e) after-piercing pores after treatment, f) No pores 5 minutes after treatment. 145

Figure 5.9 Plasma glucose levels after insulin administration..... 146

Figure 5.10 Plasma insulin levels after insulin administration. 147

LIST OF TABLES

Table 1.1 Custom and commercial 3D printable materials that have been employed for direct microneedle printing. The exact composition of the commercial resins mentioned here is proprietary and minimal information on the constituents is available.	34
Table 2.1 Microneedle Computer Aided Design (CAD) dimensions.	50
Table 2.2 Margins of safety for different microneedle geometries.	66
Table 3.1 Secondary structure of insulin in pure solution, insulin-polymer solutions and insulin-polymer films after rehydration in PBS 7.4, estimated by CDSSTR.	84
Table 3.2 Secondary structure of insulin-polymer films after storage at $4\pm 1^{\circ}\text{C}$ for 14 days and subsequent rehydration in PBS 7.4, estimated by CDSSTR.	86
Table 3.3 Parameters of linear regression of the calibration curve.	89
Table 3.4 Repeatability (Intraday) test.	90
Table 3.5 Reproducibility test.	90
Table 3.6 Accuracy evaluation.	91
Table 3.7 Coating efficiency for insulin-polymer coated microneedle arrays.	92
Table 4.1 CAD dimensions of hollow microneedles.	98
Table 4.2 Theoretical and experimentally measured dimensions and dimensional error of tall hollow microneedles (Ellipsis600200) printed by SLA. Experimentally obtained dimensions are given in mean \pm SD.	106
Table 4.3 Theoretical and experimentally measured dimensions and dimensional error of short hollow microneedles (Ellipsis400300) printed by SLA and DLP. Experimentally obtained dimensions are given in mean \pm SD.	109
Table 4.4 Theoretical and experimentally measured dimensions and dimensional error of short hollow microneedles (Ellipsis300150) printed by SLA and DLP. Experimentally obtained dimensions are given in mean \pm SD.	111
Table 4.5 Mechanical properties and margin of safety of tall and short 3D printed hollow microneedles.	119
Table 5.1 Pharmacodynamic parameters of insulin administration.	148
Table 5.2 Pharmacokinetic parameters of insulin administration.	148

ABBREVIATIONS

2PP	Two Photon Polymerisation
3D	Three Dimensional
3DMNMEMS	3D Microneedle Microelectromechanical System Device
AM	Additive Manufacturing
ASTM	American Society for Testing of Materials
CAD	Computer Aided Design
CD	Circular Dichroism
CIJ	Continuous Inkjet
DoD	Drop-on-Demand
DLP	Digital Light Processing
FDA	Food and Drug Administration
FDM	Fused Deposition Modelling
HPLC	High Performance Liquid Chromatography
LOD	Limit of Detection
LOQ	Limit of Quantification
MEMS	Microelectromechanical System
MN	Microneedle
OCT	Optical Coherence Tomography
P127	Pluronic 127
PVP	Polyvinylpyrrolidone
R&D	Research and Development
SD	Standard Deviation
SEM	Scanning Electron Microscopy
SFF	Solid Freeform Fabrication
SLA	Stereolithography
TDD	Transdermal Drug Delivery
UV	Ultraviolet
μCT	Micro Computer Tomography

CHAPTER 1

INTRODUCTION AND LITERATURE REVIEW

Very few newly introduced technologies have had such a universally transformative impact as 3D printing. Since its launch in the 1980s, 3D printing has revolutionised numerous fields, as it enables the fast and accurate production of structures and components with levels of complexity that are unattainable through conventional techniques. 3D printing is viewed by industries as a promising alternative to lengthy, labour intensive processes for prototyping and production of functional parts, able to proactively contribute to the minimisation of fabrication times and the simplification of production lines.

In the biomedical field, the use of 3D printing has already had a significant effect, with numerous products currently available in the market (Liaw and Guvendiren 2017) and diverse research output, including hard tissue restorations (Chen *et al.* 2016; Khorsandi *et al.* 2021; Pan *et al.* 2020), models for surgical preparation and educational purposes (Anderson 2019; Ballard *et al.* 2020) and tissue engineering (Wang *et al.* 2020; Hassan *et al.* 2019; Nestic *et al.* 2020). Moreover, scientists have envisioned the unique prospects of 3D printing, due to its fast and customisable nature, to fundamentally alter how patients are treated, aiming at taking modern therapeutics from the massively produced to the customised. The shift towards a more personalised patient care is a global trend in medicine and pharmaceuticals. In this context, traditional fabrication methods of drug delivery systems that are mass-produced and mass-oriented are questioned in terms of permitting the tailoring of dosages according to individual patients' needs in a cost-effective and direct manner. Indeed, 3D printed implants and prosthetics have been proposed, with tailored, patient-specific characteristics (Wong 2016). As anticipated, endeavours to explore the potential of this sophisticated technology in drug delivery have already been fruitful, with the first 3D printed oral administration tablet, *Spritam*, to gain FDA approval and the term 'pharmacoprinting' to be introduced (Jacob *et al.* 2016; Goyanes *et al.* 2015; Di Prima *et al.* 2015).

Estimations of a booming market for 3D printed pharmaceuticals of up to 522\$ million by 2030 (Jaiswal and Srivastava 2017) have ignited vast interest in these products with

vivid research being conducted on the applicability of different 3D printing technologies on the development of tablets and drug delivery devices (Trenfield *et al.* 2019; Mao *et al.* 2017).

Among the various drug delivery routes, the transdermal one can be profoundly benefited by the adoption of advanced Additive Manufacturing techniques. Transdermal Drug Delivery (TDD) systems were revolutionised by the introduction of microneedle devices and 3D printing can tackle challenges associated with their traditional manufacturing methods. Evidently, the versatility, simplicity, high reproducibility and accuracy in the microscale associated by default with 3D printing have encouraged research on its applicability on the fabrication of transdermal microneedle systems.

In the present thesis, the untapped potential of 3D printing as a viable, reliable and efficient transdermal microneedle manufacturing technique are investigated. In this chapter, a systematic literature review is put forward, in order for the respective challenges and opportunities to be identified.

1.1 The structure and barrier function of the human skin

The skin is a large organ in the human body, with a surface area ranging between 1.5-2 m² in adults (Waugh and Grant 2014). It has a multifunctional role and is instrumental in critical functions of the human organism such as in maintaining homeostasis and hydration, protection from exogenous threats, thermoregulation and sensory perception. The skin also bears accessory appendages such as hair follicles, sebaceous and sweat glands (Vasudeva and Mishra 2016). Owing to the nature of its unique, multilayered structure, the skin furnishes a highly selective, mostly impermeable barrier. The human skin features a laminate-like configuration, consisting of physiologically distinct layers, namely the epidermis and the dermis, followed by the subcutaneous tissue, called the hypodermis (Figure 1.1).

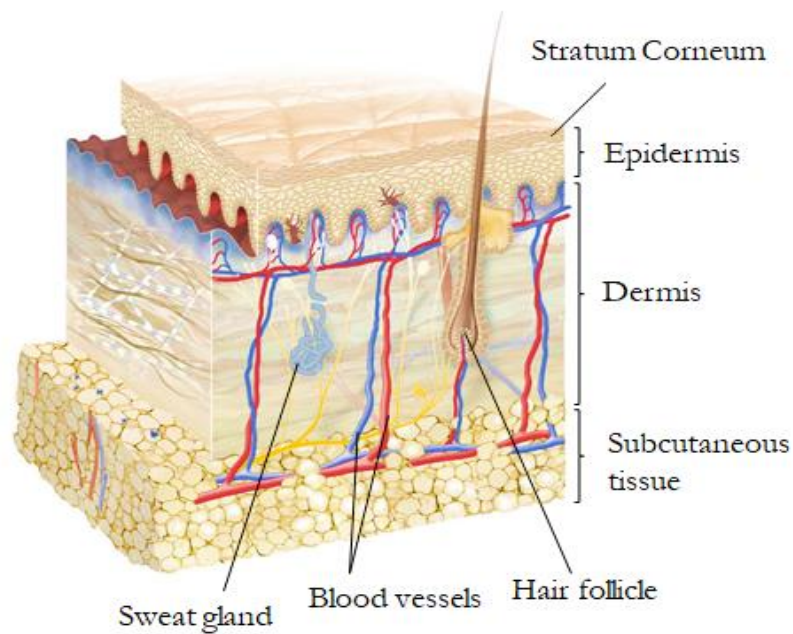


Figure 1.1 Skin structure

The hypodermis or subcutis, comprises connective (areolar) and adipose (fat) tissue and connects the skin with the underlying organs (e.g. muscle and bones). Above the hypodermis, the dermis is the thickest skin layer and consists of collagen and elastic fibres. It contains the dermal capillary system as well as nerves, glands, lymphatic vessels and hair follicles (Agarwal and Krishnamurthy 2019).

Shielding the dermis, the epidermis is the superficial layer of the skin. It is thinner, devoid of blood vessels and features its own distinctive stratification (Yousef *et al.* 2020). Among the epidermal layers (*strata*), the *stratum spinosum* contains dendritic (Langerhans) cells, which are considered as ‘first line defenders’ against pathogens, contributing to the stimulation of the immune response (Yousef *et al.* 2020). The outermost layer, the *stratum corneum* plays the dominant role in the impermeability of the skin barrier since it is very dense and very low in hydration (15-20%). It primarily consists of compressed keratin filled corneocytes (terminally differentiated keratinocytes), arranged in a laminate fashion. The corneocytes are embedded in a lipophilic matrix in a brick-and-mortar arrangement which enmeshes the diffusion conduits, endowing hence the membrane with very low permeability.

Despite the barrier function of the skin, owed to the physiology of the *stratum corneum*, the application of various therapeutic substances such as herbal ointments and various drugs on the human skin is an ancient practice for medical as well as for cosmetic purposes. Skin has always offered a large, ‘easily’ accessible area for drug administration and the increasing interest in the transdermal route is illustrated by the vivid scientific progress in the field during the past decades (Prausnitz and Langer 2009; Alkilani, McCrudden and Donnelly 2015; Pastore *et al.* 2015).

1.2 Transdermal Drug Delivery

TDD is an appealing alternative to the traditional administration routes, orally or through hypodermic injections. The oral route has been associated with efficiency issues in cases of partial drug absorption, gastrointestinal metabolism-related complications and lags in its effect that render it prohibitory for emergency cases. On the other hand, hypodermic injections are invasive and irritating, pose risks of infection (e.g. poor sanitation, immunosuppressed patients, needle re-usage in developing countries), require administration by medically trained professionals and generate medical waste (Awodele, Adewoye and Oparah 2016). On the contrary, in transdermal delivery the drug does not pass through any metabolic systems, potentially yielding higher degrees of bioavailability while it can be used as a tool to promote the sustained and controlled drug release. Moreover, due to the plethora of dendritic cells in the skin, vaccination through TDD is a promising alternative to typical vaccination routes. Furthermore, it is a patient-friendly approach since it is non-invasive, contributing thus to the psychological welfare of the patient. TDD delivery systems do not also require professional care and experience when repositioning, removal or replacement is required, promoting patients’ independence.

Albeit its numerous advantages, the progress of TDD has been hampered by the nature of the skin barrier. Traditional systems, wherein a molecule is expected to naturally permeate the skin and reach the rich capillary bed of the dermis, suffer from the high selectivity of the *stratum corneum* in regard to the molecules that are ‘allowed’ to permeate the skin barrier. In such systems, percutaneous drug absorption is driven by passive diffusion kinetics, governed by the Fick’s law (Couto *et al.* 2014):

$$\frac{dm}{dt} = \frac{DK(C_d - C_r)}{h} \quad \text{Equation 1.1}$$

Where:

$\frac{dm}{dt}$: rate of permeation (flux)

D: diffusion coefficient,

C_d : concentration in donor (surface on SC)

C_r : concentration in recipient (body)

K: partition coefficient of solute between membrane and bathing solution

h: thickness of the membrane

Equation 1.1 depicts that an increased rate of permeation is generated by molecules of high diffusion coefficients (e.g. low molecular masses) and high partition coefficients. The aforementioned demonstrate that the right physicochemical properties are a precondition for drugs that are candidates for transdermal delivery via passive diffusion. Indeed, only relatively small (>500 Da) and lipophilic molecules can cross the skin in therapeutically significant amounts (Bos and Meinardi 2000). Moreover, the pharmacological potency of the drug is an essential attribute to achieve a therapeutically significant effect. Evidently, these limitations narrow down the drug palette notably, while pose serious challenges regarding the transdermal delivery of a broader range of drugs with larger molecular masses or hydrophilic features as well as of peptides and macromolecules. Circumventing, neutralizing or bypassing this impermeable barrier has been the actual research subject behind the TDD science and simultaneously the key to its future progress.

1.3 Passive Transdermal Drug Delivery Systems

The first TDD systems featured the application of the medicine-containing formulation directly onto the skin, allowing for the absorption of drug molecules and their entrapment within the stratum corneum. The latter then operated as a tank, slowly channelling the drug into the epidermis. In the early systems, the whole drug amount

was administered in one single dosage, through the topical application of ointments, gels and sprays, a method applied mainly for treating vascular diseases and hormone replacement (Prausnitz and Langer 2009).

A major step in the evolution of transdermal therapy was the transition from the patchless delivery modes to the TDD patch in the 1970s. The introduction of the scopolamine patch (Graybiel, Knepton and Shaw 1976) aiming to a more sustained, controlled and safe mode of drug delivery, commenced a new era in the field.

The drug-storing transdermal patch is a multi-layered structure that generates a steady drug flux to the skin, permitting thus the continuous delivery within a prolonged period of time. Patches are designed following two distinct strategies; the first design, the 'reservoir patch', includes a compartment where the drug is stored in an appropriate formulation, while a membrane governs the delivery to the skin surface. This design yields generally stable release rates (Shaw and Theeuwes 1985), yet overdose incidents have been reported due to defective membranes (Mansfield and Jatoi 2013). On the other hand, the 'matrix patch' was designed in an attempt to avoid the drawbacks of the reservoir-type patch and features the incorporation of the drug uniformly into a matrix, from which it is released to the skin (Pastore *et al.* 2015). There are two main subcategories of this design, the first consists of a drug-containing polymer, while an adhesive substance is added to the system to reassure a stable fitting onto the skin. Alternatively, the design includes only the adhesive, where the drug is contained.

TDD patches initially gained a significant popularity with a number of patch-based systems actually being commercialised. Nowadays, there is a range of commercial patches for the administration of various drugs, such as antidepressants under the name Emsam (Jessen, Kovalick and Azzaro 2008), contraceptives under the name Evra™/Ortho Evra™ (Abrams *et al.* 2002) and for the treatment of Alzheimer's symptoms under the name Exelon (Dhillon 2011).

However, the broader adoption and application of the transdermal patch was hampered by a number of restrictive factors. Initially, due to the fact that after the absorption the drug is initially stored into the stratum corneum and then is gradually diffused to the lower tissues, there is a time interval between the system application and the effective drug concentration reaches a minimum therapeutic value. In this framework, efficiency issues may arise in case of drug crystallisation on the skin until diffusion or within the

formulation during storage (Hadgraft and Lane 2016). Moreover, the microporous membranes employed in the reservoir-type patch, reassure that the delivery rate is much lower than the rate of natural skin absorption, which hinders the potential of delivery in higher rates. Therefore, it is evident that for both patch designs, the maximum delivery rate reachable is equal to the one that is naturally permitted by the physiology of the stratum corneum. The forenamed limitations illustrate that those systems are unsuitable for fast, bolus-type drug administration.

1.4 Drug Penetration Enhancers

To circumvent the aforementioned issues, several permeability enhancing methods have been introduced over the years, aiming at modulating the permeability of the skin and boosting transdermal drug transportation. Such methods include iontophoresis, through the use of low-level electrical current (Ita 2016), electroporation, through the application of high-voltage pulses (Escobar-Chávez *et al.* 2009), microdermabrasion to abrade the stratum corneum (Andrews *et al.* 2011), ultrasounds (Oberli *et al.* 2014) and chemical enhancers (B. Ita 2015). It is nonetheless notable, that the majority for these approaches has been associated with excessive costs, skin irritation and pain (Alkilani, McCrudden and Donnelly 2015).

1.5 Microneedles

After the limited success that permeation enhancers had in incorporating a larger variety of drugs in cost-effective and patient-compliant solutions, the idea that changed the way those systems are perceived and developed is summed up in the question: *Why not simply bypass the stratum corneum?* In this rather entrepreneurial logic, the concept of small, minimally invasive, micro-sized puncturing devices called microneedles was developed. Such devices efficiently disrupt the outermost, most impermeable layers of the skin to create drug transportation pathways directly to the dermal microcirculation. Microneedles and their applications have been the subject of thorough investigation in the previous few decades and they are considered significantly promising since their potential is not circumscribed by the permeability restrictions of the stratum corneum

(Prausnitz 2004). In that logic, the introduction of microneedles opened new pathways in the TDD field, wherein their potential for the delivery of hydrophilic drugs, vaccines and macromolecules was acknowledged early on (Vrdoljak *et al.* 2016; Wang, Hu and Xu 2017; Zhao *et al.* 2017).

Microneedles are designed in multimember arrays, with varying microneedle numbers, anchored on a substrate. Their design goal is twofold: disrupt the epidermal barrier while causing minimal pain. Hence, their dimensions, while varying, range within values that serve this goal. Their height (150 to 1500 μm) reassures that the needles will reach the depth of the skin's capillary system, while their diameter (50 to 250 μm in width and 1 to 25 μm in tip) ascertains that nerves contained in the dermis layer will remain intact upon application (Waghule *et al.* 2019). This absence of pain in combination to the ability of self-application, makes microneedle systems highly patient-compliant.

1.5.1 Microneedle types and delivery mechanisms

Microneedle systems enable the realisation of multiple drug delivery approaches, either using the device solely as a permeation enhancer (e.g., 'poke and patch') or to actively drive the drug through the skin to the systemic circulation. In the latter, the microneedle role is twofold, as they effectively puncture the skin while they operate as vessels carrying the Active Pharmaceutical Ingredient (API). Each drug delivery mechanism requires a different type of microneedle, which can be classified to solid, hollow, dissolvable and hydrogel-forming (Rzhevskiy *et al.* 2018) and can be very diverse in regard to the materials they are constructed from. Figure 1.2 schematically illustrates the various microneedle types and delivery mechanisms.

- Solid

Solid microneedles were employed in initial studies as a permeability enhancer prior to the application of a drug loaded patch, a strategy dubbed as 'poke-and-patch' (Wermeling *et al.* 2008). Silicon, polymeric or metallic microneedle arrays have been utilised to create pores on the skin surface that facilitated the drug diffusion towards lower tissues (Larrañeta *et al.* 2016). Extensive work has also been conducted on the pre-application coating of solid microneedles with the desired therapeutic substance.

Various methods such as dip coating, gas jet drying, spray coating, inkjet coating and electrohydrodynamic atomisation have been tested and employed for the coating of titanium, steel, silicon and polymeric microneedles (Haj-Ahmad *et al.* 2015). Coated microneedle systems have succeeded in the percutaneous rapid bolus delivery of macromolecules, drugs and vaccines, however there is a serious restriction regarding the amount of API that they can carry (e.g. less than 1 mg for a typical array) (Kim, Park and Prausnitz 2012).

- Hollow

Larger amounts of drugs have been successfully delivered by another type of microneedle array that imitates the shape and function of the typical needle injection, called hollow microneedles. These systems form a mesh of transdermal micro-canals that connect the surface with the lower layers of the skin. Through these transdermal microconduits, a drug-containing formulation is inserted through pressure, electrically driven flow or passive diffusion. The fabrication of metallic, ceramic, glass or polymeric hollow microneedles has been reported (Larrañeta *et al.* 2016). Variations of this system where the API flows from a patch through the microneedle to reach the lower skin tissues, include the porous microneedle arrays that feature multiple drug-releasing pores on the microneedle body (van der Maaden *et al.* 2015).

- Dissolving

Extensive research has also been conducted on another approach that features the incorporation of the API within a dissolving material, that is used for the fabrication of the microneedles (Ita 2017). The gradual disintegration of the matrix material channels the API into the skin in a sustainable manner that is intrinsically dependent on the material composition. This dependency brings out the potential of controlling the rate of delivery by modulating the synthesis of the matrix material. Polymeric, biopolymeric and sugar-based dissolving or biodegradable microneedle arrays have been proposed for the delivery of a variety of APIs (Migalska *et al.* 2011; Garland *et al.* 2012; Tsioris *et al.* 2012; Bediz *et al.* 2014; Hong *et al.* 2013; Ling and Chen 2013; Lahiji, Dangol and Jung 2015) as well as vaccines (Leone *et al.* 2017).

- Hydrogel-forming

Hydrogel-forming microneedles are primarily fabricated from water absorbing polymers (crosslinked hydrogels) such as hyaluronic acid, chitosan and polyvinyl alcohol (Donnelly *et al.* 2012). Due to the hydrophilic nature of their constituent materials, they swell when in contact with the interstitial fluid of the skin. Exploiting this ability to extract and retain interstitial fluid where multiple biomarkers are detectable, hydrogel-forming microneedles have been used as diagnostic microdevices (Samant and Prausnitz 2018). Moreover, such systems have been employed as drug delivery devices, either through the incorporation of the API into the microneedle material, or by attaching a drug-containing reservoir on the base of the array, allowing for its diffusion through the microneedle shafts (Turner *et al.* 2021).

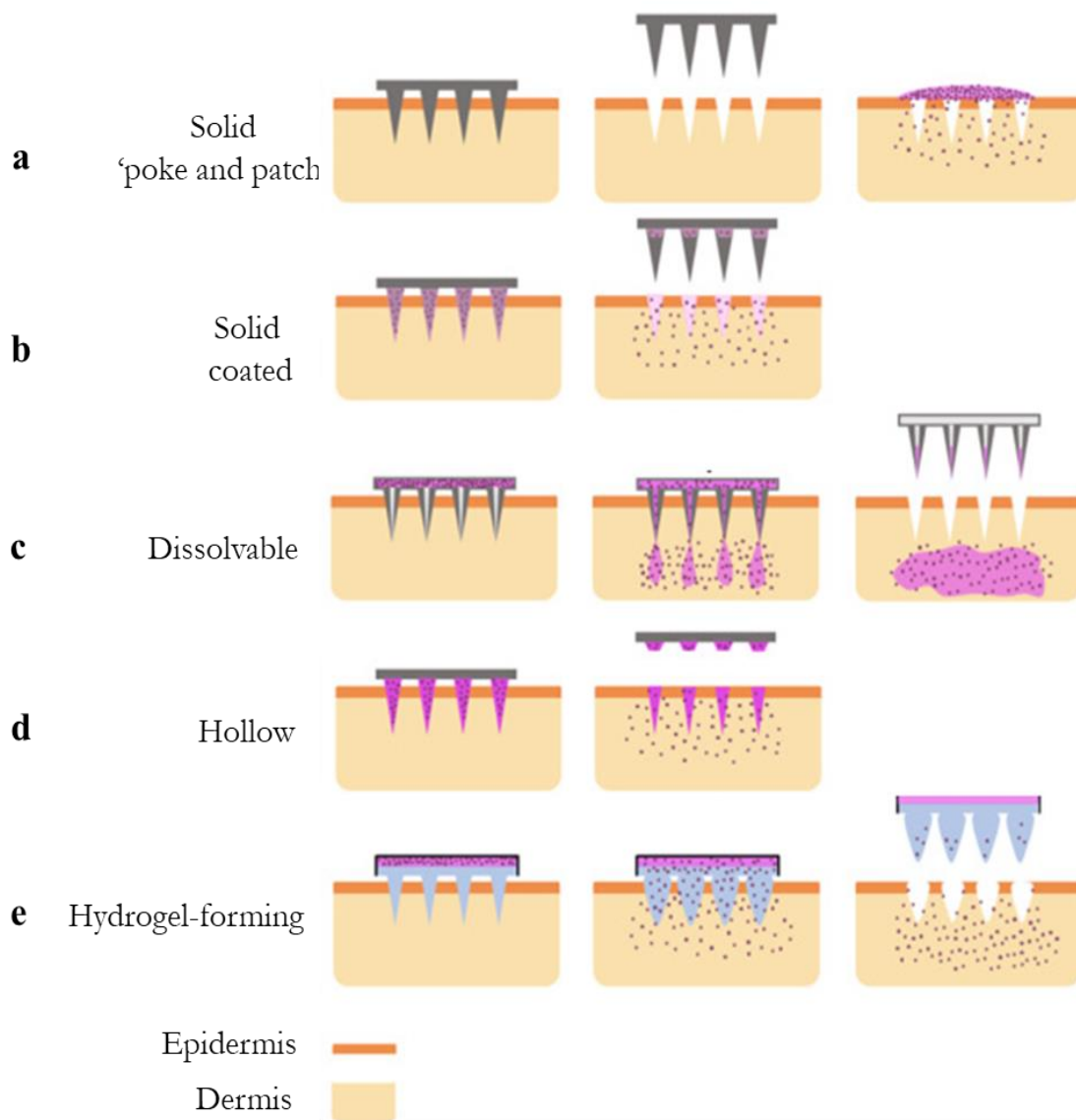


Figure 1.2 Microneedle types and delivery mechanisms (a) Solid microneedles that are applied and removed to create transient micropores, followed by application of the API on the skin; (b) Solid microneedles coated with drug for instant delivery, which are removed after the coating material dissolves; (c) Soluble polymeric microneedles containing drug that dissolves in skin interstitial fluid over time, thereby delivering the drug; (d) Hollow microneedles for delivery of fluids containing drug; (e) Novel hydrogel-forming polymeric microneedles for controlled transdermal drug delivery

1.5.2 Conventional microneedle manufacturing methods

The success of a microneedle system is highly interrelated to its fabrication technique, since the latter must guarantee the production of a delicate and reproducible geometry in the microscale, bearing all the characteristics that guarantee the pain-free application to the patient and the efficient transportation of the drug to the systemic circulation. Modern technology offers a wide variety of techniques that have been used for the fabrication of microneedle such as micromoulding, micromachining, etching and lithography, solely or combinatorially (Larrañeta *et al.* 2016; Park, Allen and Prausnitz 2005). While having been extensively used in research for the development of such systems with proven performance, they often pose restrictions in terms of scalability, customisability or financial viability, in the sense that they involve complex multi-step fabrication regimes and highly sophisticated and costly equipment, which hinder the future up-scaling of the production from the laboratory to the industrial level. Injection moulding processes for instance, due to high initial tooling and equipment costs, can only be profitable for production lines that yield large unit numbers (Karania and Kazmer 2007). Moreover, the need for mould fabrication or procurement introduces additional costs, which is particularly problematic in the R&D stage, wherein the tailoring of prototypes for studying and optimising of microneedle geometrical parameters (i.e. shape, length, width, tip diameter, interspace, aspect ratio) is required (Krieger *et al.* 2019). Other typical microfabrication methods in the range of micromachining, etching and lithography are often costly, labour and time intensive, complex, multistep and require scientific expertise and expensive equipment (Liu *et al.* 2017). Such processes are often difficult to be integrated in production lines in an economical and time-effective fashion. Replacing such methods with new manufacturing solutions that take into advantage cutting-edge technological advances, can tackle the aforementioned issues and establish fast, reliable and cost-effective microneedle fabrication processes.

1.5.3 Microneedle-mediated diabetes therapy

Diabetes mellitus is a family of metabolic diseases, clinically manifesting through chronic hyperglycemia. Its root cause is anchored to insulin secretion and action and can be classified into different types. Type 1 diabetes mellitus is caused by the deficient or completely impaired insulin production by the beta cells in the Langerhans islets,

contained in the pancreas. Depending on its cause, Type 1 can be further classified to Type 1A, wherein the impairment of beta cells is owed to an autoimmune mechanism, or Type 1B, when the reason is unclear (idiopathic diabetes). Type 2 diabetes mellitus is characterised by insulin resistance and progressively lack thereof, and is attributed to genetic, lifestyle and dietary factors (Ng and Gupta 2020).

Diabetes was a lethal disease up until the discovery of insulin in 1921, which is considered as one of the most significant advances in biomedical history (Mayer, Zhang and DiMarchi 2007). Insulin is an endocrine peptide hormone, the frequent administration of which is imperative for the management of Type 1 and advanced Type 2 diabetes. Due to enzymatic degradation in the gastrointestinal tract, the oral route is unsuitable for insulin administration and although alternative routes such as pulmonary and nasal have been proposed (Liu *et al.* 2020), subcutaneous injections are the overwhelmingly selected solution. The transdermal route is an appealing alternative to recurring injections, to tackle issues such as pain, needle phobia, local nerve damage to injection sites and fat necrosis (Halder *et al.* 2020). Nonetheless, the poor permeability of insulin due to its high molecular weight, has prohibited its delivery through systems that rely on passive diffusion across the skin barrier.

The microneedle-mediated administration of insulin for diabetes therapy has attracted attention as a promising strategy to replace typical subcutaneous injections. Various microneedle types and delivery mechanisms have been proposed, such as solid microneedles with the ‘poke and patch’ approach (Martanto *et al.* 2004; Zhou *et al.* 2010), solid coated microneedles (Ross *et al.* 2015), hollow microneedles (Gupta, Felner and Prausnitz 2009; Davis *et al.* 2005; Resnik *et al.* 2018) and dissolving microneedles (Liu *et al.* 2012; Ling and Chen 2013; Lahiji, Dangol and Jung 2015).

Recently, our research group has put forward a combination of 3D printing and inkjet coating for the development of polymeric microneedle arrays, coated with insulin containing formulations. The patches induced rapid blood glucose regulation to diabetic mice, demonstrating improved performance compared to subcutaneous injections (Pere *et al.* 2018; Economidou *et al.* 2019). This advancement highlights the immense potential of such systems in diabetes treatment. Further work is however needed in building a robust and transferable design and additive manufacturing strategy, and in elucidating the key parameters pertaining to the development stage that influence drug

transdermal permeation. Moreover, the feasibility of 3D printing technologies to achieve the fabrication of other microneedle types, aiming at their incorporation in sophisticated drug delivery devices is still unexplored.

1.6 3D printing

Additive Manufacturing (AM) or Solid Freeform Fabrication (SFF), as 3D printing is alternatively known, is a family of different techniques that enable the processing of various types of materials (e.g. polymeric, metallic, ceramic) by inducing the appropriate physicochemical processes. 3D printing technologies share the commonality of building a physical object through the sequential fabrication of adjacent, coalescing layers on the basis of a virtual Computer Aided Design (CAD) model, that takes place into a single piece of equipment, the 3D printer.

Several technologies in the range of inkjet, photopolymerisation and extrusion-based 3D printing have shown promising results for microneedle 3D printing (Figure 1.3). The

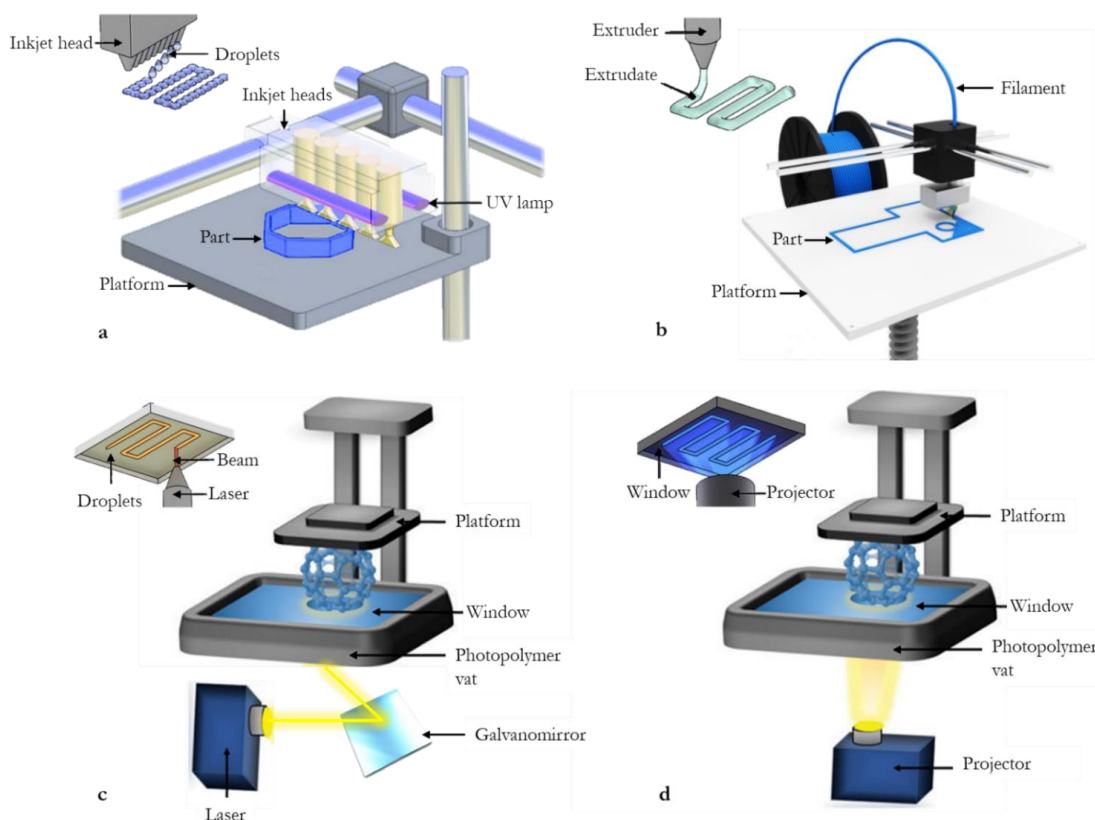


Figure 1.3 Schematic illustration of 3D printing technologies that have been used for the fabrication of TDD systems. a) Inkjet; b) Fused Deposition Modelling (FDM); c) Laser Stereolithography (SLA); d) Digital Light Processing (DLP)

literature findings include the use of such technologies both as a direct microneedle manufacturing method (direct printing) or as a tool for micromould fabrication (indirect printing). Herein, a systematic literature review is put forward, aiming at recording the state-of-the-art developments in the field.

1.6.1 Inkjet 3D printing

Inkjet printing is a general term that describes the formation of structures through the sequential deposition of small droplets by a numerically controlled printing head. The head uses a thermal or piezoelectric system to deposit the droplets in a continuous (Continuous Inkjet; CIJ) or in a drop-on-demand (DoD) manner. Typical inkjet printing systems deposit coalescing droplets of photosensitive polymers, which are then solidified to form layers through exposure to radiation. In other inkjet 3D printers, droplets of binding material are jetted onto a powder bed resulting in the selective solidification of a layer onto a moving platform. After the completion of each layer, the moving platform lowers and a new powder bed is formed. Successive building of layers results to the structure designed.

Although the ability of presently commercial inkjet printers to build complex three-dimensional structures has been explored in medicine (Barinov *et al.* 2015), this function of the technology has not been applied yet on TDD systems. However, several studies have employed inkjet apparatuses and use the same principals to build two-dimensional patterns, a form of 2D printing that acts as a predecessor of the respective 3D technology. In those studies, the capability of controlled and selective (DoD) deposition of materials and formulations on suitable substrates has been exploited in developing TDD systems. Boehm *et al.* used piezoelectric inkjet printing to deposit quantum dots on microneedle surfaces, highlighting the potential of the method to electively coat the surface of microneedles (Boehm *et al.* 2011). Through the usage of inkjet printing, the coating process is endowed with versatility, since the printing of various agents in the same microneedle array for combined therapy is enabled.

In other studies of the same framework, the same technology was successfully employed to coat microneedles with anti-fungal agents. The studies illustrated that the coated and blank microneedles presented no significant morphological differences, demonstrating that the inkjet printing process does not produce alterations, while coated arrays presented the desired anti-fungal activity (Boehm *et al.* 2013; Boehm *et al.*

2014). Moreover, Ross et al. used insulin-containing polymer formulations to coat metallic microneedle arrays via piezoelectric inkjet printing in multiple coating layers. The study, involving diffusion evaluation in porcine skin, shows that the coated microneedles generated rapid insulin release profiles (Ross *et al.* 2015). The selection of inkjet printing as a coating method reassured the uniformity of the coating within the microneedle array and significantly contributes to the reproducibility of the results. On the other hand, Uddin et al. followed the same strategy to coat metallic microneedles with anti-cancer drug-containing formulations. Using piezoelectric inkjet printing, they developed layers of a graft co-polymer containing 5-fluorouracil (5-FU), curcumin and cisplatin on the microneedles, with the release profiles in porcine skin appearing increased (Uddin *et al.* 2015). In the same logic but following a slightly alternative strategy, Allen et al. used a piezoelectric DoD inkjet system to dispense colour-containing formulations in silicon mould cavities, that were later used to cast microneedle arrays, creating thus dissolvable microneedles with encapsulated formulations (Allen *et al.* 2016).

An attempt to exploit the capability of inkjet printing technology to produce 3D structures for TDD systems was successful in 2012 when *Innoture Limited* published a patent for a ‘Method of producing a microneedle or microimplant’ (Kirby 2012). The patent states that the apparatus forms arrays of microneedles by ‘*i) depositing a first portion or droplet of substance onto a first surface; and (ii) forming a solid needle from the substance, wherein step (ii) comprises sequentially depositing a plurality of portions or droplets of substance onto the first portion or droplet of substance*’. It is evident that the methodology that *Innoture Limited* has implemented employs Drop-on-Solid (DoS) and DoD strategies to form a base on a suitable substrate and then gradually form the microneedle shaft, as one drop is deposited and solidified upon-the-other. The company has introduced a microneedle patch to the market called Radara® Targeted Skincare that is used for cosmetic purposes to deliver hyaluronic serum for skin rejuvenation (wrinkle restoration).

Inkjet printing is in general a technology of high resolution and the possibility of selective deposition that it enables, renders it a very promising technology for microneedle coating purposes for the development of personalised dosages and complex drug profiles with high reproducibility. Further applications on TDD have not yet been explored, which is likely linked to specific disadvantages of the technology, especially

the limited material selection. Materials compatible with the inkjet process need to satisfy specific requirements pertaining to liquid material properties (viscosity, surface tension) that allow the formation of cohesive droplets with specific spreading behaviours (Napadensky 2009). Such requirements in combination with biocompatibility and sterilisability prerequisites limit the technology's potential as a manufacturing technique for medical devices.

1.6.2 Photopolymerisation-based 3D printing

Another major group of 3D printing technologies is based on the ability to selectively polymerise photo-sensitive polymers through laser emissions or projections of light. These technologies enable the fabrication of structures through the consecutive layer-wise polymerisation of UV-sensitive polymers, through a curing process named photopolymerisation. In a vaguely similar manner to inkjet printing, the digitally controlled printing head selectively emits light on a vat of uncured resin onto a building platform to build a single layer. After the fabrication of each layer, depending on the configuration of the printer, the building platform either moves down and a layer of uncured resin covers the previous one, ready to be cured as well. In this configuration, the light-emitting head is located above the building platform while the already built part of the object remains submerged in the resin until the printing is completed and the object emerges from the bath of uncured resin ('top-down printing'). Alternatively, in the other commercial configuration, the platform rises after the building of each layer as much as the layer height, allowing the last layer to touch the uncured resin before it is photopolymerised, to ensure the adhesion between consecutive layers. In the so called 'bottom-up printing', the already built structure is constantly out of the uncured resin vat while the printing head is located below the building platform.

Depending on how the uncured polymer is exposed to the polymerisation-inducing light, the technologies are classified as laser stereolithography (SLA), where a laser beam is emitted and 'draws' lines of solidified polymer, and Digital Light Processing (DLP), where a high-definition projector flashes the whole cross-section of the object at once, in the form of volumetric pixels (voxels). DLP is usually faster than SLA since the whole layer is fabricated simultaneously. In many of the following studies, SLA and DLP are put under the umbrella term 'stereolithography' and they are further distinguished as 'scanning-based SLA' and 'projection-based SLA', respectively (Choi

et al. 2009). In the two groups, the respective specialised technologies, Two-Photon Polymerisation (2PP) and Continuous Liquid Interphase Printing (CLIP) are also included (Schmidleithner and Kalaskar 2018).

Two-Photon Polymerisation (2PP) enables the building of elaborate, complex structures in the microscale and nanoscale. Prior to printing, a drop of resin is placed on a glass substrate and is constrained between spacers and a cover. The laser beam then, being directly focused inside a liquid resin droplet, solidifies the focal point volume by two-photon absorption. As a result, the longitudinal spatial resolution is governed by the focal spot size itself allowing the solidification of very small voxels (Sun and Kawata 2006). Thus, the specific technology can produce structures with detail dimensions of less than 100 nm (Lee *et al.* 2008; Gittard *et al.* 2010). It is however noteworthy, that the technology is associated with high costs and small print volumes, which prohibit its use for mass production.

CLIP employs the same printing principles as DLP, diverging by the presence of an oxygen permeable membrane between the resin and the light window. The oxygen inhibits photopolymerisation forming a ‘dead zone’ of liquid resin between the advancing structure and the window. After the completion of each layer, the printed structure moves allowing for a fresh resin layer to be naturally drawn in. Therefore, mechanisms of resin redistribution at the start of a new layer, which are essential for other SLA technologies, are omitted. As a result, the process is continuous which substantially accelerates prints while yielding smoother surfaces (Tumbleston *et al.* 2015).

1.6.2.1 Laser Stereolithography: Two-Photon Polymerisation and conventional technologies

Laser SLA employs a focused laser beam to ‘write’ within the liquid photopolymer resulting to the formation of adjacent, coalesced solid material ‘roads’. The diameter of the laser beam focal point is a determinant factor of the resolution. The first laser SLA technology to successfully 3D print microneedles directly and indirectly was the specialised 2PP. The adoption of photopolymerisation-based 3D printing technologies for the manufacturing of TDD systems is an appealing concept due to the versatility in terms of geometric complexity and resolution that these technologies provide.

In a study by Gittard *et al.*, microneedle micromoulds were created using masters that had been fabricated through 2PP. The microneedles were subsequently casted using a Class IIa biocompatible polymer (eShell 200) and they sufficiently penetrated human skin, creating pores that would possibly facilitate the transdermal permeation of insulin and other protein-based agents (Gittard *et al.* 2009). In recent studies, a hollow microneedle prototype was developed by Faraji Rad *et al.* using a 2PP 3D printer which was then employed to generate negative moulds and subsequently thermoplastic replicas by hot embossing. The 3D printed prototypes featured sharp tips and uniform microchannels interconnecting the shafts. The replicas showed a high degree of fidelity to the 3D printed prototype (Faraji Rad *et al.* 2017). Following a similar methodology, 2PP was also employed to produce pyramidal microneedle masters with bio-inspired surface microstructures. Despite the intricate microgeometries of the 3D printed masters, they were accurately replicated through micromoulding (Plamadeala *et al.* 2020). Along the same lines, 2PP was employed by Cordeiro *et al.* to fabricate microneedle templates of various shapes and sizes that were subsequently reproduced as dissolvable and hydrogel-forming microneedles through micromoulding. The work proposes a strategy to evaluate and compare various microneedle designs in a fast and cost-effective manner (Cordeiro *et al.* 2020). Overall, these studies demonstrate that 3D printing can be a valuable prototyping intermediate step for microneedle fabrication, especially when the 3D printable material does not possess the necessary biocompatibility features for the direct fabrication of microneedle patches.

Direct microneedle printing was achieved by Ovsianikov *et al.*, that proposed 2PP fabricated hollow microneedle arrays from hybrid inorganic-organic co-polymers reinforced with inorganic silanated particles (Ormocer). Subsequent human epithelial keratinocytes culture revealed no negative impact on cell viability and growth (Ovsianikov *et al.* 2007). The same group in a subsequent study employed the forenamed material and printing method to produce microneedles that distributed a PEG-amine quantum dot solution rapidly in porcine skin in comparison with topical administration (Doraiswamy *et al.* 2010). Finally, in the work of Kavaldzhiev *et al.*, cylindrical, conical and pyramidal microneedles were successfully created using the 2PP technology and then endowed with magnetic properties through coating with iron via sputter deposition (Figure 1.4). Subsequent cell culture studies showed excellent biocompatibility of the microneedle arrays (Kavaldzhiev *et al.* 2017). An

implementation of 2PP 3D printing for direct solid and hollow microneedle manufacturing was reported by Aksit et al. and Szeto et al. The microneedles were of very good sharpness and although used to investigate the in-vitro perforation of guinea pig round window membrane (Aksit *et al.* 2018) and perilymph sampling (Szeto *et al.* 2021), the methodology can be easily transferred to transdermal systems. Similarly, 2PP was used by Moussi et al. for the direct fabrication of a biocompatible hollow microneedle patch, with excellent skin insertion capabilities. The patch, being connected to a reservoir, was potentially suitable for implantation, transdermal extraction of fluid for diagnostic purposes and drug delivery (Moussi *et al.* 2020).

It is noteworthy that although the exceptional resolution of 2PP printing technologies enables the formation of microneedles with very sharp tips, the cost associated with this technology is far higher than other commercial 3D printing technologies. Moreover, the printing volumes are typically small (e.g. 100 x 100 x 8 mm³ for the Photonic Professional GT system by Nanoscribe GmbH) hampering the production upscaling. Evidently, there has been a shift towards research using more cost-effective photopolymerisation 3D printing methods such as desktop laser SLA and DLP.

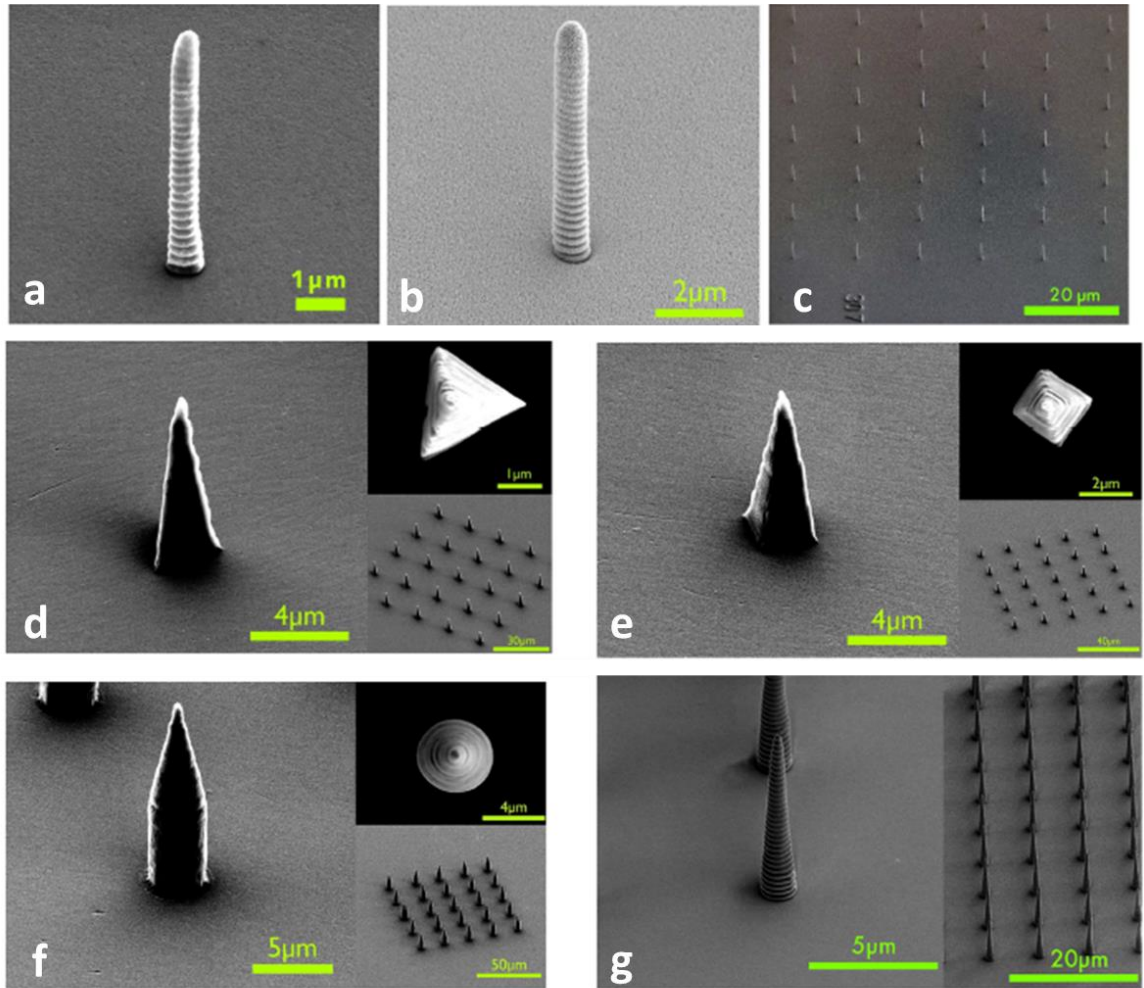


Figure 1.4 SEM images of 2PP printed microneedles. (a) cylindrical polymer microneedle, blank and (b) coated with a 120 nm thick Fe layer; (c) patch of cylindrical needles after coating with 6 μm length and 12 μm pitch on a silicon substrate; (d) 3D printed pyramid microneedle with triangular base and (e) square base; (f) cylindrical microneedle with sharp tip and (g) conical needles with their respective arrays on a Si polished substrate (Kavalzhiev *et al.* 2017).

Laser SLA has recently attracted notable attention for microneedle manufacturing. This technology combines reliability, reproducibility, easy implementation and small production times with relatively low processing costs. The micron-level resolution of commercial laser SLA printers renders the technology a promising candidate for direct and indirect microneedle manufacturing. Indeed, Krieger *et al.* employed a commercial laser SLA printer to 3D print microneedle masters that were subsequently used to create moulds. The study indicates the potential of this technology to indirectly fabricate microneedles by introducing a methodology for rapid and inexpensive production of

easily customisable microneedle moulds (Krieger *et al.* 2019). Similarly, Lopez-Ramirez used the same premise of involving 3D printing in a three-step microneedle manufacturing process, producing positive moulds via laser SLA. The masters were employed to create dissolving microneedles containing API and Mg microparticles; the latter induced a pumping effect that enhanced diffusion (Lopez-Ramirez *et al.* 2020). Another study by Amer *et al.* demonstrated that microneedle micromoulding can be further facilitated by laser SLA, through the direct printing of moulds, thereby reducing the mould development stage to a one step process. The biodegradable microneedles casted to the 3D printed moulds were loaded with plant extracts with antioxidant action in the aim to reduce the appearance of cellulite (Amer *et al.* 2020).

Extensive work on the applicability of laser SLA for the direct, one step fabrication of solid microneedles has also been conducted. Kundu *et al.* developed a 3D printed cone-shaped microneedle and investigated the effect of printing and post-process curing parameters on the microneedle quality. Mechanical testing showed that the force required for fracture was approximately 4 times higher than the forces required for model skin insertion, indicating safety during application (Kundu, Ausaf and Rajaraman 2018).

A combined methodology of laser SLA 3D printing and inkjet 2D printing was developed to produce solid microneedles of various designs coated with drug containing films. The cone, pyramid and spear shaped microneedles were designed, 3D printed using a biocompatible Class I resin and subsequently coated with solutions of insulin and sugar carriers. The implementation of inkjet printing endowed the coating process with versatility, accuracy of the drug dosage and eliminated drug losses. The carriers reassured protein stability and rapid dissolution of the film in diabetic mice, achieving fast insulin onset action and a sustained hypoglycemic effect compared to subcutaneous injections (Pere *et al.* 2018; Economidou *et al.* 2019). Following the same logic, cross shaped laser SLA printed microneedles were coated with an anticancer agent using the aforementioned inkjet coating technique. The microneedle geometry enabled the deposition of increased drug loading of up to 770 µg. *In vivo* trials on skin tumours developed on Balb/c nude mice showed fast cisplatin release, 100% tumour regression in the course of a few days and 100% animal survival rate (Uddin *et al.* 2020). The above studies illustrate that the described combined printing methodology of laser SLA

and inkjet enables the fast customisation of microneedle systems on the basis of the specific application requirements for various drug delivery purposes.

Laser SLA microneedles have also been tested for their ability to enhance transdermal delivery of model dyes using the ‘poke and patch’ rationale. Xenikakis et al. developed a 3D printed patch which was employed to create microchannels within human skin. The microneedles were subsequently removed to allow permeation of the studied molecules, showing significant permeation enhancement compared to non-microneedle-treated skin (Xenikakis *et al.* 2019).

Hollow microneedles have also been successfully 3D printed using laser SLA. Farias et al. developed a two-part system featuring hollow microneedles for extrusion of microencapsulated cells. The study reported that there was no statistical difference between the viability of extruded and non-extruded cells, indicating that the 3D printed hollow microneedle device protected the cells from shear during extrusion (Farias *et al.* 2018). Moreover, an integrated microfluidic-enabled hollow microneedle system was developed by Yeung et al. to allow for the in situ mixing of multiple fluids and their subsequent delivery through a hollow microneedle patch. The device was fabricated by a one-step laser SLA printing process and can potentially enable the simultaneous transdermal administration of various therapeutics (Yeung *et al.* 2019).

1.6.2.2 Projection Stereolithography: Digital Light Processing and Continuous Liquid Interphase Printing

In contrast with laser SLA that uses a focused light emission to induce local photopolymerisation, DLP technologies illuminate the whole cross-section of the in-print structure at once for every layer, through a high-definition projector. This differentiation from laser SLA by definition denotes comparatively smaller printing times (Schmidleithner and Kalaskar 2018). DLP has been employed by researchers in an analogous manner as laser SLA, following the indirect microneedle printing rationale, wherein the printing technology is part of an intermediate step in micromoulding processes, as well as for direct microneedle printing.

Boehm et al. utilised micro-stereolithography (DLP) to create micromoulds, from which they obtained the microneedles for several studies (Boehm *et al.* 2011; Boehm *et al.* 2012; Boehm *et al.* 2014). Johnson and Procopio employed a standard DLP 3D printer

to investigate the potential of this technology to create microneedle masters, readily usable for micromoulding techniques, and validated the effect of printing parameters on the microneedle quality (Johnson and Procopio 2019). Furthermore, Sayed et al. developed nanoparticle-loaded dissolvable microneedles in micromoulds created on the basis of DLP fabricated master templates (El-Sayed, Vaut and Schneider 2020). The study highlighted the simplification of the microneedle design optimisation process for better skin insertion, that was enabled by the use of 3D printing. Moreover, DLP was used in like fashion in another study, that presented a dissolvable composite microneedle patch, loaded with iron oxide nanoraspberry, for the treatment of alopecia (Fang *et al.* 2020). The usage of 3D printing for the fabrication of the microneedle array, even in an indirect fashion, contributes significantly towards the customisation of the therapeutic approach, since the geometry of the needles can be easily tailored to deliver the agent in different intradermal depths such as epidermally, dermally or subdermally.

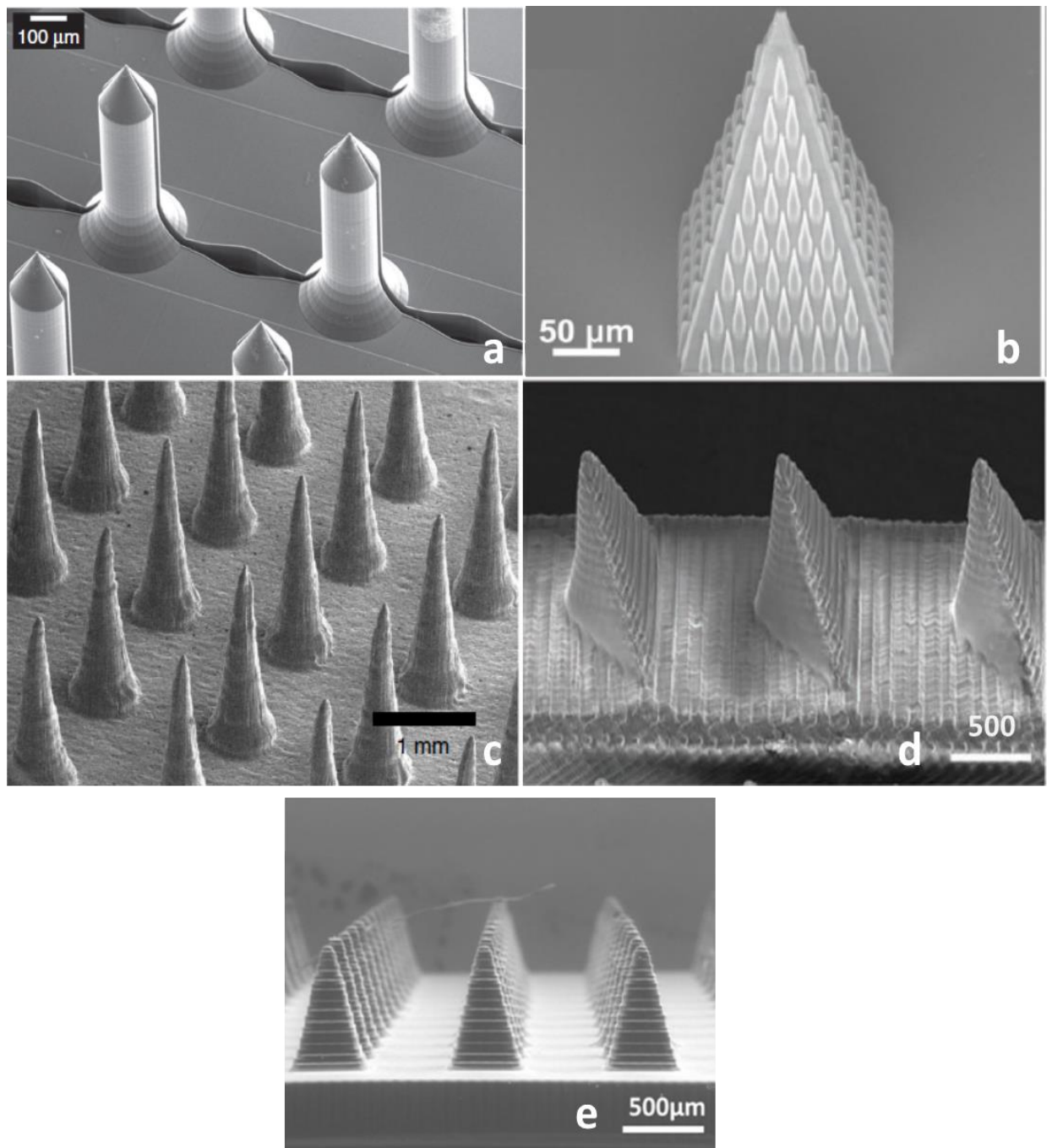


Figure 1.5 Photopolymerisation-based 3D printing of microneedle masters for micromoulding. a) hollow prototypes with interconnecting channels fabricated by 2PP (Faraji Rad *et al.* 2017), b) pyramidal microneedle masters with bio-inspired surface microstructures made by 2PP (Plamadeala *et al.* 2020), c) microneedle basins made by laser SLA, d) microneedle masters fabricated via laser SLA (Lopez-Ramirez *et al.* 2020) and e) microneedle prototypes made by DLP (Johnson and Procopio 2019).

The direct, single-step fabrication of microneedles using DLP has also been proposed. Yao et al. achieved the manufacture of multifunctional hydrogel microneedles using a customised 3D printing resin. The microneedles were initially soaked in a drug-containing solution and their efficacy to convey their cargo into artificial skin was investigated. The reverse approach was utilised for drug detection studies showing promising results (Yao *et al.* 2020). This study demonstrates that the introduction of customised resins can be a key step to open new prospects for microneedle 3D printing. Another work integrated anti-skin cancer drug (Dacarbazine) into the polymeric blend before the photopolymerisation through a micro-stereolithographic (DLP) apparatus that created the microneedle arrays. Subsequent release studies revealed that the drug can be controllably delivered for five weeks (Lu *et al.* 2015). The latter study demonstrates that the incorporation of some specific agents (here a chemotherapy drug) in the polymer prior to photopolymerisation can successfully yield drug-containing microneedles, however this approach is limited to radiation-immune compounds.

In other works, microneedle arrays were directly printed through DLP and then subjected to coating processes. Gittard et al. fabricated microneedles through DLP of an acrylate-based polymer, to be potentially used in wound healing. The arrays were then coated with silver and zinc oxide films by means of pulsed laser deposition to provide them with antimicrobial attributes. In the same logic, microneedle-containing devices were also manufactured featuring a cross shape, in the aim to hold the skin together during wound healing. The antimicrobial role of the coated microneedles was demonstrated via agar diffusion assay study (Gittard *et al.* 2011).

Noteworthy advances in the area of patient-specific microneedle devices have also been made. Lim et al. fabricated a microneedle-featuring splint device for the treatment of trigger finger using a DLP 3D printer. Using the device to puncture the skin prior to the topical administration of diclofenac gel, they effectively increased the drug amount that permeated the skin (from 5 to 15 μg of drug per cm^2 in the first 3 hours), proving thus that 3D printed patient-customised microneedle devices can be efficacious in systems designed according to the ‘poke-and-patch’ strategy (Lim, Ng and Kang 2017). Along these lines, the same one-step printing approach was applied to fabricate personalised microneedle eye patches based on 3D scanned human face models. The 3D printed microneedles, consisting of a polymer with proven biocompatibility with human cells, were used to enhance absorption of anti-wrinkle peptides via the ‘poke and patch’

method. The work shows the potential of 3D printing in combination with advanced 3D scanning techniques to facilitate the development of personalised transdermal systems (Lim *et al.* 2020).

The specialised DLP technique, CLIP, has also been utilised for microneedle development. CLIP fabricated microneedles, which were firstly introduced by Johnson *et al.* in 2016 (Johnson *et al.* 2016), were coated using customised coating masks, manufactured by the same 3D printing technology. The 3D printed masks were utilised to coat the microneedles with model proteins and subsequent *in vivo* trials revealed that the coated microneedles achieved a more sustained protein delivery over time, in comparison to subcutaneous injections (Caudill *et al.* 2018). This work illustrates the multifunctional role that such 3D printing technologies can play in facilitating and broadly modernizing microneedle-mediated transdermal therapy.

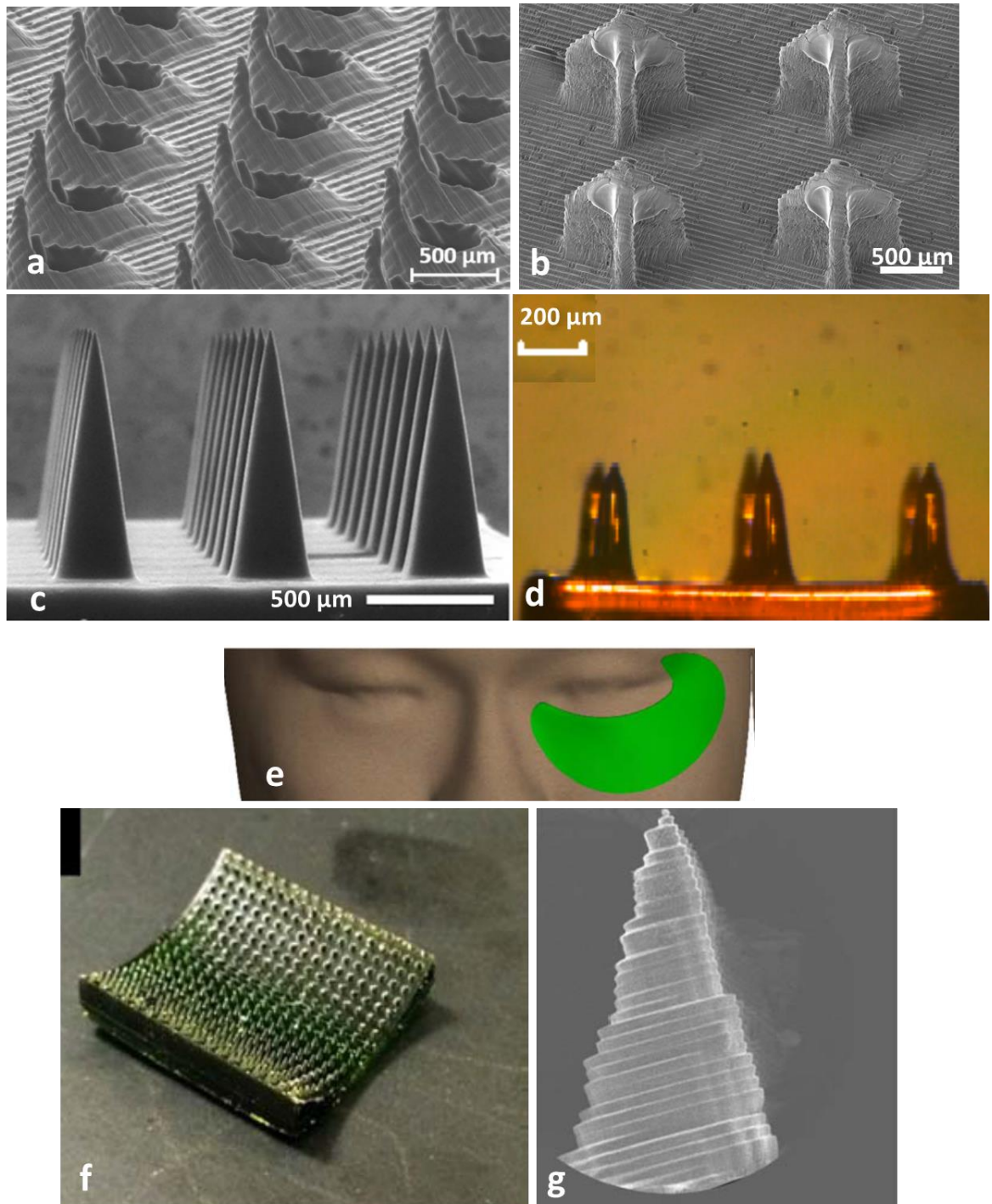


Figure 1.6 SLA and DLP microneedle printing using the direct, single step approach. (a) Hollow laser SLA printed microneedles (Yeung *et al.* 2019), (b) solid laser SLA printed microneedles coated by inkjet 2D printing with anti-cancer agents, (c) CLIP fabricated polycaprolactone microneedles, (d) multifunctional hydrogel microneedle fabricated via DLP (Yao *et al.* 2020) and (e) 3D scan of human volunteer employed to print customized microneedle patches (f), (g) SEM image of the microneedle on the curved patch (Lim *et al.* 2020).

1.6.3 Extrusion-based printing

Extrusion-based technologies constitute a large portion of the 3D printing family, with the known shortcoming of inferior resolution capabilities compared to photopolymerisation based techniques. Hence, the applicability of these technologies for microneedle development is problematic due to the inability to accurately form tips sharp enough to pierce the skin painlessly and efficiently.

A prominent extrusion-based 3D printing technology is Fused Deposition Modelling (FDM), which is based on the hot melt extrusion process. Typical FDM printers employ a thermoplastic material in the form of filament, which is fed into a nozzle head, where is heated above its glass transition temperature (T_g). The extruder head then deposits the semi-molten filament onto a printing platform, forming thus consecutive layers, as the platform lowers after the completion of each layer. FDM is a versatile, safe and user-friendly technique, with a wide range of commercial machines ranging from low budget, small printers to larger industrial ones. Their major drawbacks include the connection between end-product quality and selected process parameters as well as the limited variety of materials they can handle. The applications of FDM in medicine are limited; in the field of TDD, Goyanes et al. has performed a relative study where they mixed commercially produced Flex EcoPLA (FPLA) and polycaprolactone (PCL) with salicylic acid via hot-melt extrusion (HME) and created filaments, with which they printed nose-shaped devices for the treatment of acne. The same devices were also fabricated through SLA, employing different polymers (polyethylene glycol diacrylate and polyethylene glycol). The study concluded that the SLA fabricated devices induced faster diffusion rates than the FDM ones (Goyanes *et al.* 2016).

Regarding microneedle fabrication, the inferior resolution capabilities of extrusion-based printing has been inhibitory. Hence, no relevant applied research was previously found until recently, when extrusion-based 3D printing was combined with post-process etching in the aim to manufacture microneedles. FDM was employed to fabricate biodegradable polymer microneedles, the tips of which were subsequently refined by subjecting them to chemical etching. The microneedles were loaded by submersion in a model dye solution and *in vitro* release testing on porcine showed that they conveyed 100% of their cargo in 36 hours (Luzuriaga *et al.* 2018). The application of FDM is an interesting concept due to its low cost, however the imperative step of chemical post-processing is likely to introduce variabilities in the end-product quality.

Another combinatorial approach to tackle the poor resolution issue of extrusion-based printing for sharp microneedle manufacturing was applied by Wu et al. The study proposes the fabrication of microneedles using a combined process of dual extrusion bioprinting and subsequent stretching of the shafts, to achieve the formation of sharp tips. The constituent material was prepared in the form of composite bioinks containing glucose-responsive insulin for self-regulating diabetes treatment. Images of the microneedles immediately after bioprinting and prior to stretching (Figure 1.7 a,b) reveal the imperative need for post-printing processing to refine the microneedles and render them suitable for clinical application (Wu *et al.* 2020). Evidently, the aforementioned studies give prominence to the need for further technical advancing that will improve resolution of extrusion-based printing, allowing thus the one-step production of microdevices.

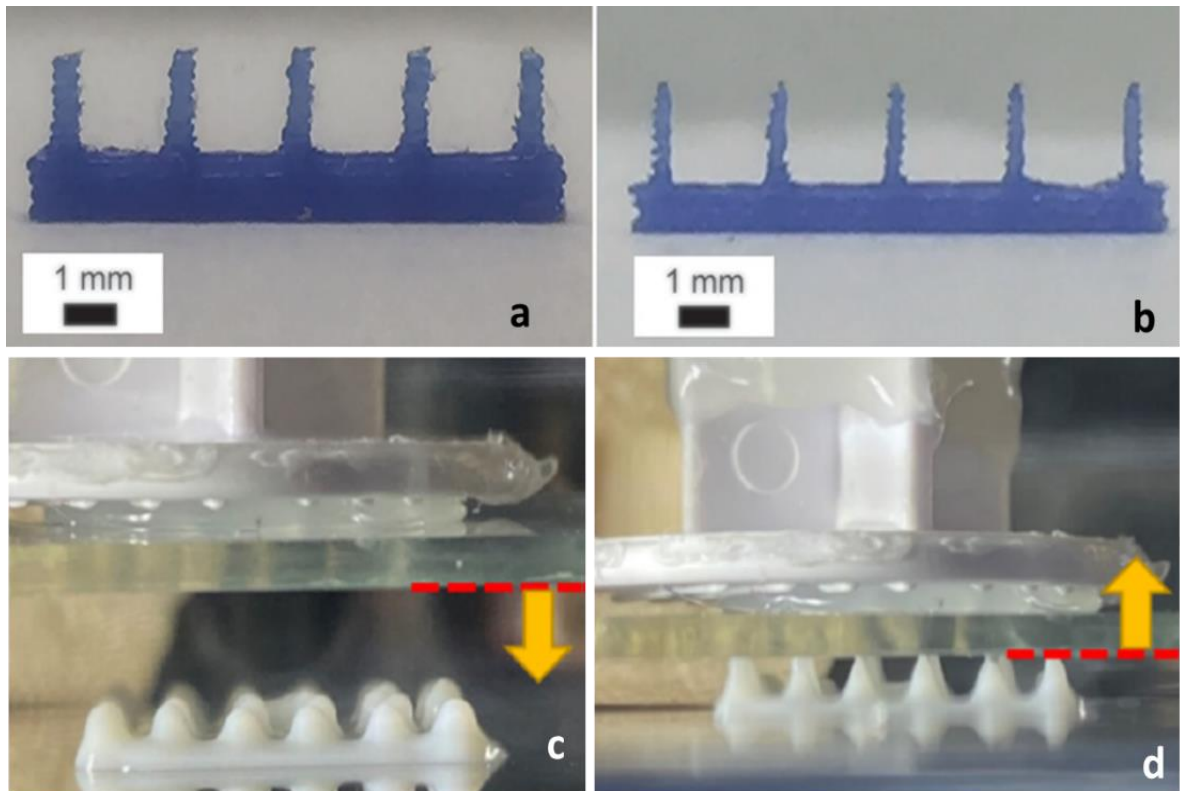


Figure 1.7 Extrusion based microneedle printing using the direct approach, combined with post-printing processing for microneedle refinement. (a) FDM printed microneedles before and (b) after chemical etching (Luzuriaga *et al.* 2018), (c) bioprinted microneedles before and (d) after stretching (Wu *et al.* 2020).

It has been proven that the FDM technology suffers from limitations in terms of resolution, questioning the current ability of the technology to build elaborate structures in the microscale. Another factor that may obstruct the usage of the method for sophisticated pharmaceutical applications stems from the innate sensitivity that FDM produced structures present to the selected fabrication parameters. The identification of these interdependencies is frequently achieved by trial-and-error methods complicating thus the standardisation of the process. However, despite its limitations and problems, the FDM technology can be an appealing possible choice as a fabrication technique for TDD systems, since the formation through extrusion eliminates the usage of solvents (Goole and Amighi 2016). Moreover, it could be effectively combined with HME processes in the aim to produce a wide range of drug/polymer blends that can be easily formed into final products through cost-effective FDM printers. Nonetheless, it is noteworthy that the potential applicability of the FDM in TDD relies significantly on the improvement of the technical disadvantages of the technology.

1.7 Applicability of 3D printing for microneedle fabrication: Technical challenges

The review of the current trends in the field of 3D printed systems for microneedle-mediated drug delivery reveals that, albeit seemingly abundant, the choices stemming from the variety of 3D printing technologies and respective materials suffer limitations, posed by the requirements of the target application. The selection of the optimal printing technology and material combination is the cornerstone of the prototyping stage and can determine the outcome of the endeavour. For microneedles, two central parameters are commonly and repetitively identified by researchers as the key influential factors that need to be taken into consideration; the printing resolution and the material properties.

1.7.1 Resolution

Printers feature numerically controlled moving parts that move based on the processed virtual design of the object. The printing resolution is governed by the smallest displacement (step) of the moving parts in the XY and Z dimensions, determining thus the degree of accuracy in detail formation. Other determinant factors pertain to the nature of the technology (nozzle size for extrusion-based techniques, focal point for laser-based techniques etc.). Printing resolution in the microscale is of paramount

importance for microneedle manufacturing. High nominal resolution improves the definition and accurate representation of micro-sized features, which is essential for elaborate microneedle designs, especially for hollow structures. Most importantly, high resolution enables the formation of sharp microneedle tips, which is critical for the minimisation of the force required for skin insertion that would entail the minimisation of pain (Gill *et al.* 2008). Typically, laser-assisted printing technologies offer superior resolution compared to e.g. extrusion-based ones. George *et al.* compiled a thorough review on the accuracy and reproducibility of medical models printed by various technologies (George *et al.* 2017). The study reports that the best resolution is obtained by vat photopolymerisation technologies (z-axis: 0.02–0.2 mm, x-y-axis: 0.075–0.2 mm) while the worst by FDM (z-axis: 0.1–0.5 mm, x-y-axis: 0.1–0.4 mm). The aforementioned justify that the vast majority of research on microneedle printability employs SLA, DLP and 2PP 3D printers. Indeed, researchers that attempt extrusion 3D printing for microneedles report that post-printing processing for tip refinement is necessary (Luzuriaga *et al.* 2018; Wu *et al.* 2020).

However, detail accuracy is not solely dependent upon the inherent technical resolution specifications, and measures can be taken to achieve better detail formation and fidelity to the virtual design. This can be achieved through tuning of the printing set parameters, since their effect on end-product quality is well-established.

In photopolymerisation technologies, studies have confirmed that printing angle affects the microneedle dimensional accuracy and tip sharpness (Yeung *et al.* 2019). This is owed to the mechanical stresses induced by the printing process, wherein the printed structure is detached from the optical window after completion of each layer. These stresses can cause serious defects and even print failures. A simple way to minimise these stresses is to minimise the contact area with the optical window by printing the microneedle array at an angle. Indeed, optimum quality for printed microneedle was obtained at 45° in respect to the horizontal printing platform (Yeung *et al.* 2019).

Layer height has been shown to have a pronounced effect on DLP printed microneedle quality. Increased layer height values produce faster prints and reduce the possibility of a printing failure since fewer layers are needed. However, they induce the ‘stair stepping’ effect, a form of a stair-like surface roughness featuring distinctly visible layers, that has a negative impact on mechanical behaviour and structural integrity. By

decreasing the layer height, the ‘stair stepping’ effect diminishes and smoother microneedles are produced, with the trade-off of longer printing times (Johnson and Procopio 2019; Krieger *et al.* 2019).

Along the same lines, printing speed in photopolymerisation 3D printing is generally adversely proportional to end-product quality, meaning that higher quality may entail longer printing times. This is not however the golden rule for other technologies such as FDM. A study by Alhijaj *et al.* on FDM printed solid dosage forms, showed a minimal effect of printing speed on accuracy, with dimensional discrepancies from the virtual model to be manifested at low speeds. Moreover, the study highlights the inverse effect of the printing temperature on raster width, wherein higher temperatures cause the material to spread more upon extrusion (Alhijaj *et al.* 2019). Raster overspreading can be a source of structural distortion and careful adaptation of the printing settings must be applied. Other factors that were found to play a role were printing plane, orientation angle and filling pattern (Camposeco-Negrete 2020). However, the interplay between set parameters and quality in FDM is generally difficult to predict due to the number of variables involved, and researchers often need to conduct trial and error tests to improve their prints.

1.7.2 Materials

The selection of the constituent material is an inherently fundamental challenge for microneedle systems. Commonly, limitations stem from the requirement for biocompatible, mechanically strong and sterilisable materials, while the suitability for parenteral delivery is needed. Further constraints arise depending on the nature of the microneedle system, e.g. biodegradable/dissolving materials for dissolvable systems, inert materials for solid/coated/hollow systems (Ali *et al.* 2020). The usage of 3D printing, when employed directly for microneedle fabrication as opposed to mould manufacture, introduces additional limitations due to the narrow material variety that is readily processable by each distinct technology (Tappa and Jammalamadaka 2018). The lack of suitable materials justifies the plethora of studies that employ 3D printing to assist in mould development, as described earlier.

As the field will start rapidly moving from using 3D printing to develop microneedle models and prototypes to the production of customisable microneedles, a careful consideration should be given to the selection of the materials due to the strict

regulatory environment. The selection should entail material screening, manufacturability and scalability in order to allow the delivery of innovative, safe and effective microneedle devices to patients.

The introduction of novel materials that combine printability, mechanical strength, sterilisability and other properties dictated by the needs of the microneedle application can be a pivotal step in the field. Several researchers have proposed customised materials and have performed cytotoxicity and mechanical property studies (Moussi *et al.* 2020; Plamadeala *et al.* 2020; Yao *et al.* 2020). Table 1.1 summarises the 3D printable materials that have been employed for the direct additive manufacturing of microneedles.

Table 1.1 Custom and commercial 3D printable materials that have been employed for direct microneedle printing. The exact composition of the commercial resins mentioned here is proprietary and minimal information on the constituents is available.

Material	Biocompatibility	3D printing technology	Type	Application	Ref.
Acrylate-based (eShell 200, EnvisionTEC)	Biocompatible, Class IIa (EnvisionTEC 2011)	DLP	Solid, coated	Coating with zinc and silver oxide for obtaining antimicrobial purposes and hold the skin together during wound healing	(Gittard <i>et al.</i> 2011)
		DLP	Hollow	Microneedle patch with integrated carbon fibers for electrochemical measurements	(Miller <i>et al.</i> 2011)

Poly-propylene fumarate (PPF) with BAPO ⁱ	Biocompatible (Lu <i>et al.</i> 2015)	DLP	Biodegradable	Delivery of the enclosed anti-skin cancer agent (Dacarbazine)	(Lu <i>et al.</i> 2015)
Acrylate-based (3DM Castable)	Printed material non cytotoxic, 100% human dermal fibroblast viability (Lim, Ng and Kang 2017)	DLP	Solid, 'poke and patch'	Delivery of diclofenac for the treatment of trigger finger	(Lim, Ng and Kang 2017)
			Solid, 'poke and patch'	Customisable microneedle eye patch to create microchannels to improve permeation of anti-wrinkle peptides	(Lim <i>et al.</i> 2020)
Co-polymers reinforced with inorganic silanated particles (Ormocer [®] US-S4)	Ormocer [®] is ISO certified as non-toxic and inert. No negative impact on keratinocyte viability and growth induced by printing (Ovsianikov <i>et al.</i> 2007)	2PP	Hollow	Prototype intended for blood extraction and drug delivery; transdermal delivery of quantum dots	(Ovsianikov <i>et al.</i> 2007; Doraiswamy <i>et al.</i> 2010)

Acrylic (IP-Dip, Nanoscribe)	Cell cultures on iron coated microneedles showed high biocompatibility	2PP	Solid	Coated with iron for attaining magnetic properties, for potential applications in tissue engineering, drug delivery, etc.	(Kavalzhiev <i>et al.</i> 2017)
Acrylic (IP-S, Nanoscribe)	Minimal cytotoxicity (about 10% decrease in cell viability in 2 days) (Moussi <i>et al.</i> 2020)	2PP	Solid, hollow	Perforation of guinea pig round window membrane and perilymph sampling	(Aksit <i>et al.</i> 2018; Szeto <i>et al.</i> 2021)
			Hollow	Delivery of fluorescent dye in mouse skin	(Moussi <i>et al.</i> 2020)
Methacrylate-based (Clear, Formlabs)	Preliminary studies on HL-1 cells (Hart <i>et al.</i> 2020) and L929 and gingival fibroblasts showed satisfactory cell viability, dependent on post-printing curing (Kurzmann <i>et al.</i> 2017).	Laser SLA	Solid	Prototype, potentially usable for transdermal drug delivery applications	(Kundu, Ausaf and Rajaraman 2018)
			Hollow	Extrusion of microencapsulated cells	(Farias <i>et al.</i> 2018)

Methacrylate-based (Dental SG, Formlabs)	Biocompatible, Class I, USP IV (Vertex 2016)	Laser SLA	Solid, coated	Coated with insulin and anti-cancer agents and tested on diabetic and skin cancer animal models.	(Pere <i>et al.</i> 2018; Economidou <i>et al.</i> 2019; Uddin <i>et al.</i> 2020)
Methacrylate-based (Castable, Formlabs)	Not investigated	Laser SLA	Solid, 'poke and patch'	Enhancement of model dye permeation in human skin	(Xenikakis <i>et al.</i> 2019)
Methacrylate based (Dental LT Clear)	Biocompatible, Class IIa (Formlabs 2017)	Laser SLA	Hollow	Microfluidic-enabled microneedle system for mixing of fluids and transdermal delivery	(Yeung <i>et al.</i> 2019)
Polyethylene glycol diacrylate (PEGDA) with Phenylbis ⁱⁱ	PEGDA 3D printing resins have shown promising biocompatibility features (Warr <i>et al.</i> 2020; Mau <i>et al.</i> 2019)	DLP	Hydrogel	Multifunctional microneedles for rhodamine B delivery and detection	(Yao <i>et al.</i> 2020)
Polyethylene glycol dimethacrylate (PEG)		CLIP	Solid, coated	Transdermal delivery of model proteins	(Caudill <i>et al.</i> 2018)

with TPO ⁱⁱⁱ	Biocompatible, constituents are FDA approved (Johnson <i>et al.</i> 2016)		Hydrogel, swellable	Sustained transdermal delivery of rhodamine B through diffusion	(Johnson <i>et al.</i> 2016)
Polycaprolactone trimethacrylate with TPO ⁱⁱⁱ			Biodegradable		
Polyacrylic acid with TPO ⁱⁱⁱ			Dissolvable	Water soluble microneedles for fast rhodamine release	
Poly(lactic acid) (PLA)	Biocompatible, FDA approved (Luzuriaga <i>et al.</i> 2018)	FDM + etching	Biodegradable	Transdermal delivery of fluorescein	(Luzuriaga <i>et al.</i> 2018)
Sodium alginate with hydroxyapatite (HA)	Constituents are biocompatible (Wu <i>et al.</i> 2020)	Extrusion bioprinting + stretching	Biodegradable	Transdermal delivery of glucose-responsive insulin for the treatment of diabetes	(Wu <i>et al.</i> 2020)

ⁱ BAPO: Bis (2,4,6-trimethylbenzoyl)-phenylphosphineoxide

ⁱⁱ Phenylbis: (2,4,6-trimethylbenzoyl) phosphine oxide

ⁱⁱⁱ TPO: Diphenyl(2,4,6-trimethyl-benzoyl-)phosphine oxide

Consideration of sterilisation practices is also necessary and pertinent to material selection. Interestingly, several studies have proposed that FDM produced parts, provided that the printing platform and chamber are sterile, have been subjected to some degree of sterilisation due to the high temperatures reached by the process (Rankin *et al.* 2014; Walker *et al.* 2016; Wong and Pfahnl 2014). Indeed, a subsequent study reported high, but not 100%, sterility of FDM printed surgical tools (Kondor *et al.* 2013). It is

evident that the adaptation of 3D printing equipment is required to achieve aseptic manufacturing. Currently, 3D printed devices are sterilised post-manufacturing, hence constituent materials must be chosen to withstand exposure to radiation, chemicals or steam associated with common procedures such as autoclave, hydrogen peroxide gas plasma and ethylene oxide gas (Culmone, Smit and Breedveld 2019). Examples of commercial biocompatible materials with confirmed compatibility with sterilisation procedures that have not yet been used for microneedle printing are PC-ISO (Stratasys 2017), ABS-M30i (Stratasys 2020) and MED610 (Stratasys 2011).

1.8 Regulatory framework

Conforming to the requirements of the regulatory authorities is a prerequisite for the commercialisation of TDD systems. The application of 3D printing for microneedle manufacturing introduced new challenges in the regulatory perspective. Although, as mentioned above, the first 3D printed oral tablet has already been FDA-approved, in the case of a TDD system the regulatory requirements may differ.

Microneedles that are used in the diagnosis, treatment, prevention of a disease or affect body function in any way, are viewed by regulatory bodies as medical devices (Lee *et al.* 2020). In 2017, the “Regulatory Considerations for Microneedling Devices” was issued by the FDA, compiling a set of guidelines on manufacturing, evaluation, testing and quality control (FDA 2017a). Since microneedles are perceived as devices, the fabrication strategies of microneedle patches must obey the current Good Manufacturing Practice (cGMP) described in the Quality System regulations (21 CFR 820), wherein the necessary requirements to ensure safety and effectiveness of the manufactured products, are described (Di Prima *et al.* 2015). Following the increasing tendency to adopt 3D printing for medical device manufacturing, the FDA issued the “Technical Considerations for Additive Manufactured Medical Devices” (FDA 2017b). Microneedle product developers that explore pathways to incorporate 3D printing in their production line will need to take into consideration both sets of guidelines combinatorially.

The new guidelines, although similar to the respective for typical manufacturing methods, introduce new requirements. For instance, the manufacturing information is expected to be provided and reviewed by the FDA. The developers are encouraged to describe their manufacturing line in detail, step by step, and include information like

simple printing settings (e.g., building orientation). The need for thorough review of every manufacturing step stems from the high parameter-sensitivity of these processes and the innate relationship between process and quality. Furthermore, the directives propose some in-process and post-process quality control actions (non-destructive testing, mechanical testing, evaluation of dimensional accuracy). Also, it is suggested that an overview of the processes followed for post-fabrication cleaning of excess material, sterilisation and biocompatibility evaluation must be included. Those guidelines are specified as ‘non-binding recommendations’ and it is specifically clarified that alternative approaches may be applicable as long as they comply with the respective statutes and regulations (FDA 2017b).

The guidelines bring out some interesting points on the design of ‘patient-matched devices’ that need to be addressed by the manufacturer such as imaging effects and patient data protection. A notable directive pertains to patient-specific medical devices that are based on individual anatomy. The FDA raises the issue of time between patient imaging and device use, in the sense that anatomical changes due to disease or ageing can come into effect, thus rendering the personalised device unusable.

In a relevant study the issue of microneedle sterilisation was put forward as a regulatory requirement. The author proposes that even if the fabrication process results in disinfected microneedle surface, absolute sterilisation may need to be guaranteed. The study concluded that steam sterilisation and dry heat sterilisation destroyed the polymeric microneedles, while a gamma sterilisation-based protocol may finally be suitable, after additional investigation is carried out (McCrudden *et al.* 2014).

Regarding the use of custom 3D printing materials, the FDA highlights that all the chemical changes induced by the printing process, due to recurring melting and cooling, photopolymerisation etc., must be identified and noted. Thus, unwanted chemicals that may endanger patients’ health will be detected. An additional consideration pertains to dissolvable microneedle systems, in the sense that the drug of choice must be immune to the physicochemical alterations induced by the 3D printing process. Hence, for applications involving FDM or other thermal extrusion technologies, the thermal stability of the API in the temperature range of the process needs to be evaluated. Similarly, selecting drugs that are immune to radiation is a prerequisite for photopolymerisation 3D printing of drug-loaded resins.

1.9 3D printed microneedles: Potential market and societal impact

TDD systems might be the solution sought by patients and physicians towards a simple, self-administrative, pain-free pharmaceutical therapy that will simultaneously circumvent the drawbacks of traditional administration routes such as needle phobia, pain or digestive issues. Regardless of their advantages and the extensive scientific interest they have attracted, the pharmaceutical industry is still reluctant to invest in the introduction of new microneedle products. Currently, there are only 13 commercially available microneedle products for cosmetic purposes, drug and vaccine delivery (Halder *et al.* 2020; Lee *et al.* 2020). However, the market for microneedle products is anticipated to expand at a Compound Annual Growth Rate (CAGR) of 7.1% (Data Bridge Market Research 2020).

The application of additive manufacturing presents a unique opportunity for the transdermal drug delivery field. Technical and economical limitations posed by traditional manufacturing methods are likely to have disfavored investments, especially from start-ups and small or medium size enterprises (SMEs). Injection moulding equipment and tooling for instance come at a high cost and investing in the technology to introduce new products in starting, small batches may be viewed as non-economical. The introduction of cost-effective 3D printing solutions minimises starting budgets, while the necessary equipment is reduced to one single device, commonly of small volume, shortening production lines and simplifying business models. Although arguably 3D printing may not be yet comparable in economical effectiveness with traditional industrial equipment for mass production (Kubáč and Kodym 2017), the simple and fast nature of the technology can encourage the introduction of customised product lines, realise demand-driven production and facilitate R&D.

The unique ability of 3D printing to enable easy and fast customisation is a strong asset. In the R&D setting, the versatile, easily customisable character of 3D printed systems simplifies and accelerates prototyping, as demonstrated by various studies in the present review. Moreover, the fast nature of 3D printing technologies can benefit the implementation of an ‘on demand’ production system, wherein production can be tailored to the market needs. Following the rationale of the ‘Just-In-Time’ model (Shidid *et al.* 2016), 3D printing can enable the alignment of demand and production, improving efficiency and reducing inventory costs and waste (Kubáč and Kodym 2017; Attaran 2017). These advantages can have a significant impact on the competitiveness

of new and existing players and attract investments, which can transform the market outlook.

3D printing has the dynamic to impose not only a quantitative impact on the microneedle market, but also a qualitative one, by promoting the concept of personalised therapeutics, wherein the production will shift from the massive to the individual. Such technologies enable the flexibility to design the product based on the application in a cost-effective and fast manner. The individual needs of the patient can be taken into consideration while multifunctional treatments can be combined in customised systems without significant alteration of production lines. The layer-by-layer fabrication rationale which is the cornerstone of the 3D printing technology may be thoroughly exploited in favour of the TDD in several aspects. Systems can be designed and printed featuring layers with various drug concentrations for gradually increasing or decreasing doses or for forming of priming doses; alternating layers with different drug contents, designed along the lines of the therapeutic process, are also a prospect. Systems can be designed taking into consideration several factors that influence the drug absorption rates that are varying among patients, such as the degree of hydration within the skin and the thickness of the skin layers. Such factors vary across different ethnicities (Rawling 2006) and even individually. Moreover, specific systems can be tailored to meet the needs of children, to whom conventional transdermal systems have been reported to cause irritation (Liebelt and Shannon 1993). Hence, the adoption of such technologies cannot only increase the accessibility of transdermal drug delivery systems but can also help to adapt and improve therapeutic regimes for more effective and targeted treatments.

In the field of vaccination, microneedles broadened the potential of TDD systems (Marshall, Sahm and Moore 2016). Needle-free systems will have a notable impact in the third world where poor sanitation, scarce medical resources and needle re-use cause infections or transmittable disease outbreaks. Although conventional jet injectors have been employed in mass vaccinations, the technology does not guarantee that pathogens will not be transmitted, as the costs of single usage disposable nozzles are prohibitive in the third world. The 3D printing technology can serve this purpose, as long as serious effort is made in the future to lower the costs through the adoption of more cost-effective additive manufacturing methods.

1.10 Key objectives

The central motivation behind this research stemmed from the foreseen transformational impact that the cutting-edge technology of 3D printing can have on microneedle prototyping and production. The research plan was set out as a series of progressive steps, starting from the design and manufacturability studies and proceeding to evaluating the drug delivery performance of the systems *in vitro* and *in vivo*. More specifically, the goals of the present work were to:

1. Explore the potential of cost-effective 3D printing technologies as efficient, reliable and straightforward manufacturing techniques for microneedle-mediated transdermal delivery systems. The goal was to establish microneedle printing strategies by identifying the core influential parameters that determine printing success. In this context, the effects of design and manufacturing parameters on performance will be thoroughly investigated.
2. Develop solid microneedles with different geometries and hollow microneedles with different heights. The microneedles will be evaluated for their efficacy to safely pierce the skin without compromise of their structural integrity.
3. Implement sophisticated coating techniques to develop solid coated microneedle patches with specific insulin cargos. The effect of the microneedle geometry on the morphology of the coating and hence the dissolution into the skin will be assessed. The effect of polymer additives as insulin stabilisers will be explored.
4. Investigate the integration of 3D printed hollow microneedles with microelectromechanical systems into a novel platform device for controlled drug delivery. The goal is to enable the *in-situ* customisation of the drug administration to facilitate personalisation of pharmaceutical treatment.
5. Conduct transdermal delivery studies of insulin administered with the developed systems *in vitro* and *in vivo* using a diabetic animal model.

CHAPTER 2
3D PRINTED SOLID MICRONEEDLES
DESIGN, MANUFACTURING, OPTIMISATION AND MECHANICAL
PERFORMANCE

2.1 INTRODUCTION

Solid microneedles have known wide acceptance in research, while they comprise the majority of the currently available microneedle products in the market. Due to their presently increasing popularity in cosmetology, six products have been introduced to the market by 2019 (Waghule et al. 2019). Solid microneedles can realise drug delivery through the ‘poke and patch’ method, wherein they are used as a pretreatment of the skin before a solution is applied, or by carrying the API in the form of a surface coating (Alkilani, McCrudden and Donnelly 2015).

The acceptance of solid microneedles is owed to a number of favourable characteristics that often make them the preferred choice over other types. For instance, the microneedle manufacturing and drug loading are two distinct and autonomous processes. This is particularly advantageous over dissolvable systems, wherein manufacturing may require adaptations to suit the individual API and polymer combination. Moreover, alterations of the mechanical properties may occur, depending on the drug content (e.g. in cases that the drug has plasticizing effects). Other advantages include simpler manufacturing processes in comparison to hollow microneedles, the complex and delicate structure of which is restraining in terms of process versatility. The clinical application of solid microneedles is also generally simple, as opposed to systems using hollow systems, that require a flow instigator.

Multiple manufacturing methods of solid microneedles are reported in literature, such as chemical etching, micromoulding, reactive ion etching, lithography and laser cutting (Larrañeta et al. 2016) . The previous decade, several research endeavours have been concentrated towards the adoption of 3D printing, mainly of the photopolymerisation-based range, for the direct solid microneedle fabrication (Gittard et al. 2011; Lim, Ng and Kang 2017; Kavaldzhiev et al. 2017). The studies demonstrate the potential of 2PP and DLP for solid microneedle manufacturing, due to their high resolution in the microscale, which is critical for the successful microneedle fabrication. The

applicability of the more cost-effective laser Stereolithography, has not yet been fully explored. Overall, a more systematic approach regarding the technical aspects of microneedle photopolymerisation 3D printing is needed to universalize research outcomes and build robust technical knowledge that is readily transferrable to a wider range of applications pertinent to microneedles.

Implementing a new methodology to manufacture structures as intricate as microneedles, poses challenges. The design and prototyping stage is the first and foremost step, as it can have a significant impact on the clinical performance, production, cost and scale-up potential of the system. Typically, the parameters needed to be considered at the design stage can be classified in two groups: 1) requirements related to the application and 2) parameters pertinent to the manufacturing process. Indeed, a new concept emerged alongside with the evolution of 3D printing, the Design for Additive Manufacturing (DfAM). DfAM attempts to simultaneously correlate the design process with the particular nature and respective constraints of Additive Manufacturing (Kerbrat, Mognol and Hascoët 2011). Thompson et al. defines DfMA as *“the practice of designing and optimizing a product together with its production system to reduce development time and cost, and increase performance, quality, and profitability”* (Thompson et al. 2016). It is evident that exploring the applicability of 3D printing for microneedle fabrication introduces new design criteria that have not yet been thoroughly mapped.

2.1.1 Aims and objectives

The main objective of the present experimental Chapter is to lay out a strategy for the development of laser SLA microneedles. The outcomes of this work will provide valuable insight regarding crucial design and manufacturing decisions, to researchers that aim at using laser SLA for microneedle production. The aims of the study are:

- Identification of the key design criteria that balance application goals and manufacturing restrictions.
- Application of DfAM principles to design microneedle arrays that are effectively and reliably 3D printable.
- Optimisation of the printing quality and performance by investigating the effects of printing and post-printing processes.
- Evaluation of the effect of microneedle geometry on mechanical behaviour.

2.2 MATERIALS AND METHODS

2.2.1 Computer Aided Design (CAD)

Three microneedle geometries were designed using the PTC Creo Computer Aided Design (CAD) software (PTC, Boston, MA, USA). Based on shape, the geometries were named ‘cone’, ‘pyramid’, and ‘spear’. The microneedles were designed to protrude from a square patch of 15 mm × 15 mm × 0.5 mm in a symmetrical configuration of 7 rows and 7 columns. Moreover, solid cylinders were designed in accordance with the requirements of the ASTM D695-15 protocol. The cylinders of \varnothing 12.7 mm and length 25.4 mm were intended for mechanical testing to investigate the effect of curing conditions on compressive properties.

2.2.2 Additive Manufacturing and printing material

The microneedles were fabricated using the biocompatible Class I acrylic resin, Dental SG (Formlabs, GoPrint3D, North Yorkshire, UK). A Form2 (Formlabs, GoPrint3D, Ripon, North Yorkshire, UK), a 3D printer based on the technology of laser SLA, was employed to manufacture microneedle patches. Prior to printing, the virtual models were imported in the printer software, PreForm (Formlabs, Somerville, MA, USA), in order for the final printing file to be generated. The layer thickness was set at 50 μ m and structure supports were manually added with a touchpoint size of 0.4 mm. A base was used to connect the supports with the printing platform for each microneedle array. The patches were rotated at 0°, 90°, and 45° to the printing platform to study the effect of the printing orientation on microneedle quality and dimensional accuracy. The code generated by the printing software was imported in the 3D printer that was equipped with a vat of unpolymerised Dental SG resin. The printed structures were submerged in an isopropyl alcohol (USP grade) bath to rinse away any unpolymerised resin residues. The printed structures were then cured in a UV-A heated chamber (MeccatroniCore BB Cure Dental station, GoPrint3D, Ripon, North Yorkshire, UK) at a wavelength of 405 nm. The cylinders for mechanical testing were subjected to 9 different curing regimes, each combining a preset curing time (30 min, 45 min, and 60 min) and chamber temperature (40 °C, 50 °C, and 60 °C). The combination of curing parameters that was found to optimize material mechanical behaviour was applied for the curing of microneedle patches.

2.2.3 Dental SG compression testing

The effect of different curing conditions on the mechanical properties of the printing material was explored. The printed resin cylindrical specimens were subjected to compression testing, complying with the ASTM D695 – Standard Test Method for Compressive Properties of Rigid Plastics, international testing protocol. A Tinius Olsen universal testing machine was employed, equipped with a 25kN load cell and two flat, cylindrical test fixtures. The specimen was positioned at the centre of the fixed test fixture while the driven one was moving downwards along the specimen longitudinal axis at a constant speed of 1.5 mm/min. Continuous force and displacement data were recorded for every specimen. The generated data were processed according to the offset curve method. True stress and true strain data were calculated along with the compressive moduli and yield strengths for all curing regimes. A total of 5 specimens were tested for each set of curing conditions.

2.2.4 Scanning Electron Microscopy (SEM)

The microneedle arrays were mounted onto aluminium stubs using a double-sided carbon adhesive tape (Agar scientific, UK). Each array was examined by SEM (Hitachi SU 8030, Japan) using a low accelerating voltage (1.0 kV). A low accelerating voltage was used to avoid electrical charges on the microneedles. The images were captured digitally from a fixed working distance (11.6 mm) using different magnifications. Processing the images and measurements were conducted through the software ImageJ (Fiji package) (NIH image, Bethesda, MD, USA).

2.2.5 Preparation of porcine skin samples

Full-thickness abdominal porcine skin was collected from a local slaughterhouse (Forge Farm Ltd., Kent, UK) and was then shaved using a razor blade. The fatty tissue below the abdominal area was removed using a scalpel. Samples of full-thickness skin tissue were sliced and used for the piercing tests.

2.2.6 Piercing tests in porcine skin

The 3D printed cone, pyramid, and spear microneedles were subjected to piercing tests in porcine skin. A TA.HD plus Texture Analyser (Stable Micro Systems, Surrey, UK) equipped with a 5 kg of load cell was employed. The microneedle arrays were fixed on

the moving probe of the machine using double-sided adhesive tape. Samples of full-thickness abdominal skin were placed on waxed petri dishes and were secured on the bottom, fixed probe of the machine. Continuous force and displacement measurements were recorded to identify the point of needle insertion. The speed of the moving probe was 0.01 mm/s and all experiments were repeated 5 times.

2.2.7 Axial force mechanical testing

To evaluate the fracture strength of the cone, pyramid, and spear microneedles, fracture tests were conducted employing a Tinius Olsen H25KS mechanical testing machine (Tinius Olsen TMC, Horsham, PA, USA), equipped with a 25 kN load cell and two flat, cylindrical test plates. The microneedles were mounted on the fixed plate of the machine using double-sided tape and were compressed by the moving flat steel plate until fracture. Continuous force and displacement measurements were recorded. The speed of the moving probe was 1 mm/s and each experiment was repeated 5 times.

2.2.8 Margin of safety

Data obtained from piercing tests and axial force mechanical tests were employed to calculate the margin of safety for all designs, from the following equation:

$$\text{margin of safety} = \frac{F_{fracture}}{F_{insertion}} \quad \text{Equation 2.1}$$

Where $F_{fracture}$ and $F_{insertion}$ are the fracture and insertion forces, respectively. Values higher than 1 are considered to reassure safety upon application.

2.3 RESULTS AND DISCUSSION

2.3.1 Microneedle design

The design process of a new microneedle patch is one of the crucial steps in its development. The decisions made in this stage are critical for the soundness of the fabrication process, as well as for the performance of the patch during clinical application. In this study, all design decisions, were made by adhering to the following

rationale: to design microneedles that will serve their therapeutic mission while also be compatible with the 3D printing technology of choice.

From the clinical perspective, Lutton et al. pointed out the principal efficiency requirements that need to be met by a microneedle patch : 1) to penetrate the skin, 2) to reach a required skin depth, 3) to possess sufficient strength to avoid failure and 4) to deliver their load (Lutton et al. 2015). In this context, four geometrical parameters, namely microneedle height, aspect ratio, interspacing and tip size, were considered as main influential factors of the aforementioned aspects of microneedle performance.

Microneedle height influences penetration depth, drug delivery and mechanical strength. The range of microneedle heights that has been proposed in literature is notably wide, spanning from 150 μm to 1500 μm (Waghule *et al.* 2019). In this study, the height was chosen at 1000 μm , which is anticipated to reassure that a sufficient penetration depth is reached upon application, even if the microneedle insertion is partial (not 100% of the height is inserted). This is essential to ensure that the drug cargo reaches the dermal capillary bed. Moreover, in solid microneedle systems intended for coating applications, a longer microneedle shaft creates a larger lateral surface, thereby increasing the area available for coating (i.e. the maximum drug cargo).

It has also been found that the microneedle height affects the mechanical strength through its directly proportional relationship with the aspect ratio (typically ratio of height to base width). More specifically, the microneedle aspect ratio, has been found to have a significant, inversely proportional effect on the strength of the needles (Gittard *et al.* 2013). Based on literature findings, an aspect ratio of 1:1 was chosen to avoid microneedle failure due to buckling and ensure successful skin insertion (Park and Prausnitz 2010).

Microneedle interspacing, which is defined as the center-to-center distance, influences the piercing behaviour of the array. Arrays with high microneedle density, i.e. positioning of the shafts too close from one another, fail to pierce the skin due to pressure reduction at the microneedle tips, a phenomenon dubbed as ‘bed of nails’ effect. Theoretical and finite element analyses have demonstrated that the ‘bed of nails’ effect is pronounced affecting insertion forces, for microneedle interspacing values below 150 μm . For interspacing >150 μm , there is no significant effect on piercing force (Olatunji *et al.* 2013). Moreover, experimental studies have not detected any

interrelationship between interspacing and penetration depth (Donnelly *et al.* 2010). In this study, an interspacing of 1850 μm was set for all microneedle designs, a value well above the 150 μm threshold.

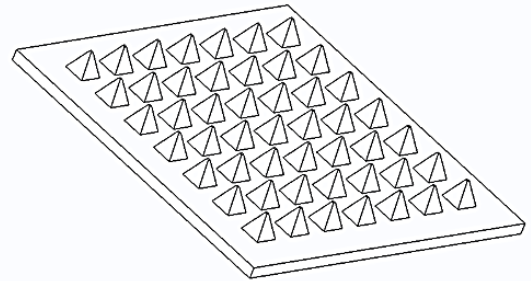
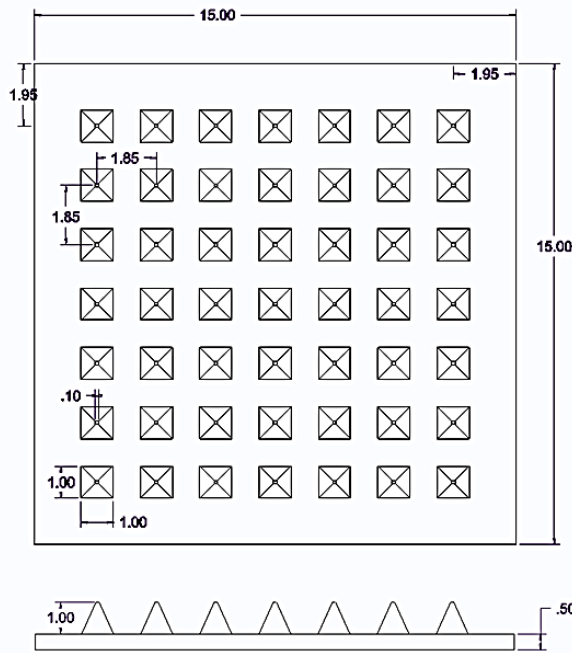
The microneedle sharpness, quantified by tip diameter or curvature, governs the piercing behaviour and is determinant of the force required for insertion (Davis *et al.* 2004). The insertion force in turn is the main determinant of the pain experienced by the patient upon application (Gill *et al.* 2008). In literature, microneedle tip diameters vary. For this design parameter, a major restriction was imposed by the 3D printing technology, pertaining to resolution. The specific desktop SLA technology employed was equipped with a laser featuring spot size of 140 μm , yielding minimum feature sizes at the xy plane of 150 μm (Formlabs 2021). Hence, while the tip was designed in respect to the technical limitation, smaller dimensions than the minimum feature size were considered potentially attainable. The hypothesis was that through tuning of the printing parameters, a microneedle tip smaller than 150 μm could be obtained.

Maintaining the same height, base width and interspacing, three microneedle geometries were designed, featuring cone, pyramid, and spear shapes. Their nominal dimensions are displayed in Table 2.1.

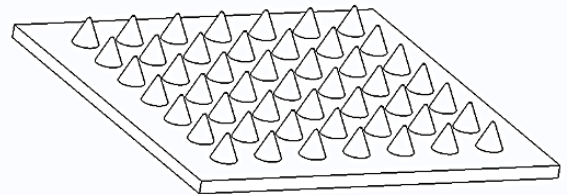
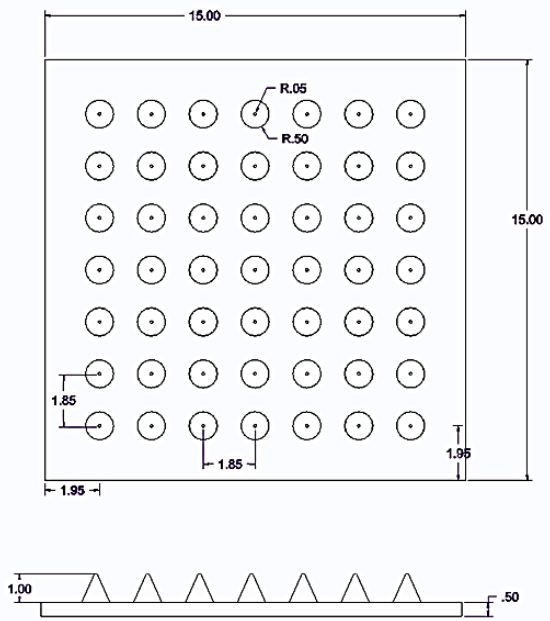
Table 2.1 Microneedle Computer Aided Design (CAD) dimensions.

	Pyramid	Cone	Spear
Height (μm)	1000	1000	1000
Base (μm)	1000 \times 1000	\varnothing 1000	1000 \times 80
Tip (μm)	100 \times 100	\varnothing 100	100 \times 80
Tip angle ($^{\circ}$)	48.5	48.5	97

The respective 7 \times 7 symmetric patches were developed using the PTC Creo Parametric design software. The engineering designs are illustrated in Figure 2.1.



a



b

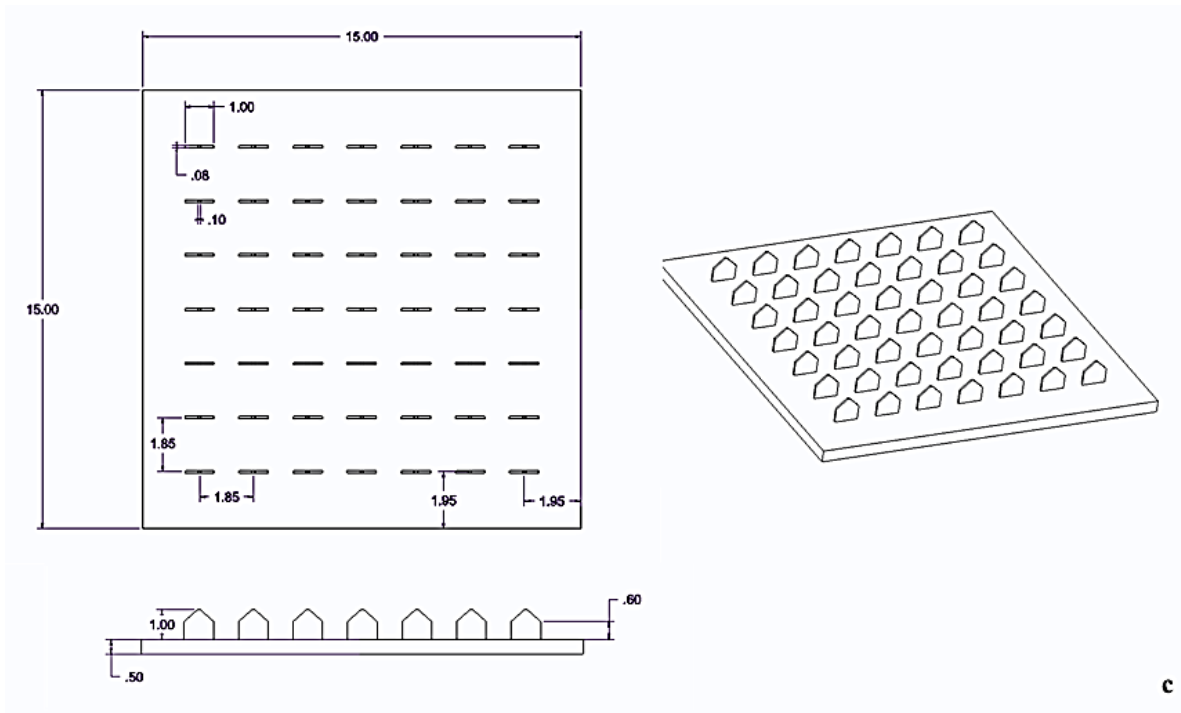


Figure 2.2 Engineering drawings of a) pyramid, b) cone and c) spear microneedle patch.

2.3.2 3D printing

After the designs were finalised, the virtual models were ‘sliced’ using the software (creation of the .stl file) and imported in the printer software where the printing parameters were selected. The layer thickness was set at 50 μm , which was the highest resolution obtainable for the specific material. Resolution is adversely proportional to the printing time for this technology; however the importance of high end-product definition was considered a priority over production time. The touchpoint size of 0.4 mm was found to allow subsequent removal of the supports without damaging the delicate microneedle structures.

The 3D printer followed the standard building process of typical laser SLA. A building platform was submerged in a vat of unpolymerised photocurable resin and through an optical window, the laser ‘wrote’ on the resin, selectively polymerizing fine, coalescing roads and forming consecutive layers. After each layer, the printing platform moved upwards, detaching the printed structure from the optical window and allowing for a mechanical sweeper blade to recoat the surface with fresh unpolymerised resin. After

completion, the microneedle patches were rinsed in isopropyl alcohol to remove unpolymerised resin residues.

It is noteworthy that SLA MNs required no post-printing etching to sharpen the tips in contradiction to respective work using Fused Deposition Modeling (FDM), that typically features inferior resolution capabilities (Luzuriaga *et al.* 2018). Thus, the production becomes faster, cheaper and easier to scale-up, while ensuring no variations on the end-product quality. Another advantage of SLA over FDM pertains on the mechanical behavior of the printed structures. On the one hand, FDM parts exhibit anisotropic and laminate-like behavior, depending on the raster (printing ‘road’) orientation (Dey and Yodo 2019). These traits add complexity to the mechanical analysis by introducing variations of the mechanical properties dependent on direction, thus complicating the design stage. Moreover, the FDM technology has been associated with poor adhesion between adjacent layers, which can lead to failure due to delamination (Rahim, Abdullah and Md Akil 2019). However, it has been documented that SLA printed parts are considered isotropic (Dizon *et al.* 2018) and delamination is not a risk associated with the SLA technology.

For the purpose of this study, we employed a commercial Class I biocompatible resin as the microneedle manufacturing material. The printed material, having been subjected to the post-printing washing and curing protocol described here, has been found to comply with ISO biocompatibility standards and thereby rendered biocompatible. The aforementioned testing, encompassing systemic injection (acute systemic toxicity), intracutaneous and implantation tests, concluded classification of the material as USP IV according to the United States Pharmacopeia and National Formulary (USP-NF) (Vertex 2016). These findings coincide with other reports found in the literature (Kurzmann *et al.* 2017; Kreß *et al.* 2020). The verified biocompatibility of the polymer is a prerequisite for the potential clinical applicability of the proposed microneedle patch.

2.3.3 Optimisation of post-printing curing conditions for enhanced mechanical properties

Prior to post-printing curing of microneedles, the effect of curing conditions on the mechanical properties of the material was evaluated. It was hypothesised that the post-printing curing regime influences the cross-linking density, which has been documented

to be closely associated with Young's modulus and ultimate strength (Oakdale *et al.* 2016; Karalekas *et al.* 2002). The aim of this study was to identify the curing settings that yield optimal material mechanical properties, thereby improving the mechanical behaviour of the microneedles. As microneedles are mainly subjected to compressive stresses along their longitudinal axis during application, the focus of this study was put on improving the compressive properties of the material. Hence, standard cylindrical specimens for compression testing (ASTM 2002) were designed and printed using the same material and settings as the microneedles. Different curing regimes were imposed featuring varying durations of UV-A exposure and chamber temperature, in the respective ranges permitted by the manufacturer (30 to 60 min and 40 to 60 °C). Visual observation of the specimens revealed a gradual deepening of the colour with the increase of both exposure time and temperature (Figure 2.2a), which indicates an increasing degree of cross-linking (Bi *et al.* 2011).

During compression testing, the specimen progressively attained a barrel shape, an effect known as 'barrelling', which is associated with ductility (Figure 2.2b). Furthermore, it was found that the 25 kN load cell of the testing machine was not sufficient for the determination of ultimate strength. Instead, the yield strength was calculated. The exposure time was found to have a more pronounced and sustained effect on both properties than chamber temperature, with longer exposure times to lead to increased mechanical properties (Figure 2.2c,d). Indeed, the influence of chamber temperature was found to weaken with increasing exposure time and practically vanished for specimens exposed for 60 min. Both compressive modulus and yield strength maximum values, 2.2 GPa and 83 MPa respectively, were reached for curing at 40 °C and 60 min. The latter were employed as the standard post-printing curing regime for the duration of the present study. These findings suggest that optimising the post-printing curing regime is a crucial step for photopolymerisation printed microneedles, in the sense that a mechanically strong material reduces the chances of microneedle failure during application and increases confidence in the system.

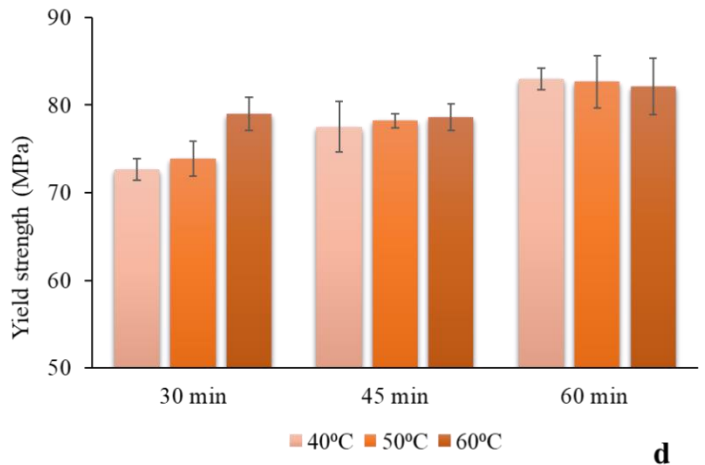
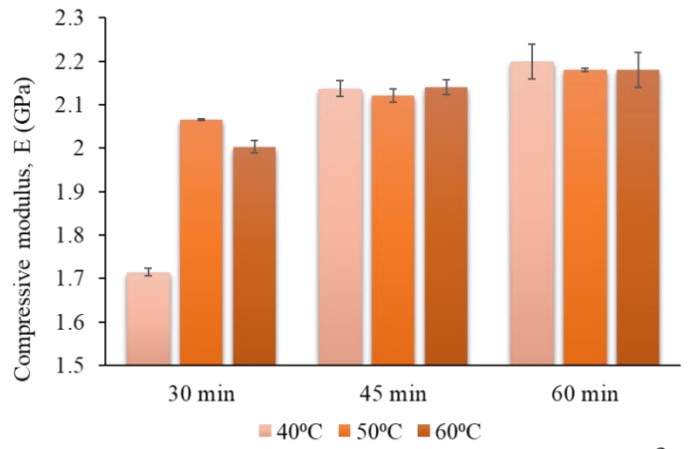
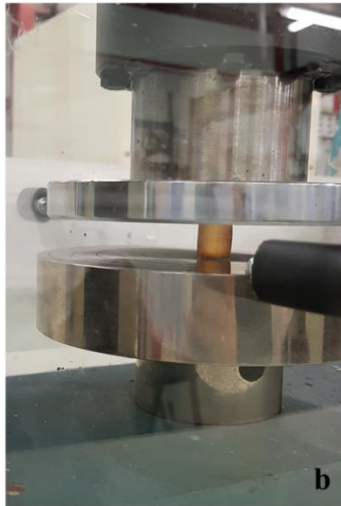
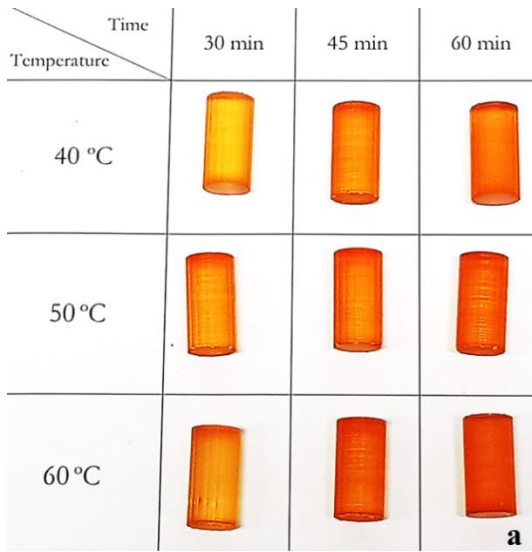


Figure 2.2 Optimisation of post-printing curing regime in respect to compressive mechanical properties: (a) Digital image of compression specimens for different curing settings, (b) compression testing in progress, with the specimen displaying the ‘barrelling’ effect, (c) compressive moduli, and (d) yield strengths obtained by specimens subjected to different curing regimes.

2.3.4 Optimisation of printing angle

After optimisation of the post-printing curing conditions, the effect of the printing angle on microneedle quality and dimensional accuracy was studied. The starting hypothesis of this study was based on two arguments: 1) The printing angle has an effect on the shape of the laser focal point as it focuses on the resin, thereby changing the sharpness of detail definition and 2) depending on the printing angle, the surface area in contact

with the optical window changes. The latter influences the magnitude of the mechanical stress induced by the printing process, particularly when upon completion of each layer the structure is detached from the optical window by being drawn upwards. Therefore, reducing the cross-sectional surface in the z axis is anticipated to reduce the in-process mechanical stress which, if extended, can introduce severe defects and printing failures.

Three printing angles were applied, by rotating the microneedle arrays at 0° , 90° , and 45° in respect to the printing platform. Figure 2.3 features SEM images of microneedles printed at different angles. The effect of the angle on microneedle quality is visually obvious, with microneedles built at 0° (Figure 2.3e–g) and 90° (Figure 2.3i–k) to appear blunter. Noticeably, the spear built at 90° (Figure 2.3k) showed significant structural defects. This is a typical example of in-process developed stresses that cause detrimental flaws to the point of printing failure. When built at 90° , the surfaces in contact with the optical window are the consecutive cross-sectional areas along the fine thickness of the spear, which are not able to withstand the mechanical stress during detachment. Nonetheless, at 45° the quality seems to improve significantly, and the microneedles appear sharper with no structural manufacturing failures detected (Figure 2.3m–o).

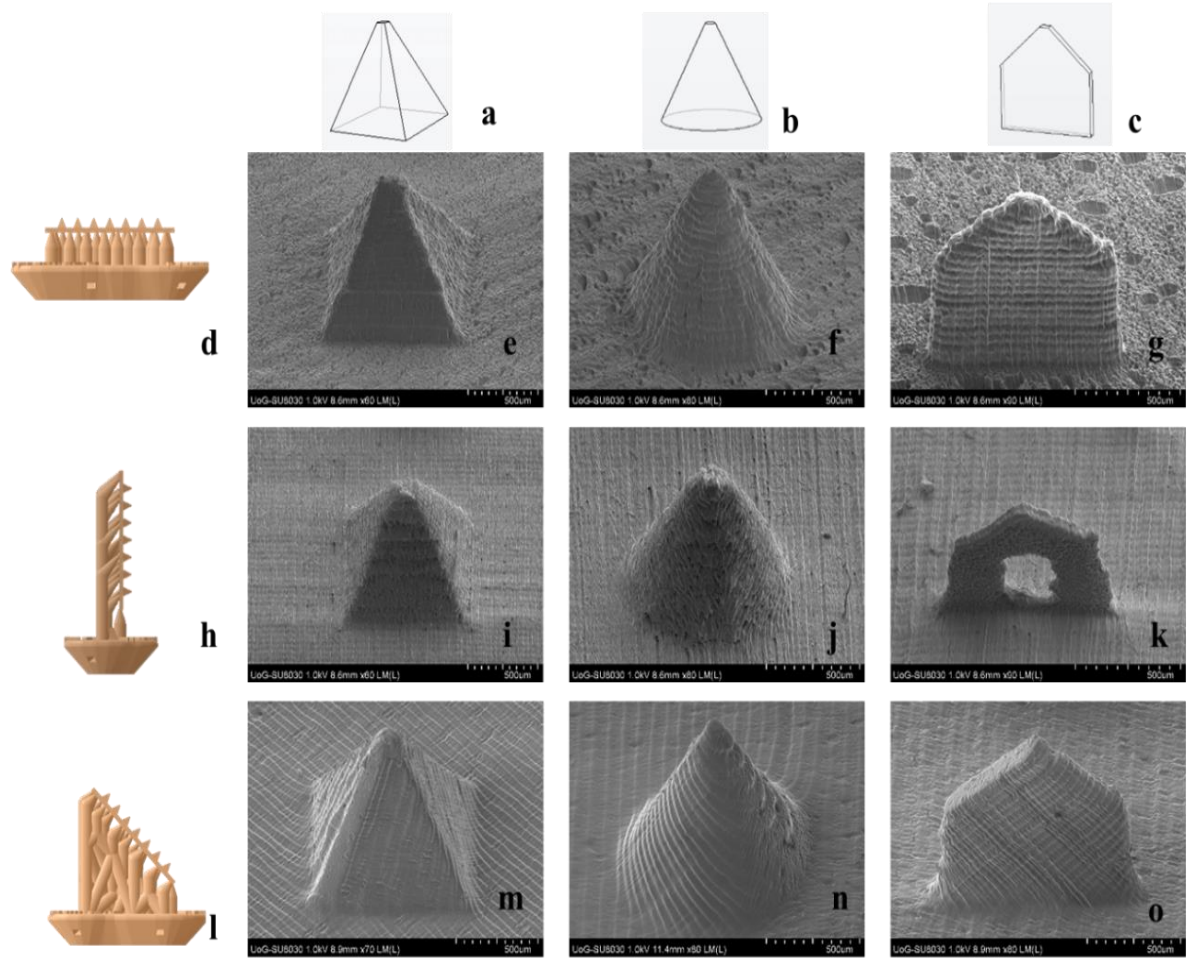


Figure 2.3 Optimisation of the printing angle. (a,b,c) CAD captions; (d,h,l) virtual models of supported microneedle arrays for 0° , 90° and 45° , where the bottom of the base is adhered to the printing platform; (e,f,g) SEM captions of microneedles built at 0° ; (i,j,k) SEM captions of microneedles built at 90° ; and (m,n,o) SEM captions of microneedles built at 45° .

To further elucidate the visually distinguishable impact of a printing angle on microneedle quality, the dimensional discrepancies of the printed structures in comparison to the original CAD dimensions (Table 2.1) were quantified. Three critical parameters, tip diameter, height at the longitudinal axis, and width at the base, were measured for all angles (Figure 2.4).

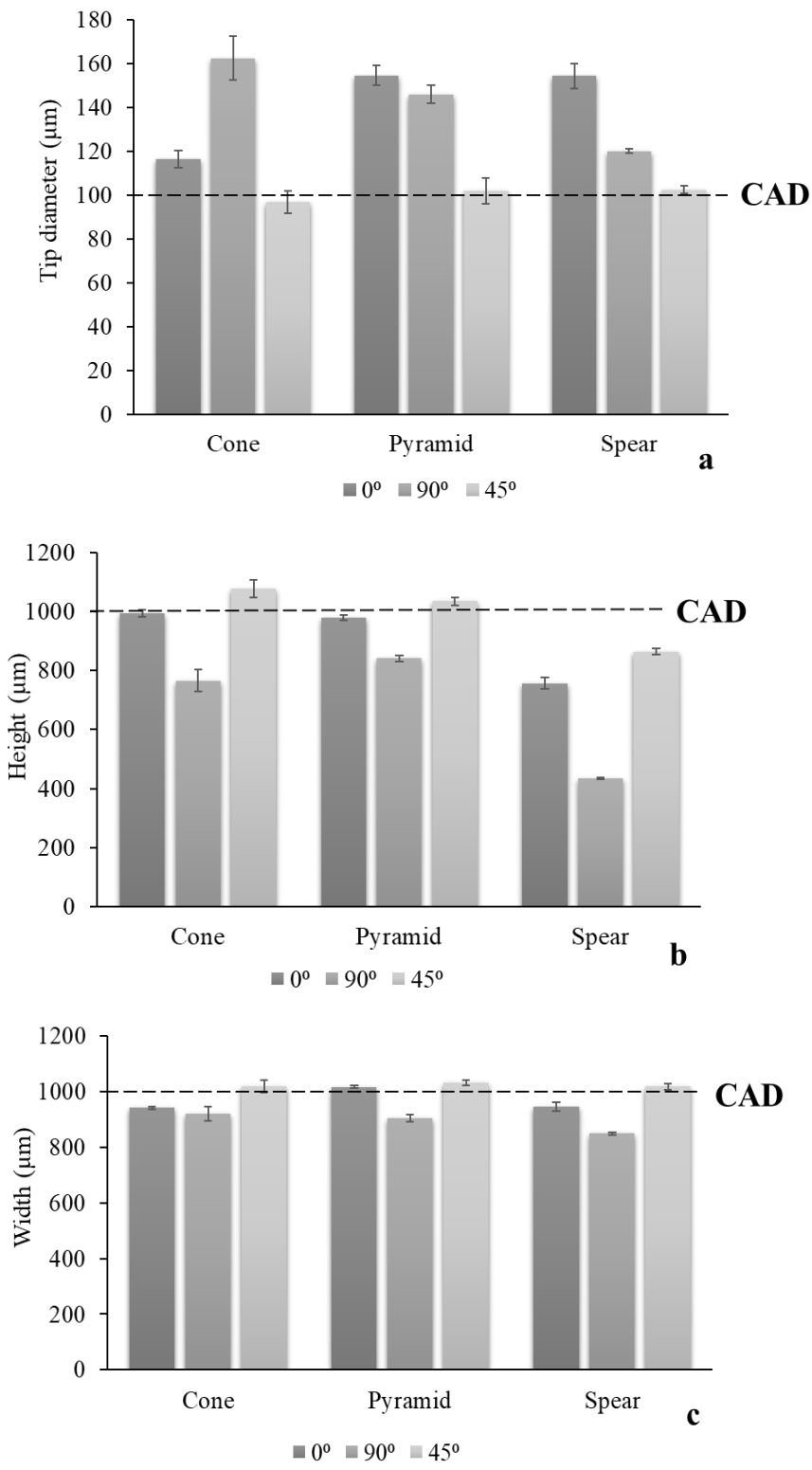


Figure 2.8 Dimensional discrepancies of printed microneedles in respect to printing angle; (a) tip diameter; (b) height at the longitudinal axis; and (c) width at the base.

In accordance with visual evidence, printing at 45° yielded the optimal dimensional fidelity to the nominal CAD dimensions. The parameter that was found to be more sensitive to the printing angle was the microneedle tip diameter, wherein the larger dimensional discrepancies were detected. At the same time, it is considered the most significant parameter, as increased microneedle sharpness is crucial for clinical application and is associated with the minimisation of pain (Gill *et al.* 2008). Microneedle designs were not equally prone to structural defects, with spear being more susceptible due to its fine thickness.

Dimensional discrepancies have been found to occur repetitively in 3D printed microneedles. Evidently, researchers report that microneedles are printed with different than designed aspect ratios, e.g. shorter and wider than specified (Krieger *et al.* 2019). This study validates that these discrepancies are a byproduct of incorrectly set printing parameters. By tuning the printing angle, the improvement in aspect ratio was dramatic.

The results suggest that the contact area with the optical window plays a prominent role, however it should not be considered solely. This can be observed in the case of 45° and 90°, where the area in contact with the optical window during printing is similar. Nonetheless, the dimensional discrepancies between both designs are large, leading to the conclusion that the amount of support that has been printed for each new printing cycle is critical. At 45° a sufficient amount of support structure has already been printed prior to initiating the fabrication of the microneedle patch. This provides a wider adhesion area to the building platform and hence a larger area for stress distribution. On the other hand, at 90°, the supports are printed simultaneously with the microneedle. The smaller support area for each new layer leads to increased mechanical stresses imposed on the microneedles during printing, and thus defective prints.

It is noteworthy that printing in an angle has another notable benefit, pertaining to the surface quality of the printed parts. While the characteristic layer-by-layer morphology, which is innate to all 3D printed structures, is visible, the microneedle surfaces are generally smooth. The ‘stair stepping’ effect that has been reported elsewhere for solid DLP fabricated microneedles (Johnson and Procopio 2019) is not manifested. This effect is not only visually unappealing but can also affect the mechanical performance of the microneedles.

The findings of this study suggest that the effect of printing orientation for 3D printing technologies that involve a recurring mechanical detachment of the structure from a surface intermediately between layers, is generally underplayed. The hypothesis that the build-up of mechanical stresses causes geometrical discrepancies and often detrimental structural flaws, was validated. It was also demonstrated that minimising the z axis cross sectional area should also be combined with careful thought of support placement, so that the microneedle is adequately supported during manufacturing. The optimised printing angle of 45° , which was used for the remaining of the present work, is in agreement with a respective study on hollow microneedles (Yeung *et al.* 2019).

2.3.5 Piercing tests

The 3D printed cone, pyramid, and spear microneedles were subjected to piercing testing using porcine skin to elucidate the effect of design on the maximum force required for successful insertion. A Texture Analyser and full-thickness porcine skin samples were employed (Figure 2.5).

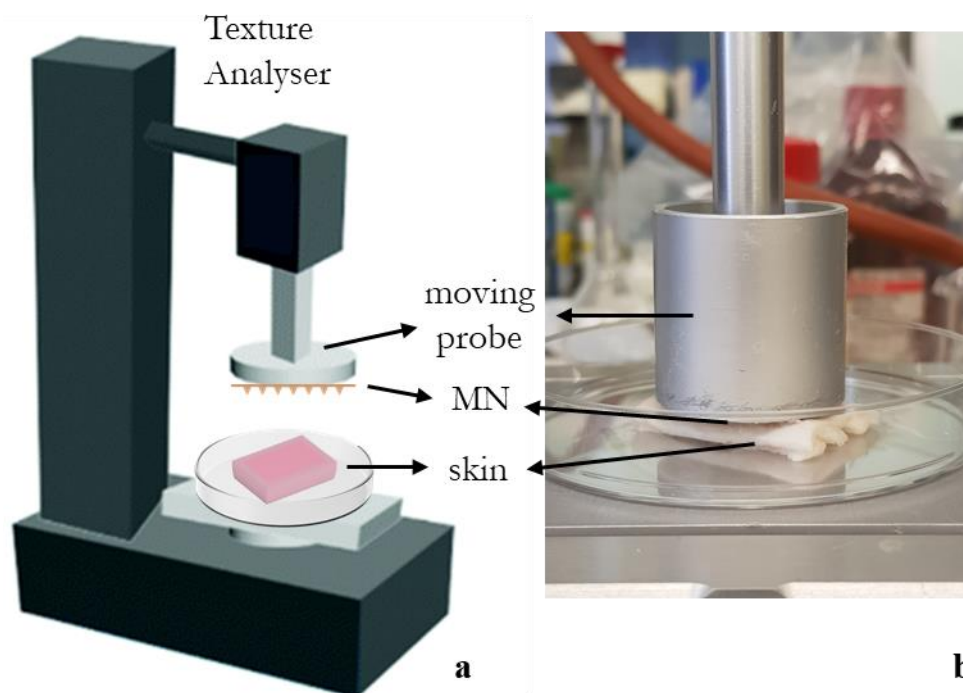


Figure 2.5 Piercing tests (a) schematic configuration, (b) digital photograph captured when the moving probe has inserted the microneedles into the skin sample.

The symmetrical 7×7 configuration of the arrays is a prerequisite for a uniform distribution of the externally applied force, permitting the calculation of the piercing

force required for individual needles, so that the results are readily transferable to larger arrays.

All microneedle designs demonstrated similar piercing behaviour, leaving visually observable pores on the skin after testing (Figure 2.6a,c,e). No microneedle failure was reported during experimentation. Thereafter, the microneedles were separated from the skin tissue and examined via SEM, to investigate for geometrical alterations or damage around the tip area caused by the insertion (Figure 2.6b,d,f). No microneedle blunting,

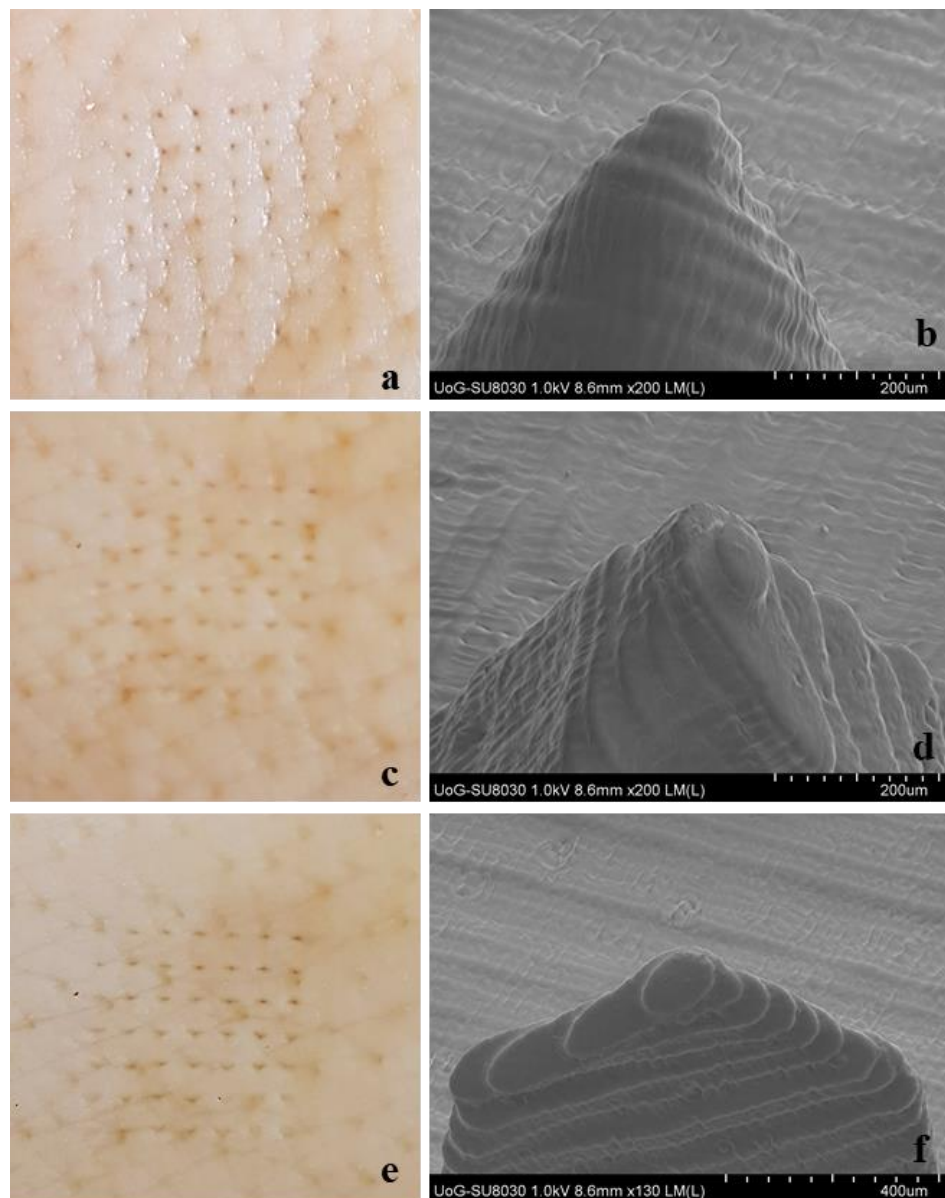


Figure 2.6 Post-piercing digital images of the porcine skin samples with (a) cone, (c) pyramid, and (e) spear microneedles; and (b,d,f) post-testing SEM images of the microneedle tips.

flattening, abrasion, or bending of the tip was observed. Regarding the microneedle tip, dimension measuring did not conclude statistically significant ($p < 0.05$) differences.

Figure 2.7a illustrates the force vs displacement data recorded throughout the skin insertion test. In accordance with findings described in the literature (Davis *et al.* 2004; Gittard *et al.* 2013), piercing is not identified as a single event, but rather as a series of gradual tears of the skin as the microneedle proceeds further through the tissue. This explains the constant change of slope prior to the insertion point. Skin is considered to behave as an elastic material in the load range of 0–20 N (Pailler-Mattei, Bec and Zahouani 2008), hence curve linearity (constant slope) would be anticipated if this was simple skin deflection. On the contrary, the slope changed constantly, indicating progressive tearing of the skin, until a sharp drop of load or an abrupt change in slope indicated the point of insertion. Then, the microneedles remained inserted in the tissue and further increase of force was attributed to the compression of the skin-microneedle system.

All microneedle designs required minimal insertion forces. The insertion force was found to be affected by the microneedle design, with the cone requiring the lowest and spear the highest externally applied load (Figure 2.7b). Aoyagi *et al.* demonstrated that for single needles, the tip angle is proportional to puncture force (Aoyagi, Izumi and Fukuda 2008). The spear geometry was designed with a tip angle of 97° , as opposed to cone and pyramid where the tip angle was 48.5° (Table 2.1), which explains that spear microneedles required the highest force for piercing. Moreover, regarding the cone and pyramid that feature identical tip angles, the magnitude of the microneedle surface area is anticipated to affect microneedle insertion, in the sense that friction forces develop during gradual penetration. The lateral pyramid surface is larger by 21% compared to the respective cone surface, which justifies that the pyramid microneedles require higher forces for skin insertion.

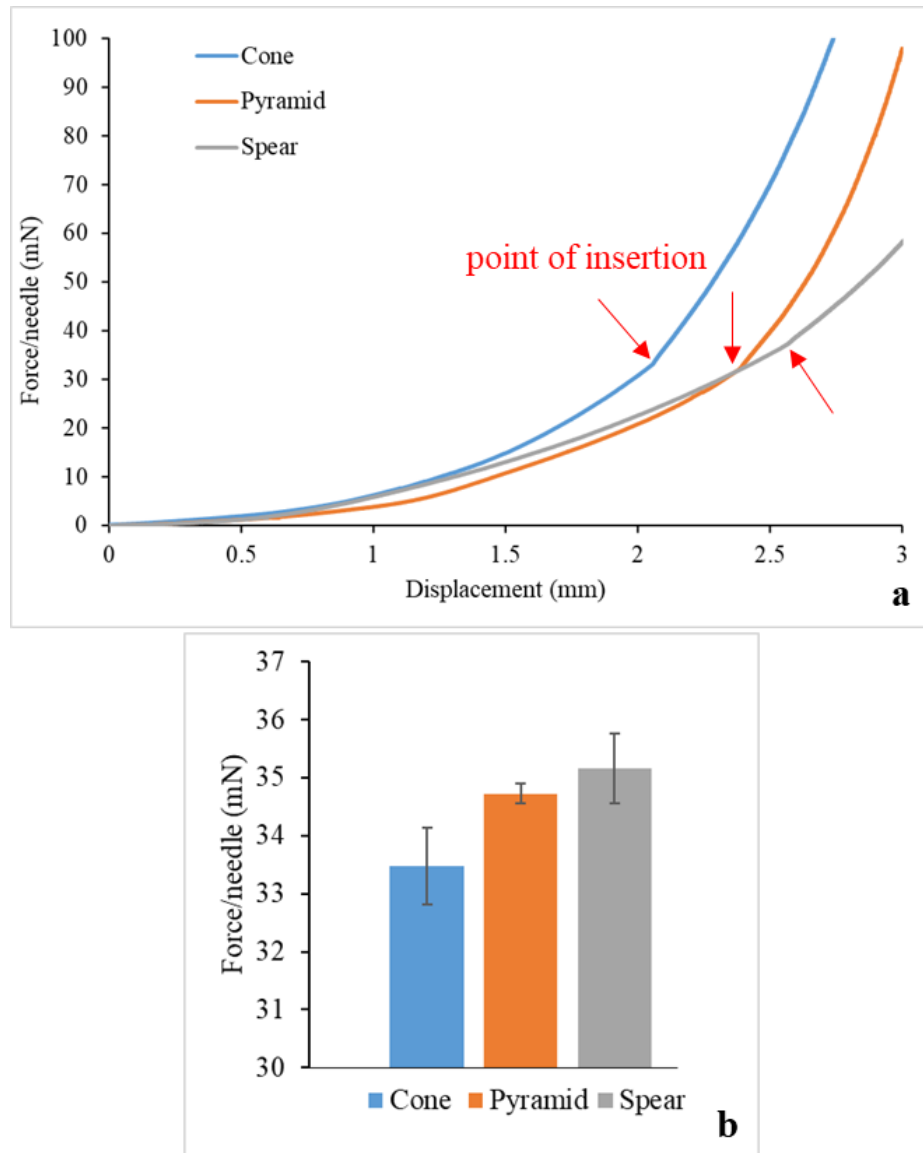


Figure 2.7 Data derived from piercing tests: (a) force/needle vs displacement data for all designs; (b) insertion force/needle.

2.3.6 Microneedle axial force mechanical testing

The fracture strength of the microneedles was examined, in order to assess the possibility of a fracture during clinical application and to compare the mechanical behaviour of the designs. The microneedles were compressed against a flat metal plate (Figure 2.8a) and the force-displacement data obtained during experimentation are displayed in Figure 2.8b. The point of fracture is identified by an apparent discontinuity of the curve. For the cone and pyramid designs, the slope is mainly constant until the fracture force is reached, meaning that in this load range the microneedles can withstand

the forces preserving their structural integrity without significant plastic (permanent) deformations. On the other hand, the spear design generated a curve with a changing slope before fracture, which can be attributed to bending. Indeed, these findings are in agreement with visual observations during testing; while the cone and pyramid designs failed at the direction parallel to the loading axis with an initial failure of the tip, the spear design failed at the base due to bending. Hence, the fracture force for the spear microneedles was found to be lower than the pyramid and cone ones (Figure 2.8c). Nevertheless, the fracture forces for all designs (reported in N) were significantly higher than the respective forces required for piercing (reported in mN).

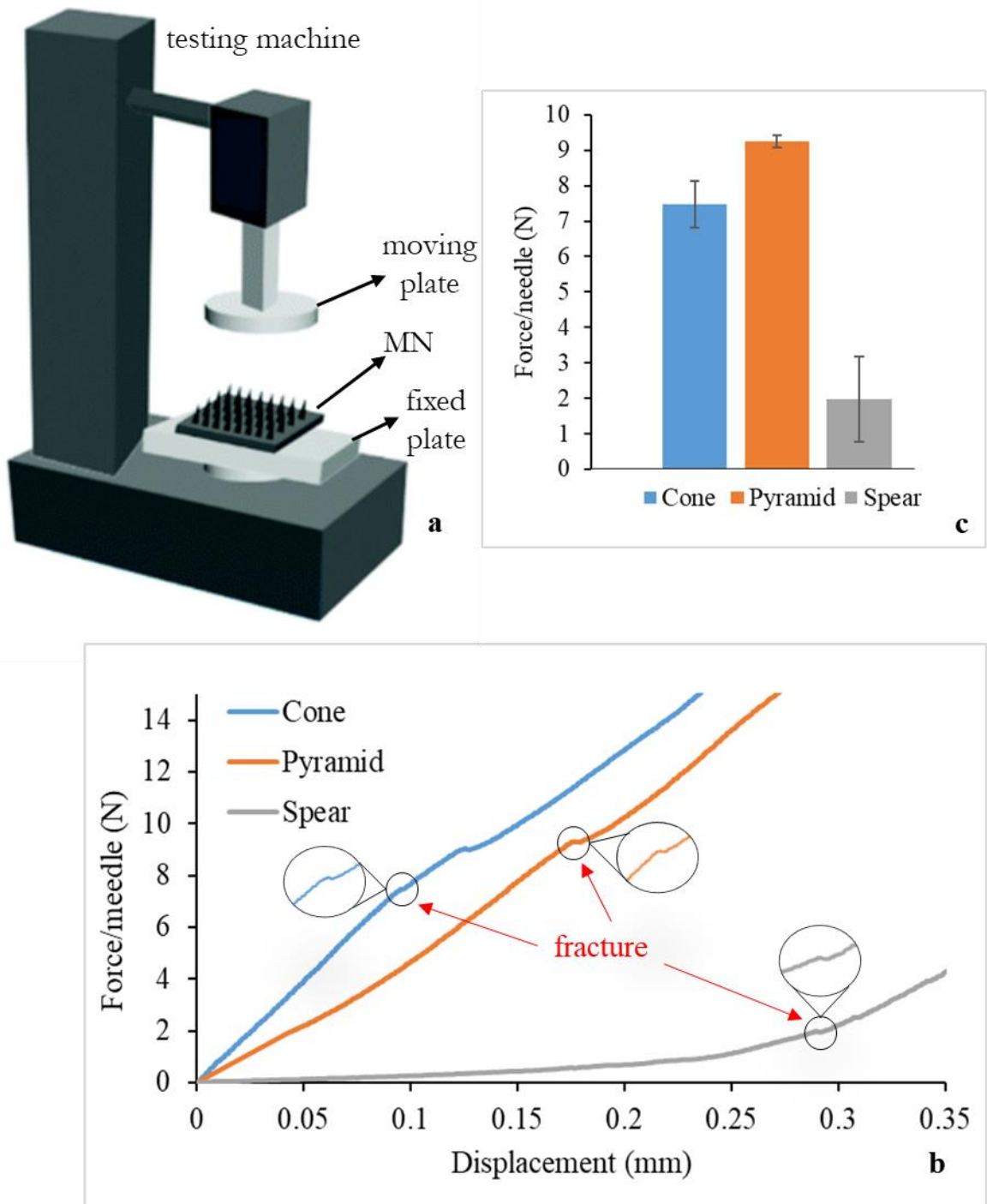


Figure 2.8 Microneedle fracture testing for different microneedle geometries (a) Schematic representation of the experimental configuration, (b) Force vs. displacement curve, featuring magnified captions at the fracture points and (c) fracture forces.

2.3.7 Safety Index

The results derived from the piercing and fracture testing can provide valuable insight regarding the safety of the microneedles upon application. Microneedle fracture while inserted in the skin is a highly undesirable occurrence and The margin of safety has been proposed by Prausnitz (Prausnitz 2004) as the ratio of fracture force to insertion force. Typically, the value of the margin needs to be higher than one, however the reliability of the microneedle system increases with higher values. The margins of safety calculated by Equation 2.1 are displayed in Table 2.2.

Table 2.2 Margins of safety for different microneedle geometries

Microneedle geometry	Margin of safety
Cone	223
Pyramid	266
Spear	55

The spear design exhibits the lowest value as anticipated, however all margins of safety are well above 1, which is promising evidence that the microneedles will be safe for clinical application.

2.4 CONCLUSIONS

The application of 3D printing for microneedle manufacturing establishes new challenges and calls upon the building of a different rationale behind microneedle design and development. The present study investigated the relationships between geometrical and manufacturing parameters with microneedle quality and performance, the knowledge of which is essential for tailoring and optimisation.

It was shown that post-printing curing conditions influenced the mechanical properties of the material and microneedles due to the degree of cross-linking. Optimisation with respect to the compressive properties is imperative to reassure the mechanical robustness of the arrays. Moreover, it was demonstrated that the printing angle affected microneedle quality and dimensional fidelity, with the tip to be the most prone to manufacturing defects. Microneedle geometry had an impact on piercing force, with cone-shaped microneedles requiring the least force for skin insertion. Accordingly,

geometry impacts fracture forces, with the spear-shaped microneedles proving to be significantly weaker. All designs were found to be mechanically safe for application.

Overall, it is assessed that the main goal of the present chapter that entailed building a robust design and 3D printing strategy for SLA microneedles was achieved. It is anticipated that the present study will contribute to building knowledge in the field of 3D printing of solid transdermal microneedles and promote further research. Although the proposed solid microneedles can be readily used to assist transdermal absorption (e.g., ‘poke and patch’ approach), their combination with advanced coating technologies can generate sophisticated systems with high controllability of drug cargo and thus high therapeutic accuracy. This concept is explored thoroughly in the following Chapter.

CHAPTER 3

INKJET 2D PRINTING OF DRUG FILMS ON 3D PRINTED SOLID MICRONEEDLES

THE EFFECT OF MICRONEEDLE GEOMETRY ON INSULIN DELIVERY

3.1 INTRODUCTION

Coated microneedles compose a large portion of the progress on microneedle-mediated transdermal drug delivery. Their attractiveness is justified by the plethora of published studies, that report the painless administration of macromolecules, proteins, nanomedicines, DNA and vaccines, with fast drug release rates owed to the fast dissolution of the thin film coatings in the skin (Pearton *et al.* 2012; Kim *et al.* 2012; Baek, Shin and Kim 2017; Larraneta *et al.* 2016).

Coated microneedles combine a several advantages over hollow and dissolvable systems. For instance, unlike dissolvable microneedles, the drug loading process is independent from the microneedle manufacturing process. This translates to a significant advantage in regard to mechanical performance, since the amount of drug loaded to the array does not affect the strength and piercing ability of the microneedles (Ingrole and Gill 2019). This independence also endows the production stage with versatility as blank microneedle arrays from the same batch can be loaded with different therapeutic molecules based on product demand (Gill and Prausnitz 2007). It has also been documented that preserving actives in a solid state may increase stability, prolonging their shelf life (Manning *et al.* 2010).

For the development of reliably coated microneedle systems, the adoption of advanced coating techniques is imperative. Amongst the key criteria that render a coating process effective are uniformity and reproducibility, accuracy so the drug is only deposited on the microneedles, low process temperatures to avoid drug degradation, and a strong bonding of the coating film on the microneedle surface to reassure that drug will not remain on the skin surface upon piercing (Gill and Prausnitz 2007). Numerous methods have been applied for this purpose, such as immersion of the whole patch (Chandler *et al.* 2018), drop coating (Vinayakumar *et al.* 2015), and spray coating (Ning *et al.* 2020), which are prone to allow contamination of the microneedle substrate by the coating material. The prominent coating techniques that reassure localised coating formation

exclusively on the microneedle bodies with no drug deposition on the substrate, are dip-coating and inkjet printing (Ingrole and Gill 2019). Dip-coating has had numerous applications on microneedle coating (Gill and Prausnitz 2008; Caudill *et al.* 2018; Jeong *et al.* 2020) because of its simplicity; however, issues regarding the accuracy of the coated drug amount have emerged. On the other hand, inkjet printing is a reliable, reproducible, and accurate coating method that enables spatially controlled film creation and has been successfully applied on microneedles (Ross *et al.* 2015; Uddin *et al.* 2015). However, the effect of microneedle geometry on the morphology of the inkjet-coated films has not yet been fully understood.

Microneedle coating processes inevitably involve drying of the drug-containing formulation and subsequent rehydration when in contact with the skin interstitial fluid. It is documented that dehydration can induce irreversible conformational changes to proteins (Prestrelski *et al.* 1993). Hence, the use of drug carriers was considered imperative in this work, in order to reassure protection of the drug from processing stresses (shear during the inkjet process, dehydration and rehydration) and reassure longevity of the product's shelf-life. Polymer carriers have shown promising potential in preventing protein aggregation and absorption-mediated conformational changes (Ohtake, Kita and Arakawa 2011). Amongst them, hydrophilic polymers have been employed for the engineering of gels (Bajpai and Bhanu 2004; Agrawal *et al.* 2010) and nanoparticles (Mansoor *et al.* 2019) for insulin delivery. Likewise, respective applications of amphiphilic co-polymer surfactants (poloxamers) on nanoparticle (Xiong, Tam and Gan 2005; Mansoor *et al.* 2019) and gel-based insulin delivery systems (Barichello *et al.* 1999; Barichello 1999), have also been proposed. However, the impact of such excipients on the stability of non-encapsulated insulin in solution, or upon dehydration, storage and subsequent rehydration has not yet been fully investigated.

3.1.1 Aims and objectives

The main objective of this experimental Chapter is to apply a precise piezoelectric inkjet 2D printing technique to coat 3D printed microneedles with insulin-containing films. The central hypothesis under investigation in the framework of this study, is that the microneedle shape affects the coating morphology and hence its dissolution into the skin. To test this hypothesis, the following research aims were set:

- Development and application of reliable inkjet coating regimes to obtain uniform, spatially controlled insulin films on the microneedle surfaces.
- Identification of the key geometrical parameters that affect the *in vitro* drug release profiles generated from 3D printed microneedles.
- Investigation of the ability of two polymeric excipients, a hydrophilic polymer and an amphiphilic non-ionic co-polymer, to maintain insulin stability as additives to the coating formulation.

The outcome of this study will provide insight to inform design practices, aiming at optimising 3D printed microneedles for tuneable and customisable drug delivery.

3.2 MATERIALS AND METHODS

3.2.1 Materials

Insulin derived from bovine pancreas (10 mg mL⁻¹) and Saline Phosphate Buffer (PBS) pH 7.4 were acquired from Sigma-Aldrich (Gillingham, UK). Polyvinylpyrrolidone (PVP, Kollidon 17PF) and Poloxamer 407 (Pluronic F-127) were purchased from BASF (London, UK). All solvents were of analytical grades.

3.2.2 Coating formulations

Insulin-polymer formulations were developed at a ratio 5:1 (wt/wt). The polymers, PVP and P407, were weighed and added individually to the insulin solution. For each formulation, 10 mg of insulin and 2 mg of polymer were mixed, to create a 5:1 insulin to polymer ratio. The formulation was stirred on a magnetic stirrer until complete dissolution of solids. The formulations were coded as Ins:PVP and Ins:P407, for PVP and poloxamer 407, respectively.

3.2.3 Inkjet 2D printing of insulin films on 3D printed microneedles

The insulin-polymer solutions were deposited on the cone, pyramid, and spear microneedles lateral surfaces in the form of fine droplets using an inkjet printer (NanoPlotter II, Gesim, Germany), equipped with a piezo-driven dispenser (PicPip 300). All microneedle arrays were fixed on a metal stub at 45° relative to the dispenser. For each coating cycle, 10 dots of 2 droplets were dispensed along the longitudinal axis of each microneedle. The process was repeated for 32 jetting cycles for each side of the

array (two lateral microneedle surfaces were coated) resulting in 5 IU (175 μg) of insulin per array. The solvent (deionised water) was allowed to evaporate through incubation for 24 h at room temperature.

3.2.4 Scanning Electron Microscopy

The microneedle arrays were mounted onto aluminium stubs using a double-sided carbon adhesive tape (Agar scientific, UK). Each microneedle array was examined by SEM (Hitachi SU 8030, Japan) using a low accelerating voltage (1.0 kV). A low accelerating voltage was used to avoid electrical charges on the microneedles. The images of the microneedles were captured digitally from a fixed working distance (11.6 mm) using different magnifications. Processing the images and measurements were conducted through the software ImageJ (Fiji package) (NIH image, Bethesda, MD, USA)

3.2.5 Circular Dichroism (CD)

Pure insulin and insulin-polymer formulations were developed at a ratio 5:1, as described in section 3.2.2. The formulations were diluted to 1.0 mg mL⁻¹ in deionised water. Films of the insulin-polymer formulations were developed on glass slides by solvent evaporation at room temperature. The films were weighed and rehydrated in PBS 7.4 to obtain insulin concentrations of 1 mg mL⁻¹ for each sample. CD spectra were recorded at 20 °C between 190 and 260 nm by CD (Chirascan, Applied Photophysics, UK) using a 0.1 mm polarisation certified quartz cell (Hellma, Müllheim, Germany). A step size of 1 nm, a bandwidth of 1 nm, and an acquisition time of 1 s were applied. Four scans were recorded for each sample, their means were calculated, and the corresponding baseline spectrum was subtracted from each spectrum. The data were analysed on DICHROWEB and the CDSSTR method was employed to estimate the effect of polymeric carriers, dehydration and subsequent rehydration on the secondary structural composition of insulin.

3.2.6 Stability of insulin films

To assess the ability of the polymer carriers to maintain insulin stability, insulin-polymer films were kept at the fridge for 14 days, at 4 \pm 1°C. The films were then rehydrated in PBS 7.4 and samples were analysed by CD. Their spectra recorded at day

14 (T₁₄) were compared with respective data from films analysed at day 0 (T₀). Correlations were also done with pure insulin solution, at concentration of 1 mg mL⁻¹, in order to compare the structural composition of the drug that has been subjected to dehydration, storage and rehydration with the standard insulin, as administered for antidiabetic therapy. The secondary structure of insulin was estimated on DICHROWEB, using the CDSSTR method.

3.2.7 Geometrical modelling of droplet on a curved surface

The effect of the substrate geometry on the droplet shape was assessed by comparing the contact angles formed on flat and curved surfaces. To accomplish this, the contact angle of a droplet on a curved surface was predicted using a wetting model (Wu *et al.* 2015). For reasons of simplification, it was assumed that effects pertaining to non-ideal surface morphology or surface-liquid interactions were non-existent (smooth, stiff, homogenous, inert, i.e., ideal surface). The effect of gravity on the droplet shape was also considered negligible and the liquid, incompressible.

The intrinsic contact angle is a documented constant for specific combinations of liquids and surface materials. By applying the Young's theory on interface energy and taking into account the geometrical parameters of the system, the intrinsic contact angle on a flat surface, θ'_0 is equal to the intrinsic contact angle on a curved surface, θ_0 .

Let V_L be the volume of the liquid droplet and R the curvature radius at the point the droplet is in contact with the surface. The apparent contact angle, i.e. the angle between the solid surface and the tangent to the liquid fluid interface, for the cone is θ_{cone} . The proposed wetting model establishes a relation between the geometrical parameters of the system, described by the dimensionless wetting equation:

$$V^* = \frac{\sin^3 \theta^*}{\sin^3 \theta_{cone}} f(\theta_{cone}) - f(\theta^*) \quad \text{Equation 3.1}$$

$$f(x) = \frac{(2 - 3\cos x + \cos^3 x)}{4} \quad \text{Equation 3.2}$$

$$V^* = \frac{V_L}{\frac{3}{4}\pi R^3} \quad \text{Equation 3.3}$$

$$\theta^* = \theta_{cone} - \theta'_0 \quad \text{Equation 3.4}$$

The above model describes the contact angle on the cone surface, as a function of the intrinsic contact angle on the respective ideal flat surface, droplet volume and curvature radius. The parameters used in this model were $V_L=300$ pL, in accordance with the single droplet volume produced by the inkjet and $R=250$ μm , assuming that the droplet lies on the middle of the cone longitudinal axis. The intrinsic contact angle for water droplet on ideal acrylic surfaces was found in literature at 71° (Diversified Enterprises 2020). Equations 3.1, 3.2, 3.3, 3.4 were combined and solved in MATLAB (Mathworks, Natick, MA, USA). The algorithm composed can be found in Appendix I.

3.2.8 High Performance Liquid Chromatography (HPLC) method and validation

An existing reversed-phase HPLC method (Pissinato Pere 2019) was applied for the detection of insulin delivered by the microneedles at the *in vitro* release studies. Prior to analyses, the method was validated following the standards of the British Pharmacopeia and the ICH Q2 (R1). The validation was carried out in respect to specificity, linearity, accuracy, precision, limit of detection and limit of quantification.

The HPLC system (Agilent Technologies, 1200 series, Cheshire, UK) was equipped with a Phenomenex Jupiter 5u c18 300 Å, LC Column (250 mm \times 4.60 mm, particle size 5 μm , Macclesfield, UK). According to the documented method, the mobile phase consisted of water with 0.1% trifluoroacetic acid (TFA) and acetonitrile with 0.1% TFA (66:34 v/v) in isocratic elution mode. The flow rate and injection volume were set at 1 mL min^{-1} and 20 μL , respectively. Prior to analysis, the system was left to run for one hour at constant flow rate (1 mL/min) at 35 $^\circ\text{C}$ for 1 hour, to reassure that the column had reached the equilibrium state. The eluent was analysed with a UV detector at 214 nm. The results were integrated using the Chemstation® software.

The validation of the insulin detection method was conducted starting with the preparation of stock solutions, in two different days. The insulin was diluted with PBS pH 7.4 in volumetric flasks, to obtain a concentration of 100 $\mu\text{g}/\text{mL}$.

- *Specificity*: The process tested the ability of the method to detect specifically insulin in a formulation containing other components. For that purpose, PVP and P407 were added solely in insulin samples and the resulting formulations were analysed.

- *Linearity*: Five standards were made by dilution of the stock solution, with resulting concentrations of 10, 20, 30, 40 and 50 µg/mL. The standards were analysed and the peak areas were used to obtain the respective calibration curve. The linearity was assessed by evaluating the parameters of the regression line. The threshold for the coefficient of determination, R^2 , was set at 0.990.
- *Precision*: The precision of the method was tested in respect to:
 - Repeatability: Intraday analysis was performed. Samples at low, medium and high concentrations (10, 30 and 50 µg/mL, respectively) were analysed in triplicates, in 6 different times within the same day.
 - Reproducibility: Samples at low, medium and high concentrations (10, 30 and 50 µg/mL, respectively) were analysed in triplicates, in two different days.

For both tests, the mean peak areas, standard deviations (SD) and coefficient of variations (CV) were calculated. The precision criterion for this study was set as $CV < 5\%$.

- *Accuracy*: The average values of the experimental insulin concentrations obtained from the previous tests for low, medium and high insulin concentrations (10, 30 and 50 µg/mL, respectively) were calculated. The accuracy was calculated from the following equation:

$$\% \text{ Accuracy} = \frac{C_{\text{experimental}}}{C_{\text{theoretical}}} 100\% \quad \text{Equation 3.5}$$

- *Limit of Detection (LOD) and Limit of Quantification (LOQ)*: To identify the limits of detection and quantification the initial stock solution was diluted down to the point that the analyte was not detectable. The following equations give the LOD (Equation 3.6) and the LOQ (Equation 3.7):

$$LOD = \frac{3.3 SD}{S} \quad \text{Equation 3.6}$$

$$LOQ = \frac{10 SD}{S} \quad \text{Equation 3.7}$$

Where SD is the standard deviation of the y intercepts of the regression lines and S, the slope of the calibration curve.

After validation, the described method was employed for the detection and quantification of the insulin coated on the microneedles (experimental calculation of the drug amount coated on individual arrays). Moreover, samples collected from the receptor compartments of the Franz diffusion cells during the *in vitro* drug release studies were similarly analysed. Statistical analysis was performed using a Mann-Whitney non-parametric test (InStat, GraphPad Software Inc., San Diego, CA, USA). Samples were considered statistically significant for $p < 0.05$.

3.2.9 Coating efficiency

The coating efficiency was assessed by experimentally analysing the amount of insulin coated on the microneedles and comparing it with the expected/theoretical amount. Microneedles, coated with 5 IU, were put in glass vials with 8 mL of PBS 7.4 each. The vials were sonicated for 5 min, and samples were filtrated and analysed via HPLC. The experimental concentration obtained was used to calculate the insulin cargo actually carried in the coatings. Coatings with both formulations were tested in triplicates. The experimental drug cargo was correlated with the amount theoretically deposited on the array, and the coating efficiency (CE%) was calculated from Equation 3.8:

$$CE(\%) = \frac{\text{experimental drug cargo}}{\text{theoretical drug cargo}} 100\% \quad \text{Equation 3.8}$$

3.2.10 Preparation of porcine skin samples

The remaining skin was pinned onto a polystyrene block and wiped with ethanol (70%). Samples of 1.0 ± 0.1 mm thickness were extracted by applying a Dermatome (Padgett Dermatome, Integra LifeTMSciences Corporation, Princeton, NJ, City, State, USA) at an angle of $\pm 45^\circ$. The thickness of the skin was measured using a caliper and 20 mm \times 20 mm tissue samples were cut using a scalpel. The skin samples were placed onto filter paper soaked in a small amount of saline phosphate buffer (pH 7.4) for 2 h. The Dermatome-treated skin samples were employed for the *in vitro* release studies.

3.2.11 *In vitro* release of insulin

The delivery of insulin loaded on the microneedles was studied, using abdominal porcine skin. The *in vitro* testing was carried out in Franz diffusion cells (PermeGear, Inc., Hellertown, PA, USA). Dermatomed skin samples were placed in phosphate

buffered saline (PBS; pH 7.4) for 1 hour prior to experimentation. The microneedle arrays were inserted into the skin samples using manual finger pressure. The skin and microneedle array was mounted onto the donor compartment of a Franz diffusion cell. The temperature of the Franz cells was maintained at 37 °C using an automated water bath (Thermo Fisher Scientific, Newington, USA). Sample fractions (6–6.5 mL/h) were collected using an auto-sampler (FC 204 fraction collector, Gilson, City, State, Middleton, WI, USA) attached to the Franz diffusion cells. Statistical analysis for the drug release was performed by using a Mann–Whitney nonparametric test (InStat, GraphPad Software Inc., San Diego, CA, USA), where samples were considered to be statistically significant at $p < 0.05$.

3.3 RESULTS AND DISCUSSION

3.3.1 Inkjet Coating

Insulin-polymer coatings were deposited on the surfaces of the 3D printed microneedles using a nanoploter, equipped with an inkjet printing piezoelectric dispenser (Figure 3.1a). The instrument operates on the basis of a tunable algorithm, which the user can easily adapt to the individual geometry of the microneedles. Taking into account the user input, the nanopipette moves from shaft to shaft, depositing drug-containing droplets exclusively on the microneedle surfaces. Figure 3.1b features an image captured by the instrument microscope after drug deposition, that shows that the process produces spatially controlled microneedle coating.

The process parameters, namely the applied voltage and pulse duration were optimised previously (Ross *et al.* 2015), so that each droplet had a volume of 300 pL. Consecutive coating cycles were implemented, so that the coalesced droplets to create uniform coating films on the microneedle surfaces. Each microneedle was coated on both sides, resulting in arrays loaded with 5 IU (175 µg). After coating, the microneedles were incubated at room temperature for 24 hours, which was found to suffice for solvent (deionised water) evaporation and solid film formation. Figure 3.1c illustrates SEM images of coated cone microneedles. Evidently, the spatial accuracy of the film placement and the absence of satellite droplets on the microneedle substrate assert the high reliability of the system and are good indications that no drug losses occurred.

The thickness of the coating film plays a crucial role during application. The effectiveness of a coating method is assessed among other factors by its ability to form thin coatings. Bulky films may detach from the microneedle surface during piercing and stay on the skin, which can lead to drug losses. Figure 3.1d shows an SEM image of coated spear microneedles, captured at a 0° angle. By visual evaluation, the films appear uniform, with minimal thickness, which is promising for the system's clinical potential.

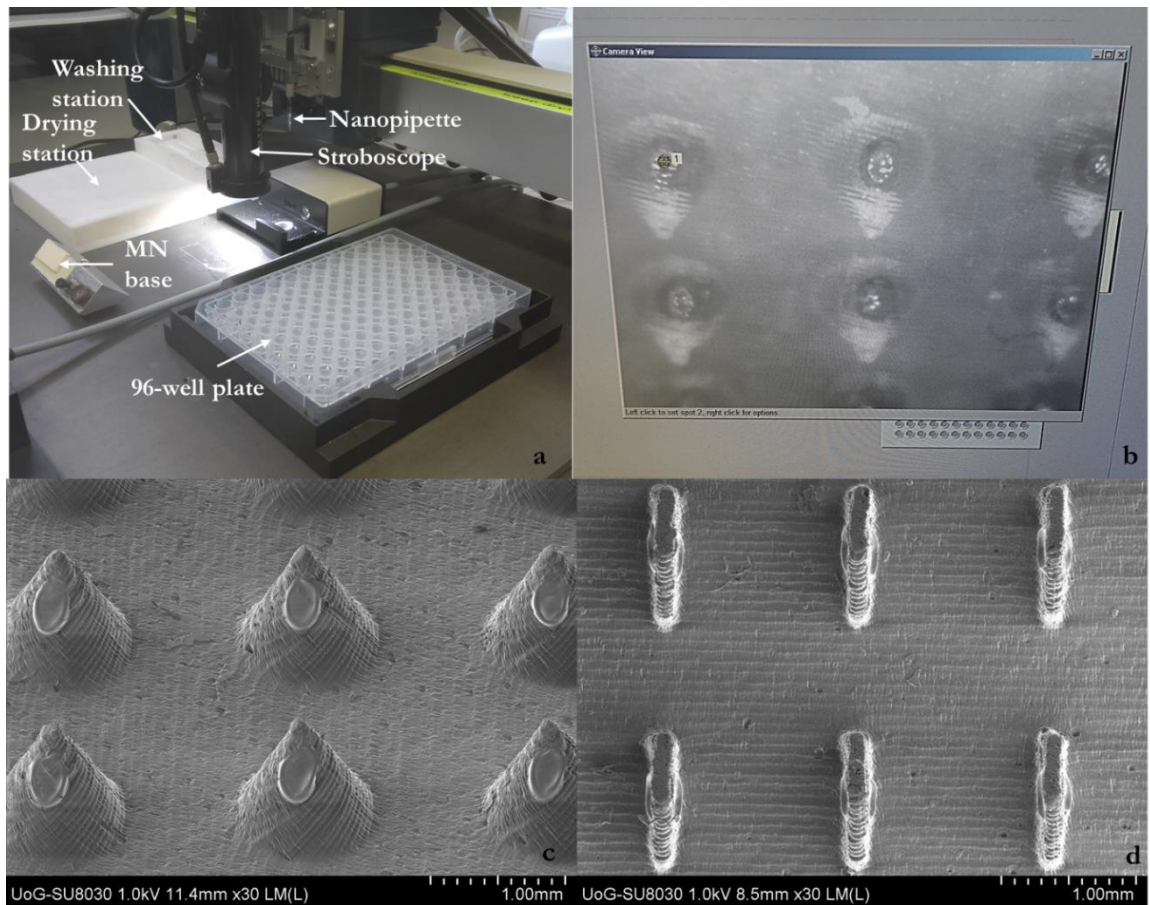


Figure 3.1 Microneedle coating. (a) Nanoplotter coating configuration, (b) Nanoplotter camera caption post-coating, showing the coalesced droplets prior to solvent evaporation and film formation, (c) SEM caption showing the spatially controlled coating on the 3D printed microneedles and (d) SEM caption of spear microneedles coated on both lateral surfaces.

Preliminary evidence on the behaviour of the coating upon insertion was drawn by a study performed by our group, that investigated whether the film adhesion to the microneedle surface was sufficient to prohibit shear-driven dislodgement during

application. X-ray computer microtomography (μ CT) was employed to visualise insertion of an inkjet-coated microneedle into eight plies of parafilm (Economidou *et al.* 2019). The experiments illustrated that the microneedle retained the coating, transported it through the parafilm, whereas there was no visual evidence that any material remained on the parafilm surface. The findings of this study provide a preliminary indication that the described coating regime (which was similar to the one applied here) results in robust films that withstand insertion without damage or dislodgement. Further evidence is expected to be drawn from the *in vitro* studies.

3.3.2 Correlation of microneedle geometry with coating morphology

In the framework of this study, it was hypothesised that microneedle geometry influences coating morphology and thereby, dissolution. To get a better understanding of this hypothesis, the process of droplet impingement and spreading on the microneedle surface was examined. Upon impact on a surface, a droplet spreads radially and its spreading behaviour typically depends on impinging velocity, liquid properties, and impact surface (Yonemoto and Kunugi 2014). The surface influences droplet shape and spreading not only in terms of material wettability (i.e., being hydrophilic or hydrophobic), but also through its geometry. Factors such as surface curvature and inclination have been found to play an important role on droplet impact dynamics (Wu *et al.* 2015; Sahoo *et al.* 2020).

The effect of surface curvature on droplet shape can be interpreted by examining the apparent contact angle when a droplet reaches an equilibrium on a flat vs. a convex surface. A theoretical model developed by Wu *et al.* was applied to predict the apparent contact angle of the inkjet droplet on the curved cone surface (Wu *et al.* 2015). For reasons of mathematical simplification, it is assumed that the droplet is deposited at the middle of the shaft length and the convex surface is part of a sphere of radius equal to the cone radius at that point ($R = 250 \mu\text{m}$). In addition, the surface is considered smooth and the droplet volume used was in accordance with the respective volume produced by the inkjet nanoplotter. The intrinsic contact angle, which is a known constant for specific combinations of liquids and surface materials, was found in the literature as $\theta_{\text{flat}} = 71^\circ$ for a water droplet on an acrylic surface (Diversified Enterprises 2020). Based on the Wu model, the apparent contact angle for water on the cone surface at the middle of its length is $\theta_{\text{convex}} = 77.8^\circ$, which constitutes an increase of almost 10%. Figure 3.2a,b

schematically illustrate the effect of surface curvature on contact angle and droplet shape.

It has been documented that by increasing the surface radius (reducing the curvature), the thickness of the film is decreased (Bakshi, Roisman and Tropea 2007). The aforementioned indicate that the film deposited on the curved cone surface is likely thicker than the respective one deposited on the pyramid. The variations may be minimal, however a distinct impact on the dissolution profiles is expected.

microneedle design introduces another significant parameter pertaining to the resulting coating morphology, which is surface inclination. Upon impact on a horizontal hydrophilic surface, the droplet stays put and oscillates and/or spreads into a film (Farshchian *et al.* 2018). Oblique surfaces bring in the effect of gravity that, if the inclination is high enough, can activate non-uniform spreading, with the top contact angle to recede and the bottom to advance (Guilizzoni 2011).

The inkjet coating methodology applied requires positioning of all microneedle arrays at 45° in respect to the horizontal surface plane, however the geometry of the individual designs alters the inclination of the droplet impingement surface. Figure 3.2c-e display the real inclination angle of the impingement surface for all microneedle designs. By default, cone and pyramid microneedles create the same inclination angle, calculated at $\theta_{\text{cone}} = \theta_{\text{pyra}} = 18.5^\circ$, whereas for the spear microneedles the respective inclination is at $\theta_{\text{spear}} = 45^\circ$. Sahoo *et al.* conducted a study wherein visual evidence of the effect of the inclination angle on droplet spreading is provided (Sahoo *et al.* 2020). For angles higher than 20° the droplet seems to slide and elongate downwards creating a bottom ridge. The phenomenon is intensified as the inclination angle increases. The conclusions of this study coincide with the SEM images of the coated microneedles (Figure 3.2f-h). The film on the spear microneedle appears to be thinner with an intensified bottom ridge. In contradiction, the other microneedle design that features a flat surface but a significantly lower inclination angle (pyramid), bears a film of higher yet more uniform thickness.

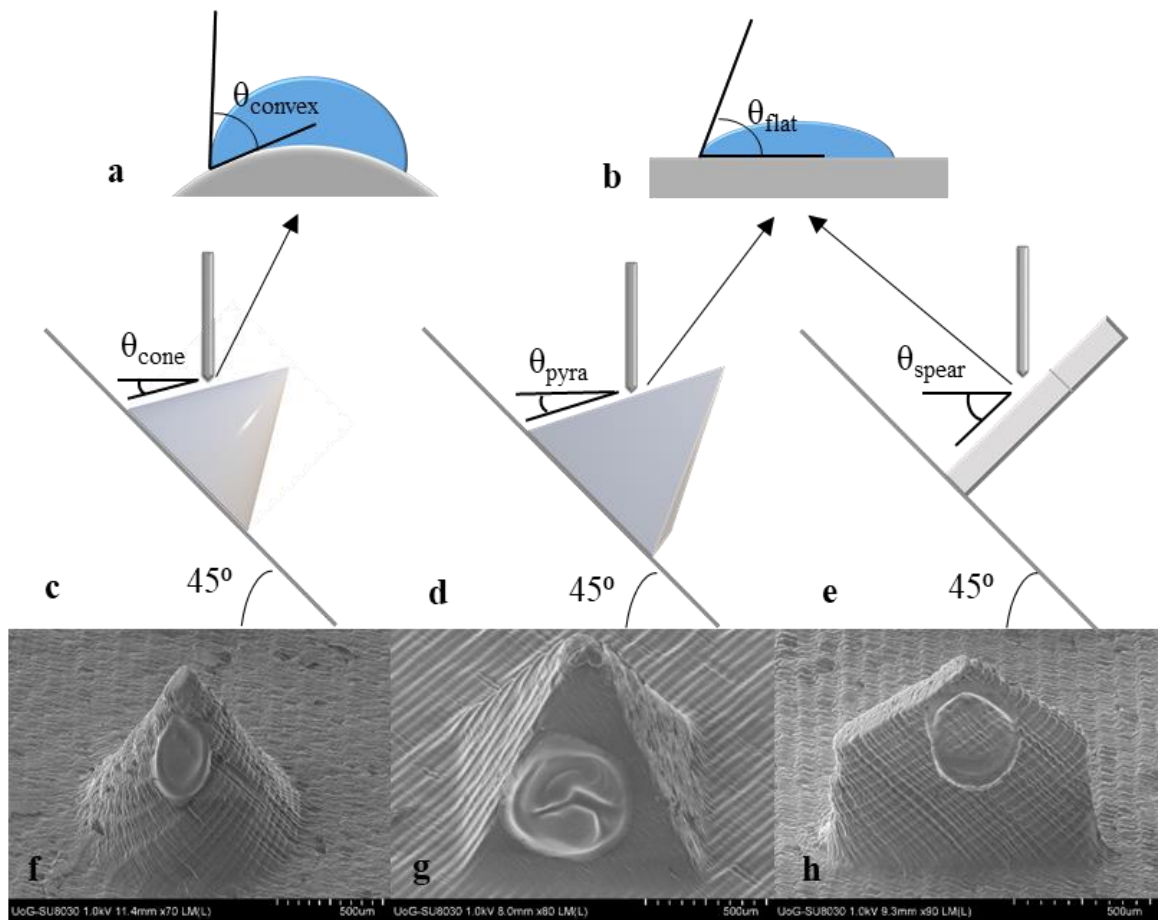


Figure 3.2 Inkjet coating; (a,b) static contact angle of inkjet droplet upon impingement on the microneedle surface for convex (cone) and flat (spear and pyramid) surfaces; (c,d,e) scheme of the coating configuration for cone, pyramid, and spear microneedles; and (f,g,h) SEM images of the coated microneedles.

3.3.4 Circular Dichroism (CD)

Circular Dichroism has been widely employed in the study of proteins due to its ability to provide data on protein structure, structural changes and ligand binding (Kelly and Price 2000). Spectra in the far UV region (240 to 190 nm) are routinely used to quantify protein structural components.

The far UV spectrum of insulin is illustrated in Figure 3.3. Two negative minima are identified at 209 nm and 221 nm, which is characteristic of α -helix predominant proteins

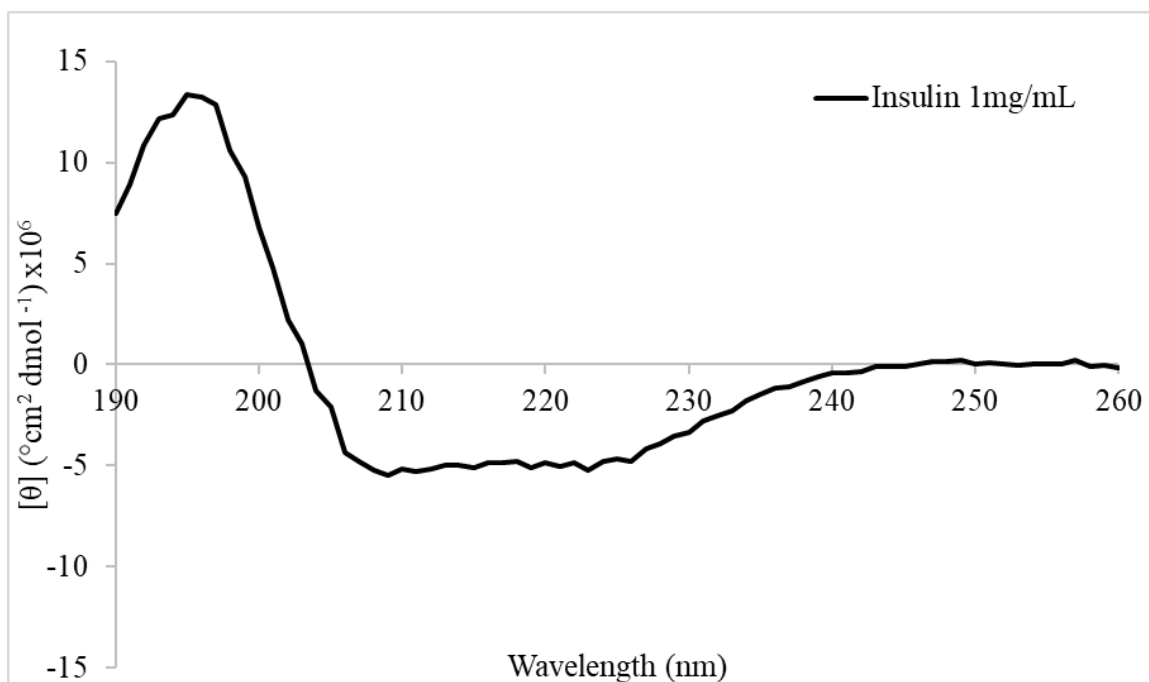


Figure 3.3 Far UV CD spectrum of insulin solution (1 mg mL^{-1}).

(Andrade *et al.* 2015).

For the purpose of this work, two polymers were chosen as insulin carriers. The polymers employed was a polymer surfactant, poloxamer 407 (P407) and a hydrophilic polymer, polyvinylpyrrolidone (PVP), which have been both approved for parenteral delivery by the U.S. Food and Drug Administration (FDA) (Dumortier *et al.* 2006; Kurakula and Rao 2020). Their effect on insulin structure in a solution as well as in solid state was assessed through CD. Figure 3.4 depicts the far UV CD spectra of insulin and insulin-polymer solutions. All spectra showed double minima around 209 and 222 nm, in accordance with the spectrum derived for the pure insulin solution.

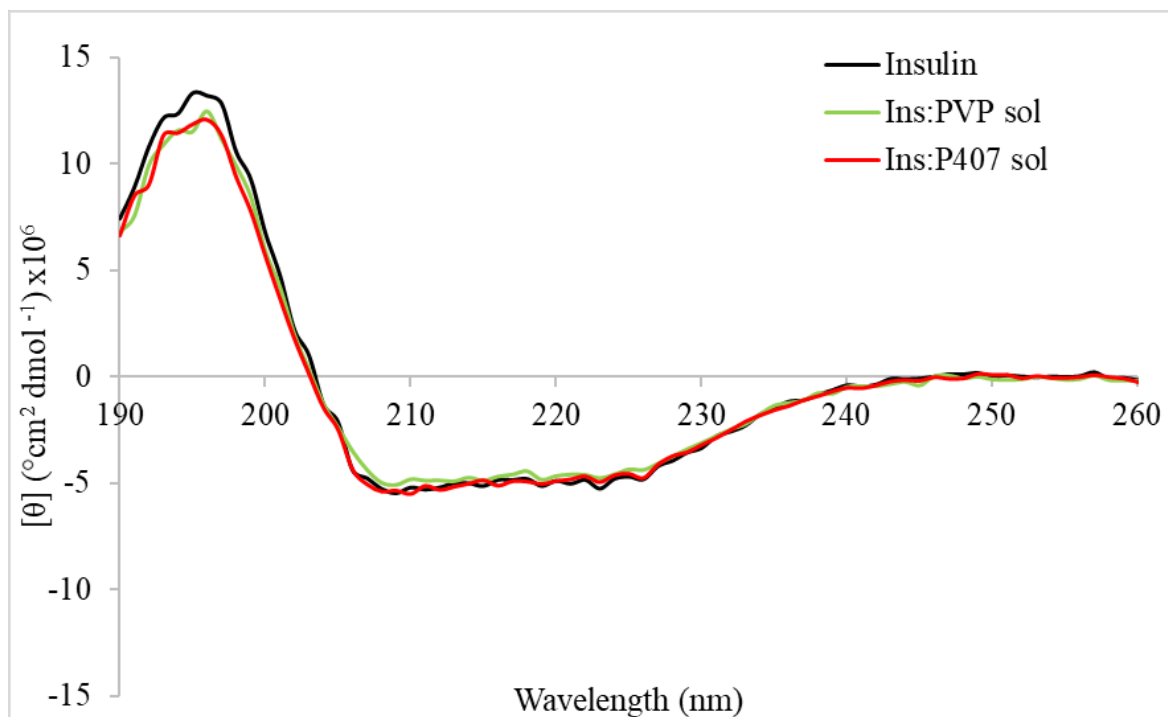


Figure 3.9 Far UV spectra of pure insulin solution (1 mg mL^{-1}) and insulin-polymer formulations in solution (5:1).

In a solution, the effect of the polymers on the insulin spectrum is minimal. The Molar ellipticity spectrum of the pure insulin solution coincides with the one recorded in the presence of PVP. A slight increase of α -helical content in the presence of P407 is indicated, while PVP does not seem to induce significant changes.

During dehydration, the removal of water can alter the protein structure and cause aggregation after rehydration and thus render the protein vulnerable to chemical degradation (Chang *et al.* 1996). Specifically, three scenarios may occur: 1) the protein maintains its native structure throughout processing, 2) the protein unfolds during dehydration but refolds during rehydration and 3) the protein unfolds during dehydration and remains unfolded during rehydration (Ohtake, Kita and Arakawa 2011). In the presence of the protein stabilisers, the more favourable scenarios can be promoted. To assess the impact of the polymers and dehydration-rehydration on insulin stability, insulin-polymer films were developed and rehydrated in PBS 7.4. The CD spectra are depicted in Figure 3.5.

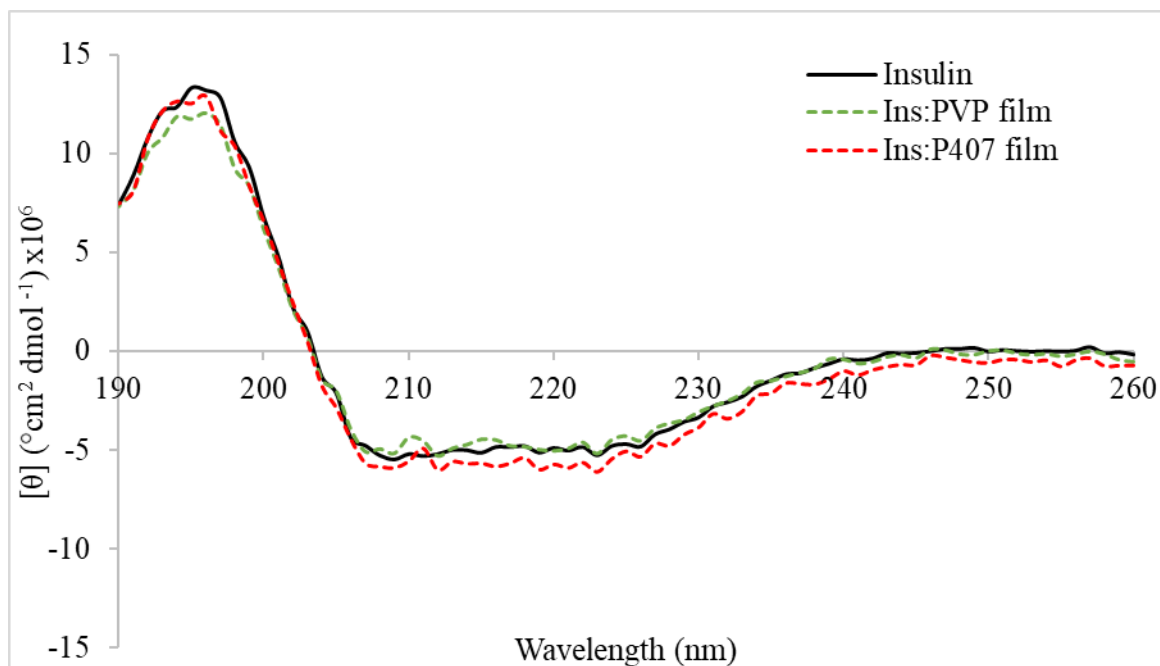


Figure 3.5 Far UV spectra of insulin-polymer films rehydrated in PBS 7.4 and insulin solution (1 mg mL^{-1}).

The effect of the P407 on the insulin stabilisation seems to intensify after dehydration and rehydration, with the respective spectrum to indicate an increase of the α -helical content. The PVP does not seem to induce significant changes, in agreement with the findings derived from the solution analysis.

To evaluate the effect of the polymers and hydration-rehydration process on the insulin structure, the secondary structural contents were estimated. The CD spectra were analysed on DICHROWEB and the CDSSTR method was applied to quantify the content of the insulin secondary structural components (Sreerama and Woody 2000; Whitmore and Wallace 2008; Whitmore and Wallace 2004). The percentage contents for pure insulin solution (1 mg mL^{-1}), insulin-polymer solutions are tabulated in Table 3.1.

Table 3.1 Secondary structure of insulin in pure solution, insulin-polymer solutions and insulin-polymer films after rehydration in PBS 7.4, estimated by CDSSTR.

	Insulin solution (%)	Ins:PVP solution (%)	Ins:P407 solution (%)	Ins:PVP film (%)	Ins:P407 film (%)
α -helix	65	65	67	66	70
β -sheet	13	7	4	6	6
Turn	10	6	7	7	9
Random coil	13	21	20	21	14

In accordance with the conclusions derived from the spectra, the secondary structure analysis shows that both polymers have a protective action on the insulin molecule. PVP maintains the α -helical content in the solution and slightly increases it in the dried and rehydrated form. On the other hand, the presence of P407 increases the α -helical content in the solution and further intensifies this effect for the film. This difference stems from the varying mechanisms that are into place when proteins interact with hydrophilic and amphiphilic polymers in a solution.

In the case of PVP, that exhibits hydrophilic character, the molecular crowding effect plays the dominant role in protein stabilisation. Therein, the insulin molecules tend to maintain their native form, which is more compact and offers smaller surface area for exclusion. Essentially, the polymer forces the insulin molecule to an equilibrium wherein its surface is minimised, promoting thus the stabilisation of the native structure (Ohtake, Kita and Arakawa 2011).

On the other hand, P407 is a triblock co-polymer, consisting of two hydrophilic blocks of ethylene oxide and a middle hydrophobic block of propylene oxide. Its structure endows it with amphiphilic properties, governed by its hydrophilic-hydrophobic balance (Dumortier *et al.* 2006). The protein stabilisation capabilities of such polymers differ from purely hydrophilic excipients and can be multifactorial. For instance, due to the presence of the hydrophobic moiety, the protein stabilisation activity depends on the balance between volumetric exclusion and hydrophobic interaction. The latter takes place when upon unfolding of the protein, its hydrophobic moieties bind with the polymer. Hence, both the native and the unfolded structure can be stabilised due to

steric exclusion and hydrophobic interaction, respectively (Ohtake, Kita and Arakawa 2011). However, protein-polymer binding at the hydrophobic areas can also promote suppression of aggregation. Another central stabilising mechanism is related to the ability of poloxamers to prevent surface denaturation, by antagonising the proteins for surface area and thus preventing conformational alterations pertaining to adsorption (Carpenter *et al.* 1999). Finally, surfactant copolymers have been reported to play the role of chaperones and promote refolding (Carpenter, Izutsu and Rarldolph 2010).

The above brief analysis of the typical protein stabilisation mechanisms that likely come into play in the presence of PVP and P407, illustrate that insulin stabilisation by the amphiphilic surfactant P407 in can occur through multiple mechanisms. Further and more specialised research is required to identify the exact effect and underlying acting mechanisms of the additives on insulin in the molecular level.

3.3.5 Insulin stability

The ability of the polymers to maintain insulin stability in the solid state, stored at $4\pm 1^{\circ}\text{C}$ for 2 weeks (14 days), was evaluated by CD. The films were rehydrated in PBS 7.4 on day 14 (T_{14}) and analysed via CD. The data presented at Section 3.3.4 were used as measurements at day 0 (T_0). Figure 3.6 displays the far UV spectra obtained from the rehydrated samples and Table 3.2, the secondary structural composition after analysis with the CDSSTR method.

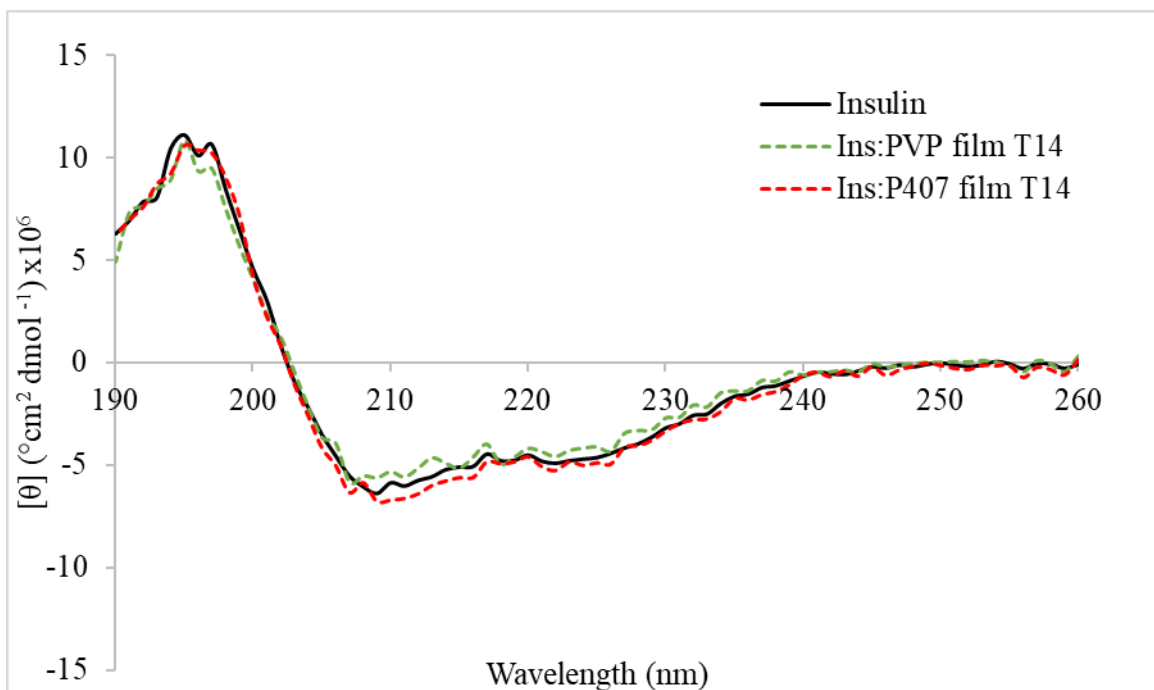


Figure 3.6 Far UV spectra of insulin solution (1 mg mL^{-1}) and insulin-polymer films after storage for 14 days at $4 \pm 1^\circ\text{C}$ and rehydration in PBS 7.4.

Table 3.2 Secondary structure of insulin-polymer films after storage at $4 \pm 1^\circ\text{C}$ for 14 days and subsequent rehydration in PBS 7.4, estimated by CDSSTR.

	Ins:PVP film T14 (%)	Ins:P407 film T14 (%)
α -helix	65	64
β -sheet	6	12
Turn	10	11
Random coil	19	12

The results from the insulin stability study illustrate that the α -helical contents of the insulin-polymer films after storage are maintained in high levels, comparable to the respective of the pure insulin in solution (Table 3.1). Interestingly, the stabilisation effect of insulin by the P407 that was observed in the analysis of the rehydrated films at T_0 (Section 3.3.4), diminishes after storage. Contrarily, the stabilisation effect by the PVP is preserved for both T_0 and T_{14} (Figure 3.7). It appears that the use of P407 is more suitable to reliably preserve the stability of insulin for applications that entail storage for short periods.

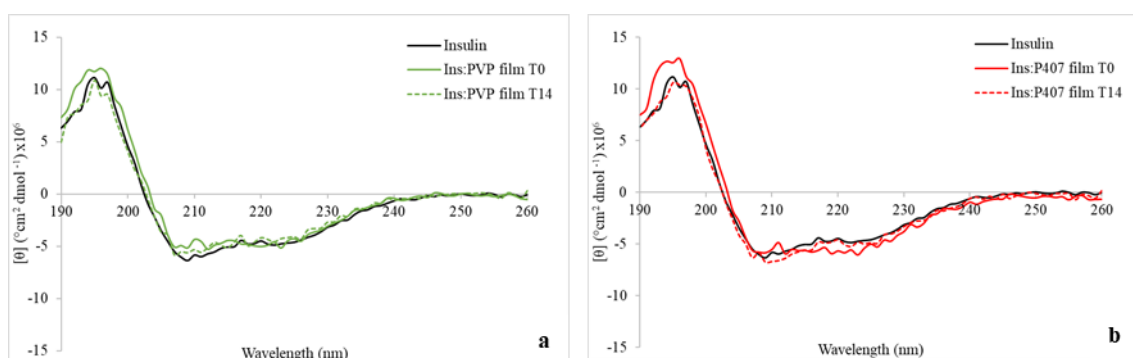


Figure 3.7 Far UV CD spectra of the rehydrated insulin-polymer films in PBS 7.4, analysed at (a) T_0 and (b) T_{14} .

3.3.6 High Performance Liquid Chromatography (HPLC) method and validation

High Performance Liquid Chromatography is a useful analytical tool used to separate, identify and quantify components in a formulation. The primarily employed mode in pharmaceutical analysis, the reversed-phase HPLC, includes a non-polar stationary phase and a relatively polar mobile phase consisting of solvents such as water and acetonitrile. For the detection of insulin in this study, a documented reversed-phase HPLC method was applied (Pissinato Pere 2019). Preliminary tests showed that the method generated a symmetrical insulin peak, analysed at 214 nm and with the retention time to be around 4.6 min. The method was validated in respect to specificity, linearity, accuracy, precision, limit of detection and limit of quantification, according to the standards of the British Pharmacopeia and the ICH Q2 (R1).

○ *Specificity*

The ability of the method to detect insulin in formulations where other components were present was investigated. Formulations containing insulin as well as PVP and P407 individually in saline phosphate buffer pH 7.4 (ratio 5:1), were analysed to check the effect of the polymers on the insulin chromatogram. Figure 3.8 illustrates the obtained peaks for pure insulin (a), Ins:PVP (b) and Ins:P407 (c). The addition of the polymers does not seem to interfere with the insulin peak, thereby verifying the specificity of the method for insulin detection.

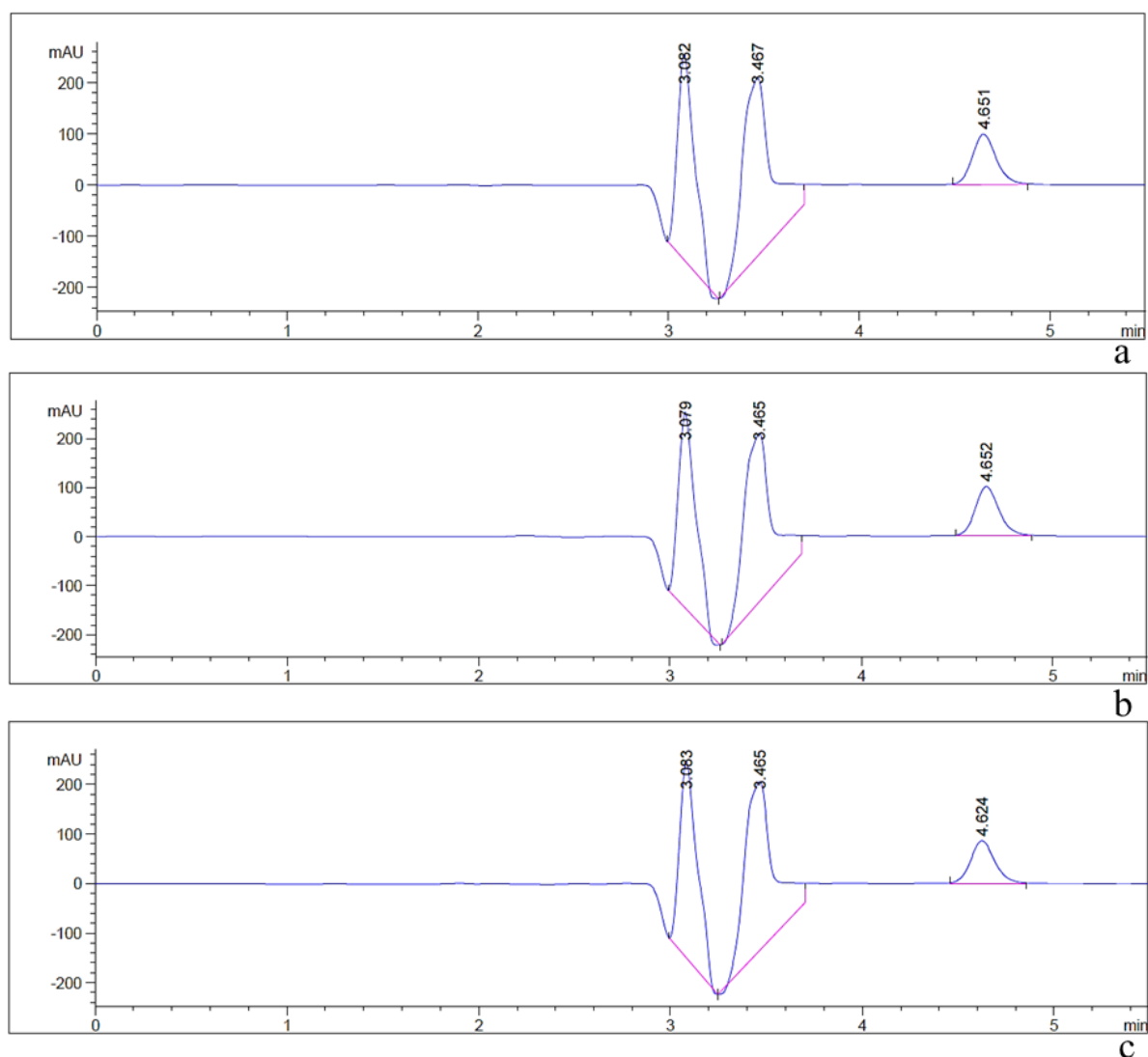


Figure 3.810 Chromatograms of (a) pure insulin solution, (b) insulin-PVP formulation and (c) insulin-P407 formulation.

○ *Linearity*

Standards of known concentrations (10, 20, 30, 40 and 50 µg/mL) were analysed to obtain the calibration curve, the regression line of which was used to assess the linearity of the method. Figure 3.9 shows the linear regression of the data and Table 3.3 display the parameters of the linear regression.

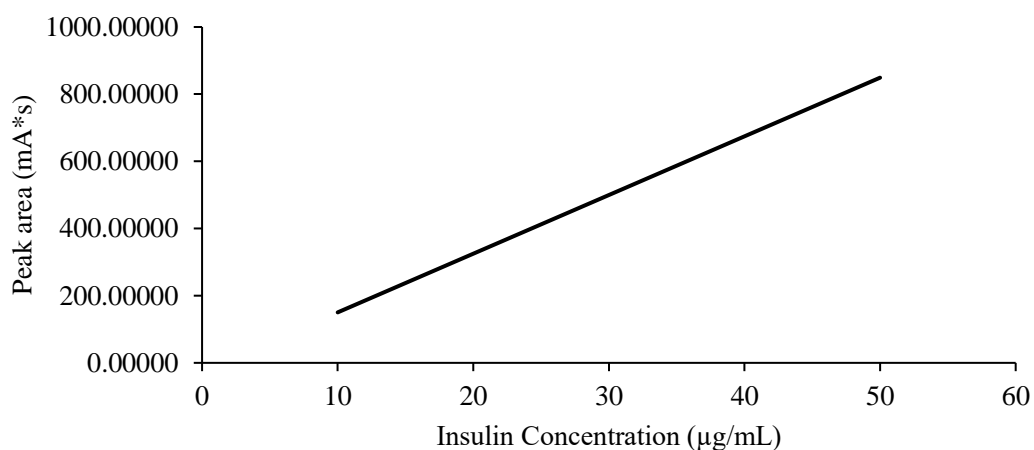


Figure 3.9 Calibration curve and regression line of the HPLC method for insulin detection and quantification.

Table 3.3 Parameters of linear regression of the calibration curve

Parameter	Value
Linearity range	10 to 50
Angular coefficient (slope)	17.468
Intercept	-24.345
Coefficient of determination (R²)	0.999

The results show that the method yields good linearity. The coefficient of determination, R^2 , was calculated at 0.999 which denotes that the data are very close to the regression line. Indeed, the result is well above the 0.990 limit that was set for this study.

○ *Precision*

Precision tests assess the degree of agreement between various measurements conducted on the same as well as on different days. The repeatability test compares measurements taken on the same day (intraday test) while the reproducibility test compares data that were recorded on different days. Both tests were conducted at low, medium and high concentrations (10, 30 and 50 µg/mL, respectively). The means of the recorded results, the standard deviations (SD) and the coefficients of variation (CV) are displayed in the following tables.

Table 3.4 Repeatability (Intraday) test

$C_{\text{theoretical}}$ (µg/mL)	Mean Peak Area (mAU*s)	SD	CV (%)
10	161.188355	1.515245	0.940
30	486.67099	8.22217	1.689
50	862.85437	12.37024	1.433

Table 3.5 Reproducibility test

$C_{\text{theoretical}}$ (µg/mL)	Mean Peak Area (mAU*s)	SD	CV (%)
10	161.74302	2.06991	1.279
30	496.868635	18.419815	3.707
50	856.39447	5.91034	0.690

The repeatability and reproducibility data generated low coefficients of variations, below the 5% threshold that was set for this study. The results show that the proposed HPLC method offers high precision.

○ *Accuracy*

The accuracy evaluation compares the theoretical concentration values to the ones experimentally obtained by the proposed method. The following table displays the theoretical and experimental values for low, medium and high concentrations (10, 30 and 50 µg/mL, respectively) and the accuracy values calculated from Equation 3.5.

Table 3.6 Accuracy evaluation

$C_{\text{theoretical}}$ ($\mu\text{g/mL}$)	$C_{\text{experimental}}$ ($\mu\text{g/mL}$)	Accuracy (%)
10	9.89	98.9
30	30.22	100.73
50	49.88	99.76

The reported data verify that the experimental concentration values generated by the proposed method approximate the theoretical ones with high accuracy. Therefore, the method is considered accurate for insulin quantification.

○ *Limit of Detection (LOD) and Limit of Quantification (LOQ)*

The LOD and LOQ refer to the lowest concentrations of insulin which permit its detection and quantification, respectively. Based on previous studies and literature review, the concentrations that were examined for the identification of the LOD and LOQ were in the range of 3 to 10 $\mu\text{g/mL}$. It was visually observed that the method was able to detect but not quantify insulin for all the concentrations studied, which was preliminary evidence that the LOD is lower than 3 $\mu\text{g/mL}$ and the LOQ is within the range. Figure 3.10 shows the insulin chromatogram at 7 $\mu\text{g/mL}$.

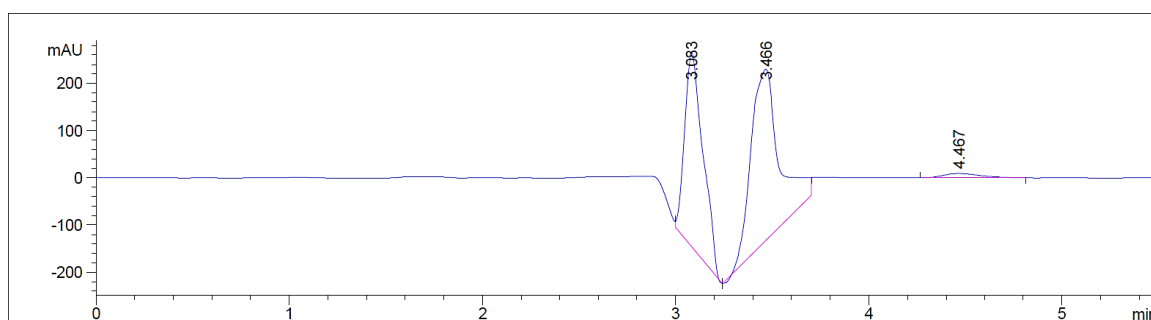


Figure 3.10 Insulin chromatogram at 7 $\mu\text{g/mL}$

By applying Equations 3.6 and 3.7, the LOD was calculated at 1.981 $\mu\text{g/mL}$ and the LOQ was calculated at 3.342 $\mu\text{g/mL}$. Those values are considered acceptably low, hence the method is considered suitable for the intended application.

3.3.7 Coating efficiency

The efficiency of the coating was tested by quantitatively determining the amount of insulin deposited on individual arrays and comparing it with the theoretical amount of 5 IU (175 μg). Coatings developed with both insulin-polymer formulations were tested and the coating efficiency was calculated from Equation 3.8. Table 3.7 displays the results.

Table 3.7 Coating efficiency for insulin-polymer coated microneedle arrays

	Theoretical cargo (μg)	Experimental cargo (μg)	CE (%)
Ins:PVP	175	173.85 \pm 3.1	99.34%
Ins:Polox	175	178.06 \pm 4.2	101.75%

The results show that the experimentally quantified insulin content was in good agreement with the theoretical one, which shows that the proposed coating method is able to create films with controlled drug amounts.

3.3.8 *In vitro* release studies

The coated microneedles were tested for their ability to deliver their insulin cargo in porcine skin. Figure 3.11 shows the cumulative release for all designs. PVP showed better performance overall in releasing the drug, owed to it being hydrophilic as opposed to P407 that features a middle hydrophobic block and two end hydrophilic blocks. Thus, a faster dissolution of the insulin-PVP coatings is justified. The sustained release of insulin due to the choice of the specific carriers served the purpose of this study, as rapid release generated by a different carrier is likely to have masked important effects, such as the dependence of coating dissolution on design.

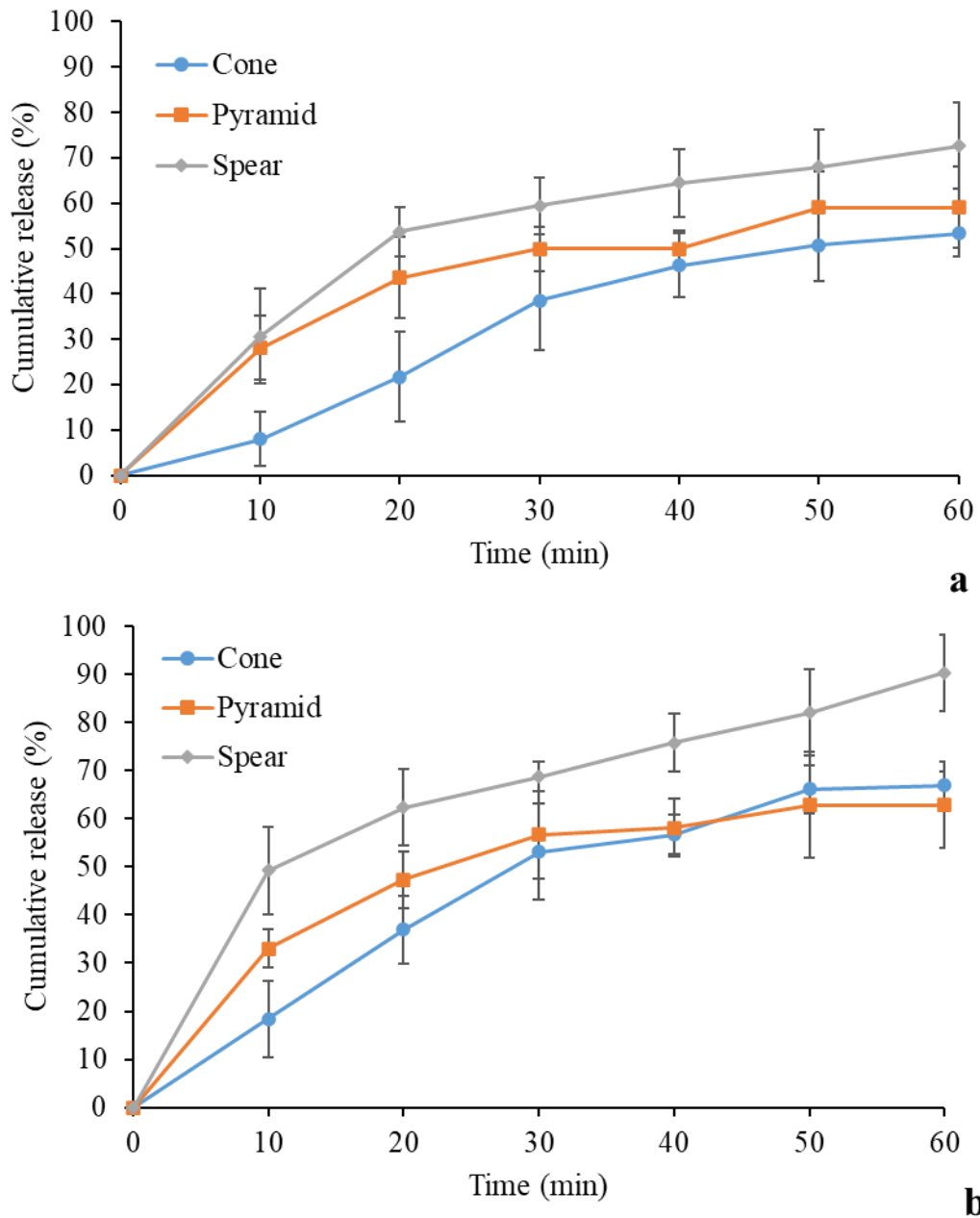


Figure 3.11 Cumulative release profiles for insulin delivered by 3D printed coated microneedles with polymers as carriers; (a) P407; (b) PVP.

The highest drug revenue was delivered by the spear design for both polymer carriers, reaching up to 70% and 90% for P407 and PVP, respectively. Conversely, the cone design seems to have the least satisfactory performance for insulin-P407, whereas its release for the PVP group improves. This is probably owed to the fact that the cone coating is likely bulkier and lags in releasing its cargo. This is further supported by the observation that for both pyramid and cone designs, the cumulative release was below

65% for 60 min. It is likely that the duration of the *in vitro* study was insufficient for complete coating dissolution for the two designs, in line with the above-described hypothesis of comparatively bulkier films, induced by microneedle geometry. It is anticipated that the entirety of the insulin cargo would be released by all designs for extended experimental duration, however additional data are required to verify this claim.

The results of this study support the hypothesis drawn earlier that microneedle geometry influences coating morphology in the described fashion, and thereby affects coating dissolution. In accordance with the geometrical explanation described earlier, drug release studies verified that the cone microneedle furnishes a surface prone to developing bulkier coatings, while the spear developed finer films. These findings are of high significance for applications in which gradual drug release is aimed at.

3.4 CONCLUSIONS

In this work, 3D printed solid microneedles featuring different geometries were successfully coated with insulin via a piezo-driven 2D inkjet printing technique. The coating method produced uniform, spatially controlled drug-containing films, with high degree of accuracy of the drug amount. A wetting model was applied to aid the interpretation of the effect of microneedle geometry on the morphology of the coated film. It was found that microneedle curvature and lateral surface inclination play an important role in the formation of the coating film and hence in its dissolution. The efficacy of polymer additives on the stabilisation of insulin in a solution, during rehydration followed by rehydration as well as in storage was evaluated. Both polymer carriers exhibited a protective action on insulin. An isocratic HPLC method for insulin detection and quantification was validated and used for the evaluation of drug cargo on microneedle arrays. *In vitro* insulin release studies in porcine skin verified that microneedle geometry influences the coating dissolution.

The present experimental Chapter proposed a strategy for the development of 3D printed microneedle patches with, albeit easily customisable, yet fixed amounts of drug cargos. A different approach must be considered to enable real personalisation of treatments based on individual requirements, that can be adapted *in-situ*. An excellent candidate to serve this purpose are hollow microneedles.

CHAPTER 4
3D PRINTED HOLLOW MICRONEEDLES
DESIGN, MANUFACTURING, OPTIMISATION AND MECHANICAL
PERFORMANCE

4.1 INTRODUCTION

The previous experimental Chapters of the present thesis demonstrated that commercial laser Stereolithography (SLA) can be a valuable tool for fast, cost-effective and readily customisable manufacturing of biocompatible solid microneedles with tailored drug loadings. In the microneedle development process studied, although the drug loading was easily customisable through the inkjet printing technique employed, the microneedle patch by default carried fixed amounts of the therapeutic substance. The need for real-time, *in-situ* control of the drug administration prompted the investigation of alternative systems. For this purpose, the development of hollow microneedles by 3D printing was investigated.

Hollow microneedles have emerged as an alternative to typical injections, tackling issues such as pain, needle phobia and the requirement for a trained professional to perform the drug administration (McConville, Hegarty and Davis 2018). Such systems have known limited applications due to mechanical strength issues (Wang et al. 2006), which highlights the need for robust structures that pierce the skin without compromise of their structural integrity. Hollow microneedles are manufactured through several techniques, mainly micromoulding and micromachining which can often be multistep, time-consuming, challenging to scale-up and difficult to readapt according to individual application requirements. 3D printing is by definition a promising alternative to the traditional microneedles manufacturing techniques. However, there is limited progress on the applicability of 3D printing for hollow microneedle systems recorded in the past few years due to several challenges.

The printing resolution has been a major restrictive factor. Although a high degree of fidelity between virtual and physical model is an innate advantage of 3D printing, high accuracy in detail formation in the microscale often exceeds the capabilities of the printer. As a consequence, issues of reliability arise, especially regarding the microneedle tip sharpness and the formation of the shaft openings, which are critical for

the successful insertion into the skin and the diffusion of fluid. Another challenge stems from the limited material palette that is readily processable with the various 3D printing technologies and is further narrowed down by the requirement of biocompatibility. Indeed, there is only a small number of biocompatible, printable materials across the whole family of printing technologies.

A small number of studies have reported the successful implementation of 3D printing as a manufacturing technique for hollow microneedles, intended for transdermal purposes. Two photon polymerisation (2PP), the specialised photopolymerisation printing technique, has been used for the development of microneedle masters for micromoulding (Faraji Rad *et al.* 2017), as well as for the direct fabrication of patches. Ovsianikov *et al.* employed 2PP to fabricate hollow microneedles, reporting that the manufacturing process had no adverse effects on cell viability and growth (Ovsianikov *et al.* 2007). The same technology was also employed to develop a combined hollow microneedle and reservoir patch that can be potentially incorporated in transdermal and implantable systems (Moussi *et al.* 2020). This technology favours microneedle fabrication due to its exceptional resolution, hereby enabling the formation of sharp microneedles. However high costs, longer printing times and small printing volumes (Schmidleithner and Kalaskar 2018), hamper the production in larger numbers, raising questions regarding the technology's potential for broad clinical applications.

To overcome the latter challenges, exploring the applicability of more accessible printing technologies, is imperative. Only one relevant study has followed such approach, proposing an integrated microfluidic-enabled hollow microneedle system to enable the in situ mixing of multiple fluids and their subsequent transdermal delivery. The device was fabricated by a one-step laser SLA printing process and can potentially enable the simultaneous transdermal administration of various therapeutics (Yeung *et al.* 2019).

4.1.1 Aims and objectives

The main objective of this experimental Chapter was to explore the challenges associated with the Additive Manufacturing process, mainly those pertaining to resolution, for hollow microneedles and complex microneedle-bearing patches. More specifically, the aim of this study was to obtain microneedle systems that effectively pierce the skin, maintain their structural integrity during application and removal, allow

the flow of drug-containing solutions to the skin through their internal microstructures and openings, while being reliably additively manufacturable. To achieve this, the following research goals were set:

- Development of engineering designs for hollow microneedles and investigation of their printability. The development strategy followed the rationale of balancing application requirements with manufacturing restrictions, in the logic of Design for Additive Manufacturing (DfAM).
- Investigation of the hollow 3D printed microneedles piercing and fracture behaviour, to assess their performance in potential applications wherein effective and reliable piercing through the skin tissue without mechanical failures is required.
- Testing of the printability of tall and short microneedles, employing laser SLA and Digital Light Processing (DLP) 3D printers, followed by assessment of the dimensional accuracy to allow the comparison of the technologies.
- Development of two types of complex patches to enable the fluid provision and distribution from a flow instigator to the microneedles. The designed patches composed of microneedles, internal microstructures for fluid distribution and an opening for fluid provision.
- 3D printability investigation of the complex patches with both studied technologies to elucidate the effect of resolution on functionality.

The findings of the present study are expected to build useful knowledge on the largely unexplored field of 3D printed hollow microneedles.

4.2 MATERIALS AND METHODS

4.2.1 Materials

Two different photopolymers were employed in this study, each compatible with the respective 3D printing technology. For laser SLA, the material used was a biocompatible Class I photopolymer consisting of methacrylic oligomers and phosphine oxides as photoinitiators, branded as Formlabs Dental SG (GoPrint3D, North Yorkshire, UK). For DLP, the material used was a biocompatible (EN ISO 10993-1) Class II

photopolymer branded as DETAX Freeprint Splint 2.0 (iMakr, Hackney, London, UK). Its composition is proprietary. Isopropyl alcohol was of laboratory grade.

4.2.2 Computer Aided Design (CAD) of hollow microneedles and complex patches

An engineering CAD software (PTC, Boston, MA, USA) was employed to design the structures studied. Tall and short hollow microneedles were designed with varying opening sizes, to investigate the impact of printing resolution on the dimensional fidelity. All microneedles were cone-shaped and featured internal bores, with a wall thickness of 100 μm . Each array featured 49 microneedles in a 7x7 symmetrical configuration, built on 500 μm thick square substrate (15 mm \times 15 mm). The design dimensions of the hollow microneedles are presented in Table 4.1.

Table 4.12 CAD dimensions of hollow microneedles.

	Tall			Short	
	Bevel	Ellipsis 400150	Ellipsis 600200	Ellipsis 400300	Ellipsis 300150
Height (μm)	890	1000	1000	500	500
Width \varnothing (μm)	1000	1000	1000	550	500
Tip \varnothing (μm)	100	100	100	50	50
Opening (μm)	\varnothing 80	300x150	600x200	400x300	300x150
Bore \varnothing at base (μm)	800	800	800	300	300

To enable the distribution of liquid from an external source to the hollow microneedles, complex patches were designed featuring microfluidic internal structures. The thickness of the microneedle substrate increased to 1.5 mm and a fluid provision nozzle of 4.30 mm in internal diameter and 6.30 in external diameter was designed at the microneedle base, to fit to a standard commercial syringe. The nozzle was connected to an internal fluid circulation system. Two systems were designed; the first comprised an internal reservoir and the second a conduit of horizontal microchannels. Both circulation systems communicated with the hollow microneedle bores through vertical

microchannels. The microneedle population was decreased to 16 in a 4x4 symmetric configuration. For printing using laser SLA, tall microneedles were designed on the patch (Ellipsis600200) while for the DLP printing, short microneedles were used (Ellipsis400300). Prior to printing, all CAD models were converted to .stl files.

4.2.2 Additive Manufacturing: Stereolithography and Digital Light Processing

Two photopolymerisation-based 3D printing technologies were employed for the printing of hollow microneedles and complex patches. For laser SLA, the CAD models were imported in the Preform software (Formlabs, MA, USA). The microneedle patches were manufactured using the Form2 SLA 3D printer (Formlabs, MA, USA). For DLP, the CAD files were reported in the Asiga Composer software (Asiga, Sydney, Australia) and printing was conducted using the Asiga Max (iMakr, Hackney, London, UK). The designs Bevel, Ellipsis400150, Ellipsis600200, Ellipsis400300 were printed rotated at 45° to the horizontal platform, while Ellipsis300150 was printed at 0°, to investigate the effect of printing angle on the quality of the DLP printed microneedles. Post-printing, the structures were cleaned from any unpolymerised resin residues in isopropyl alcohol bath. Internal washing through driven flow with a syringe was also carried out on complex patches, to remove residues from the internal microstructures. All printed structures were cured for 60 min at 40 °C under UV radiation using the MeccatroniCore BB Cure Dental station (GoPrint3D, UK).

4.2.3 Scanning Electron Microscopy

The microneedle arrays were mounted onto aluminium stubs using a double-sided carbon adhesive tape (Agar Scientific, UK). Each array was examined by SEM (Hitachi SU 8030, Japan) using a low accelerating voltage (1.0 kV). A low accelerating voltage was used to avoid electrical charges on the microneedles. The images were captured digitally from a fixed working distance (11.6 mm). Dimensions were measured using the microscope's software built-in tool. Five microneedle samples from each design, fabricated at different print jobs but with identical printing and post-printing parameters, were scanned. The dimensions of critical geometrical features were measured and used for the calculation of the %error of the printing process, from Equation 4.1:

$$\%error = \frac{|experimental-theoretical|}{theoretical} 100\% \quad \text{Equation 4.1}$$

4.2.4 Preparation of porcine skin for insertion tests

Full-thickness abdominal porcine skin was collected from a local slaughterhouse (Forge Farm Ltd., Kent, UK) and was then shaved using a razor blade. The fatty tissue below the abdominal area was removed using a scalpel. Samples of full-thickness skin tissue were sliced and then used for the piercing tests.

4.2.5 Insertion tests in porcine skin

The ability of the 3D printed hollow microneedles to effectively pierce porcine skin and determine the force needed for penetration was investigated. To achieve this, the TA.HD plus Texture Analyser (Stable Micro Systems, Surrey, UK) equipped with a 5 kg load cell was employed. The microneedle arrays were fixed on the moving probe of the machine using double-sided adhesive tape. Samples of full-thickness abdominal skin were placed on waxed petri dishes and were secured on the bottom, fixed probe of the machine. Continuous force and displacement measurements were recorded to identify the point of needle insertion. The speed of the moving probe was 0.01mm/s and all experiments were repeated 5 times.

4.2.6 Axial force compression testing

To evaluate the fracture strength of the microneedles, fracture tests were conducted employing a Tinius Olsen H25KS mechanical testing machine, equipped with a 25kN load cell. The microneedles were mounted on the fixed probe of the machine using double-sided tape and were compressed against the moving flat steel plate until fracture. Continuous force and displacement measurements were recorded, and the speed of the moving probe was 1 mm/s. Each experiment was repeated 5 times. In cases where there was not a clear discontinuity in the force-displacement curve, the load of fracture was identified based on the ultimate point that the curve maintained linearity.

4.2.7 Margin of safety

Data obtained from piercing tests and axial force mechanical tests were employed to calculate the margin of safety for hollow microneedles, from the following equation:

$$\text{margin of safety} = \frac{F_{\text{fracture}}}{F_{\text{insertion}}} \quad \text{Equation 4.2}$$

Where F_{fracture} and $F_{\text{insertion}}$ are the fracture and insertion forces, respectively. Values higher than 1 were considered to reassure safety upon application.

4.3 RESULTS AND DISCUSSION

3D printing of hollow microneedles is inherently challenging. Apart from the known restriction that printing resolution imposes on microneedle sharpness, another limitation pertaining to resolution is the formation of the opening. The microneedle opening is of critical importance in terms of clinical effectiveness of the system, since its inaccurate replication can result in blocked hollow shafts and hence, inadequate fluid distribution into the skin. The main objective behind this study was to explore the challenges associated with the Additive Manufacturing process, mainly those pertaining to resolution, for hollow microneedles. Two photopolymerisation-based 3D printing technologies were employed and their potential as microneedle manufacturing methods was explored.

4.3.1 Design and Additive Manufacturing of tall hollow microneedles

Tall hollow microneedles (height=1000 μm) were designed, and their printability was tested. Following the DfAM principles that were identified as significant in Chapter 2, the microneedle design criteria considered were that the microneedles would be reliably printable, while they reach a sufficient penetration depth, pierce the skin, sustain the mechanical stress during insertion and serve their clinical goal. The latter pertains to the formation of an opening on the shaft of the hollow structure, to connect the microneedle bores with the skin interstitial fluid and allow the delivery of the therapeutic solution. Hence, the length of the microneedles was maintained at 1000 μm , the aspect ratio at 1:1, while the tip at 100 μm in diameter. Moreover, the printing angle was set at 45° to the building platform to achieve optimal dimensional fidelity to design, in agreement with the findings described in Chapter 2.

The impact of printing resolution on the formation of the opening was still unexplored and actually, unpredictable. To the author's knowledge, there is no scientifically sound method to predict the actual outcome of the printing process in terms of detail accuracy and dimensional fidelity to design. Improvement is mostly obtained by trial-and-error; however, the simple, user-friendly and fast nature of this technology simplifies and

accelerates the prototype development. In this logic, the printability of different microneedle designs was examined, with varying placement and size of the bore opening.

The catalytic effect that printing resolution has on hollow microneedle design and final structure was highlighted in the only documented attempt to 3D print a hollow microneedle patch through laser SLA (Yeung *et al.* 2019). Albeit achieving sharp microneedle tips, the openings generated by the reported printing strategy were quite sizeable, possibly leading to drug losses upon application, in cases of partial skin insertion. Hence, in this work we aimed at achieving accurate printing of microneedles with smaller openings, which would also be beneficial in terms of mechanical performance.

The first design that was studied was the Bevel, inspired by the geometry of standard bevel needles. The microneedle shaft was designed as a hollow cone and sectioned at 125° to the longitudinal axis. The tip of the microneedle was trimmed, leaving a top opening of $80\ \mu\text{m}$ in diameter (Figure 4.1a). After printing, images acquired via SEM revealed that the formation of the top bore opening was unsuccessful, demonstrating that the model dimensions obviously exceeded the detail size that can be realised with this technology (Figure 4.1b). To achieve the formation of the opening, its diameter should be increased, resulting by default to decreased sharpness and thus inferior piercing capabilities (Wang *et al.* 2006).

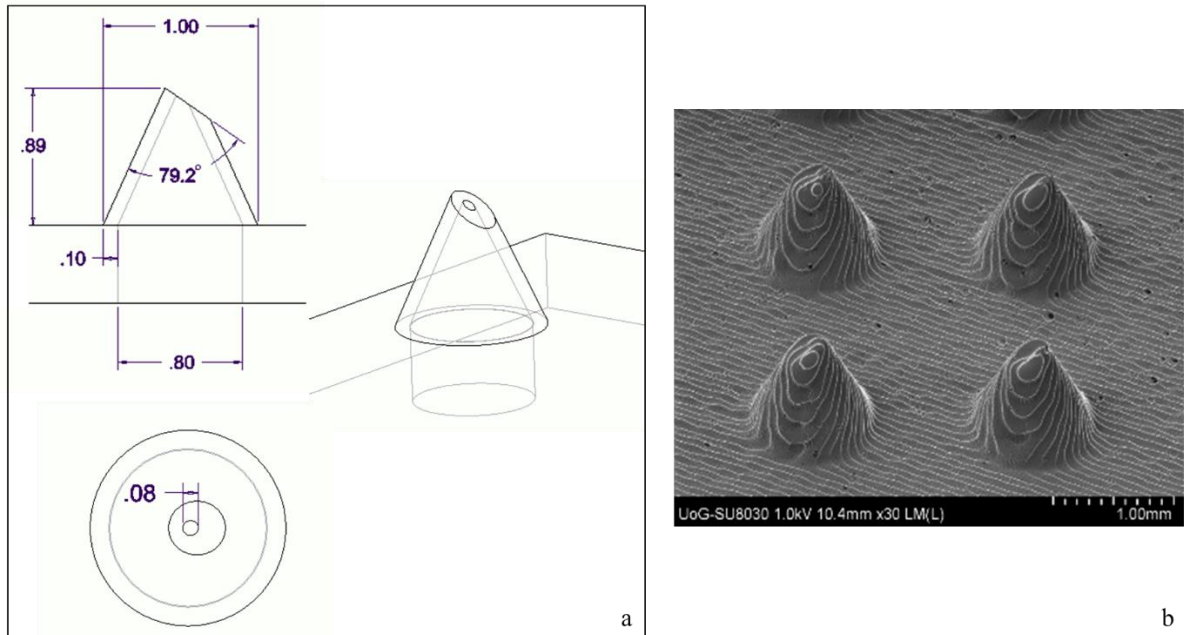


Figure 4.1 Tall Bevel microneedles. (a) Engineering designs and (b) SEM of the printed structures.

Since a top opening was unfeasible from the manufacturing perspective, the positioning of a side opening was attempted. This strategy would enable the formation of the clinically relevant hollow microneedle opening, avoiding the negative impact on the sharpness. Hence, the second design tested was the Ellipsis400150. The hollow cone featured an elliptical opening of 400 μm in length and 150 μm in width (Figure 4.2a). These dimensions were theoretically within the resolution capabilities of the laser SLA printer, according to the manufacturer. However, SEM images of the printed structures revealed that the formation of the opening was unsuccessful. Although a trace at the area of the opening can be observed, additional material was solidified, blocking the access from the microneedle bore (Figure 4.2b).

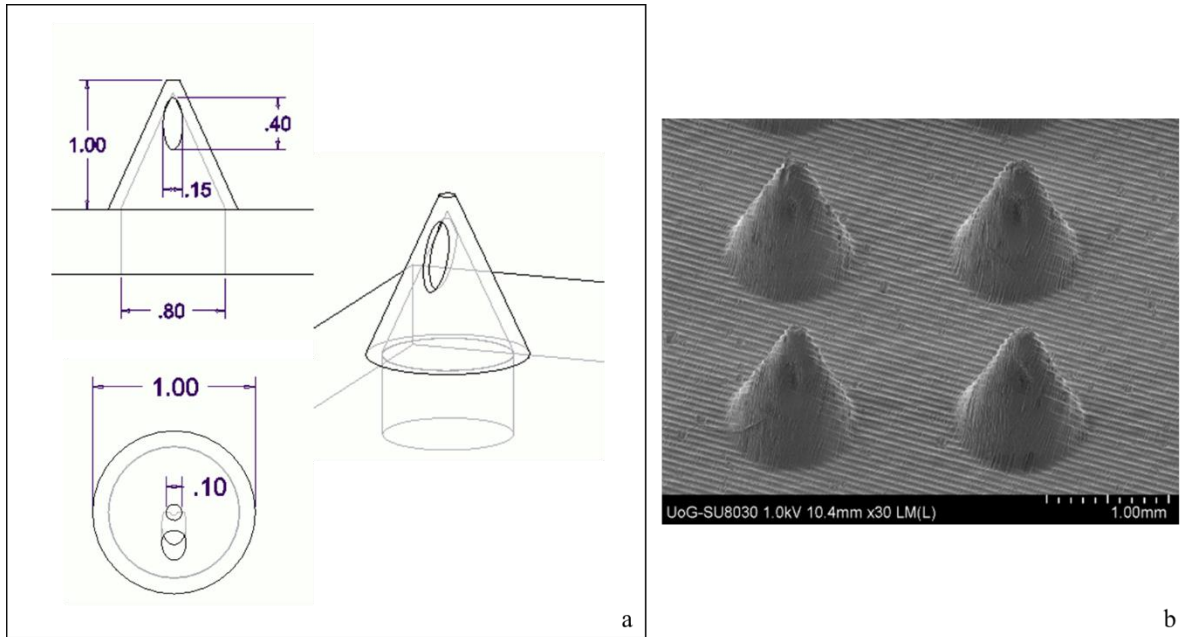


Figure 4.2 Tall Ellipsis400150 microneedles. (a) Engineering designs and (b) SEM of the printed structures.

This effect can be easily explained by examining the morphology of the laser beam spot. The intensity of radiance of the spot features a Gaussian distribution (Francis, Stadler and Roberts 2016), meaning that it does not have strictly defined margins. As a result, material in the circumference of the focal point can also be exposed to radiation. This radiation is typically of low intensity and thus unable to produce significant local solidifications and dimensional discrepancies. However, when at different times the laser emits light at two spots that are in close proximity, recurring exposure to the Gaussian tails of radiance distribution can induce terminal solidification (Figure 4.3).

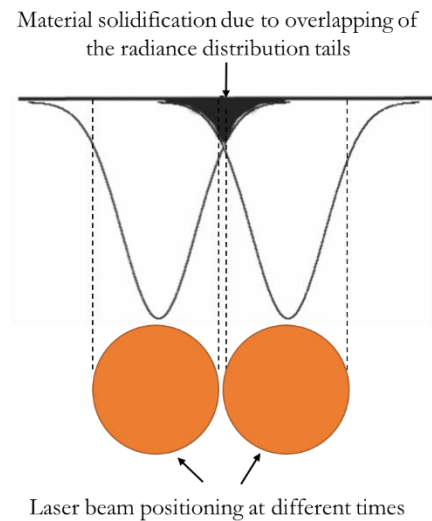


Figure 4.3 Gaussian distribution of laser radiance when the laser cures two spots in close proximity. Recurring exposure due to overlapping of the Gaussian tails can cause dimensional discrepancies.

this design generated uniform and reproducible hollow microneedles with openings that allow access from the bore. The side opening was successfully printed because its larger dimensions eliminated or suppressed the above-described effect (Figure 4.4).

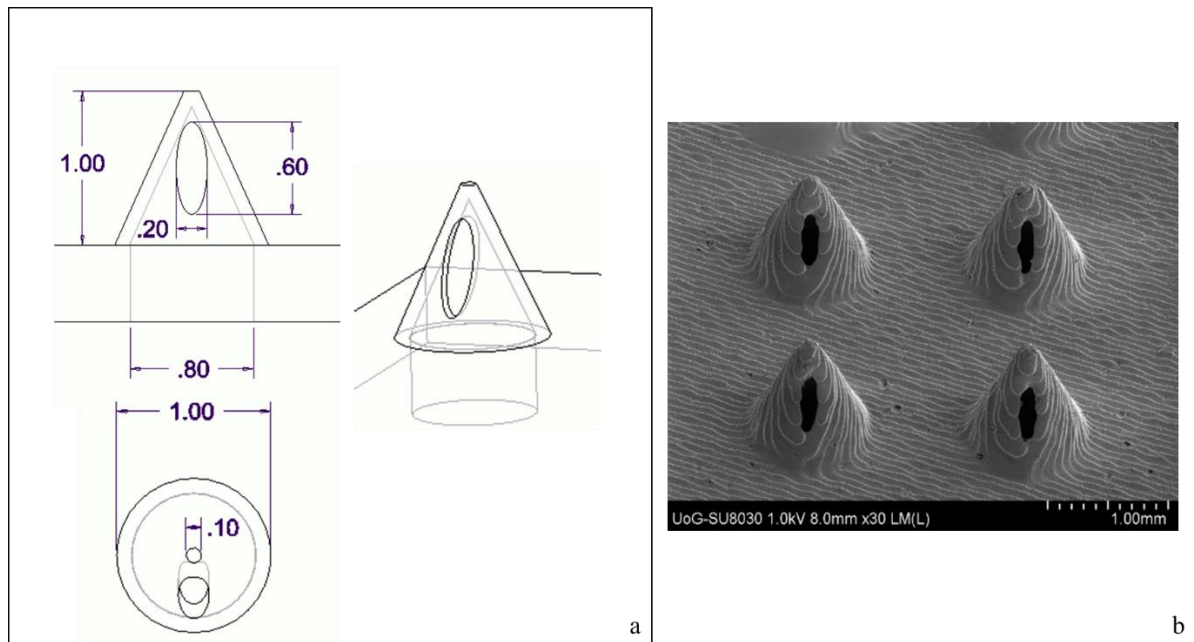


Figure 4.4 Tall Ellipsis600200 microneedles. (a) Engineering designs and (b) SEM of the printed structures.

To evaluate the dimensional fidelity of the printed microneedles to the virtual design and assess the degree of unwanted curing due to overlapping of the radiance distribution tails, the dimensional accuracy was investigated. The dimensions of critical geometrical parameters were measured and compared with the design ones. The error was quantified by using Equation 4.1 and the results were tabulated in Table 4.2.

Table 4.2 Theoretical and experimentally measured dimensions and dimensional error of tall hollow microneedles (Ellipsis600200) printed by SLA. Experimentally obtained dimensions are given in mean \pm SD.

	Dimension (μm)		%Printing Error
	Design	Printed SLA	
Height	1000	1002 \pm 1.6	0.2
Width \emptyset	1000	1004.75 \pm 1.6	0.475
Tip \emptyset	100	103.3 \pm 5.1	3.3
Length of opening	600	408.5 \pm 8.7	31.92
Width of opening	200	150.75 \pm 4.9	24.625

The dimensional fidelity calculated for the Ellipsis600200 design regarding height, width and tip diameter illustrate that the printing angle optimisation conducted in Chapter 2 equally applies for hollow microneedles. Although obtaining finer details by tuning the printing parameters was feasible, this approach is not always applicable. In the case of the tip, altering the building orientation has enabled the formation of tips with diameters smaller than the nominal resolution of the printer (140 μm). The optimised printing angle however did not seem to induce a similar effect of increased accuracy in the case of the side opening. It appears that tuning the building orientation must be applied strategically to improve the morphology of selected, suitable features, rather than to be viewed as a panacea for the universal optimisation of the printed quality. Evidently, in reference to the opening dimensions, the overlapping of radiance distribution tails affects dimensional fidelity by curing adjacent areas. As a result, the dimensions of the side opening are significantly altered in comparison to the designed ones, leading to the formation of a much smaller opening.

4.3.2 Design and Additive Manufacturing of short hollow microneedles

A multitude of applications require the development of shorter microneedles for drug delivery (e.g., transdermal delivery to body areas with thinner skin, animal testing). The well-established limitation of printing resolution has hampered the application of 3D printing for the manufacturing of such transdermal systems. Indeed, in the only documented fabrication of 3D printed hollow microneedles with laser SLA, the minimum height obtained was 700 μm (Yeung *et al.* 2019). Moreover, to the author's knowledge the implementation of DLP for the fabrication of hollow microneedles for transdermal drug delivery purposes, has not yet been reported in literature.

In this work, short hollow microneedles with a height of 500 μm and a tip diameter of 50 μm were designed, and their printability was examined. Two photopolymerisation-based 3D printers were employed, with different light emission mechanisms and different nominal resolutions. The technologies also differ significantly in terms of printing time, which is an inherent difference between the two technologies, emanating from the light emission mode. In laser SLA, the laser spot travels within the resin vat, solidifying the structure, in a line-to-line manner. On the other hand, in the DLP process, a high-definition projector projects the whole layer structure, solidifying whole layers at once. Indeed, the printing time for a single microneedle was 1.5 hours for the SLA and 1 hour for the DLP. Nonetheless, it is worth noting that for the DLP, due to the projection system, the printing time does not increase proportionally for multiple arrays in the same print job, and it mainly depends on the height of the object (i.e., the number of layers). The longer printing duration of the laser SLA is however balanced by the typically larger printing volume (145 mm \times 145 mm \times 175 mm for the Form2 SLA as opposed to 119 mm \times 67 mm \times 75 mm for the Asiga MAX DLP) which enables the simultaneous manufacturing of more microneedle arrays in a single print job. Specifically, for the microneedle patches described here, the maximum number of arrays that can be obtained per print job for the laser SLA is 49 in 3 hours, while for the DLP, the respective number of patches is 6 in 1 hours.

The most notable difference between the two technologies is the xy plane printing resolution. For the DLP, xy plane resolution is governed by the smallest dimensions of the volumetric pixels ('voxels') whereas in laser SLA the focal point plays the dominant role. This technical variation enables the DLP technology to achieve substantially better resolution (62 μm vs 140 μm for the Asiga MAX and Form2, respectively). The

following microneedle printability studies aim to compare the effect of resolution of the two technologies on microneedle quality.

Two microneedle designs were developed, with varying opening dimensions. Ellipsis400300 was designed featuring an opening of 400 μm and 300 μm in length and width, respectively. The dimensions were decided on the basis of the findings reported above, to reassure successful formation of the opening by the laser SLA printer. The aspect ratio was initially set to be 1:1, however the geometrical incompatibility of the opening with the 500 μm width at the base, mandated its increase at 550 μm (Figure 4.5a). The design was printed with both laser SLA and DLP at an angle of 45° to the printing platform and Figure 4.5b,c illustrate the respective SEM images.

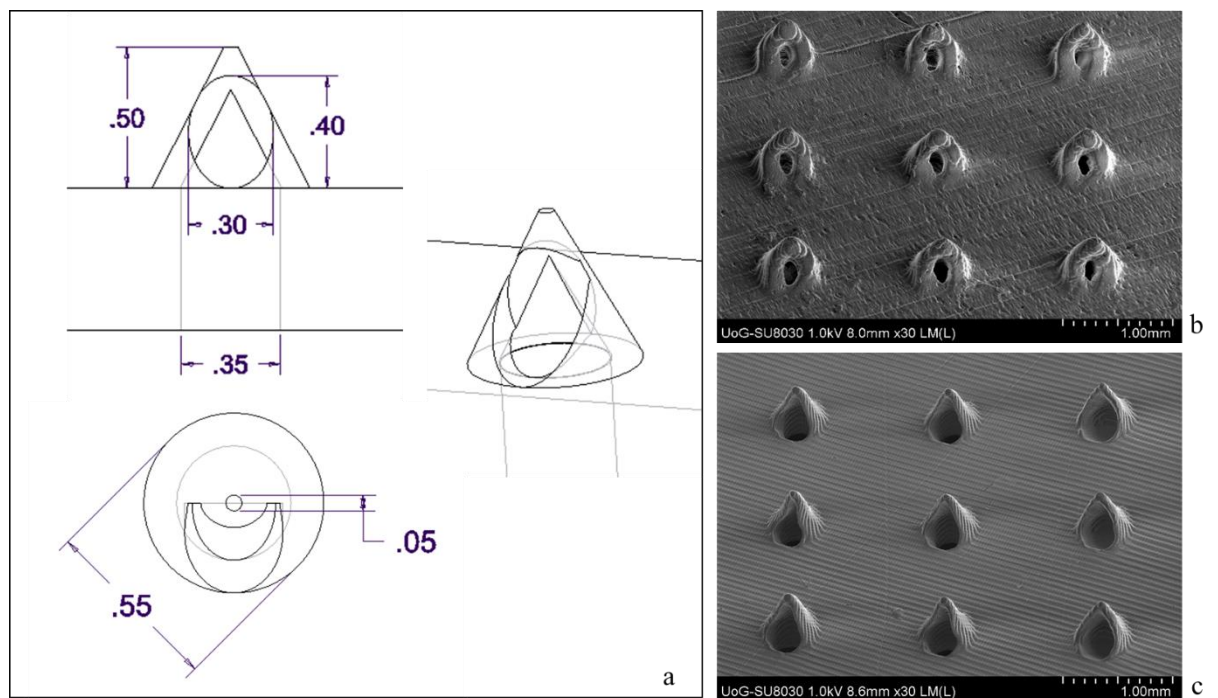


Figure 4.5 Short Ellipsis400300 microneedles. (a) Engineering designs and SEM images of the structures printed with (b) laser SLA and (c) DLP.

The superior resolution accomplished by the DLP process is easily verified by simple visual evaluation of the SEM images. The DLP microneedles bore greater resemblance to the virtual design and their quality was improved. To quantify the dimensional

fidelity, the %error (Equation 4.1) per geometrical parameter was calculated (Table 4.3).

Table 4.3 Theoretical and experimentally measured dimensions and dimensional error of short hollow microneedles (Ellipsis400300) printed by SLA and DLP. Experimentally obtained dimensions are given in mean \pm SD.

	Dimension (μm)			%Printing Error	
	Design	Printed SLA	Printed DLP	SLA	DLP
Height	500	501 \pm 6.4	516.5 \pm 13	0.20	3.30
Width \emptyset	550	507.75 \pm 3.1	550.67 \pm 5	7.68	0.12
Tip \emptyset	50	93.4 \pm 9.2	51.58 \pm 1	86.8	3.15
Length of opening	400	221.75 \pm 26.6	433.25 \pm 9.5	44.56	8.31
Width of opening	300	139 \pm 13.5	305 \pm 21	53.67	1.67

Regarding the laser SLA microneedles, the geometrical parameters that have been shown in the present thesis to be sensitive to discrepancies (i.e. tip, opening dimensions) were inaccurately fabricated, as expected. On the other hand, the dimensional errors illustrate that the improvement achieved by the use of the DLP technology is remarkable. Geometrical parameters were replicated generally accurately. A discrepancy was detected for the length of opening, that was printed larger than designed.

These promising results prompted additional investigation on the DLP-mediated manufacturing of short hollow microneedles with smaller openings, that were found to be unattainable though laser SLA. Thus, microneedles of 500 μm in height, with an opening of 300 μm in length and 150 μm in width were designed and 3D printed via DLP. To assess the effect of the printing angle on the end-product quality, particularly on the sharpness, the microneedles were built at 0° in reference to the building platform.

The engineering designs of the Ellipsis300150 and the corresponding SEM images of the printed structures are depicted in Figure 4.6.

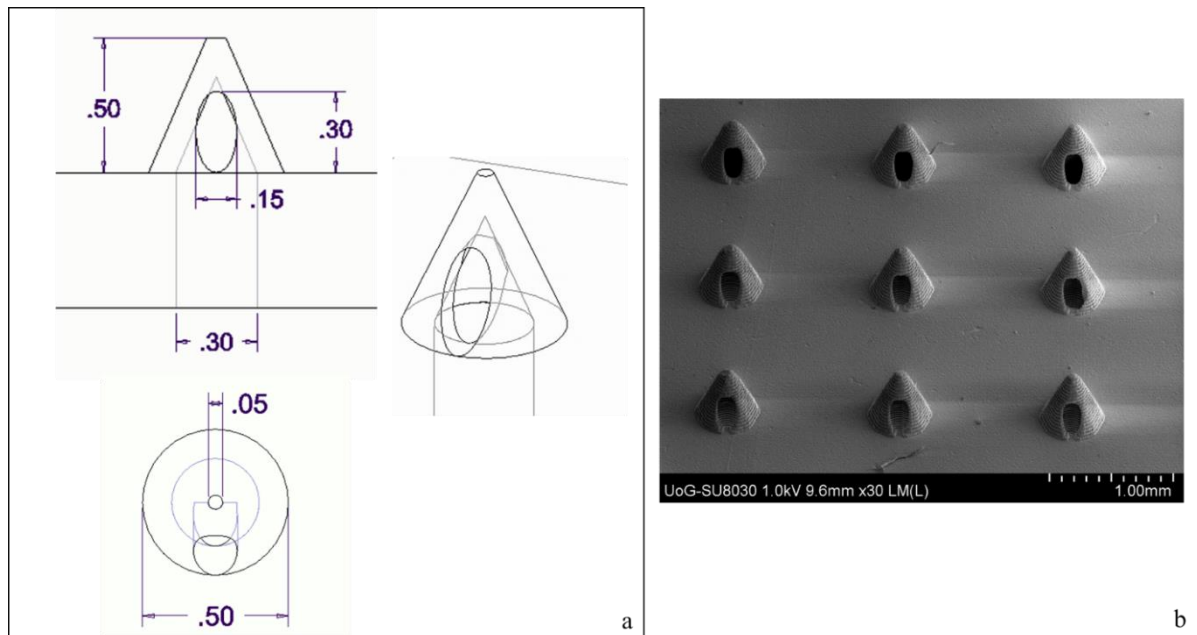


Figure 4.6 Short Ellipsis300150 microneedles. (a) Engineering designs and (b) SEM images of the structures printed with DLP.

In contradiction to laser SLA that failed to generate similarly small openings, the higher resolution of the DLP enabled their accurate fabrication. The dimensional accuracy of the printing process was evaluated by calculating the dimensional error for critical geometrical parameters from Equation 4.1 and the results are shown in Table 4.4.

Table 4.4 Theoretical and experimentally measured dimensions and dimensional error of short hollow microneedles (Ellipsis300150) printed by SLA and DLP. Experimentally obtained dimensions are given in mean \pm SD.

	Dimension (μm)		%Printing Error
	Design	Printed DLP	
Height	500	501.67 \pm 0.33	0.33
Width \emptyset	500	506 \pm 1.20	1.20
Tip \emptyset	50	71.2 \pm 42.40	42.40
Length of opening	300	280 \pm 6.67	6.67
Width of opening	150	149.5 \pm 0.33	0.33

The dimensional fidelity of the DLP printed hollow microneedles was verified. The dimensional discrepancy of the length of the opening reoccurred. However, the microneedle tip formation was not precise, highlighting the significance of printing in an angle. Indeed, the high resolution of the DLP technology offered a major benefit: a significant improvement in microneedle sharpness. The DLP-fabricated microneedle tip was substantially smaller due to the better resolution of the technology; nevertheless, the effect of printing angle was still shown to play a dominant role. Both designs tested featured a tip of 50 μm in diameter. When printed with SLA at 45° the tips obtained were around 80 μm , however when printed with DLP at 0° the tip was reduced at approximately 70 μm . A dramatic improvement was observed when the printing angle was set at 45°, generating a tip of 50 μm (Figure 4.7). It is noteworthy that the tip size of 50 μm is smaller than the nominal xy plane resolution of the specific 3D printer, which is 62 μm . Therefore, the primary optimisation hypothesis, initially made for laser SLA, that optimizing the printing angle enables the formation of microneedle tips that are smaller than the nominal resolution, is also verified for DLP. This is rather expected, since the DLP process, in likeness to laser SLA, also includes peeling of the structure from the bottom of the resin tank after completion of each layer. These findings confirm

the respective conclusions derived in Chapter 2 of the present thesis and verify that printing angle is a critical optimisation parameter for photopolymerisation-based 3D printing, rather than a singularity exclusive to the laser SLA process.

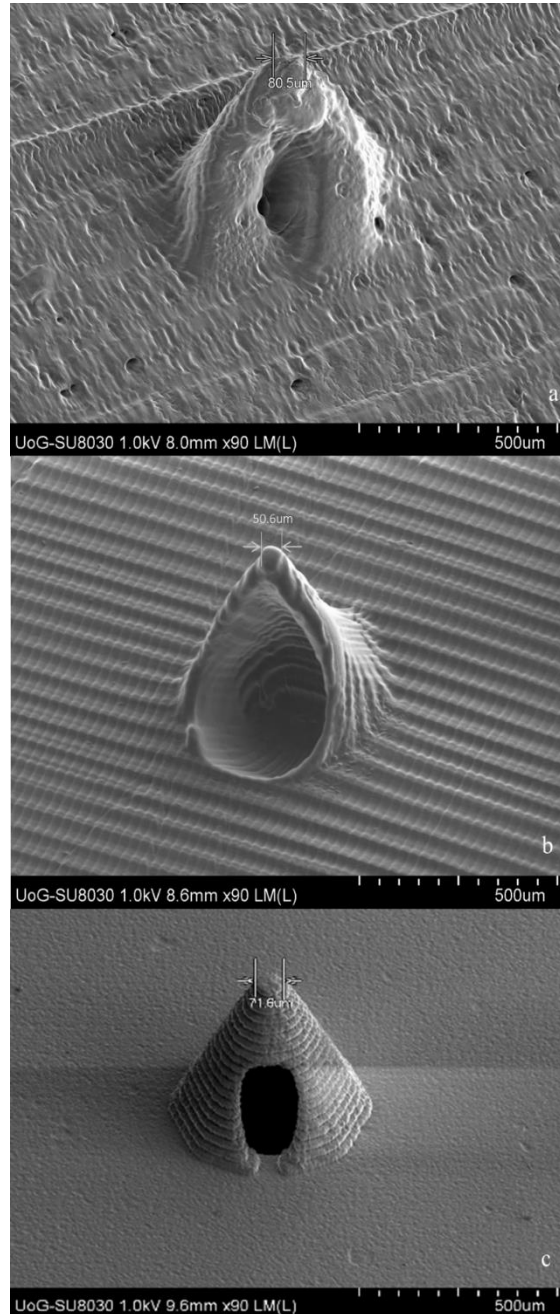


Figure 4.7 SEM images of short 3D printed microneedles (height=500 μm). (a) SLA printed Ellipsis400300, (b) DLP printed Ellipsis400300 (printing angle=45°) and (c) DLP printed Ellipsis300150 (printing angle=0°).

4.3.3 Skin insertion testing

A critical parameter of the microneedle efficiency is the size of the tip since it affects the force required to penetrate the skin, which successively influences the pain induced during application (Gill *et al.* 2008). It is therefore pertinent to ensure that the microneedles are sharp enough to require minimal loads for penetration in order to guarantee painless application. A common drawback associated with hollow microneedles is their reduced strength compared to solid microneedles that can hamper their performance (Davis *et al.* 2004). This was investigated by performing insertion tests in porcine skin whilst recording the forces developed during piercing.

For the tall hollow microneedles, SEM images revealed uniform tips of approximately 100 microns in diameter (Figure 4.4). The skin insertion behaviour of the specific tip size was previously investigated for solid microneedles (see section 2.3.4), showing effective piercing capabilities under minimal external loads (<40 mN per needle). The experimental data depicted in Figure 4.8a are consistent with the respective findings of Chapter 2; the force-displacement curves for both solid and hollow microneedles present a constant slope at the beginning of the experiment which is associated with the elastic deformation of the skin prior to any tearing. With the increase of the applied force, the slope changes although the loading remains below the threshold of 20 N, under which the skin tissue is considered purely elastic (Pailler-Mattei, Bec and Zahouani 2008). This finding is attributed to the gradual tearing of the skin until a threshold force is reached, an event represented by a discontinuity of the curve and a drop of the force. The load increased with a steep slope after the insertion, due to the compression of the skin-microneedle system against the testing probe and supporting plate, in accordance with respective literature (Davis *et al.* 2004). The hollow microneedles exhibited a similar piercing behavior to the respective solid cones, requiring insertion forces of 33 ± 2 mN per needle. The microneedles were visually inspected post-testing and no failure was reported. The skin sample was visually examined, and fine pores were observed on the piercing area (Figure 4.8b).

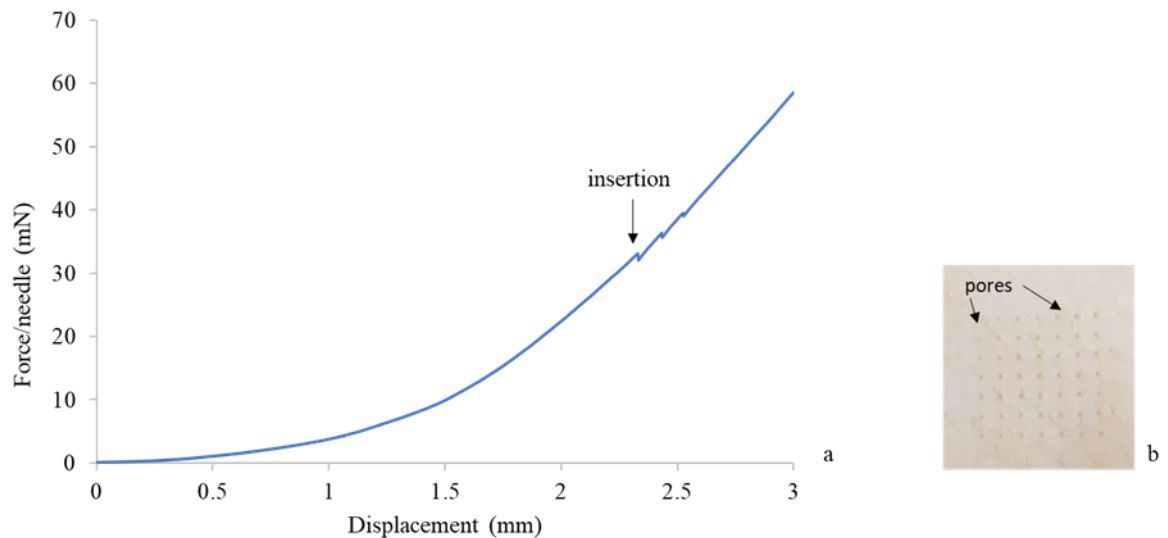


Figure 4.8 Piercing test of tall hollow microneedles. a) Force vs displacement curve obtained from microneedle insertion in porcine skin using a Texture Analyzer and b) pores in porcine skin after test.

For the short hollow microneedles, the piercing behaviour varied. Although the DLP microneedles were sharper than the tall hollow ones and thus a lower piercing force was expected in agreement with literature (Khanna *et al.* 2010), the differences in piercing forces were statistically insignificant ($p < 0.05$). This effect was attributed to the short height of the DLP microneedles ($500 \mu\text{m}$) and the fact that the skin sample is not absolutely flat. As the short shafts proceeded to elastically deflect the skin, due to their short height the substrate and probe came in contact with the skin directly. As a result, the force increased until the skin was compressed tightly between the microneedles and the fixed probe of the Texture Analyser, without de facto skin insertion. The initial portion of the curve (Figure 4.9a) corresponds to elastic compression of the skin tissue, not only by the microneedles but also directly by the substrate. At some point the skin sample is flattened under the external load and the microneedles start to tear the skin, until abrupt insertion, identified by the discontinuity in the curve. Indeed, the same behaviour was detected for the short hollow laser SLA microneedles, with significantly higher piercing forces, due to their decreased sharpness (Figure 4.9a). For the short DLP microneedles the piercing force/needle was identified as $34 \pm 5.7 \text{ mN}$ while for the laser SLA microneedles it was $56 \pm 3.2 \text{ mN}$.

The fact that insertion actually occurred was supported solely by the discontinuity of the curve, since pores were not obvious by simple visual inspection (Figure 4.9b). The

'knee'-like discontinuity of the slope cannot be interpreted differently, since such effects do not appear when piercing does not occur. This was verified by Khanna *et al.*, that conducted skin insertion testing without the microneedle patch (i.e., compression of the skin tissue) to evaluate whether any disruptions appear in the force-displacement curve. As expected, the curve exhibited no discontinuities or abrupt slope changes, in contradiction to the respective experiments with microneedles (Khanna *et al.* 2010).

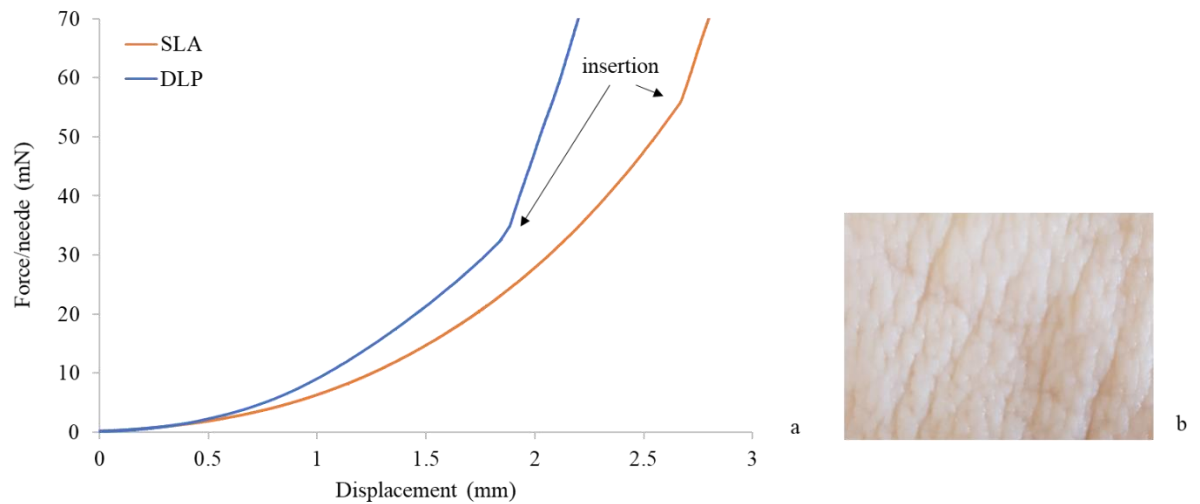


Figure 4.9 Insertion testing of short hollow microneedles printed with SLA and DLP in porcine skin. (a) Force vs displacement curve and (b) post printing image of the porcine skin sample.

The advantage emanating from the findings of the insertion testing is twofold. The microneedle insertion force has been found to be directly related to the pain experienced by the patient upon application (Gill *et al.* 2008), hence low insertion forces is a promising indicator that the proposed hollow microneedles will cause minimal or no pain. On the other hand, minimal insertion loads facilitate self-application without the need of an applicator or the intervention of a healthcare professional. This is particularly beneficial because it increases patient-compliance and reduces treatment costs.

4.3.4 Axial force compression testing

Microneedle damage during application is a highly undesirable event, likely to cause complications to patient health. Although there was no microneedle failure or damage reported during the piercing tests, to further evaluate the safety of the patches the mechanical performance of the microneedles was assessed. Axial force compressive

testing was carried out on both tall and short hollow microneedles, the latter printed with both laser SLA and DLP printing technologies. The microneedles were compressed against a flat metal plate and force-displacement curves were recorded.

The mode of failure of the tall hollow microneedles was exhibited by fracturing at the base of the cone in the direction perpendicular to the loading axis. The identical dimensions of the tall hollow and solid cone microneedles developed in the framework of this thesis, in respect to height, width and tip, allow their direct comparison in terms of mechanical behaviour (Chapter 2.3.5). It is seen thus that the mode of failure of the hollow microneedles differs from the respective fracture behaviour of the solid cone microneedles that failed gradually in the direction parallel to the loading axis. This conclusion, deduced from visual observation during experimentation is consistent with the different trends of the force-displacement curves recorded for the respective designs as seen in Figure 2.8 and Figure 4.10. Although the two curves follow different trends overall (force increases with a notably smaller slope for the hollow compared to the solid), both curves showed an initial linear segment that corresponds to the loads that the microneedles withstood without plastic deformations. This linearity designates a load range within which the microneedles maintain their structural integrity. For the tall hollow microneedles, the threshold of linearity is identified at approximately 2 ± 2.8 N per needle. As expected, the solid microneedles were able to withstand higher loads before yield compared to the hollow ones; however, the yield point for the hollow design corresponded to forces that are well above the respective loads required for insertion to skin.

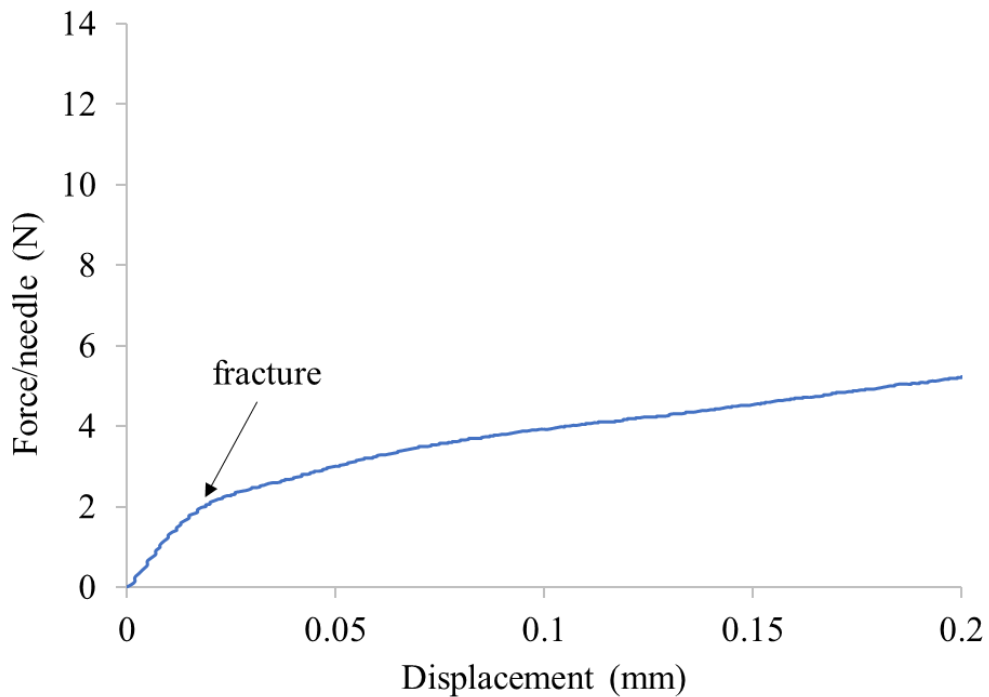


Figure 4.10 Force per needle vs displacement curve from fracture testing of tall hollow microneedles.

Respective tests were conducted for the short hollow microneedles (Ellispis400300) built with both SLA and DLP technologies. The mode of failure was similar for the two technologies, evinced by similar trends of the force-displacement curves (Figure 4.11). An easily distinguishable discontinuity, consistent with the point of fracture, was not apparent. There was a likelihood that the data acquisition resolution of the testing machine was not sufficient to capture the delicate changes in force, produced by the cracks propagating within the fine 500 μm microneedles. The fracture load was derived by linear regression of the curve (intercept at 0,0), at the point where the slope changed, in accordance with the method described for the tall hollow microneedles. For the DLP microneedles the fracture force per needle was estimated at 1 ± 0.5 N and for the SLA, at 1.5 ± 1.1 N. The morphology of the shafts, with the different sizes of the opening due to the technology-related dimensional discrepancies shown above, is likely the reason behind the SLA microneedles withstanding higher forces.

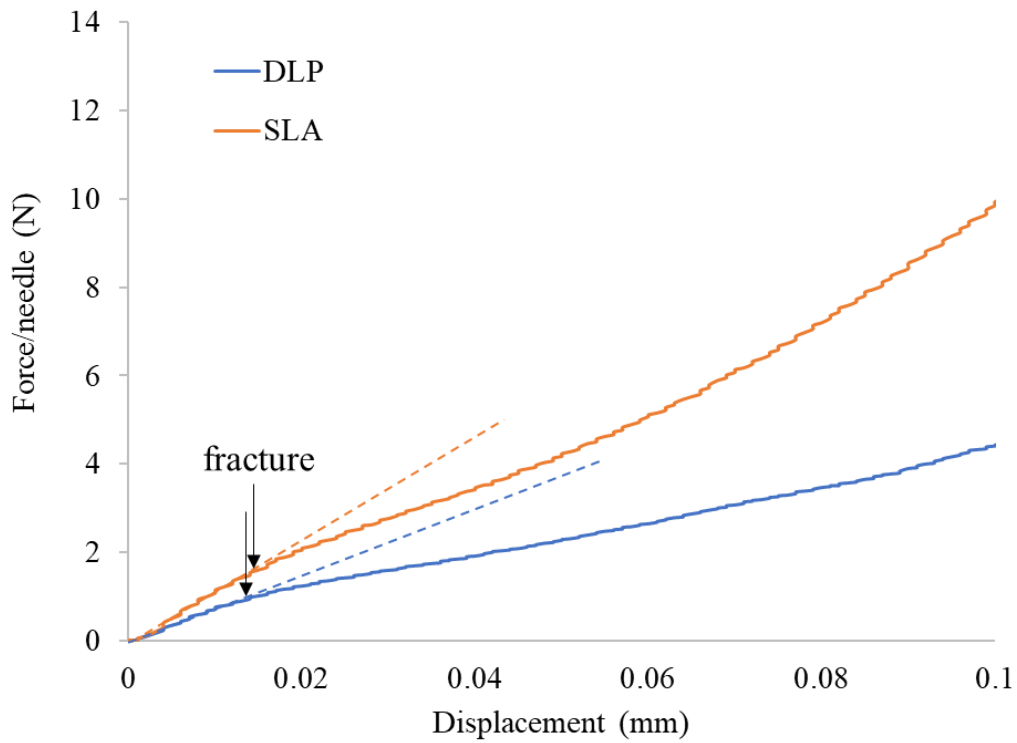


Figure 4.11 Force per needle vs displacement curve from fracture testing of short hollow microneedles printed by laser SLA and DLP. Dash lines are linear regressions of the initial segment with intercept at (0,0).

4.3.6 Margin of safety

Combining the data derived from the piercing and axial force compression tests, the margin of safety, which is defined as the ratio of the fracture force to the insertion force was calculated, using Equation 4.2 (Prausnitz 2004). The results, along with the mechanical properties calculated from the previous tests are displayed in Table 4.5.

Table 4.5 Mechanical properties and margin of safety of tall and short 3D printed hollow microneedles.

Microneedle geometry		Piercing force (mN)	Fracture force (N)	Margin of safety
Tall	SLA	33 ± 2	2 ± 2.8	61
Short	SLA	56 ± 3.2	1 ± 0.5	27
	DLP	34 ± 5.7	1.5 ± 1.1	29

Given that all numbers are significantly higher than 1, the safety of the microneedles is reassured. Furthermore, the aforementioned values are significantly higher compared to respective findings in literature. Forvi et al. reported margins of safety ranging between 6 and 9 for solid silicon microneedles (Forvi *et al.* 2010), while Davis et al. calculated values between 5 and 20 for polymeric hollow MNs (Davis *et al.* 2004). The comparatively increased margins of safety of the microneedles proposed in this study are attributed to the high strength of the polymers (Formlabs 2016; DETAX 2019) and the ability of the microneedles to pierce the skin under minimal applied forces.

4.3.7 Development of complex microneedle patch with microfluidic internal structures

To enable the connection of the hollow microneedles with the fluid source and a flow instigator, the development of a complex patch was put forward. The concept involved the design of a combination system that comprised 3 segments: a) the microneedles with their bores, elongated to microchannels within the substrate, b) an internal circulation system that disseminates the fluid to the microneedle bores and c) a fluid entry nozzle. The fluid entry nozzle was designed to fit tightly with typical commercial syringes. Two types of internal circulation systems were examined, by investigating their printability with laser SLA and DLP. The printing outcome was assessed by visually examining the fluid circulation within the internal structure and its ejection from the microneedle openings.

The prominent challenge when printing one-piece devices with microfluidic-like networks is avoiding blockages. Such issues occur when thorough cleaning of the internal cavities is troublesome, resulting to unpolymerised resin residues remaining after printing, that solidify during post-printing curing. This phenomenon is intensified when the resin has high viscosity (Bhattacharjee *et al.* 2016). Evidently, the 3D printing industry has attempted to tackle this problem and broaden the use of 3D printing for microfluidics by introducing low viscosity resins specifically for such applications. Gong *et al.* conducted a study on 3D printed microfluidics, testing custom and commercial resins with viscosities ranging from 57 to 1262 mPa s. The study concluded that resins in the higher viscosity range generated narrower microfluidic channels (Gong *et al.* 2015). Therefore since the Dental SG has a viscosity of 800–1500 mPa s (Formlabs 2016), its suitability for the fabrication of microfluidics was viewed with skepticism. However, the biocompatibility of the material was considered a prerequisite in the framework in this study, limiting the selection of materials strictly to biocompatible ones, that typically have higher viscosities.

The first design that was composed featured an internal reservoir. Its role was to receive the fluid entering from the entry nozzle and disseminate it to the microchannel extensions of the microneedle bores. The engineering designs along with captions of the 3D virtual model sectioned in critical planes are displayed in Figure 4.12.

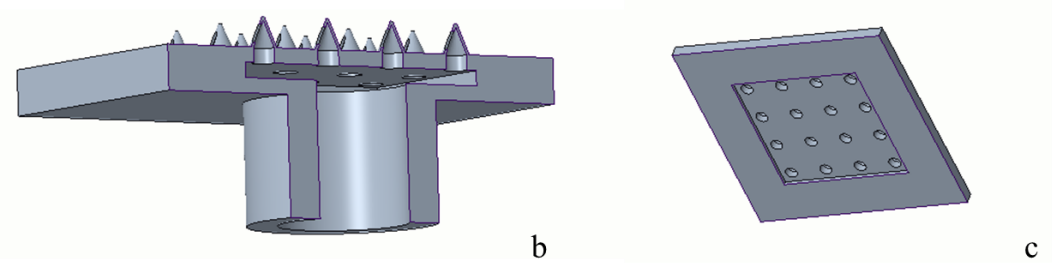
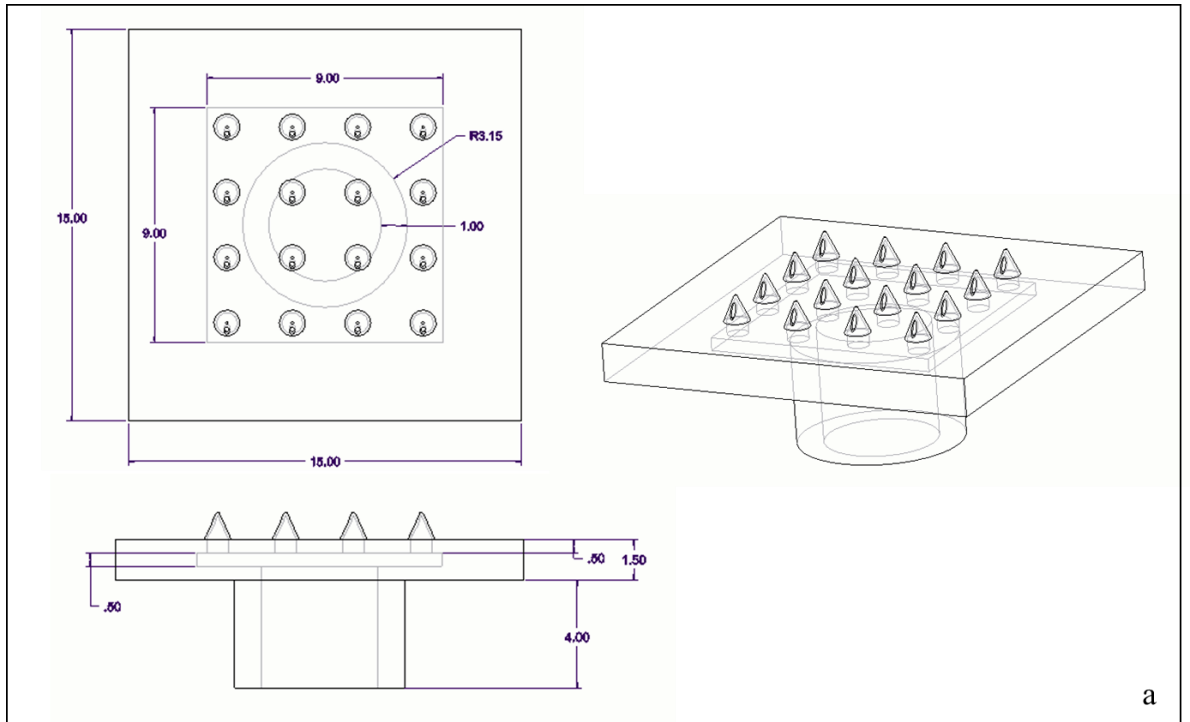


Figure 4.12 Complex microneedle patch for fluid entry and circulation with internal reservoir. (a) Engineering designs. Virtual 3D model sectioned at (b) a plane parallel to the microneedle height and (c) the plane perpendicular to the patch thickness, at the height of the reservoir.

The patch was printed through laser SLA at 45° to printing platform. By trial and error, it was found that one of the most important steps of the post-printing treatment was the drainage of resin residues from the internal structures prior to curing.

When not washed thoroughly via pressure-driven isopropanol flow through a standard syringe, obstructions occurred. Such defects did not only appear within the finer structures (e.g., microchannels below the microneedle bores) but also within the reservoir, especially closer to the edges. Meticulous application of the described process generated unobstructed internal cavities, allowing the ejection of liquid from all microneedles, as evinced by the images displayed in Figure 4.13.

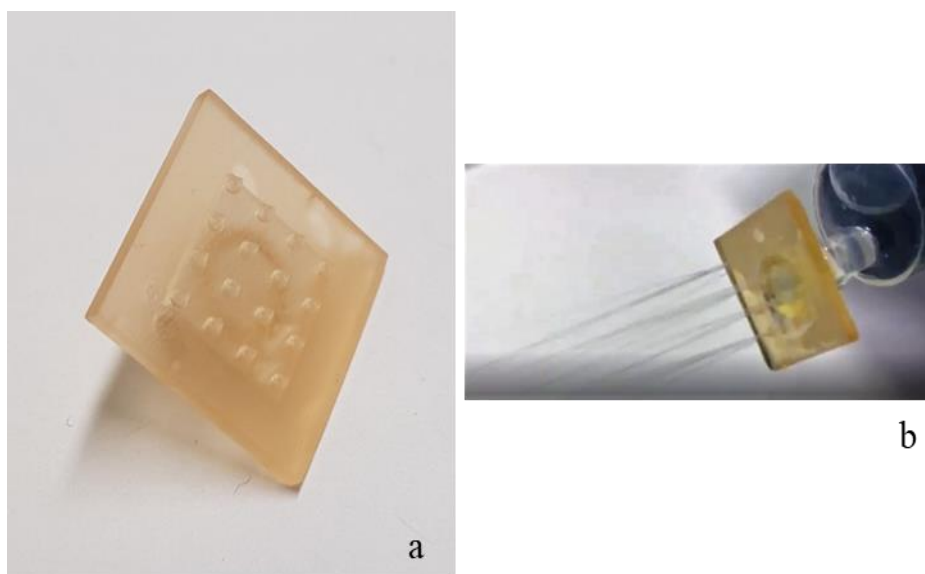


Figure 4.13 Digital images of the complex microneedle patch with internal reservoir printed with SLA. (a) Post-curing image and (b) ejection of fluid from the microneedles.

In general, all hollow microneedle delivery systems similar to the one proposed here, have an inherent disadvantage: a small amount of drug will remain within the internal microstructures and will be inevitably discarded. The volume of solution losses (i.e., dead volume) equals to the volume of the internal cavities. The geometry of the complex patch entails by default a certain ‘dead volume’ that can be decreased by substituting the internal reservoir with a microchannel-based circulation approach. Hence, the design of a patch featuring internal microchannels was conducted and the engineering designs along with captions of the 3D virtual model sectioned in critical planes are displayed in Figure 4.14.

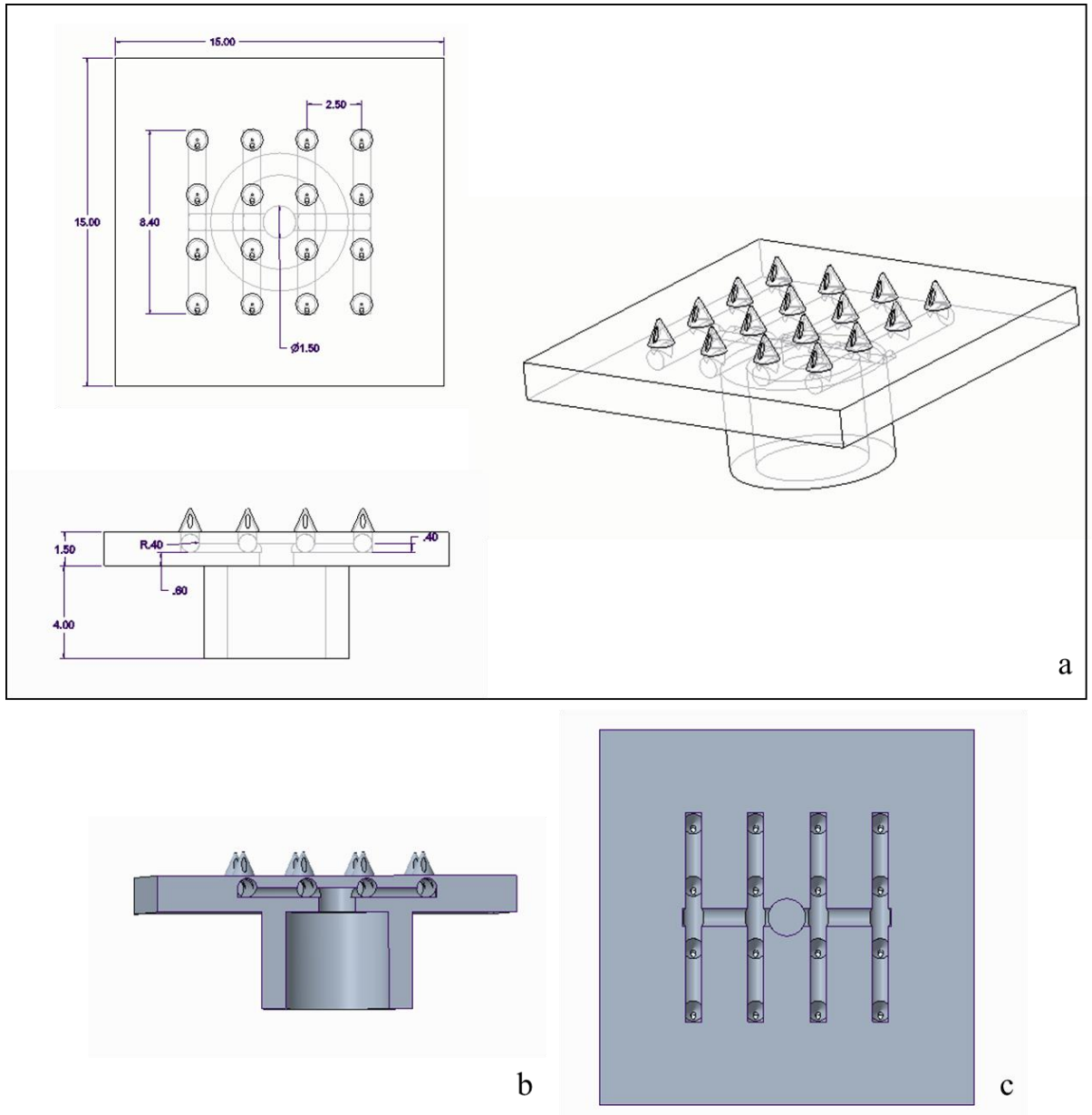


Figure 4.14 Complex microneedle patch for fluid circulation and distribution with internal microchannels. (a) Engineering designs. Virtual 3D model sectioned at (b) a plane parallel to the microneedle height and (c) the plane perpendicular to the patch thickness, at the height of the microchannels.

The microchannel patch was printed with both SLA and DLP. During post-printing cleaning of the SLA patch and prior to curing, it was immediately observed that the internal microchannels circuit was only partially formed and fluid circulation to the microneedles was obstructed. This issue is most probably the product of the above examined effect of unwanted curing in the circumference of the laser spot, due to the small diameter of the microchannels and the overlapping of the radiance distribution

tails. Figure 4.15a displays the partial formation of the channels. Their formation would potentially be feasible by increasing their diameter, however it was concluded that such a design intervention would not serve the goal of decreasing the dead volume.

On the contrary, the superior resolution of the DLP technology along with the resin drainage process described, replicated the microchannels with good accuracy (Figure 4.15b). This finding demonstrates the potential of this technology to fabricate complex microneedle patches with intricate internal circulation structures. Also the low viscosity of the biocompatible DLP resin (DETAX 2019) enabled the successful removal of residues prior to curing.

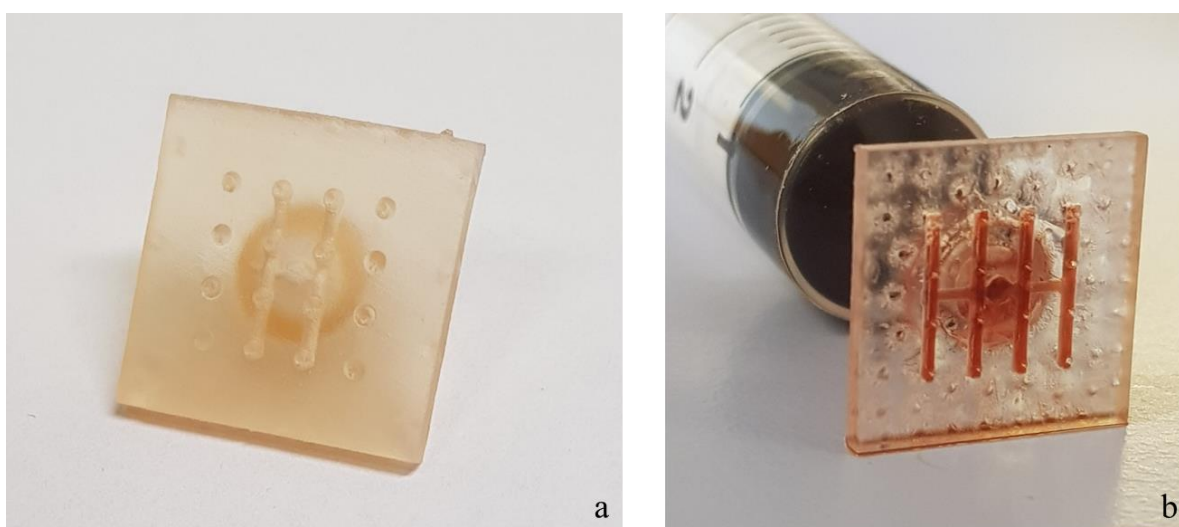


Figure 4.15 Complex microneedle patches with internal microchannel circulation systems. (a) SLA printed patch, featuring tall hollow microneedles. The formation of the microchannels was unsuccessful. (b) DLP printed patch, featuring short hollow microneedles, filled with red dye (spots are residuals of the support contact points, which are superficial on the bottom of the patch and not influence functionality).

Summarising, the studies on the printability of complex microneedle patches illustrated that each technology has varying strengths and weaknesses. Therefore, the selection of the printing technology must be done on the basis of the requirements of the application. This work has shown that for applications that require longer microneedles, multiple devices developed in one single print job, while larger drug losses are considered affordable, the SLA complex patch proposed in this study is a viable option. On the contrary, when high resolution is a prerequisite, short and sharper microneedles are clinically essential and the cost of the drug is high, the DLP technology is more suitable,

with the tradeoff that multiple print jobs must be executed to obtain a significant number of patches.

Another difference that plays an important role in choosing between the two technologies pertains to the biocompatibility of the two photosensitive materials, each compatible with the respective technology. In general, a known issue affecting the widespread adoption of 3D printing for biomedical devices is the limited selection of biocompatible, non-cytotoxic materials that are compatible with a specific printing technique. In this work, a commercial Class I biocompatible resin was employed for the laser SLA printed microneedles. The biocompatibility of the polymer, having been printed on a Formlabs and post-cured, has been found to conform with multiple ISO biocompatibility standards and is certified as USP IV (Vertex 2016), which reassures that no toxic effects were observed in acute systemic toxicity and intracutaneous testing. The claim was further supported by additional, respective studies (Kurzman *et al.* 2017; Kreß *et al.* 2020). The printed polymer is also autoclavable, meaning that the microneedles can be sterilised. On the other hand, the material used for DLP has been classified as Class II, while is also autoclave sterilisable according to ISO 17664 (DETAX 2019). From the regulatory perspective, Class II medical devices require extra special controls. Evidently, additional cytotoxicity research is required, specialised on the transdermal application of the specific material.

4.4 CONCLUSIONS

The design, manufacturability and quality optimisation of hollow microneedles and hollow microneedle microfluidic patches, fabricated by 3D printing were studied. Two commercial photopolymerisation 3D printers, a laser SLA and a DLP, were employed and their performance was assessed and compared. The effect of resolution on the end-product quality, as the critical manufacturing restriction, was investigated by a series of printing trials. This is inevitable when the printing resolution boundaries are challenged by attempting very fine details, since, to the author's knowledge, there is no scientifically systematic way to predict printing outcomes. For microneedles, the central variable was the formation of the opening and its dimensional fidelity to the virtual design and for complex microfluidic patches, the success criterion was the formation of the internal structures, and the ejection of solution from the microneedle openings.

Tall hollow microneedles (height=1000 μm) were successfully fabricated by laser SLA, only when the opening was designed at the lateral surface. The effect of unwanted additional solidification due to overlapping of the radiance distribution tails when the laser spot polymerises lines in close proximity, was found to cause dimensional discrepancies and blockages of the opening. Hence, the commercial SLA printer failed to generate elliptical openings smaller than 220 x 140 μm , and only when the dimensions were designed larger.

Short microneedles (height=500 μm) were fabricated with laser SLA and DLP for the first time. The comparatively superior resolution of the DLP managed to generate good dimensional fidelity to the virtual design, even for designs with smaller openings, without severe dimensional discrepancies. For DLP, optimisation of the printing angle was not found to affect dimensional fidelity for major geometrical parameters, with the only exception of the tip. The piercing and fracture behaviour of all microneedles was investigated, and all designs were found to be mechanically robust.

Complex hollow microneedle patches with internal microfluidic structures were designed and 3D printed. Internal reservoirs were reliably fabricated with laser SLA. Patches with internal conduits of microchannels were printable only by taking into advantage the high resolution capabilities of the DLP technology. Post-printing purging of the internal cavities from unpolymerised residues was critical. Solution was inserted through the nozzle of the patches, distributed to the microneedle bores through the internal microfluidic structures and ejected from the openings.

In conclusion, the present work compiled and evaluated the efficacy of a 3D printing strategy for tall and short hollow microneedles and complex patches. The findings of this study are anticipated to contribute to the adoption of such additive manufacturing technologies for transdermal drug delivery devices, featuring hollow microneedles. Further research on the integration of such systems into novel drug delivery devices is still required, an attempt which is intrinsically linked to the identification of suitable flow instigation systems. The following experimental Chapter explores the use of advanced microelectromechanical technology in combination with 3D printing for the development of a novel microneedle drug delivery device.

CHAPTER 5

3DMNMEMS

A 3D PRINTED MICRONEEDLE MICROELECTROMECHANICAL SYSTEM FOR TRANSDERMAL DRUG DELIVERY

5.1 INTRODUCTION

Personalisation of clinical care is nowadays in the spotlight of research on drug delivery. Finding new pathways that allow the individualisation of treatments will improve efficiency, patient compliance and limitation of adverse effects. ‘Personalised medicine’ is attracting worldwide interest, with sophisticated drug delivery systems being a key element (Crommelin, Storm and Luijten 2011). The use of 3D printing is a valuable tool towards this goal, since it offers the unique ability of direct and fast customisation, based on the application. The advantages of 3D printed hollow microneedles developed in the framework of this thesis, render them promising candidates for transdermal devices that allow the individualisation of the drug delivery process. Thus, in this work, a platform device featuring 3D printed hollow microneedles is developed.

In hollow microneedle drug delivery systems, the drug-containing solution must be supplied to the patch, in order to be delivered to the skin through the microneedle openings. Several approaches have been explored, which in their majority rely on passive diffusion. In such systems, the patch was either prefilled with the solution (Wang *et al.* 2006) or connected to an external reservoir (Davis *et al.* 2005). However, real control of the drug administration requires the instigation and regulation of the flow from the solution source to the patch. Active flow regulation has been achieved using the plunger of a standard syringe (Stoeber and Liepmann 2005) or through gas pressure regulators (Martanto *et al.* 2006). These approaches may fulfil their goal in the research setting, but their application can be troublesome and costly in the clinical setting.

In this work, the integration of 3D printed hollow microneedles in a device that can be readily used in the clinical setting is put forward. For this purpose, the use of a sophisticated Microelectromechanical System (MEMS) is explored. MEMS have emerged as a valuable tool to achieve controlled and accurate brain, ocular, gastrointestinal and transdermal drug delivery (Lee *et al.* 2018). Extensive work has

been done on wearable insulin pumps, nonetheless these devices must be worn constantly, and commercial insulin pumps are often avoided by diabetics due to aesthetic and practical reasons (Robertson *et al.* 2020). Moreover, MEMS have been integrated in close-loop systems where a sensor monitors the levels of a specific physiological signal and triggers the release of the respective therapeutic agent (Yu *et al.* 2017). Although such systems are intelligent and do not require the patient to proactively manage the treatment, they must be worn or implanted. Also, they are targeted to a specific application and restricted to respond to the physiological stimulus for which they have been designed, and thus not suitable for universal drug delivery. Therefore, this work proposes an adaptable, non-wearable, stimulus-independent MEMS for administration of a variety of drug-containing solutions.

5.1.1 Aims and objectives

The main objective of the present experimental Chapter is the integration of 3D printed hollow microneedles with MEMS for the development of a universal transdermal drug delivery system. The device, dubbed 3DMNMEMS, was developed with the aim of permitting the direct control of the drug administration by the user, hence enabling the personalisation of treatment. A staggered, modular approach was adopted for the development and efficacy evaluation of the device, consisting of the following research aims:

- Fabrication of a hollow microneedle patch through SLA additive manufacturing, exploiting the research outcomes of Chapter 4 of the present thesis.
- Integration of the complex patch with a MEMS, in a simple, user-friendly device and evaluation of its accuracy in terms of the administered liquid volume.
- Visualisation of the liquid distribution instigated by the device within skin tissue in real time. To achieve this, the use of sophisticated optical imaging techniques was put forward to elucidate whether the pumped liquid disseminates or accumulates in depots.
- Evaluation of the novel 3DMNMEMS in terms of customised drug delivery *in vitro*, administering a model hydrophilic molecule in different dosages as well as insulin.
- Investigation of the device performance in treating diabetes by administering insulin to diabetic animals.

5.2 MATERIALS AND METHODS

5.2.1 Materials

The material used was a biocompatible Class I photopolymer Formlabs Dental SG (GoPrint3D, North Yorkshire, UK). The insulin (aspart, Novorapid) was bought from Novo Nordisk (London, Crawley, UK). The sodium fluorescein and Saline Phosphate Buffer (PBS) pH 7.4 were acquired from Sigma-Aldrich (Gillingham, UK). Streptozotocin ($\geq 75\%$ α -anomer basis, $\geq 98\%$) and citric acid were both purchased from Merck Chemical Co. (Darmstadt, Germany). All solvents were of analytical grades.

5.2.2 Fabrication of the hollow microneedle patch

The design and manufacturing process developed in Chapter 5 was followed. The complex patch featuring tall (height=1000 μm) hollow microneedles and an internal reservoir was chosen. The number of microneedles was reduced to 4 in a 2×2 symmetrical configuration and hence the internal reservoir was reduced at $3.5 \text{ mm} \times 3.5 \text{ mm} \times 0.5 \text{ mm}$. A laser SLA (Form2, Formlabs, MA, USA) was used for the fabrication of the complex patches. Post-printing, the patches were purged in isopropanol bath. Unpolymerised resin residues were drained from the internal cavities through pressurised flow of isopropanol, using a standard syringe. The patches were dried overnight and cured in a heated UV chamber (MeccatroniCore BB Cure Dental station, GoPrint3D, UK), at 40°C for 60 minutes.

5.2.3 Microelectromechanical System (MEMS)

For this study, a customised diaphragmatic microdosing pump was employed (Bürkert Fluid Control Systems, Ingelfingen, Germany). The system requires connection to an electric source of 24 V that can either be supplied through a standard power source and transformer or batteries for portability. The MEMS was designed to pump single strokes of defined volume of a few microliters while allowing the tailoring of stroke frequency, mode of flow and final amount supplied.

The stroke volume accuracy supplied by the MEMS was determined using a simple method. Single strokes of a solution of known concentration of sodium fluorescein salt were pumped into volumetric flasks and then diluted with deionised water. The solutions were then analysed via UV/Vis spectrophotometry to quantify the

experimental concentrations, which were then used to calculate the experimental single-stroke output. The results were compared to the expected (theoretical) concentrations based on the 5 μL value given by the manufacturer. The experiment was performed in triplicate and the single stroke volume % error was calculated by Equation 5.1:

$$\%error = \frac{|v_{theor} - v_{exp}|}{v_{theor}} 100 \% \quad \text{Equation 5.1}$$

Where v_{theor} and v_{exp} the theoretical and experimental volumes of a single stroke.

5.2.4 X-ray Micro Computer Tomography

X-ray Micro Computer Tomography (μCT) scans were performed on the 3D printed hollow microneedle patch. The equipment employed was a Bruker Skyscan 1172, with an SHT 11 Megapixel camera and a Hamamatsu 80 kV (100 μA) source. The samples were mounted vertically on a portion of dental wax and positioned 259.4mm from the source. No filter was applied to the X-Ray source and a voltage of 80 kV was applied for an exposure time of 1050 ms. The images generated were 2664 \times 4000 pixels with a resolution of 6.75 μm per pixel. The images were collected, and a volumetric reconstruction of the sample generated by Bruker's CTvol software. The threshold for this attenuation signal was set manually to eliminate speckle around the sample, and then further cleaned with a thresholding mask using Bruker's CTAn software.

5.2.5 Preparation of porcine skin samples

Full-thickness abdominal porcine skin was collected from a local slaughterhouse (Forge Farm Ltd., Kent, UK) and was then shaved using a razor blade. The fatty tissue below the abdominal area was removed using a scalpel. The skin was pinned onto a polystyrene block and wiped with ethanol (70%). Samples of 1.0 \pm 0.1 mm thickness were extracted by applying a Dermatome (Padgett Dermatome, Integra LifeTMSciences Corporation, USA) at an angle of $\pm 45^\circ$. The thickness of the skin was measured using a caliper and 20 \times 20 mm tissue samples were cut using a scalpel. The skin samples were placed onto filter paper soaked in a small amount of saline phosphate buffer (pH 7.4) for 2 h. The Dermatome-treated skin samples were employed for OCT and *in vitro* release studies.

5.2.6 Optical Coherence Tomography

The Optical Coherence Tomography (OCT) system used in this study employs a swept-source operating at a central wavelength of 1050 nm with a tuning range of roughly 100 nm, and has been described elsewhere (Marques *et al.* 2018). The axial/lateral resolutions of this system during imaging were roughly 10 μm and 15 μm , respectively, with a lateral field of view of $25 \times 25 \text{ mm}^2$. OCT data was processed using the Complex Master/Slave (CMS) method (Rivet *et al.* 2016), which allowed for direct visualisation of the structures being imaged. The 3DMNMEMS device was manually compressed against a sample of full-thickness porcine skin so that the microneedles were inserted into the tissue. A solution of powdered milk in water was pumped and a series of consecutive scans in equal time intervals were recorded.

5.2.7 *In vitro* release studies in porcine skin

The ability of the 3DMNMEMS device to disrupt the skin barrier and deliver molecules *in vitro* was assessed using Franz diffusion cells (PermeGear, Inc., PA, USA). Dermatomed porcine skin with a thickness of $1.0 \pm 0.1 \text{ mm}$ was employed. The skin samples were mounted on the donor compartments of a Franz diffusion cell array. The temperature of the Franz cells was maintained at $37 \text{ }^\circ\text{C}$ using an automated water bath (Thermo Fisher Scientific, Newington, USA). The microneedle patch, fitted on the MEMS, was pressed to the skin to ensure insertion. Thereafter, the MEMS was set to administer a solution of sodium fluorescein salt in deionised water (2 mg/mL). Three different pumping regimes were implemented, consisting of 1, 2 and 4 serial single-stroke cycles, resulting in three different dosages: $5 \mu\text{L}$, $10 \mu\text{L}$ and $20 \mu\text{L}$, respectively. For the samples receiving 2 and 4 strokes, fixed time intervals of 2 s were maintained between each individual stroke. Sample fractions ($6\text{--}6.5 \text{ mL/h}$) were collected every 10 minutes using an auto-sampler (FC 204 fraction collector, Gilson, USA) attached to the Franz diffusion cells system. The experiment was repeated administering $10 \mu\text{L}$ (2 strokes) of insulin (100 IU/mL) as a bolus dose in porcine skin, and its permeation was studied for 1 hour. Statistical analysis for the drug release was performed with a Mann-Whitney nonparametric test and t-test analysis for the *in vitro* studies (InStat, GraphPad Software Inc., San Diego, CA, USA), where samples were considered as statistically significant at $p < 0.05$.

5.2.8 UV/Vis Spectrophotometry

The absorption spectra generated by the fluorescein sodium solutions were obtained employing 10 mm path length cuvettes in a Perkin Elmer Lambda 365 at a nominal resolution of 1 nm. The spectra were recorded at room temperature (20°C), using deionised water as reference. The corresponding spectrum of water was subtracted from the recorded spectra. The corrected spectra were used to quantify the concentration of sodium fluorescein salt in the samples. The quantification was done on the basis of a calibration curve, developed by analysing 5 standards (1, 2, 3, 4 and 5 µg/mL). The standards were created by dilution of a stock solution (10 µg/mL) of fluorescein salt in deionised water.

5.2.9 High-performance liquid chromatography (HPLC)

The amount of insulin collected from the receptor fluid of the Franz cells was determined by HPLC (Agilent Technologies, 1200 series, Cheshire, UK) equipped with a Phenomenex Jupiter 5u c18 300 Å, LC Column (250×4.60 mm, particle size 5 µm, Macclesfield, UK). The mobile phase consisted of water with 0.1% Trifluoroacetic Acid (TFA) and acetonitrile with 0.1% TFA (66:34 v/v), with a 1 mL min⁻¹ flow rate. The column was equilibrated at 35 °C, the injection volume was 20 µL and the eluent was analysed with a UV detector at 214 nm. The results were integrated using Chemstation® software and the samples were analysed in triplicates.

5.2.10 *In vivo* clinical studies

The effectiveness of the 3DMNMEMS device to administer insulin *in vivo* was tested on Swiss albino female mice. Before the start of the study, all animals, weighing 120 ± 10 g, were given free access to solid bottom cages with controlled diet for 3 days. To create a diabetic animal model, diabetes was chemically induced by a single subcutaneous injection of streptozotocin (70 mg/kg) in citric acid buffer (pH 4.5), in the flank. The induction of diabetes was confirmed by measuring the fasting blood glucose at scheduled times using a one-touch glucometer (ACCU-CheckVR Active, Roche, Germany), with mice that presented blood glucose higher than 300 mg/dl to be rendered diabetic. 24 h before experimentation, the diabetic animals were anaesthetised and shaved on the area of 3DMNMEMS device application, using an electric razor

(Panasonic, USA). Finally, the animals were fasted for 12 h, receiving only water ad libitum.

On the day of experimentation, the animals were divided into 3 groups (n=6 each):

1. Untreated (negative control), received no treatment
2. SC (positive control), received 0.5 IU/animal via subcutaneous injection
3. 3DMNMEMS, received 0.5 IU/animal via the 3DMNMEMS

The animals treated with the 3DMNMEMS device were held gently while the microneedle array was applied on the shaved dorsal area using manual finger pressure to reassure insertion. The MEMS, connected to batteries for ease of handling, was then fitted to the patch. The aforementioned amount of fast-acting insulin was supplied, in the form of a bolus dose, to imitate the typical subcutaneous injection treatment regime and allow the comparison thereof. After administration, the system was removed immediately. For all animal groups, blood samples from the jugular vein were collected at 0, 1, 2, 3, 4, 5 and 6 h after the insulin administration and the blood glucose values were extracted, using the glucometer. Approximately 50 μ L of plasma was collected from the collected blood samples by centrifuging at 5000 rpm for 15 min. Plasma insulin concentrations were analysed using an insulin-ELISA Test kit (Diagnostic Automation Inc., CA, USA).

All animal experiments throughout this study were approved by the Research Ethics Committee (reference number 0003/17, Department of Pharmacy, Southern University Bangladesh) and conducted according to the Southern University Bangladesh policy for the protection of Vertebrate Animals used for Experimental and Other Scientific Purposes, with implementation of the 3Rs principle (replacement, reduction, refinement).

5.3 RESULTS AND DISCUSSION

5.3.1 The 3D printed microneedle patch

Following the design and 3D printing strategy established in Chapter 5, a complex patch featuring a nozzle at its base and an internal reservoir as the connection pathway to the microneedle bores, was manufactured. The engineering designs illustrated in Figure

4.12 were edited to feature 4 hollow microneedles in a 2×2 symmetrical configuration and a respectively smaller reservoir of 3.5 mm × 3.5 mm × 0.5 mm. Figure 5.1 schematically depicts the adapted microneedle patch.

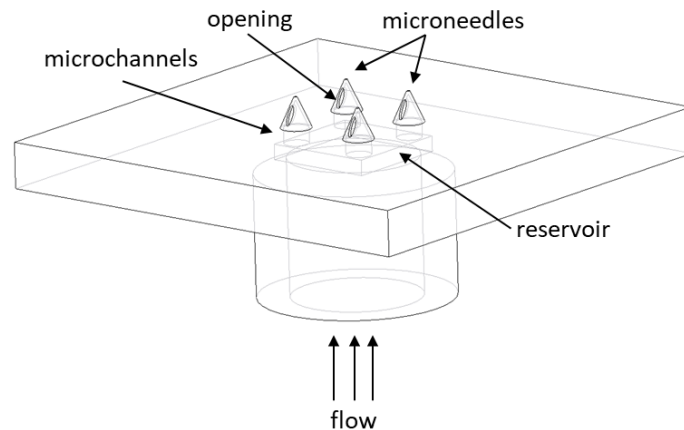


Figure 5.1 Hollow microneedle complex patch for integration with the MEMS

By reducing the dimensions of the internal reservoir, the dead volume of the patch decreased accordingly. Taking into consideration the geometrical dimensions of the internal cavities (i.e., reservoir, microchannels, bores) the dead volume of the patch was calculated at 8 μL . This volume is required to fill the patch prior to administration, while an equal amount will remain within the internal cavities post-application.

Tall microneedles featuring a height of 1000 μm (Ellipsis600200, the engineering designs are depicted in Figure 4.4) were chosen, to reassure that a sufficient penetration depth is reached during application. The specific microneedles have been found to penetrate the skin under minimal external forces, while withstanding comparatively high forces until fracture (see Sections 4.3.4 and 4.3.5). Indeed, their margin of safety was found to be significantly higher than 1 (see Section 4.3.6), which is encouraging evidence regarding to the mechanical robustness of the microneedles upon application to the skin. The laser SLA technology was selected for the printing of the microneedles due to its less laborious nature (larger printing volume allows for the simultaneous fabrication of numerous patches) and its cost-effectiveness. Since the developed patch was intended for animal testing, a determinant factor was also the biocompatibility of the laser SLA photopolymer, that is classified as Class I.

It is noteworthy that the complex patch was designed to secure a tight fit between the nozzle of the patch and the micropump, in order to prohibit liquid losses at the point of connection. This assembly approach also allows the easy attachment and changing of the microneedle patches between uses.

5.3.2 X-ray Micro Computer Tomography (μ CT)

X-ray μ CT was employed for the visualisation of the 3D printed patch and the investigation of internal and external imperfections that could impair the performance of the patch. Initially, the patch was imaged in its entirety, to investigate the defects on the outer surfaces of the microneedle patch. Such superficial defects may include structural flaws such as holes and cracks on the substrate, microneedle breakage etc. that can hamper the performance of the patch in the clinical setting. Reassuring that there are no such issues is an essential quality control step. Figure 5.2a depicts that the patch is free from observable superficial defects.

As demonstrated previously, an innate drawback of SLA printing of structures that feature internal cavities is associated with imperfect drainage of unpolymerised resin residues. In this event, the residues solidify during post-printing curing and can partially or fully block the internal channels and reservoir and thus hamper the fluid delivery. To investigate the quality of the internal cavities and reassure uniform dispersion of the solution supplied by the MEMS, μ CT was employed as a sophisticated, non-destructive technique to image the internal geometry. Figure 5.2b illustrates a perpendicular cross-section of the patch along the central axis of two microneedles; it is evident that the internal surface appears smooth with no polymerised residues and blockages in microneedle bores, internal tank and tubular opening. This is further verified by the scan of the horizontal cross-section at the base of the microneedles, where the bores are shown circular without significant alterations to their geometry caused by solidified residues (Figure 5.2c). These findings suggest that there are no imperfections to the patch introduced by the printing technology that can affect its performance as a drug delivery system.

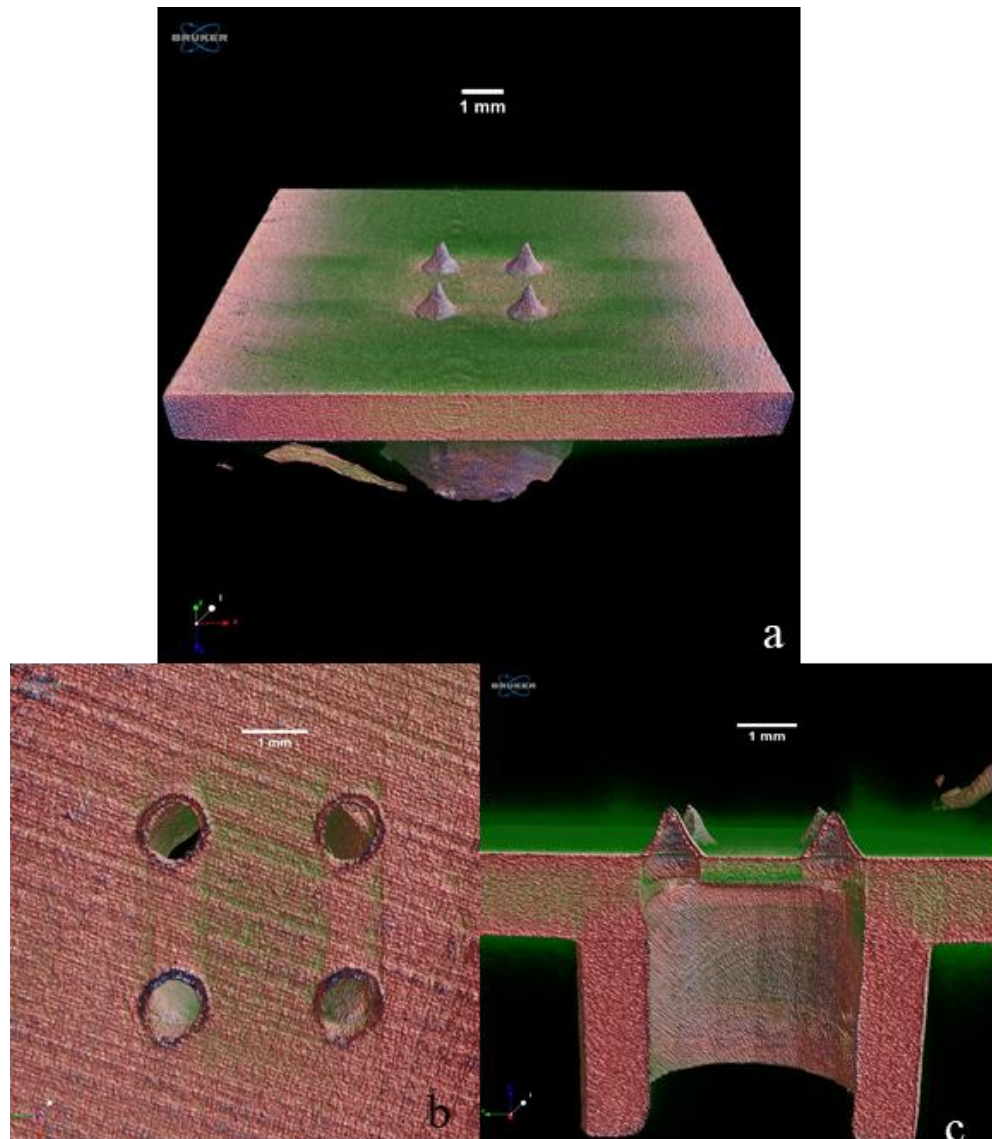


Figure 5.2 μ CT images of the hollow microneedle patch. (a) Caption of the whole patch, (b) tomographic caption of the horizontal cross section below the microneedle bores and (c) tomographic caption of the perpendicular cross section, sectioning along the longitudinal axes of the microneedle shafts. The images reveal that internal structures have been printed accurately and no internal blockages will obstruct fluid circulation.

5.3.3 Development of the 3DMNMEMS and accuracy evaluation

The main goal of this study was to create a new platform drug delivery device, combining 3D printed microneedles and a MEMS. The rationale behind selecting a

MEMS over other strategies to stimulate flow through hollow microneedles, such as coupling with typical syringes (Stoeber and Liepmann 2005; Mansoor *et al.* 2013), was to accomplish high dose accuracy and reproducibility. Hence, a diaphragmatic micropump was chosen as the MEMS due to its small, compact design and its electrical autonomy (can operate on batteries). Most importantly, the micropump enables the tailoring of the delivery process by the user through simple settings, while its handling is effortless and user-friendly.

The MEMS was designed to pump very small volumes of fluid, down to a few microliters, with a defined volume per stroke, allowing the tailoring of frequency (from 5 up to 40 Hz) and mode of dosing (continuous, single stroke etc.). The micropump featured three valves operating as the inlet, outlet and pumping diaphragm valves and is designed to pump strokes of 5 μL in volume.

Inaccuracies of typical drug delivery methods such as syringes or pen-injectors, especially for small dosages, have been well-documented (Gnanalingham, Newland and Smith 1998). To verify the accuracy of the MEMS in regard to the volume of a single stroke, a simple method was developed using a fluorescein salt solution of known concentration. Single strokes of the solution were pumped into volumetric flasks and then diluted with deionised water. UV/Vis spectrophotometry measurements generated the respective experimental concentration, which was used to calculate the single stroke volume that was initially pumped into the solution (v_{exp}). The experimental volume was compared to the theoretical volume, v_{theor} , of 5 μL according to the manufacturer.

The error was calculated as $7.9 \pm 0.82\%$ from Equation 5.1. The value was used to correct the calculations throughout this study, so they correspond to the real volumes supplied by the MEMS. The error value was considered acceptably low, particularly when compared with syringes, that have been found to overdose with an error of up to 23% for small dosages (Gnanalingham, Newland and Smith 1998). The low standard deviation of the average highlights the accuracy of the MEMS in terms of the volume supplied, which is of paramount importance for applications wherein high precision is aimed at.

The assembly of the 3DMNMEMS was conducted by connecting the hollow microneedle patch to the MEMS by tight fit, which was enabled by the design of the patch nozzle. The device is displayed in Figure 5.3. Two parts of plastic tubing were

fixed at the MEMS nozzles. The first connected the device with the solution vial and the second was embedded in the patch nozzle. Circulation trials using fluorescein dye did not reveal leaks at the connection point.

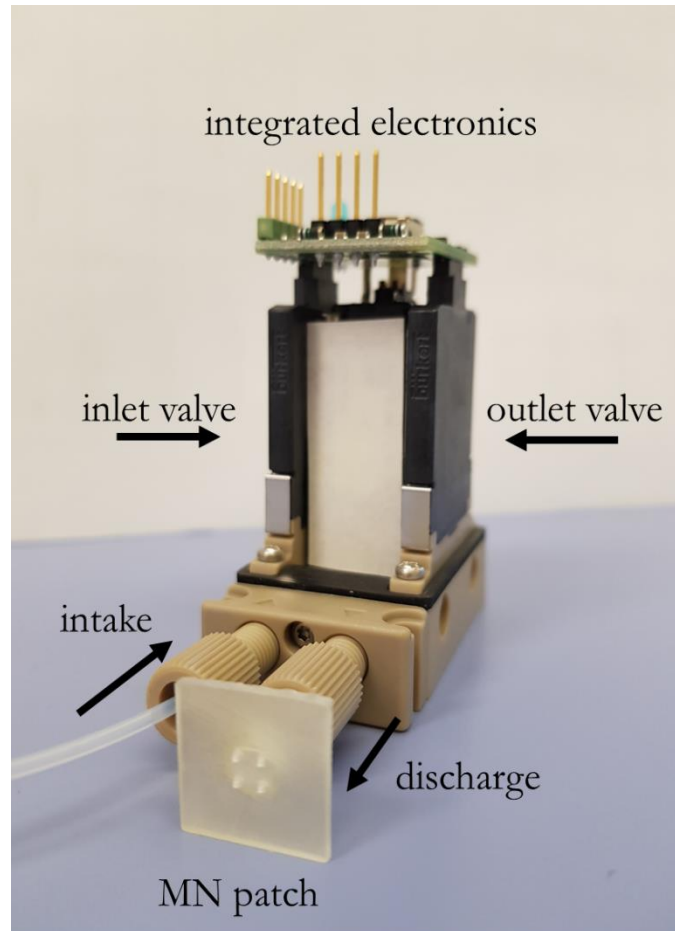


Figure 5.3 Assembled 3DMNMEMS device, featuring the 3D printed hollow microneedle patch integrated with the MEMS. The system receives the solution from the intake point and pumps it through the microneedles.

5.3.4 Optical Coherence Tomography

A well-documented issue associated with hollow microneedles, stems from the dense nature of the skin tissue which, being compressed during piercing, may hinder the infusion and dispersion of liquid formulation (Martanto *et al.* 2006). To investigate the performance of the 3DMNMEMS device on this area, Optical Coherence Tomography (OCT) was employed in an attempt to visualize the liquid transfer from the microneedles to the skin tissue. OCT is a valuable non-destructive, non-invasive

technique that captures images from within a sample, based on the capturing of low-coherence light variations reflected. It has been used extensively for biomedical imaging (Fujimoto *et al.* 2000; Walther *et al.* 2011) and imaging of microneedle piercing behaviour into skin (Donnelly *et al.* 2010; Donnelly *et al.* 2014). However, to the authors' knowledge, real-time capturing of liquid infusion from hollow microneedles inserted into biological skin tissue has not been previously reported. Here, we present for the first time, an in situ, real-time visualisation of liquid being administered by our 3DMNMEMS device within the porcine skin.

The microneedle component of the device was inserted into a porcine skin sample. Figure 5.4 shows a pre-pumping image of a lateral cross-section of the skin-microneedle system. The image depicts the insertion of approximately 70% of the total microneedle length (700 μm). This measurement is in agreement with respective ones derived via μCT when solid microneedles of similar geometry were inserted into 5 plies of parafilm (Economidou *et al.* 2019). The insertion depth reported here along with the design of the microneedle that places the lowest point of the elliptical opening at 300 μm away from the base, suggest that upon application the microneedle opening will be entirely within the skin tissue. This minimises the possibility of fluid escaping and remaining on the skin surface.

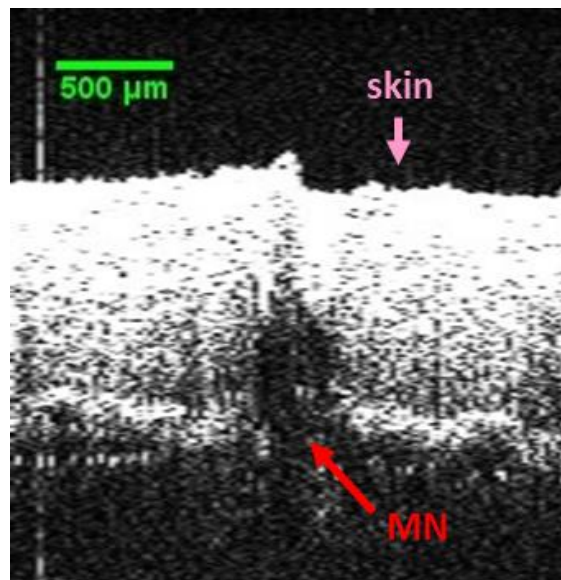
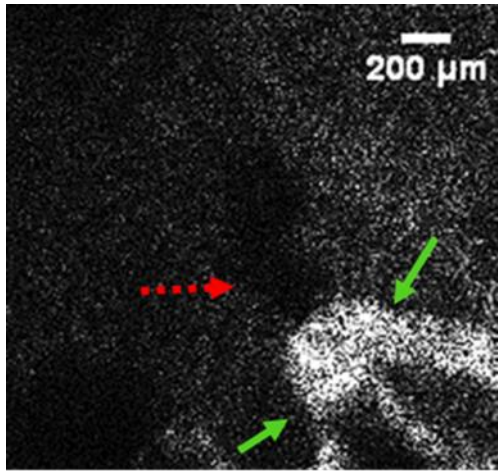
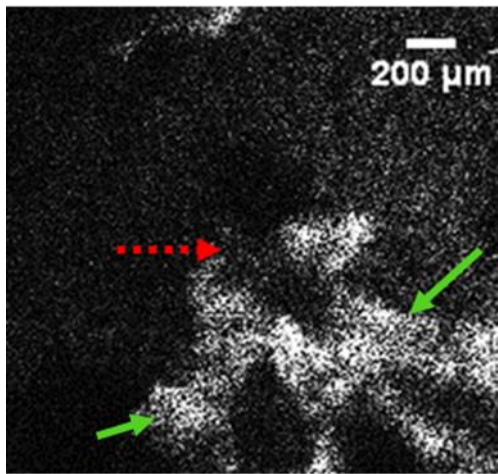


Figure 5.4 OCT image of a MN inserted in a sample of full thickness porcine skin.

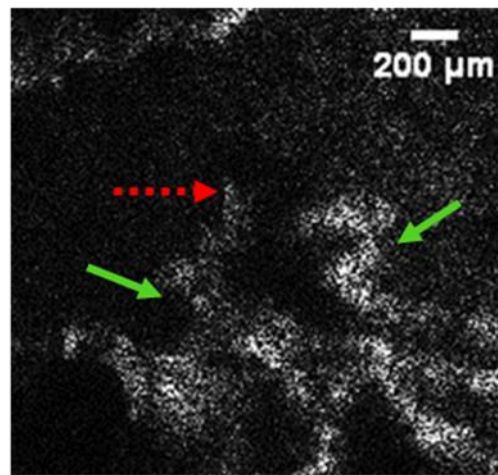
Thereafter, consecutive images of a horizontal cross-section of the skin during liquid pumping were captured, at the depth of the microneedle side opening. The images were captured perpendicular to the needle in order to allow the imaging of the fluid diffusing from the side opening of the hollow microneedles. Figure 5.5 illustrates the real-time progressive infusion of the liquid and its propagation within the tissue. The respective video is available as Supplementary Material of the published article featuring this work (Economidou *et al.* 2021).



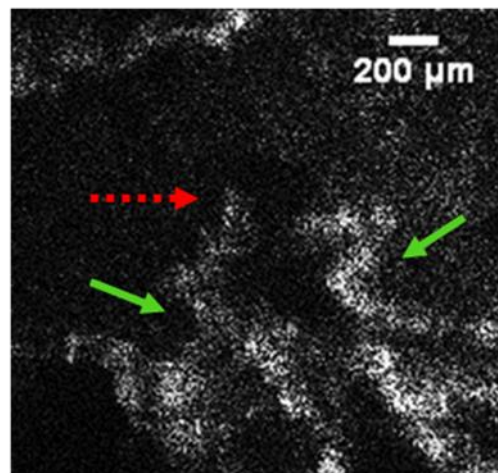
a



b



c



d

Figure 5.5 OCT captions of the progressive distribution of liquid solution (marked with green arrows) delivered from a single microneedle (red dashed arrows indicate the microneedle tip) within porcine skin tissue. The captions a-d were sequentially captured. The recorded video can be found as Supplementary Material of the respective published article (Economidou *et al.* 2021)

The captions, in chronological order, evince that the solution jets out of the microneedle opening. Initially denser close to the microneedle opening (Figure 5.5a), it proceeds to spread further at later captions (Figure 5.5b-d). The liquid distribution develops in an advancingly broader angle, which suggests that there is no creation of fluid depots within the skin that typically slow down drug absorption. This is a favourable trait in terms of clinical performance, in the sense that the drug is spreading in a wider area within the rich capillary bed of the dermal tissue and thus it is likely to be absorbed faster. This evidence strengthens the hypothesis that the 3DMNMEMS device is a promising system for efficacious transdermal drug delivery.

5.3.5 *In vitro* release through porcine skin

Prior to animal testing, the performance of the device in disrupting the skin barrier and delivering drugs *in vitro*, was tested, using Franz diffusion cells. Initially, the release of different dosages of sodium fluorescein salt in porcine skin was studied. The sodium fluorescein salt was selected as a model hydrophilic molecule.

The skin samples were pierced with the 3DMNMEMS and three different dosages of 5 μL , 10 μL and 20 μL were administered. After analysis and quantification via UV/Vis spectroscopy, it was found that for all dosages, 100% of the amount administered was detected in the receptor compartment in 30 minutes (Figure 5.6). The release was faster as the dosage increased, with almost 100% of the fluorescein salt detected in the receptor compartment in 20 min for dosages of 10 and 20 μL . The fluorescein was found to be released earlier as the dosage increased, which is attributed to the fact that with additional pumping, the solution was forced to diffuse further into the skin. As demonstrated by the findings of the OCT study, the 3DMNMEMS creates a conduit of microchannels in the skin, that propagates with each additional stroke. The network is more likely to spread all the way to the receptor compartment with more strokes, creating an interconnecting pathway with the microneedle, accelerating thus drug diffusion.

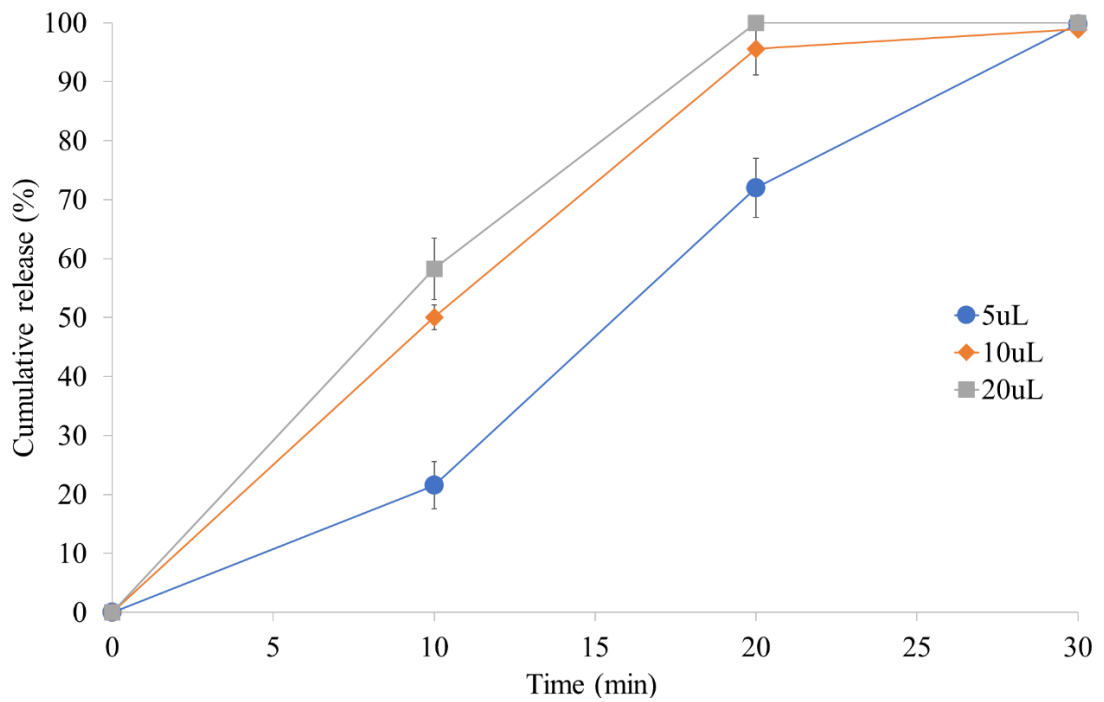


Figure 5.6 Cumulative *in vitro* release of sodium fluorescein salt injected to porcine skin by the 3DMNMEMS in three different dosages, 5 μ L, 10 μ L and 20 μ L.

Thereafter, the release of insulin in porcine skin was also examined. As seen in Figure 5.7, a single dosage of 10 μ L (0.5 IU) was fully detected in the receptor compartment in 1 hour. The release of insulin was slower compared to the sodium fluorescein. This was anticipated given the large molecular size of the insulin molecule which slows down the diffusion to the dermal microcirculation.

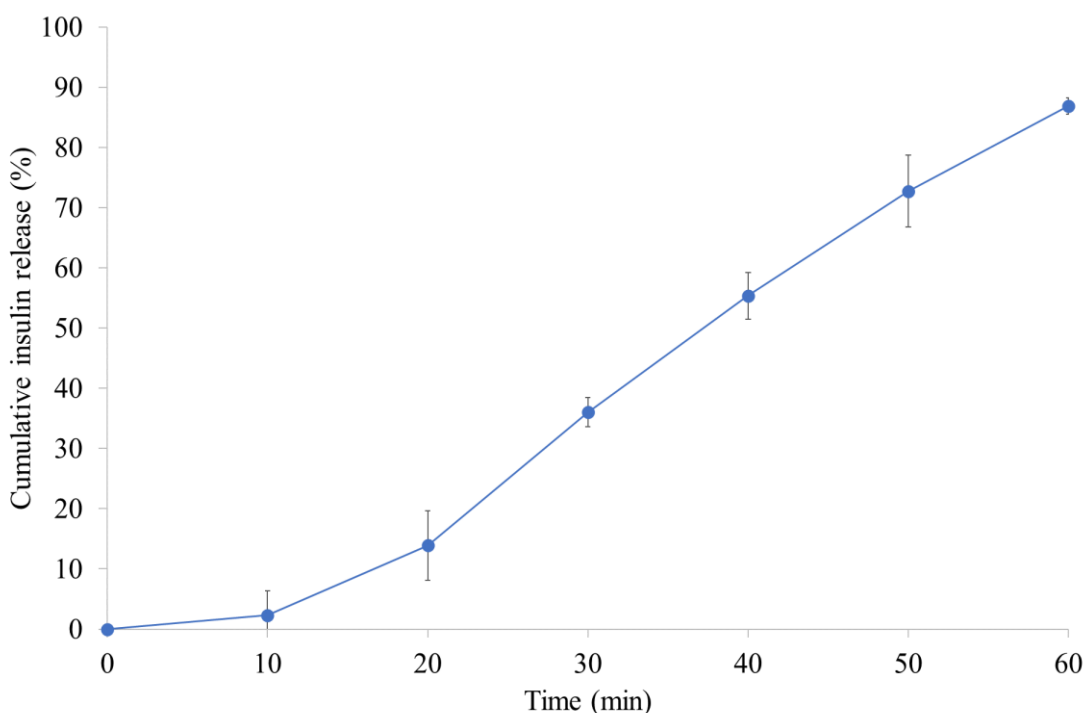


Figure 5.7 Cumulative *in vitro* release of insulin injected to porcine skin by the 3DMNMEMS.

5.3.6 *In vivo* clinical studies

The ability of the 3DMNMEMS device to administer insulin *in vivo* was investigated using a diabetic animal model, under the protocol described in the experimental section. Diabetes was confirmed after 7 days of streptozotocin administration. The preliminary diabetes (hyperglycemia) was shown as 340 ± 10 mg/dl.

The diabetic mice were divided into three groups: Untreated (negative control), subcutaneously (SC) injected (positive control) and treated with the 3DMNMEMS device. Both SC and 3DMNMEMS animal groups received the same amount of insulin (0.5 insulin units). For the animals treated with the 3DMNMEMS, the system was applied on shaved dorsal skin inserting the microneedle patch using manual finger pressure (Figure 5.7b-c). The MEMS was then coupled with the microneedle patch and the predetermined amount of insulin was administered, by adapting the pump settings. Albeit the assembled device can be readily applied on skin, conducting the application in two discreet steps enabled better control of the pressure applied on the animals. Skin pores were observed after microneedle removal which disappeared after 5 minutes (Figure 5.7e-f).

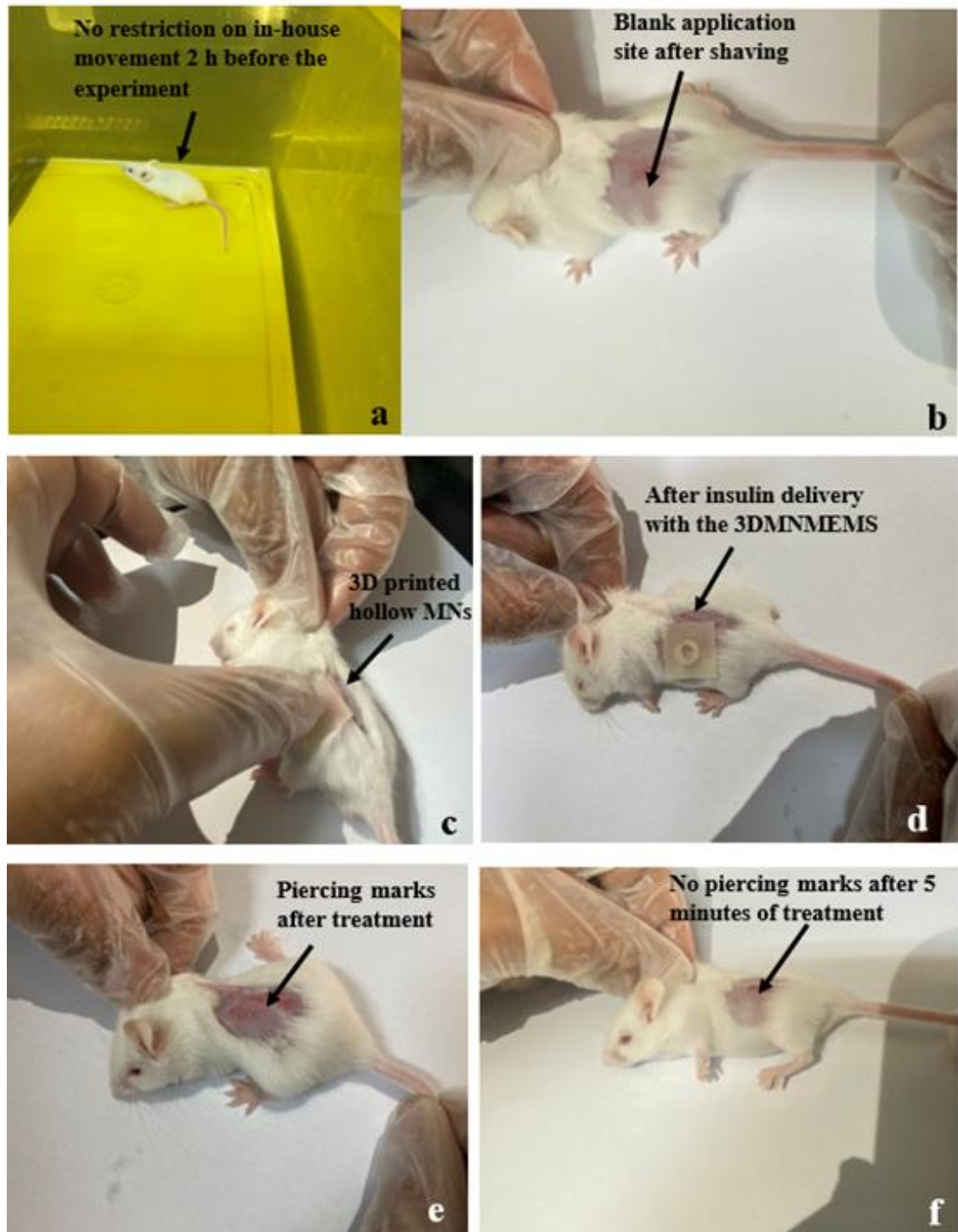


Figure 5.8 *In vivo* animal studies using a diabetic mice model for the treatment of diabetes using the 3DMNMEMS. a) No restriction of in-house movement 2 hours prior to the experiment, b) blank application site after shaving, c) application of the 3D printed hollow MN patch, d) after insulin delivery using the 3DMNMEMS, e) after-piercing pores after treatment, f) No pores 5 minutes after treatment.

The dose of 0.5 IU was selected in order to avoid hypoglycemia in mice for 6 h. The plasma glucose levels detected at each group are shown in Figure 5.9.

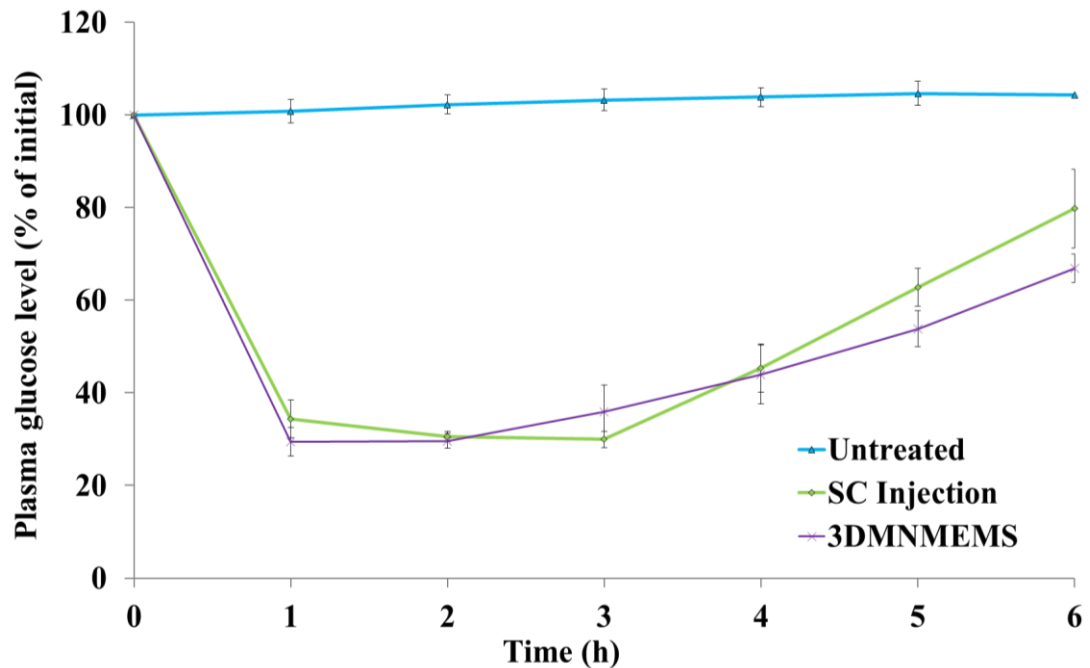


Figure 5.9 Plasma glucose levels after insulin administration to diabetic mice via subcutaneous injection and the 3DMNMEMS. The data obtained from the untreated animal group are also illustrated.

The 3DMNMEMS device demonstrated a similar release pattern as the SC group. However, it was found that the device facilitated a rapid decrease of the blood glucose levels compared to its initial value within 1 hour whereas for the SC the respective minimum was reached in 3 hours. This is owed to the fact that the injection forms a depot within the interstitial space, the content of which is slowly released due to passive diffusion. This finding further supports the OCT results that display broad liquid distribution within the skin tissue. Evidently, the device seems to enable the circumvention of a known limitation associated with the delivery of insulin via subcutaneous injection: the production of back pressure that retards drug distribution for absorption.

Along the same lines, significant improvement in terms of onset action is observed in comparison with other hollow microneedle systems tested for insulin delivery (Wang *et al.* 2006; Davis *et al.* 2005; Mcallister *et al.* 2003). As shown by these studies, the effect of the insulin administered manifests gradually and the blood glucose minima are

detected around 4 to 5 hours after administration. There is robust evidence that the comparative advantage of the 3DMNMEMS stems from the swift and broad liquid distribution within the skin tissue, induced by the pumping. Hence, the drug absorption does not rely on passive diffusion kinetics which play an important role in typical hollow microneedle-mediated drug delivery.

Figure 5.10 depicts the plasma insulin concentration which are in agreement with the reduction of plasma glucose.

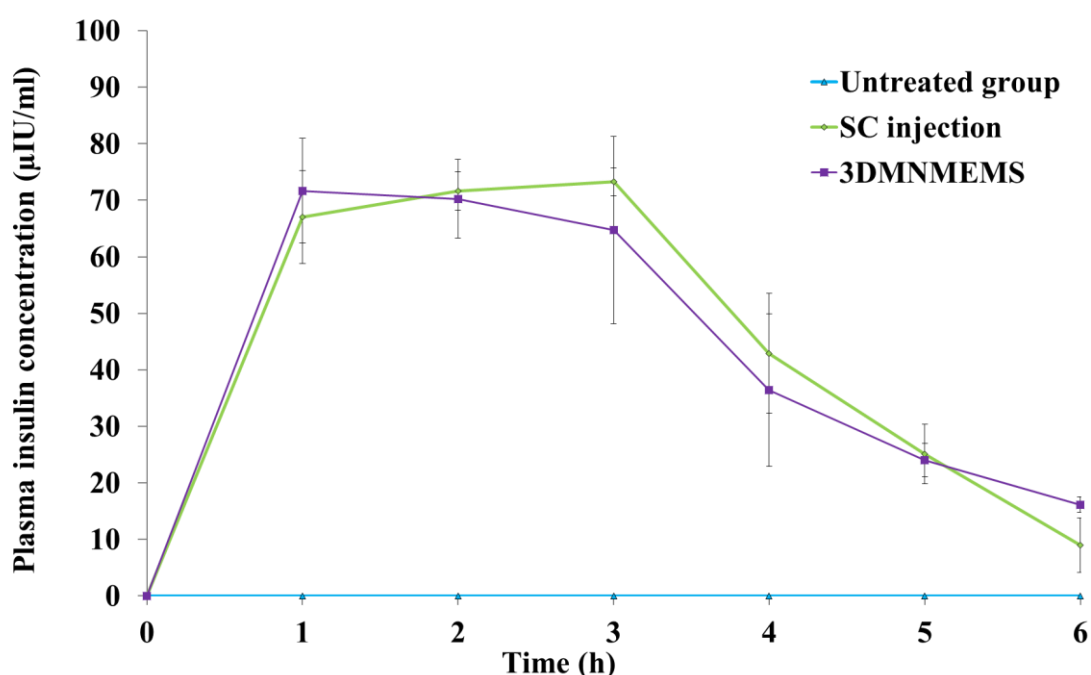


Figure 5.10 Plasma insulin levels after insulin administration to diabetic mice via subcutaneous injection and the 3DMNMEMS. The data obtained from the untreated animal group are also illustrated.

Based on the data derived from the *in vivo* studies, the minimum value of blood glucose (C_{min}) as well as the respective time point (T_{min}) were obtained from the plasma glucose vs time curve. The relative pharmacological availability (RPA) was calculated from Equation 5.2:

$$\%RPA = \frac{AAC_{3DMNMEMS} * dose_{sc}}{AAC_{sc} * dose_{3DMNMEMS}} * 100 \% \quad \text{Equation 5.2}$$

Where $AAC_{3DMNMEMS}$ and AAC_{sc} are the areas above the curve after insulin administration via the 3DMNMEMS device and subcutaneous injection, respectively. The respective doses are symbolised with $dose_{sc}$ and $dose_{3DMNMEMS}$.

Table 5.1 Pharmacodynamic parameters of insulin administration

Pharmacodynamic parameters				
	C_{min} (%)	t_{min} (h)	AAC_{0-6h}	RPA (%)
Untreated	100	0	0	0
SC	29.92	3	323.75	100
3DMNMEMS	29.47	1	340.4	105.14

The plasma insulin concentration vs time curve generated the maximum insulin concentration (C_{max}) as well as the respective time point (T_{max}). Equation 5.3 was used to calculate the relative bioavailability (RBA):

$$\%RBA = \frac{AUC_{3DMNMEMS} * dose_{sc}}{AUC_{sc} * dose_{3DMNMEMS}} * 100 \% \quad \text{Equation 5.3}$$

Where $AUC_{3DMNMEMS}$ and AUC_{sc} are the areas under the curve after insulin administration via the 3DMNMEMS device and subcutaneous injection respectively and $dose_{sc}$ and $dose_{3DMNMEMS}$ are the respective dosages.

Table 5.2 Pharmacokinetic parameters of insulin administration

Pharmacokinetic parameters				
	C_{max} (μ IU/mL)	t_{min} (h)	AUC_{0-6h}	RBA (%)
Untreated	0	0	0	0
SC	73.24	3	284.3	100
3DMNMEMS	71.6	1	274.95	96.71

The RPA values calculated in this study (Table 1), reveal that insulin administered by the 3DMNMEMS device has an enhanced pharmacological effect reducing blood

glucose compared to the injection-administered one. On the other hand, the RBA of 96.71% (Table 5.2) suggests that there is a slightly smaller insulin absorption in the 3DMNMEMS-treated group in the duration of the study. This is further supported by the trend of the plasma insulin concentration curve (Figure 5.10). While the respective data from the SC group show that the insulin concentration presents a steep decrease towards the end of the study (9 μ IU/mL at 6 hours after treatment), the plasma insulin concentration of the 3DMNMEMS group shows a more moderate decrease (16.1 μ IU/mL at 6 hours after treatment). This finding suggests that the insulin absorption in the 3DMNMEMS-treated group continued beyond the 6-hour duration of the experiment, evincing a more sustained insulin action.

5.4 CONCLUSIONS

In this work, 3D printed microneedles and MEMS were combined to develop a novel system for universal transdermal drug delivery. The system allows the *in-situ* control of drug administration by the user, rendering the system a valuable tool for personalisation of treatment. Laser SLA generated uniform and reproducible complex hollow microneedle patches. No structural superficial or internal defects that could hamper the clinical performance were detected. Employing advanced Optical Coherence Tomography, liquid being diffused from the 3DMNMEMS within skin tissue was monitored in real time. It was shown that the system facilitated broad distribution of the liquid without the creation of depots, thus accelerating drug absorption. *In vivo* clinical trials of insulin administration to diabetic animals illustrated that the 3DMNMEMS achieved slightly faster insulin onset action and prolonged duration of glycemic control compared to subcutaneous injection, but in a painless manner.

The platform device presented in this work was not designed to respond to a specific stimulus, e.g., glucose level, but leaves the full control of the administration process to the user. This practically entails that a range of drugs, suitable for transdermal delivery, can be delivered through this approach. Along the same lines, the device can be potentially utilised for the delivery of vaccines, to harvest the well-documented advantages of hollow microneedle-mediated vaccine delivery. Hence, new pathways are

opened and limitations of microneedle-based systems, e.g., fixed cargo amount for dissolvable and coated microneedles, are circumvented, maintaining the benefits of microneedle-mediated delivery. Overall, this work demonstrates that the integration of MEMS with 3D printing can be a key to the evolution of medical devices for personalised treatment.

CHAPTER 6

GENERAL CONCLUSIONS

Given the transformative impact that 3D printing has had on a multitude of scientific and industrial fields, its potential to revolutionise the field of transdermal drug delivery was explored in the present thesis. The 3D printability of transdermal microneedles was thoroughly investigated, in the aim to build coherent design and manufacturing strategies that would be readily transferable from the research to the industrial setting. The 3D printed patches were incorporated into drug delivery systems and their performance to deliver insulin via the transdermal route was demonstrated.

Photopolymerisation based 3D printing was proven to have promising potential as a microneedle manufacturing method. Solid and hollow transdermal microneedles were successfully fabricated using such technologies of the cost-effective range, namely laser Stereolithography and Digital Light Processing. The major technical restriction for both methods was the printing resolution, affecting mainly the sharpness, as well as the opening of the hollow microneedles. Adapting the microneedle designs to the technology's resolution was found to be an imperative step to reassure compatibility of the virtual model with the manufacturing technology.

The general rule that the quality of 3D printed parts is highly dependent on the printing settings was found to apply on microneedles. Parameters such as the printing angle and the post-printing curing conditions were intricately influential of the quality, dimensional fidelity and mechanical performance. All major dimensional parameters were found to be sensitive to the printing angle, with the exception of the hollow microneedle opening. The formation of the latter was mainly affected by unwanted curing due to overlapping of the radiance Gaussian distribution tails. This effect, pronounced mostly in laser SLA prints, induced severe dimensional discrepancies that in cases were detrimental. It is essential thus, to design the opening in respect to the restrictions imposed by both nominal resolution and the forenamed effect.

The design and additive manufacturability of complex hollow microneedle patches with internal microfluidic structures was also found to be influenced by the same technical limitations, the consideration of which is essential during design. The thorough post-

printing drainage of unpolymerised resin from the internal cavities was found to play a prominent role in the avoidance of internal blockages that would obstruct the liquid circulation and delivery.

The optimised microneedles generated by the proposed strategy were all found to effectively pierce the skin, requiring minimal external loads. This is in fact a prerequisite for the minimisation of pain during application. The microneedles were also found to be mechanically strong, fracturing at much higher forces than the respective piercing ones, which rendered them mechanically safe for clinical application.

For the development of the transdermal drug delivery systems, 3D printing was combined with other sophisticated technologies. A 2D inkjet printing technique was employed to create insulin films on the 3D printed solid microneedles. The process was found to be highly accurate and reproducible in terms of spatial control of the coating deposition as well as of the coated drug amount. The coating morphology and thereby, the dissolution into the skin, was found to be influenced by specific microneedle geometrical features.

For the hollow microneedles, their integration with a microelectromechanical system achieved the development of a novel platform device for controlled, personalised transdermal drug delivery. The device accomplished broad distribution of the drug-containing solution within the skin tissue, which favoured faster absorption by the rich capillary bed of the dermis. Evidently, *in vivo* trials of insulin administration to diabetic animals using the device, illustrated faster onset action and a more sustained glycemic control, compared to subcutaneous injections.

Summarising, the present thesis presented solid evidence that 3D printing is a valid microneedle manufacturing technology and has vast potential to alter the outlooks of drug delivery via the transdermal route. The author's ambition is that the reported findings will inspire and facilitate future research in the field.

CHAPTER 7

FUTURE WORK

The research featured in the present thesis aimed at developing knowledge and providing insight to the underexplored field of Additive Manufacturing of microneedle-mediated transdermal drug delivery systems. In the author's opinion, the findings reported here can be the starting point of a wide range of research endeavours pertaining to the manufacturability of transdermal microneedle systems by 3D printing.

Interesting research can be generated by exploiting the findings of this thesis as manufacturing guidelines. By faithfully adhering to the design and fabrication steps proposed herein, the microneedle systems can be readily replicated and thereafter employed for a variety of drug delivery purposes. Essentially, a standard laser SLA or DLP printer can replace typical micromoulding or micromachining processes supplying research groups with transdermal systems, tailored to the requirements of their projects. This will tackle the known disadvantages of traditional microneedle fabrication methods and promote research in the field of drug delivery via the transdermal route. Specific future experimental studies can involve the usage of the 3D printed microneedles to deliver macromolecular drugs beyond insulin as well as research in the field of microneedle-mediated vaccinations.

The 2D inkjet coating process proposed here offers another opportunity to modernise microneedle systems. The technology has several advantages due to its high accuracy and controllability. The correlation of microneedle geometry with coating morphology and hence coating dissolution, can be utilised to customise systems based on the application requirements. Further work can be conducted by applying the proposed inkjet technique to coat microneedles with a variety of substances beyond insulin. Moreover, the technology offers the possibility of depositing multiple substances in one coating regime, enabling the creation of multidrug coated microneedles. This is an interesting concept that will open new prospects for multitarget therapy.

Hollow microneedles as presented here, offer the versatility of being compatible both with the microelectromechanical system as well as standard syringes. Such systems can be utilised in combination with the flow instigator of choice to substitute standard

needles for controlled, painless drug delivery. Especially in the case of the 3DMNMEMS device, its universal character makes it an excellent candidate for research on clinical applications that require high controllability, accuracy and *in-situ* customisation of the drug administration parameters. The device can be tested for its ability to deliver a variety of drugs and potentially vaccines. Further animal testing as well as human clinical trials will further reveal the potential of the proposed device in personalising treatments.

The development of 3D printed dissolvable/degradable microneedles is an interesting concept. The main limitation has been the lack of materials with the respective biodegradability properties that are simultaneously compatible with photopolymerisation 3D printing technologies. Thus, the synthesis of novel 3D printing resins, with tailored characteristics is an essential step towards this advancement. A new pathway will open for the introduction of a new range of microneedles with incorporated actives. Prior to attempting to 3D print microneedles, the custom resins, after physicochemical characterisation, need to be tested in terms of printability. Parameter standardisation must be conducted for optimal printing quality, which is typically done through trial-and-error studies.

The applicability of 3D printing technologies, other than of the photopolymerisation-based range, will also promote the adoption of such technologies and yield additional research. It is noteworthy though, that such research should follow the advancement of these technologies in the technical level, especially in terms of resolution as well as biocompatible materials.

Overall, the application of 3D printing for microneedle manufacturing presents an interesting opportunity that has attracted notable attention. To the author's opinion, the future research in the field will be vigorous and it is expected that the findings of the present thesis will have a positive impact on its progress.

REFERENCES

- Abrams, L.S. *et al.* (2002). Pharmacokinetics of a contraceptive patch (EvraTM/Ortho EvraTM) containing norelgestromin and ethinylloestradiol at four application sites. *British Journal of Clinical Pharmacology* **53**:141–146.
- Agarwal, S. and Krishnamurthy, K. (2019). *Histology, Skin*. StatPearls Publishing.
- Agrawal, A.K. *et al.* (2010). Development and characterization of in situ gel system for nasal insulin delivery. *Pharmazie* **65**:188–193.
- Aksit, A. *et al.* (2018). In-vitro perforation of the round window membrane via direct 3-D printed microneedles. *Biomedical Microdevices* **20**:47.
- Alhijaj, M. *et al.* (2019). Impact of Processing Parameters on the Quality of Pharmaceutical Solid Dosage Forms Produced by Fused Deposition Modeling (FDM). *Pharmaceutics* **11**:633.
- Ali, R. *et al.* (2020). Transdermal Microneedles—A Materials Perspective. *AAPS PharmSciTech* **21**:12.
- Alkilani, A.Z., McCrudden, M.T.C. and Donnelly, R.F. (2015). Transdermal drug delivery: Innovative pharmaceutical developments based on disruption of the barrier properties of the stratum corneum. *Pharmaceutics* **7**:438–470.
- Allen, E.A. *et al.* (2016). Dissolvable microneedle fabrication using piezoelectric dispensing technology. *International Journal of Pharmaceutics* **500**:1–10.
- Amer, R.I. *et al.* (2020). Characterization and Pharmacological Evaluation of Anti-Cellulite Herbal Product(s) Encapsulated in 3D-Fabricated Polymeric Microneedles. *Scientific Reports* **10**:6316.
- Anderson, P.A. (2019). 3D Printing for Education and Surgical Planning in Orthopedic Surgery. In: *3D Printing in Orthopaedic Surgery*. Elsevier, pp. 55–63.
- Andrade, F. *et al.* (2015). Solid state formulations composed by amphiphilic polymers for delivery of proteins: Characterization and stability. *International Journal of Pharmaceutics* **486**:195–206.
- Andrews, S. *et al.* (2011). Transdermal Insulin Delivery Using Microdermabrasion.

Pharmaceutical Research **28**:2110–2118.

- Aoyagi, S., Izumi, H. and Fukuda, M. (2008). Biodegradable polymer needle with various tip angles and consideration on insertion mechanism of mosquito's proboscis. *143*:20–28.
- ASTM (2002). D695-15 Standard Test Method for Compressive Properties of Rigid Plastics. In: *Annual Book of ASTM Standards*. ASTM International.
- Attaran, M. (2017). Additive Manufacturing: The Most Promising Technology to Alter the Supply Chain and Logistics. *Journal of Service Science and Management* **10**:189–206.
- Awodele, O., Adewoye, A.A. and Oparah, A.C. (2016). Assessment of medical waste management in seven hospitals in Lagos , Nigeria. *BMC Public Health* **16**:269.
- B. Ita, K. (2015). Chemical Penetration Enhancers for Transdermal Drug Delivery- Success and Challenges. *Current Drug Delivery* **12**:645–651.
- Baek, S.H., Shin, J.H. and Kim, Y.C. (2017). Drug-coated microneedles for rapid and painless local anesthesia. *Biomedical Microdevices* **19**:2.
- Bajpai, A.K. and Bhanu, S. (2004). In vitro release dynamics of insulin from a loaded hydrophilic polymeric network. *Journal of Materials Science: Materials in Medicine* **15**:43–54.
- Bakshi, S., Roisman, I. V. and Tropea, C. (2007). Investigations on the impact of a drop onto a small spherical target. *Physics of Fluids* **19**:032102.
- Ballard, D.H. *et al.* (2020). Medical 3D Printing Cost-Savings in Orthopedic and Maxillofacial Surgery: Cost Analysis of Operating Room Time Saved with 3D Printed Anatomic Models and Surgical Guides. *Academic Radiology* **27**:1103–1113.
- Barichello, J. (1999). Enhanced rectal absorption of insulin-loaded Pluronic® F-127 gels containing unsaturated fatty acids. *International Journal of Pharmaceutics* **183**:125–132.
- Barichello, J.M. *et al.* (1999). Absorption of insulin from Pluronic F-127 gels following subcutaneous administration in rats. *International Journal of Pharmaceutics*

184:189–198.

- Barinov, S.M. *et al.* (2015). 3D printing of ceramic scaffolds for engineering of bone tissue. *Inorganic Materials: Applied Research* **6**:316–322.
- Bediz, B. *et al.* (2014). Dissolvable microneedle arrays for intradermal delivery of biologics: Fabrication and application. *Pharmaceutical Research* **31**:117–135.
- Bhattacharjee, N. *et al.* (2016). The upcoming 3D-printing revolution in microfluidics. *Lab on a Chip* **16**:1720–1742.
- Bi, L. *et al.* (2011). Effects of different cross-linking conditions on the properties of genipin-cross-linked chitosan / collagen scaffolds for cartilage tissue engineering. *J Mater Sci: Mater Med* **22**:51–62.
- Boehm, R.D. *et al.* (2012). Indirect rapid prototyping of antibacterial acid anhydride copolymer microneedles. *Biofabrication* **4**:011002.
- Boehm, R.D. *et al.* (2014). Inkjet printing for pharmaceutical applications. *Materials Today* **17**:247–252.
- Boehm, R.D. *et al.* (2013). Inkjet printing of amphotericin B onto biodegradable microneedles using piezoelectric inkjet printing. *Jom* **65**:525–533.
- Boehm, R.D. *et al.* (2011). Modification of microneedles using inkjet printing. *AIP Advances* **1**:1–13.
- Bos, J.D. and Meinardi, M.M.H.M. (2000). The 500 Dalton rule for the skin penetration of chemical compounds and drugs. *Experimental Dermatology* **9**:165–169.
- Camposeco-Negrete, C. (2020). Optimization of printing parameters in fused deposition modeling for improving part quality and process sustainability. *International Journal of Advanced Manufacturing Technology* **108**:2131–2147.
- Carpenter, J.F. *et al.* (1999). Inhibition of stress-induced aggregation of protein therapeutics. In: *Methods in Enzymology*. pp. 236–255.
- Carpenter, J.F., Izutsu, K.I. and Rarldolph, T.W. (2010). Freezing-and drying-induced perturbations of protein structure and mechanisms of protein protection by stabilizing additives. In: *Freeze-Drying/Lyophilization of Bharmaceutical and Biological Products*. 3rd ed. Informa.

- Caudill, C.L. *et al.* (2018). Spatially controlled coating of continuous liquid interface production microneedles for transdermal protein delivery. *Journal of Controlled Release* **284**:122–132.
- Chandler, C.E. *et al.* (2018). In vivo intradermal delivery of bacteria by using microneedle arrays. *Infection and Immunity* **86**:1–13.
- Chang, B.S. *et al.* (1996). Physical Factors Affecting the Storage Stability of Freeze-Dried Interleukin-1 Receptor Antagonist: Glass Transition and Protein Conformation. *Archives of Biochemistry and Biophysics* **331**:249–258.
- Chen, R.K. *et al.* (2016). Additive manufacturing of custom orthoses and prostheses—A review. *Additive Manufacturing* **12**:77–89.
- Choi, J.W. *et al.* (2009). Fabrication of 3D biocompatible/biodegradable micro-scaffolds using dynamic mask projection microstereolithography. *Journal of Materials Processing Technology* **209**:5494–5503.
- Cordeiro, A.S. *et al.* (2020). Two-Photon Polymerisation 3D Printing of Microneedle Array Templates with Versatile Designs: Application in the Development of Polymeric Drug Delivery Systems. *Pharmaceutical Research* **37**:174.
- Couto, A. *et al.* (2014). Dermic diffusion and stratum corneum: A state of the art review of mathematical models. *Journal of Controlled Release* **177**:74–83.
- Crommelin, D.J.A., Storm, G. and Luijten, P. (2011). ‘Personalised medicine’ through ‘personalised medicines’: Time to integrate advanced, non-invasive imaging approaches and smart drug delivery systems. *International Journal of Pharmaceutics* **415**:5–8.
- Culmone, C., Smit, G. and Breedveld, P. (2019). Additive manufacturing of medical instruments: A state-of-the-art review. *Additive Manufacturing* **27**:461–473.
- Data Bridge Market Research (2020). *Global Microneedle Drug Delivery Systems Market – Industry Trends and Forecast to 2027*. [Online]. Available at: <https://www.databridgemarketresearch.com/reports/global-microneedle-drug-delivery-systems-market>.
- Davis, S.P. *et al.* (2005). Hollow Metal Microneedles for Insulin Delivery to Diabetic Rats. *IEEE Transactions on Biomedical Engineering* **52**:909–915.

- Davis, S.P. *et al.* (2004). Insertion of microneedles into skin: Measurement and prediction of insertion force and needle fracture force. *Journal of Biomechanics* **37**:1155–1163.
- DETAX (2019). *FREEPRINT 3D Printing Materials*. [Online]. Available at: <https://sgdentalshop.com/wp-content/uploads/2019/03/DETAX-Freeprint-3D-catalogue-dental-materials-sgdentalshop.pdf>.
- Dey, A. and Yodo, N. (2019). A Systematic Survey of FDM Process Parameter Optimization and Their Influence on Part Characteristics. *Journal of Manufacturing and Materials Processing* **3**:64.
- Dhillon, S. (2011). Rivastigmine Transdermal Patch. *Drugs* **71**:1209–1231.
- Diversified Enterprises (2020). *Critical Surface Tension and Contact Angle with Water for Various Polymers* [Online]. Available at: [https://www.accudynetest.com/polytable_03.html?sortby=contact_angle DESC](https://www.accudynetest.com/polytable_03.html?sortby=contact_angle_DESC) [Accessed: 24 December 2020].
- Dizon, J.R.C. *et al.* (2018). Mechanical characterization of 3D-printed polymers. *Additive Manufacturing* **20**:44–67.
- Donnelly, R.F. *et al.* (2012). Hydrogel-forming microneedle arrays for enhanced transdermal drug delivery. *Advanced Functional Materials* **22**:4879–4890.
- Donnelly, R.F. *et al.* (2014). Hydrogel-forming microneedles increase in volume during swelling in skin , but skin barrier function recovery is unaffected. *J Pharm Sci.* **103**:1478–1486.
- Donnelly, R.F. *et al.* (2010). Optical coherence tomography is a valuable tool in the study of the effects of microneedle geometry on skin penetration characteristics and in-skin dissolution. *Journal of Controlled Release* **147**:333–341.
- Doraiswamy, A. *et al.* (2010). Fabrication of microneedles using two photon polymerization for transdermal delivery of nanomaterials. *Journal of Nanoscience and Nanotechnology* **10**:6305–6312.
- Dumortier, G. *et al.* (2006). A Review of Poloxamer 407 Pharmaceutical and Pharmacological Characteristics. *Pharmaceutical Research* **23**:2709–2728.

- Economidou, S.N. *et al.* (2019). 3D printed microneedle patches using stereolithography (SLA) for intradermal insulin delivery. *Materials Science and Engineering C* **102**:743–755.
- Economidou, S.N. *et al.* (2021). A novel 3D printed hollow microneedle microelectromechanical system for controlled, personalized transdermal drug delivery. *Additive Manufacturing* **38**:101815.
- El-Sayed, N., Vaut, L. and Schneider, M. (2020). Customized fast-separable microneedles prepared with the aid of 3D printing for nanoparticle delivery. *European Journal of Pharmaceutics and Biopharmaceutics* **154**:166–174.
- EnvisionTEC (2011). *E-Shell 200 Datasheet*. [Online]. Available at: <https://envisiontec.com/3d-printing-materials/micro-materials/e-shell-200-series/>.
- Escobar-Chávez, J.J. *et al.* (2009). Electroporation as an efficient physical enhancer for skin drug delivery. *Journal of Clinical Pharmacology* **49**:1262–1283.
- Fang, J.-H. *et al.* (2020). Transdermal Composite Microneedle Composed of Mesoporous Iron Oxide Nanoraspberry and PVA for Androgenetic Alopecia Treatment. *Polymers* **12**:1392.
- Faraji Rad, Z. *et al.* (2017). High-fidelity replication of thermoplastic microneedles with open microfluidic channels. *Microsystems and Nanoengineering* **3**:1–11.
- Farias, C. *et al.* (2018). Three-Dimensional (3D) Printed Microneedles for Microencapsulated Cell Extrusion. *Bioengineering* **5**:59.
- Farshchian, B. *et al.* (2018). Droplet impinging behavior on surfaces with wettability contrasts. *Microelectronic Engineering* **195**:50–56.
- FDA (2017a). Regulatory Considerations for Microneedling Devices FDA-2017-D-4792. [Online]:1–12. Available at: <https://www.fda.gov/regulatory-information/search-fda-guidance-documents/regulatory-considerations-microneedling-devices>.
- FDA (2017b). *Technical Considerations for Additive Manufactured Medical Devices*. [Online]. Available at: <https://www.fda.gov/regulatory-information/search-fda-guidance-documents/technical-considerations-additive-manufactured-medical-devices>.

- Formlabs (2017). *Dental LT Clear Material Data Sheet*. [Online]. Available at: https://dental-media.formlabs.com/datasheets/Dental_LT_Clear_Technical.pdf.
- Formlabs (2016). *Dental SG Material Properties*. [Online]. Available at: <https://formlabs-media.formlabs.com/datasheets/DentalSG-DataSheet.pdf>.
- Formlabs (2021). *What Does Resolution Mean in 3D Printing?* [Online]. Available at: <https://formlabs.com/uk/blog/3d-printer-resolution-meaning/> [Accessed: 27 March 2021].
- Forvi, E. *et al.* (2010). A method to determine the margin of safety for microneedles arrays. *WCE 2010 - World Congress on Engineering 2010* **2**:1550–1554.
- Francis, L.F., Stadler, B.J.H. and Roberts, C.C. (2016). *Materials Processing*. [Online]. Elsevier. Available at: <https://linkinghub.elsevier.com/retrieve/pii/C20090642872>.
- Fujimoto, J.G. *et al.* (2000). Optical coherence tomography: An emerging technology for biomedical imaging and optical biopsy. *Neoplasia* **2**:9–25.
- Garland, M.J. *et al.* (2012). Dissolving polymeric microneedle arrays for electrically assisted transdermal drug delivery. *Journal of Controlled Release* **159**:52–59.
- George, E. *et al.* (2017). Measuring and Establishing the Accuracy and Reproducibility of 3D Printed Medical Models. *RadioGraphics* **37**:1424–1450.
- Gill, H.S. *et al.* (2008). Effect of microneedle design on pain in human subjects. *Clin J Pain* **24**:585–594.
- Gill, H.S. and Prausnitz, M.R. (2007). Coated microneedles for transdermal delivery. *Journal of Controlled Release* **117**:227–237.
- Gill, H.S. and Prausnitz, M.R. (2008). Pocketed microneedles for drug delivery to the skin. *Journal of Physics and Chemistry of Solids* **69**:1537–1541.
- Gittard, S.D. *et al.* (2011). Deposition of antimicrobial coatings on microstereolithography-fabricated microneedles. *Jom* **63**:59–68.
- Gittard, S.D. *et al.* (2009). Fabrication of polymer microneedles using a two-photon polymerization and micromolding process. *Journal of diabetes science and technology* **3**:304–11.
- Gittard, S.D. *et al.* (2013). The effects of geometry on skin penetration and failure of

- polymer microneedles. *Journal of Adhesion Science and Technology* **27**:227–243.
- Gittard, S.D. *et al.* (2010). Two Photon Polymerization of Microneedles for Transdermal Drug Delivery. *Expert Opinion on Drug Delivery* **7**:513–533.
- Gnanalingham, M.G., Newland, P. and Smith, C.P. (1998). Accuracy and reproducibility of low dose insulin administration using pen-injectors and syringes. *Archives of Disease in Childhood* **79**:59–62.
- Gong, H. *et al.* (2015). Optical approach to resin formulation for 3D printed microfluidics. *RSC Advances* **5**:106621–106632.
- Goole, J. and Amighi, K. (2016). 3D printing in pharmaceuticals: A new tool for designing customized drug delivery systems. *International Journal of Pharmaceutics* **499**:376–394.
- Goyanes, A. *et al.* (2015). 3D Printing of Medicines: Engineering Novel Oral Devices with Unique Design and Drug Release Characteristics. *Molecular Pharmaceutics* **12**:4077–4084.
- Goyanes, A. *et al.* (2016). 3D scanning and 3D printing as innovative technologies for fabricating personalized topical drug delivery systems. *Journal of Controlled Release* **234**:41–48.
- Graybiel, A., Knepton, J. and Shaw, J. (1976). Prevention of experimental motion sickness by scopolamine absorbed through the skin. *Aviation Space and Environmental Medicine* **57**:1096–1100.
- Guilizzoni, M. (2011). Drop shape visualization and contact angle measurement on curved surfaces. *Journal of Colloid and Interface Science* **364**:230–236.
- Gupta, J., Felner, E.I. and Prausnitz, M.R. (2009). Minimally Invasive Insulin Delivery in Subjects with Type 1 Diabetes Using Hollow Microneedles. *Diabetes Technology & Therapeutics* **11**:329–337.
- Hadgraft, J. and Lane, M.E. (2016). Drug crystallization – implications for topical and transdermal delivery. *Expert Opinion on Drug Delivery* **13**:817–830.
- Haj-Ahmad, R. *et al.* (2015). Microneedle Coating Techniques for Transdermal Drug Delivery. *Pharmaceutics* **7**:486–502.

- Halder, J. *et al.* (2020). Microneedle Array: Applications, Recent Advances, and Clinical Pertinence in Transdermal Drug Delivery. *Journal of Pharmaceutical Innovation*.
- Hart, C. *et al.* (2020). Biocompatibility of Blank, Post-Processed and Coated 3D Printed Resin Structures with Electrogenic Cells. *Biosensors* **10**:152.
- Hassan, M. *et al.* (2019). 3D printing of biopolymer nanocomposites for tissue engineering: Nanomaterials, processing and structure-function relation. *European Polymer Journal* **121**:109340.
- Hong, X. *et al.* (2013). Dissolving and biodegradable microneedle technologies for transdermal sustained delivery of drug and vaccine. *Drug Design, Development and Therapy* **7**:945–952.
- Ingrole, R.S.J. and Gill, H.S. (2019). Microneedle Coating Methods: A Review with a Perspective. *Journal of Pharmacology and Experimental Therapeutics* **370**:555–569.
- Ita, K. (2017). Dissolving microneedles for transdermal drug delivery: Advances and challenges. *Biomedicine and Pharmacotherapy* **93**:1116–1127.
- Ita, K. (2016). Transdermal iontophoretic drug delivery: advances and challenges. *Journal of Drug Targeting* **24**:386–391.
- Jacob, J. *et al.* (2016). US 9.339.489 B2 Rapid disperse dosage form containing levetiracetam. *United states patent*.
- Jaiswal, P. and Srivastava, M. (2017). *3D Printed Drugs Market by Spritam (U.S. and Rest of World) and Other Drugs Potential Market by Scenario (Rapid Growth Scenario, Moderate Growth Scenario, and Low Growth Scenario) - Global Opportunity Analysis and Industry Forecast, 2017-2030*. [Online]. Available at: <https://www.alliedmarketresearch.com/3d-printed-drugs-market>.
- Jeong, H.R. *et al.* (2020). Safe coated microneedles with reduced puncture occurrence after administration. *Micromachines* **11**:17–19.
- Jessen, L., Kovalick, L.J. and Azzaro, A.J. (2008). The selegiline transdermal system (emsam): a therapeutic option for the treatment of major depressive disorder. *P & T* **33**:212–46.

- Johnson, A.R. *et al.* (2016). Single-step fabrication of computationally designed microneedles by continuous liquid interface production. *PLoS ONE* **11**:1–17.
- Johnson, A.R. and Procopio, A.T. (2019). Low cost additive manufacturing of microneedle masters. *3D Printing in Medicine* **5**:2.
- Karalekas, D. *et al.* (2002). Investigation of shrinkage-induced stresses in stereolithography photo-curable resins. *Experimental Mechanics* **42**:439–444.
- Karania, R. and Kazmer, D. (2007). Low volume plastics manufacturing strategies. *Journal of Mechanical Design, Transactions of the ASME* **129**:1225–1233.
- Kavaldzhiev, M. *et al.* (2017). Biocompatible 3D printed magnetic micro needles. *Biomedical Physics & Engineering Express* **3**:1–9.
- Kelly, S. and Price, N. (2000). The Use of Circular Dichroism in the Investigation of Protein Structure and Function. *Current Protein & Peptide Science* **1**:349–384.
- Kerbrat, O., Mognol, P. and Hascoët, J.Y. (2011). A new DFM approach to combine machining and additive manufacturing. *Computers in Industry* **62**:684–692.
- Khanna, P. *et al.* (2010). Sharpening of hollow silicon microneedles to reduce skin penetration force. *Journal of Micromechanics and Microengineering* **20**:045011.
- Khorsandi, D. *et al.* (2021). 3D and 4D printing in dentistry and maxillofacial surgery: Printing techniques, materials, and applications. *Acta Biomaterialia* **122**:26–49.
- Kim, Y.C. *et al.* (2012). Increased immunogenicity of avian influenza DNA vaccine delivered to the skin using a microneedle patch. *European Journal of Pharmaceutics and Biopharmaceutics* **81**:239–247.
- Kim, Y.C., Park, J.H. and Prausnitz, M.R. (2012). Microneedles for drug and vaccine delivery. *Advanced Drug Delivery Reviews* **64**:1547–1568.
- Kirby, A. (2012). Method of producing a microneedle or microimplant. **US 8192787**.
- Kondor, S. *et al.* (2013). On demand additive manufacturing of a basic surgical kit. *Journal of Medical Devices, Transactions of the ASME*.
- Kreß, S. *et al.* (2020). 3D Printing of Cell Culture Devices: Assessment and Prevention of the Cytotoxicity of Photopolymers for Stereolithography. *Materials* **13**:3011.

- Krieger, K.J. *et al.* (2019). Simple and customizable method for fabrication of high-aspect ratio microneedle molds using low-cost 3D printing. *Microsystems & Nanoengineering* **5**:42.
- Kubáč, L. and Kodym, O. (2017). The impact of 3D printing technology on supply chain. *MATEC Web of Conferences* **134**:1–8.
- Kundu, A., Ausaf, T. and Rajaraman, S. (2018). 3D Printing, Ink Casting and Micromachined Lamination (3D PICL μ M): A Makerspace Approach to the Fabrication of Biological Microdevices. *Micromachines* **9**:85.
- Kurakula, M. and Rao, G.S.N.K. (2020). Pharmaceutical assessment of polyvinylpyrrolidone (PVP): As excipient from conventional to controlled delivery systems with a spotlight on COVID-19 inhibition. *Journal of Drug Delivery Science and Technology* **60**:102046.
- Kurzmann, C. *et al.* (2017). Evaluation of Resins for Stereolithographic 3D-Printed Surgical Guides: The Response of L929 Cells and Human Gingival Fibroblasts. *BioMed Research International* [Online] **2017**:1–11. Available at: <https://www.hindawi.com/journals/bmri/2017/4057612/>.
- Lahiji, S.F., Dangol, M. and Jung, H. (2015). A patchless dissolving microneedle delivery system enabling rapid and efficient transdermal drug delivery. *Scientific reports* **5**:7914.
- Larraneta, E. *et al.* (2016). Microneedles: A New Frontier in Nanomedicine Delivery. *Pharmaceutical Research* **33**:1055–1073.
- Larrañeta, E. *et al.* (2016). Microneedle arrays as transdermal and intradermal drug delivery systems: Materials science, manufacture and commercial development. **104**:1–32.
- Lee, H.J. *et al.* (2018). MEMS devices for drug delivery. *Advanced Drug Delivery Reviews* **128**:132–147.
- Lee, K.J. *et al.* (2020). A practical guide to the development of microneedle systems – In clinical trials or on the market. *International Journal of Pharmaceutics* **573**:118778.
- Lee, K.S. *et al.* (2008). Advances in 3D nano/microfabrication using two-photon

- initiated polymerization. *Progress in Polymer Science* **33**:631–681.
- Leone, M. *et al.* (2017). Dissolving Microneedle Patches for Dermal Vaccination. *Pharmaceutical Research* **34**:2223–2240.
- Liaw, C. and Guvendiren, M. (2017). Current and emerging applications of 3D printing in medicine. *Biofabrication* **9**:024102.
- Liebelt, E. and Shannon, M. (1993). Small doses, big problems. *Pediatric Emergency Care* [Online] **9**:292–297. Available at: <http://journals.lww.com/00006565-199310000-00008>.
- Lim, S.H. *et al.* (2020). Geometrical optimisation of a personalised microneedle eye patch for transdermal delivery of anti-wrinkle small peptide. *Biofabrication* **12**:035003.
- Lim, S.H., Ng, J.Y. and Kang, L. (2017). Three-dimensional printing of a microneedle array on personalized curved surfaces for dual-pronged treatment of trigger finger. *Biofabrication* **9**:1–13.
- Ling, M.H. and Chen, M.C. (2013). Dissolving polymer microneedle patches for rapid and efficient transdermal delivery of insulin to diabetic rats. *Acta Biomaterialia* **9**:8952–8961.
- Liu, B. *et al.* (2017). Rapid Fabrication of Microneedles using Magnetorheological Drawing Lithography *Acta Biomaterialia* Rapid fabrication of microneedles using magnetorheological drawing lithography. *Acta Biomaterialia* **65**:283–291.
- Liu, H. *et al.* (2020). Recent Advances in Inhaled Formulations and Pulmonary Insulin Delivery Systems. *Curr Pharm Biotechnol* **21**:180–193.
- Liu, S. *et al.* (2012). The development and characteristics of novel microneedle arrays fabricated from hyaluronic acid, and their application in the transdermal delivery of insulin. *Journal of Controlled Release* **161**:933–941.
- Lopez-Ramirez, M.A. *et al.* (2020). Built-In Active Microneedle Patch with Enhanced Autonomous Drug Delivery. *Advanced Materials* **32**:1–10.
- Lu, Y. *et al.* (2015). Microstereolithography and characterization of poly(propylene fumarate)-based drug-loaded microneedle arrays. *Biofabrication* **7**:045001.

- Lutton, R.E.M. *et al.* (2015). Microneedle characterisation: the need for universal acceptance criteria and GMP specifications when moving towards commercialisation. *Drug Delivery and Translational Research* **5**:313–331.
- Luzuriaga, M.A. *et al.* (2018). Biodegradable 3D printed polymer microneedles for transdermal drug delivery. *Lab on a Chip* **18**:1223–1230.
- van der Maaden, K. *et al.* (2015). Microneedle-based drug and vaccine delivery via nanoporous microneedle arrays. *Drug Delivery and Translational Research*:397–406.
- Manning, M.C. *et al.* (2010). Stability of protein pharmaceuticals: An update. *Pharmaceutical Research* **27**:544–575.
- Mansfield, A.S. and Jatoi, A. (2013). Asphyxiation with a Fentanyl Patch. *Case Reports in Oncology* **6**:242–244.
- Mansoor, I. *et al.* (2013). Arrays of hollow out-of-plane microneedles made by metal electrodeposition onto solvent cast conductive polymer structures. *Journal of Micromechanics and Microengineering* **23**:085011.
- Mansoor, S. *et al.* (2019). Polymer-Based Nanoparticle Strategies for Insulin Delivery. *Polymers* **11**:1380.
- Mao, M. *et al.* (2017). The emerging frontiers and applications of high-resolution 3D printing. *Micromachines* **8**:1–20.
- Marques, M.J. *et al.* (2018). Complex master-slave for long axial range swept-source optical coherence tomography. *OSA Continuum* **1**:1251.
- Marshall, S., Sahm, L.J. and Moore, A.C. (2016). The success of microneedle-mediated vaccine delivery into skin. *Human Vaccines & Immunotherapeutics* **12**:2975–2983.
- Martanto, W. *et al.* (2006). Microinfusion Using Hollow Microneedles. *Pharmaceutical Research* **23**:104–113.
- Martanto, W. *et al.* (2004). Transdermal Delivery of Insulin Using Microneedles in Vivo. *Pharmaceutical Research* **21**:947–952.
- Mau, R. *et al.* (2019). Preliminary Study on 3D printing of PEGDA Hydrogels for Frontal Sinus Implants using Digital Light Processing (DLP). *Current Directions*

in Biomedical Engineering **5**:249–252.

- Mayer, J.P., Zhang, F. and DiMarchi, R.D. (2007). Insulin structure and function. *Peptide Science* [Online] **88**:687–713. Available at: <http://doi.wiley.com/10.1002/bip.20734>.
- Mcallister, D. V *et al.* (2003). Microfabricated needles for transdermal delivery of macromolecules and nanoparticles : Fabrication methods and transport studies. **100**:13755–13760.
- McConville, A., Hegarty, C. and Davis, J. (2018). Mini-Review: Assessing the Potential Impact of Microneedle Technologies on Home Healthcare Applications. *Medicines* **5**:50.
- McCrudden, M.T.C. *et al.* (2014). Considerations in the sterile manufacture of polymeric microneedle arrays. *Drug Delivery and Translational Research* **5**:3–14.
- Migalska, K. *et al.* (2011). Laser-Engineered Dissolving Microneedle Arrays for Transdermal Macromolecular Drug Delivery. *Pharmaceutical Research* **28**:1919–1930.
- Miller, P.R. *et al.* (2011). Integrated carbon fiber electrodes within hollow polymer microneedles for transdermal electrochemical sensing. *Biomicrofluidics* **5**:013415.
- Moussi, K. *et al.* (2020). Biocompatible 3D Printed Microneedles for Transdermal, Intradermal, and Percutaneous Applications. *Advanced Engineering Materials* **22**:1–10.
- Napadensky, E. (2009). Inkjet 3D Printing. In: *The Chemistry of Inkjet Inks*. WORLD SCIENTIFIC, pp. 255–267. Available at: http://www.worldscientific.com/doi/abs/10.1142/9789812818225_0013.
- Nesic, D. *et al.* (2020). Could 3D printing be the future for oral soft tissue regeneration? *Bioprinting* **20**:e00100.
- Ng, L.C. and Gupta, M. (2020). Transdermal drug delivery systems in diabetes management: A review. *Asian Journal of Pharmaceutical Sciences* **15**:13–25.
- Ning, X. *et al.* (2020). A Double-Layered Microneedle Platform Fabricated through Frozen Spray-Coating. *Advanced Healthcare Materials* **9**:1–9.

- Oakdale, J.S. *et al.* (2016). Post-print UV curing method for improving the mechanical properties of prototypes derived from two-photon lithography. *Optics Express* **24**:27077.
- Oberli, M.A. *et al.* (2014). Ultrasound-enhanced transdermal delivery: recent advances and future challenges. *Therapeutic Delivery* **5**:843–857.
- Ohtake, S., Kita, Y. and Arakawa, T. (2011). Interactions of formulation excipients with proteins in solution and in the dried state. *Advanced Drug Delivery Reviews* **63**:1053–1073.
- Olatunji, O. *et al.* (2013). Influence of array interspacing on the force required for successful microneedle skin penetration: Theoretical and practical approaches. *Journal of Pharmaceutical Sciences* **102**:1209–1221.
- Ovsianikov, A. *et al.* (2007). Two Photon Polymerization of Polymer Ceramic Hybrid Materials for Transdermal Drug Delivery. *International Journal of Applied Ceramic Technology* **4**:22–29.
- Paillet-Mattei, C., Bec, S. and Zahouani, H. (2008). In vivo measurements of the elastic mechanical properties of human skin by indentation tests. *Medical Engineering and Physics* **30**:599–606.
- Pan, Q. *et al.* (2020). Investigation of bone reconstruction using an attenuated immunogenicity xenogenic composite scaffold fabricated by 3D printing. *Bio-Design and Manufacturing* **3**:396–409.
- Park, J.H., Allen, M.G. and Prausnitz, M.R. (2005). Biodegradable polymer microneedles: Fabrication, mechanics and transdermal drug delivery. *Journal of Controlled Release* **104**:51–66.
- Park, J.H. and Prausnitz, M.R. (2010). Analysis of Mechanical Failure of Polymer Microneedles by Axial Force. *Journal of the Korean Physical Society* **56**:1223–1227.
- Pastore, M.N. *et al.* (2015). Transdermal patches: History, development and pharmacology. *British Journal of Pharmacology* **172**:2179–2209.
- Pearton, M. *et al.* (2012). Microneedle delivery of plasmid DNA to living human skin: Formulation coating, skin insertion and gene expression. *Journal of Controlled*

Release **160**:561–569.

- Pere, C.P.P. *et al.* (2018). 3D printed microneedles for insulin skin delivery. *International Journal of Pharmaceutics* **544**:425–432.
- Pissinato Pere, C.P. (2019). *Transdermal Microneedles for Insulin Delivery*. University of Kent.
- Plamadeala, C. *et al.* (2020). Bio-inspired microneedle design for efficient drug/vaccine coating. *Biomedical Microdevices* **22**:1–9.
- Prausnitz, M.R. (2004). Microneedles for transdermal drug delivery. *Advanced Drug Delivery Reviews* **56**:581–587.
- Prausnitz, M.R. and Langer, R. (2009). Transdermal drug delivery. *Nature biotechnology* **26**:1261–1268.
- Prestrelski, S.J. *et al.* (1993). Dehydration-induced conformational transitions in proteins and their inhibition by stabilizers. *Biophysical Journal* **65**:661–671.
- Di Prima, M. *et al.* (2015). Additively manufactured medical products – the FDA perspective. *3D Printing in Medicine* **2**:1.
- Rahim, T.N.A.T., Abdullah, A.M. and Md Akil, H. (2019). Recent Developments in Fused Deposition Modeling-Based 3D Printing of Polymers and Their Composites. *Polymer Reviews* **59**:589–624.
- Rankin, T.M. *et al.* (2014). Three-dimensional printing surgical instruments: are we there yet? *Journal of Surgical Research* **189**:193–197.
- Rawling, A. (2006). Ethnic skin types: are there differences in skin structure and function. *International Journal of Cosmetic Science* **29**:79–93.
- Resnik, D. *et al.* (2018). In Vivo Experimental Study of Noninvasive Insulin Microinjection through Hollow Si Microneedle Array. *Micromachines* **9**:40.
- Rivet, S. *et al.* (2016). Complex master slave interferometry. *Optics Express* **24**:2885.
- Robertson, C. *et al.* (2020). The Impact of Externally Worn Diabetes Technology on Sexual Behavior and Activity, Body Image, and Anxiety in Type 1 Diabetes. *Journal of Diabetes Science and Technology* **14**:303–308.

- Ross, S. *et al.* (2015). Inkjet printing of insulin microneedles for transdermal delivery. *Drug Delivery and Translational Research* **5**:451–461.
- Rzhevskiy, A.S. *et al.* (2018). Microneedles as the technique of drug delivery enhancement in diverse organs and tissues. *Journal of Controlled Release* **270**:184–202.
- Sahoo, N. *et al.* (2020). Post impact droplet hydrodynamics on inclined planes of variant wettabilities. *European Journal of Mechanics, B/Fluids* **79**:27–37.
- Samant, P.P. and Prausnitz, M.R. (2018). Mechanisms of sampling interstitial fluid from skin using a microneedle patch. *Proceedings of the National Academy of Sciences of the United States of America* **115**:4583–4588.
- Schmidleithner, C. and Kalaskar, D.M. (2018). Stereolithography. In: *IntechOpen*. Available at: <https://www.intechopen.com/books/advanced-biometric-technologies/liveness-detection-in-biometrics>.
- Shaw, J. and Theeuwes, F. (1985). Transdermal dosage forms. In: Prescott, L. and Nimmo, W. eds. *Rate Control in Drug Therapy*. Churchill Livingstone, pp. 65–70.
- Shidid, D. *et al.* (2016). Just-in-time design and additive manufacture of patient-specific medical implants. *Physics Procedia* **83**:4–14.
- Sreerama, N. and Woody, R.W. (2000). Estimation of protein secondary structure from circular dichroism spectra: Comparison of CONTIN, SELCON, and CDSSTR methods with an expanded reference set. *Analytical Biochemistry* **287**:252–260.
- Stoeber, B. and Liepmann, D. (2005). Arrays of hollow out-of-plane microneedles for drug delivery. *Journal of Microelectromechanical Systems* **14**:472–479.
- Stratasys (2020). *ABS-M30i Material Safety Datasheet*. [Online]. Available at: <https://shrinkwrapcontainments.com/Images/media/SDS Shrink Film.pdf>.
- Stratasys (2011). *MED610 Material Safety Data Sheet*. [Online]. Available at: <https://www.sys-uk.com/wp-content/uploads/2016/01/MSDS-Clear-Bio-Compatible-MED610-English-US-1.pdf>.
- Stratasys (2017). *PC-ISO Datasheet*. [Online]. Available at: <https://www.stratasys.com/materials/search/pc-iso>.

- Sun, H.-B. and Kawata, S. (2006). Two-Photon Photopolymerization and 3D Lithographic Microfabrication. In: *Advances in Polymer Science*. pp. 169–273.
- Szeto, B. *et al.* (2021). Novel 3D-printed hollow microneedles facilitate safe, reliable, and informative sampling of perilymph from guinea pigs. *Hearing Research* **400**:108141.
- Tappa, K. and Jammalamadaka, U. (2018). Novel Biomaterials Used in Medical 3D Printing Techniques. *Journal of Functional Biomaterials* **9**:17.
- Thompson, M.K. *et al.* (2016). Design for Additive Manufacturing: Trends , Opportunities , Considerations and Constraints. **65**:737–760.
- Trenfield, S.J. *et al.* (2019). Shaping the future: recent advances of 3D printing in drug delivery and healthcare. *Expert Opinion on Drug Delivery* **16**:1081–1094.
- Tsioris, K. *et al.* (2012). Fabrication of silk microneedles for controlled-release drug delivery. *Advanced Functional Materials* **22**:330–335.
- Tumbleston, J.R. *et al.* (2015). Continuous liquid interface production of 3D objects. *Science* **347**:1349–1352.
- Turner, J.G. *et al.* (2021). Hydrogel-Forming Microneedles: Current Advancements and Future Trends. *Macromolecular Bioscience* **21**:2000307.
- Uddin, M.J. *et al.* (2020). 3D printed microneedles for anticancer therapy of skin tumours. *Materials Science and Engineering C* **107**:110248.
- Uddin, M.J. *et al.* (2015). Inkjet printing of transdermal microneedles for the delivery of anticancer agents. *International Journal of Pharmaceutics* **494**:593–602.
- Vasudeva, N. and Mishra, S. (2016). Skin and its Appendages. In: *Inderbir Singh's Textbook of Human Histology*. Jaypee Brothers Medical Publishers (P) Ltd., pp. 126–126. Available at: <https://www.jaypeedigital.com/book/9789385999321/chapter/ch11>.
- Vertex (2016). *Certificate of Biocompatibility*. [Online]. Available at: https://support.formlabs.com/s/article/Certifications-and-standards?language=en_US.
- Vinayakumar, K.B. *et al.* (2015). Development of cup shaped microneedle array for

- transdermal drug delivery. *Biointerphases* **10**:021008.
- Vrdoljak, A. *et al.* (2016). Induction of broad immunity by thermostabilised vaccines incorporated in dissolvable microneedles using novel fabrication methods. *Journal of Controlled Release* **225**:192–204.
- Waghule, T. *et al.* (2019). Microneedles: A smart approach and increasing potential for transdermal drug delivery system. *Biomedicine and Pharmacotherapy* **109**:1249–1258.
- Walker, J.M. *et al.* (2016). Manufacture and evaluation of 3-dimensional printed sizing tools for use during intraoperative breast brachytherapy. *Advances in Radiation Oncology* **1**:132–135.
- Walther, J. *et al.* (2011). Optical coherence tomography in biomedical research. *Analytical and Bioanalytical Chemistry* **400**:2721–2743.
- Wang, C. *et al.* (2020). 3D printing of bone tissue engineering scaffolds. *Bioactive Materials* **5**:82–91.
- Wang, M., Hu, L. and Xu, C. (2017). Recent advances in the design of polymeric microneedles for transdermal drug delivery and biosensing. *Lab on a Chip* **17**:1373–1387.
- Wang, P.M. *et al.* (2006). Precise microinjection into skin using hollow microneedles. *Journal of Investigative Dermatology* **126**:1080–1087.
- Warr, C. *et al.* (2020). Biocompatible PEGDA Resin for 3D Printing. *ACS Applied Bio Materials* **3**:2239–2244.
- Waugh, A. and Grant, A. (2014). *Anatomy & Physiology*. 12th ed. Churchill Livingstone, Elsevier.
- Wermeling, D.P. *et al.* (2008). Microneedles permit transdermal delivery of a skin-impermeant medication to humans. *Proceedings of the National Academy of Sciences of the United States of America* **105**:2058–63.
- Whitmore, L. and Wallace, B.A. (2004). DICHROWEB, an online server for protein secondary structure analyses from circular dichroism spectroscopic data. *Nucleic Acids Research* **32**:668–673.

- Whitmore, L. and Wallace, B.A. (2008). Protein secondary structure analyses from circular dichroism spectroscopy: Methods and reference databases. *Biopolymers* **89**:392–400.
- Wong, J.Y. and Pfahnl, A.C. (2014). 3D Printing of Surgical Instruments for Long-Duration Space Missions. *Aviation, Space, and Environmental Medicine* **85**:758–763.
- Wong, K.C. (2016). 3D-printed patient-specific applications in orthopedics. *Orthopedic Research and Reviews* **8**:57–66.
- Wu, D. *et al.* (2015). Determination of contact angle of droplet on convex and concave spherical surfaces. *Chemical Physics* **457**:63–69.
- Wu, M. *et al.* (2020). Assisted 3D printing of microneedle patches for minimally invasive glucose control in diabetes. *Materials Science and Engineering C* **117**:111299.
- Xenikakis, I. *et al.* (2019). Fabrication and finite element analysis of stereolithographic 3D printed microneedles for transdermal delivery of model dyes across human skin in vitro. *European Journal of Pharmaceutical Sciences* **137**:104976.
- Xiong, X.Y., Tam, K.C. and Gan, L.H. (2005). Release kinetics of hydrophobic and hydrophilic model drugs from pluronic F127/poly(lactic acid) nanoparticles. *Journal of Controlled Release* **103**:73–82.
- Yao, W. *et al.* (2020). 3D Printed Multi-Functional Hydrogel Microneedles Based on High-Precision Digital Light Processing. *Micromachines* **11**:1–11.
- Yeung, C. *et al.* (2019). A 3D-printed micro fluidic-enabled hollow microneedle architecture for transdermal drug delivery. *Biomicrofluidics* **13**:064125.
- Yonemoto, Y. and Kunugi, T. (2014). Wettability model for various-sized droplets on solid surfaces. *Physics of Fluids* **26**:082110.
- Yousef, H. *et al.* (2020). *Histology, Skin Appendages*. StatPearls Publishing.
- Yu, J. *et al.* (2017). Bioresponsive transcutaneous patches. *Current Opinion in Biotechnology* **48**:28–32.
- Zhao, X. *et al.* (2017). Formulation of hydrophobic peptides for skin delivery via coated

microneedles. *Journal of Controlled Release* **265**:2–13.

Zhou, C.-P. *et al.* (2010). Transdermal delivery of insulin using microneedle rollers in vivo. *International Journal of Pharmaceutics* **392**:127–133.

APPENDIX I

MATLAB code for the solution of the wetting model presented in Chapter 3.

```
VL=0.0003; %microliters

R=0.25;    %mm

theta0=1.23918; %71 degrees in rad

Vstar=VL/((4/3)*pi()*R^3);

syms x

f=@(y) (2-3*cos(y)+cos(y)^3)/4;

sol=vpasolve(((sin(x-theta0)^3)*f(x)/sin(x)^3)-f(x-theta0)==Vstar, x);

theta=pi-mod(-sol,pi);

%Rad to degrees

thetadeg=theta*180/pi
```